UNIVERSITÀ DEGLI STUDI DI PADOVA

Sede Amministrativa: Università degli Studi di Padova

Dipartimento di Fisica Tecnica

SCUOLA DI DOTTORATO DI RICERCA IN INGEGNERIA INDUSTRIALE

INDIRIZZO FISICA TECNICA

CICLO XXI

EXPERIMENTAL STUDY ON FLOW BOILING OF REFRIGERANTS INSIDE HORIZONTAL TUBES

Direttore della Scuola: Ch.mo Prof. Paolo F. Bariani
Supervisore: Ch.mo Prof. Ezio Fornasieri
Co-Supervisore: Ing. Davide Del Col

Dottorando: Andrea Padovan

TABLE OF CONTENTS

ABSTRACT

In this thesis an experimental study on flow boiling of refrigerants inside horizontal tubes is presented. Vaporization inside horizontal tubes is commonly used in evaporators of machines for refrigeration and air-conditioning applications. Most of flow boiling data, available in the open literature for HFC fluids, refer to a narrow range of saturation temperatures, resulting in a limited range of reduced pressure in the refrigerant vaporization data sets. The present data are taken at higher saturation temperature as compared to common air-conditioning applications. This allows to extend the reduced pressure range in the databases.

The adoption of new refrigerants, such as carbon dioxide, with different thermodynamic and thermo-physical properties, requires to extend the pressure range of application of existing heat transfer predictive methods. When evaporating at 2 °C, for instance carbon dioxide has a saturation pressure of 3673 kPa and 0.5 reduced pressure, which is far higher as compared to common halogenated refrigerants. For R410A, 2 °C saturation temperature corresponds to 0.17 reduced pressure, while 0.39 reduced pressure is associated to 30 °C saturation temperature.

On the other hand, an example of high evaporating temperature application of HFC refrigerants is represented by heat pump heat dryers.

In this thesis new experimental measurements of heat transfer coefficient during flow boiling of R134a and R410A at 30 °C and 40 °C saturation temperature (reduced pressure from 0.19 to 0.5) inside a horizontal microfin tube are reported and discussed for a wide range of operative conditions: mass velocity from 80 to 600 kg/(m^2 s), heat flux from 14 to 83.5 kW/m^2 and vapour quality from 0.1 to 0.99. As compared to plain tubes, the presence of the fins modifies the two-phase flow pattern; for instance, capillarity forces play a role in microfin tube, at low mass velocity, and there is need to assess the prediction capability of the heat transfer models at these same conditions. Moreover, the fins also affect the conditions leading to dry-out and partial dry-out.

The heat transfer coefficients in microfin tubes are compared with heat transfer smooth tube data for R134a and R410A at the same operating conditions.

The heat transfer models by Koyama *et al.* (1996), Thome *et al.* (1999), Cavallini *et al.* (2006), Chamra and Mago (2007) and Hamilton *et al.* (2008) are compared with the new measurements of heat transfer coefficient in microfin tube. In the case of smooth tube, heat transfer data for R134a and R410A are used to assess the accuracy of the models by Gungor and Winterton (1987), Kandlikar (1991), Liu and Winterton (1991) and Wojtan *et al.* (2005b).

The development of diabatic two-phase flow pattern maps is a key aspect to improve the understanding of the role of heat transfer mechanisms, but a flow pattern map is not yet available for flow boiling in microfin tube. Present flow boiling data in smooth and microfin tube have been here plotted in the diabatic two-phase flow pattern map by Wojtan *et al.* (2005a) for plain tube: the predicted flow patterns are discussed by analyzing the experimental heat transfer results. The transition boundary between stratified and annular flow regime, provided by Wojtan *et al.* (2005a), is compared with the transition curve from stratified to annular flow for condensation in microfin tube; in fact, during vaporization and condensation in microfin tube annular flow pattern occurs earlier as compared to a plain tube, at the same operating conditions.

The prediction of the onset of dry-out is fundamental to get a more comprehensive understanding of the validity range of flow boiling heat transfer models and then to improve the design of an evaporator; but, few predicting correlations are available in the open literature, especially for microfin tube. New measurements of dry-out inception vapour

quality in microfin tube, are here presented and discussed; the measured values are then compared with the correlation by Mori *et al.* (2000) for horizontal microfin tube.

Measurements of pressure drop in microfin tube during adiabatic two-phase flow at 30 °C and 40 °C are reported and compared with the model by Cavallini *et al.* (1999).

Addendum

An experimental study on solar energy conversion for applications in solar cooling have been also carried out during the Doctorate course. In particular a new test rig for the measurement of efficiency of solar collectors has been set up and calibrated. Moreover, a new measuring system for the measurement of solar radiation in horizontal and tilted-oriented planes has been set up. The experimental measurements of solar radiation can be used to assess models for the prediction of solar radiation components on tilted-oriented surfaces. This part of the research is presented in the appendix, by reporting two papers on this activity.

SOMMARIO

In questa tesi viene presentato uno studio sperimentale sulla vaporizzazione di refrigeranti all’interno di un tubo orizzontale con superficie liscia e microalettata. La vaporizzazione interno tubo trova applicazione nelle macchine per la refrigerazione ed il condizionamento dell’aria. La maggior parte dei dati di scambio termico in vaporizzazione per fluidi HFC, disponibili in letteratura, si riferiscono ad un ristretto intervallo di temperature di saturazione, e quindi sono caratterizzati da un intervallo limitato di pressione ridotta. I dati nella presente tesi sono misurati a temperature più alte rispetto alle comuni applicazioni di condizionamento dell’aria. Ciò consente di estendere l’intervallo di pressione ridotta nei database.

L’adozione di nuovi refrigeranti come l’anidride carbonica, con proprietà termodinamiche e termofisiche differenti rispetto ai refrigeranti di comune impiego, richiede di estendere l’intervallo di validità dei modelli per la previsione del coefficiente di scambio termico. Infatti, quando evapora alla temperature di 2 °C, l’anidride carbonica ha una pressione di saturazione di 3673 kPa e una pressione ridotta di 0.5, che è notevolmente più alta rispetto a quella dei comuni refrigeranti. Nel caso di R410A, alla temperatura di saturazione di 2 °C corrisponde una pressione ridotta di 0.17, mentre alla temperatura di saturazione di 30 °C è associata una pressione ridotta di 0.39.

Un esempio applicativo di vaporizzazione di fluidi HFC ad alta temperatura è rappresentato dalle macchine asciugatrici a pompa di calore.

In questa tesi vengono presentate nuove misure del coefficiente di scambio termico durante la vaporizzazione di R134a e R410A alla temperatura di saturazione di 30°C e 40°C (pressione ridotta da 0.19 a 0.5) all’interno di un tubo orizzontale microalettato. Le misure coprono un ampio intervallo di condizioni operative: portata di massa specifica tra 80 e 600 kg/(m^2 s), flusso termico specifico tra 14 e 83.5 kW/m^2 e titolo del vapore tra 0.1 e 0.99. Rispetto ad un tubo liscio, la presenza delle alette modifica il regime di deflusso in vaporizzazione. Per esempio a bassa portata di massa specifica, le forze di capillarità giocano un ruolo importante e c’è necessità di valutare l’accuratezza dei modelli di previsione di scambio termico a queste condizioni. La alette influenzano inoltre le condizioni operative che possono portare al dry-out.

Le misure del coefficiente di scambio termico in tubo microalettato sono state confrontate con dati di scambio termico durante la vaporizzazione di R134a e R410A in tubo liscio alle stesse condizioni operative.

I modelli per la stima del coefficiente di scambio termico di Koyama *et al.* (1995), Thome *et al.* (1997), Cavallini *et al.* (2006), Chamra e Mago (2007) and Hamilton *et al.* (2008) sono stati confrontati con le misure ad alta temperatura di saturazione effettuate per il tubo microlaettato. Nel caso del tubo liscio i dati di scambio termico in vaporizzazione per R134a e R410A sono stati confrontati con i modelli di Gungor e Winterton (1987), Kandlikar (1991), Liu e Winterton (1991) e Wojtan *et al.* (2005b).

Lo sviluppo di mappe di deflusso bifase è un aspetto decisivo per migliorare la comprensione del ruolo dei meccanismi di scambio termico; tuttavia non esiste ancora una mappa di deflusso per la vaporizzazione entro tubo microalettato. I dati di vaporizzazione di R134a e R410A in tubo liscio e microalettato sono sono stati qui diagrammati nella mappa di deflusso per vaporizzazione in tubo liscio di Wojtan *et al.* (2005a): il regime di deflusso stimato dalla mappa è stato discusso, analizzando il corrispondente comportamento dei coefficienti in scambio termico. La curva di transizione tra regime di deflusso stratificato ed anulare, fornita dalla mappa di Wojtan *et al.* (2005a), è stata confrontata con la curva di transizione tra regime stratificato ed anulare, che si ha nel caso della condensazione in tubo

microalettato; sia durante la vaporizzazione che la condensazione all'interno di un tubo microalettato il regime di deflusso anulare avviene a portate più basse rispetto al caso di un tubo liscio.

La previsione dell'inizio del regime di dry-out è un altro aspetto fondamentale per ottenere una maggiore comprensione dell'intervallo di applicazione dei modelli di scambio termico e migliorare così la progettazione dell'evaporatore. Tuttavia, poche correlazioni sono disponibili in letteratura per la stima del titolo di dry-out incipiente, soprattutto nel caso di tubo microalettato. Nuove misure del titolo di vapore di inizio dry-out, nel tubo micro alettato, sono qui presentate confrontate con la correlazione di Mori *et al.* (2000).

Misure sperimentali della caduta di pressione attraverso il tubo microalettato durante deflusso bifase adiabatico alla temperatura di saturazione di 30 °C e 40 °C sono qui riportate e confrontate con il modello di previsione di Cavallini *et al.* (1999) per tubi con superficie intensificata.

Addendum

Durante il corso di dottorato è stato inoltre condotto uno studio sperimentale sulla conversione dell'energia solare per applicazioni di "solar cooling" (raffrescamento solare). In particolare è stato installato e calibrato un nuovo impianto di prova per la misura dell'efficienza dei collettori solari ed è stato messo a punto nuovo sistema di misura della radiazione solare in piani diversamente orientati. Le misure sperimentali hanno consentito di verificare l'accuratezza dei modelli per la stima delle componenti della radiazione solare su superfici con diversa orientazione. Questa parte della ricerca è presentata in appendice riportando due articoli su questa attività.

CHAPTER 1

STATE OF THE ART ON HEAT TRANSFER DURING FLOW BOILING INSIDE HORIZONTAL TUBES

1.1 Two-phase flow patterns and heat transfer mechanisms

Flow boiling of refrigerants inside horizontal tubes is commonly used in evaporators of machines for refrigeration and air-conditioning applications. Heat transfer during in-tube vaporization is based on two main mechanisms: nucleate boiling and convective evaporation. These mechanisms are combined in a manner which depends on many variables, as saturation pressure, thermo-physical and thermodynamics properties of the fluid, vapour quality, mass velocity, heat flux and surface roughness of the tube.

During vaporization and condensation inside horizontal tubes, the two-phase flow is influenced by the effect of the gravity force, which results in the asymmetrical distribution of vapour and liquid phases. Following the specific literature, the generally accepted two-phase flow patterns are shown in Figure 1.1.

In bubbly flow, the vapour phase is distributed as numerous discrete bubbles in the continuous liquid phase and tends to travel in the upper half of the pipe; at high vapour velocity a more uniform distribution can appear. Bubbly flow occurs at high mass velocity.

Stratified flow pattern is characterized by the complete separation of the liquid and vapour phases due to the gravity force, with the liquid flowing in the lower part of the pipe; the horizontal liquid-vapour interface is relatively smooth. When the liquid-vapour interface becomes disturbed, the pattern is known as stratified-wavy flow; the amplitude of waves depends on the relative velocity of the two phases, but they do not reach the top of the tube.

Intermittent flow pattern is grouped in plug and slug flow regimes. Due to the unsteadiness of the flow, the waves intermittently wash the top of the tube while the upper surface, behind the wave, is wetted by a residual liquid film. In plug flow, elongated vapour bubbles flow in the upper part of the pipe and the liquid phase is continuous along the bottom half of the tube. In slug flow, large amplitude waves pick up to form frothy slugs in the channel.

Annular flow pattern is obtained when the liquid wets all the tube periphery with the vapour flowing in the centre of the tube. Due to gravity, the liquid film thickness is not uniform around the periphery, but it is higher at the bottom.

Mist flow is characterized by small liquid droplets entrained in the continuous vapour phase.

During in-tube flow boiling several flow patterns can appear and the two-phase flow structure influences the role of heat transfer mechanisms. For instance, Figure 1.2 reports the measured and calculated heat transfer coefficient for R134a and the corresponding flow pattern observed by Rabah and Kabelac (2008); the calculated nucleate boiling and convective components are also shown. Heat transfer coefficient increases with vapour quality until it reaches a peak, which is followed by a sharp falloff. The variation of the slope of heat transfer coefficient with respect to vapour quality may be attributed to the change in flow pattern and to the different boiling mechanisms encountered.

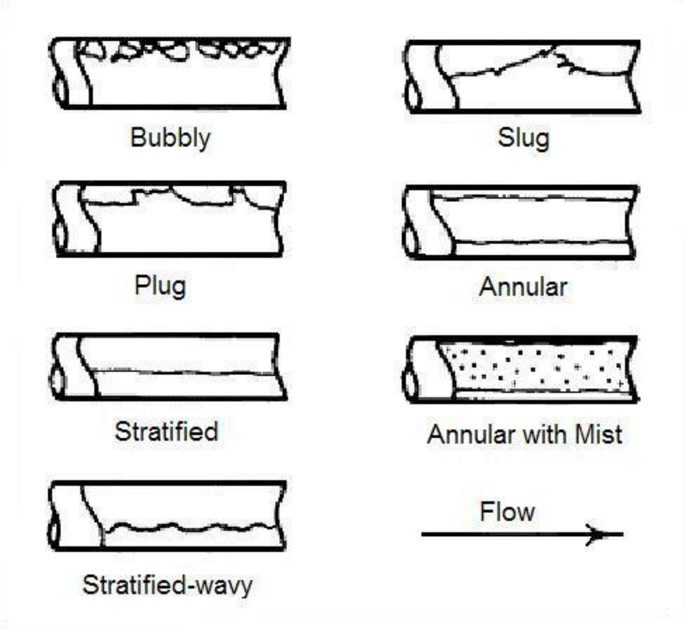

Figure 1.1. Two-phase flow patterns inside horizontal tube.

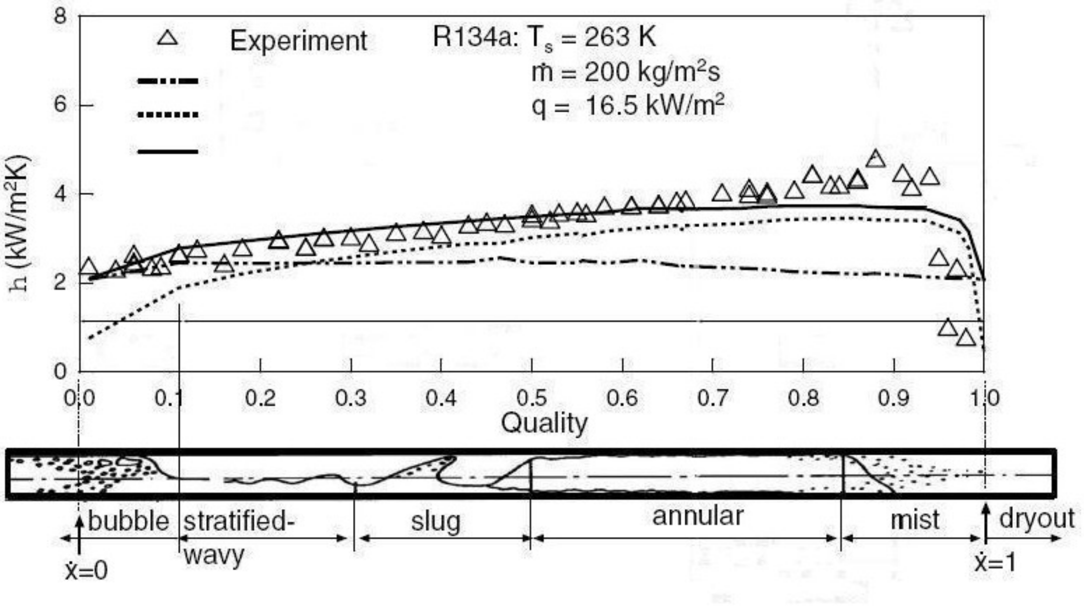

Figure 1.2. Experimental and calculated heat transfer coefficient vs. vapour quality by Rabah and Kabelac (2008). The calculated nucleate boiling and convective coefficients are reported. The two-phase flow pattern experimentally observed is depicted.

In the early stage of boiling, under 0.1 vapour quality, the flow pattern is identified as bubbly flow and nucleate boiling is known as the dominant mechanism; the calculated nucleate boiling curve agrees very well with the experimental data. In the central region, between 0.1 and 0.65, flow pattern varies from stratified to annular and both the nucleate boiling and convective mechanisms are present; the measured heat transfer coefficient matches well with the calculated ones, obtained by the combined contribution of nucleate and convective boiling. The heat transfer coefficient continues to raise until the onset of dry-out occurs.

At low vapour quality, the temperature difference between wall and fluid is high and the heat transfer is nucleate boiling dominated. However, at higher vapour quality, the two-phase flow can become annular and heat is transferred by a convective mechanism across the liquid film around the tube periphery to the liquid-vapour boundary, where evaporation occurs. The liquid film becomes thinner because of the film evaporation and the thermal resistance of the liquid film decreases: as consequence, the liquid superheat diminishes and a suppression of the nucleate boiling contribution occurs. At this condition the convective mechanism becomes dominant.

Kattan *et al.* (1998) proposed a diabatic two-phase flow pattern map for flow boiling inside a horizontal smooth tube. The map is expressed in coordinates mass velocity versus vapour quality and the evolution of the flow pattern transitions at fixed mass velocities with increasing vapour quality along the tube evaporator can be observed.

Thome and El Hajal (2002) noted how mass velocity influenced the position of the transition curves between different flow regimes and they proposed a modified version of the diabatic map by Kattan *et al.* (1998).

Wojtan *et al.* (2005a) recently published a flow pattern map for flow boiling inside horizontal plain tubes, which gives new information on annular to dry-out and dry-out to mist flow transition. Moreover, they modified the stratified-wavy region, by dividing it in three sub-regions: slug, a mixing of slug and stratified-wavy, and stratified-wavy regions. The new transition curves were integrated in the Thome and El Hajal (2002) version of the diabatic map by Kattan *et al.* (1998).

Heat transfer during in-tube vaporization and condensation can be augmented by using enhanced tubes, as low-fin, microfin, cross-grooved and herringbone tubes.

Microfin tube is a copper tube, which presents a single set of 50 - 70 spiral fins, with helix angle between 6° and 30° and fin height from 0.1 to 0.25 mm; fins can have triangular or trapezoidal shape, with an apex angle from 25° to 90°. Cross-grooved tubes present an additional set of groove at the same spiral angle, but opposite angular direction. As compared to the standard microfin tube, herringbone tube presents micro-fins running in opposite directions in the lower and upper halves of the tube. Low-finned tubes have fewer fins, less than 30, with fin height higher than 0.4 mm. Microfin tube is successfully used in refrigeration and air-conditioning industry. As compared to a plain surface, microfin and cross grooved tubes can ensure a large heat transfer enhancement with a relatively low pressure drop increase. The main geometrical parameters of a microfin tube are depicted in Figure 1.3.

The presence of the fins can modify transition boundaries between flow regimes and the role of the heat transfer mechanisms. At the moment, a diabatic two-phase flow pattern map is not available in the case of flow boiling inside microfin tube.

Yoshida *et al.* (1988) performed visual observations during vaporization in spirally grooved tubes with mass velocity between 50 and 500 kg/(m^2 s). At low mass velocity, corresponding to stratified-wavy flow in smooth tubes, they observed the presence of liquid in the grooves at the top of the tube, even at 50 kg/(m^2 s).

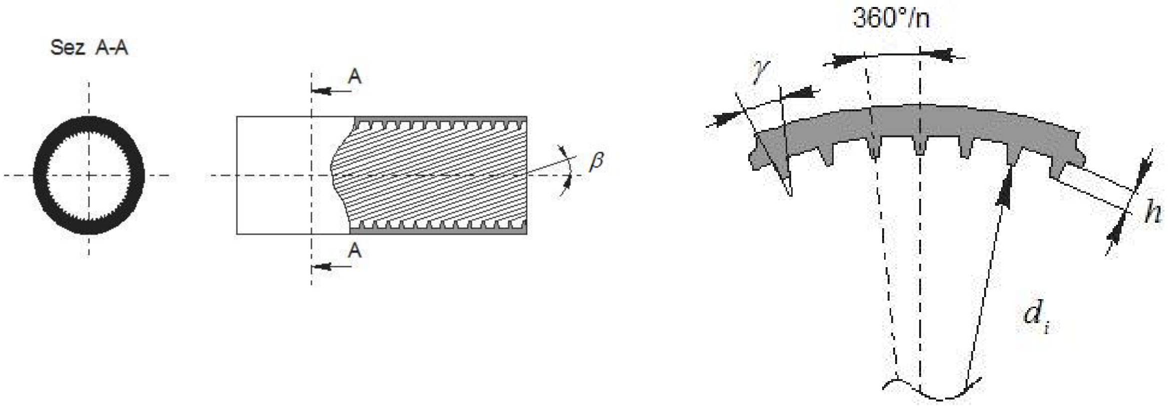

Figure 1.3. Geometrical parametrs of the microfin tube. The helix angle, β, the apex angle, γ, the fins pitch, p, the fin height, h, and the diameter at the fins tip, d_i, are indicated.

They suggested that part of the liquid in the lower region of the tube is lifted up to the top by a capillary action in the grooves with consequent thin meniscus liquid films on the sides of the grooves and high heat transfer coefficients. As the mass velocity increases, higher liquid velocities in the grooves and wider wetted portions of the grooved sides were observed. Finally, at mass velocity values higher than 200 kg/(m^2 s), annular flow exists and the fins were completely covered with liquid at vapour quality lower than 0.8. The surface tension effect should not be present when liquid fills the microfin grooves.

Chamra and Webb (1995) found equal heat transfer coefficients for condensation and evaporation in a cross-grooved tube for vapour quality greater than 0.5, under the same operative conditions. Both condensation and evaporation occur across a thin annular liquid film, suggesting that the heat transfer mechanism is the same. Under these conditions, the heat transfer during condensation is vapour shear dominated. In the low vapour quality region the evaporation coefficient is higher than the one measured during condensation, because of the nucleate boiling contribution. The nucleate boiling influenced range is smaller at higher mass velocities, suggesting a suppression of the nucleate boiling when the mass flux increases.

Singh *et al.* (1996) experimentally observed the flow pattern during flow boiling of R134a in a microfin tube. At mass velocity lower than 100 kg/(m^2 s) the two-phase flow was stratified, but, as mass velocity increased, annular flow occurred: 100 kg/(m^2 s) represented the transition mass flux value from stratified to annular flow.

Mori *et al.* (1999) measured the dry-out inception and completion quality for R134a inside horizontal smooth and microfin tubes. The dry-out inception quality is defined as the vapour quality at which the heat transfer begins to become worse because the liquid film in the upper part of the tube disappears; the dry-out completion quality is the value at which the heat transfer deterioration ends. In the microfin tube, the dry-out inception and completion qualities are larger as compared to the ones measured for the smooth tube.

Del Col *et al.* (2002) performed experimental measurements of heat transfer coefficient during condensation and vaporization in a microfin tube at equal saturation temperature. They found that the evaporation coefficient exceeded the condensation coefficient along the entire vapour quality range considered. The difference between the measured values was attributed to the nucleate boiling contribution. This result differed from the measurements by Chamra and Webb (1995) and a possible reason for this was searched in the different fins geometry and finish surface of the tube. However, the nucleate boiling component was found to give an important contribution to vaporization, especially for higher heat flux and lower vapour quality.

Yu *et al.* (2002) performed heat transfer measurements and flow pattern observations during flow boiling of R134a in horizontal microfin and smooth tubes. They measured the heat transfer coefficient at the top, side and bottom of the tube in several sections along the axial direction of the tube. In the smooth tube, when the two-phase flow was stratified, the heat transfer coefficient at the top was lower than the ones measured at the side and the bottom. In the case of the microfin tube, under the same operative conditions, the local heat transfer coefficients measured at the top, side and bottom for each tube section were relatively close. At low mass velocity, around 160 kg/(m^2 s), the flow regime observed in the microfin tube was already intermittent-slug and then annular at vapour quality greater than 0.3; in the case of the smooth tube, wavy flow still existed at these same conditions.

Filho *et al.* (2004) compared the flow pattern observed when R134a evaporates inside a microfin and a plain tube. At mass flow rate under 150 kg/(m^2 s), the grooves tend to move the liquid to the upper region of the tube, which results wetted. They observed a flow pattern similar to annular flow in smooth tubes, with a liquid layer of thickness higher than the microfins around the inner surface. When the mass velocity varies between 150 and 300 kg/(m^2 s), annular flow was visualized in the microfin tube. At 500 kg/(m^2 s) mass velocity and vapour quality around 0.5, liquid drops were visually observed in the central region of the tube and a significant reduction of the heat transfer coefficient was measured. As suggested by the authors, this could be related to the reduction in the liquid film thickness and to the consequent exposing of the fins tip in the vapour core; thus, the fins remove the liquid from the grooves and move it into the vapour core. At this same condition, the smooth tube presented an annular flow pattern.

Visual observations of the flow pattern during vaporization of R134a at -20 °C and 10 °C and R134a at -20 °C and 0 °C in a microfin tube were performed by Muller-Steinhagen and Spindler (2006) and by Spindler and Muller-Steinhagen (2009). The mass velocity ranged from 25 to 150 kg/(m^2 s). They reported the observed flow patterns in the Kattan *et al.* (1998) diabatic map for plain tubes: the experimental data show that, for the microfin tube, the transition from stratified-wavy to annular flow occurs at a lower mass velocity as compared to the transition line given by Kattan *et al.* (1998). The early transition in the microfin tube is related to the inner spiral grooves, where liquid can more easily move to the top part of the tube.

From the literature survey presented here, it can be concluded that, at low mass velocity values, the fins act to promote an annular type flow, because the liquid moves from the bottom to the upper region of the tube: the transition between stratified and not stratified flow occurs at a lower mass velocity as compared to a smooth tube. Moreover, the presence of the fins seems to reduce the range of operating conditions leading to dry-out and partial dry-out, whereas Filho *et al.* (2004) measured an early heat transfer degradation at high mass flux.

Finally, Thome (1996) attributed the large augmentation of the heat transfer coefficient of microfin tubes relative to plain tubes, operating at the same conditions, to the following characteristics:

- the increase in wetted surface area per unit length of tube, which tends to range from 1.4 to 1.9 depending on the characteristics of the fins;
- the increase in liquid phase convective heat transfer, because the fins enhance the liquid-only heat transfer coefficient similar to that for single-phase flow inside tubes, increasing the two-phase convective contribution;

- the increase in wetting around the circumference of the tube at low flow rates due to the capillary forces, which maintains the flow in the completely wetted regime rather than in a stratified flow regime;
- the effect of swirl and surface tension which can shift the mist flow or the partially dryout region at higher vapour qualities; the swirl action drives liquid droplets to the tube wall;
- the increase in nucleate boiling heat transfer due to the creation of more favourable nucleation sites between the fins, which partially shield the nucleation sites from the flow; moreover nucleate boiling occurs on the total wetted area.

1.2 Effect of thermo-physical and thermodynamic properties

Several experimental works have been published in the open literature, reporting heat transfer experimental data during flow boiling of halogenated refrigerants inside horizontal plain and enhanced tubes, and comparison with predictive models. Due to the global warming issue, carbon dioxide is candidate as new working fluid in machines for refrigeration and air-conditioning applications. Carbon dioxide is a fluid with a low critical temperature; thus, except when used as the low temperature refrigerant in cascade cycles, it is evaporated at much higher reduced pressure as compared to other refrigerants.

Besides, most of experimental data for HFC refers to conventional evaporating temperature, but new high temperature heat pumping applications require data at higher saturation temperature. An example is represented by heat pump clothes dryers, where the evaporating refrigerant subtracts heat from the hot air steam and evaporating temperature can reach higher values as compared to air-conditioning applications.

Most of predictive models are semi-empirical methods, based on experimental heat transfer data, thus, further measurements are needed to improve the prediction capability of the heat transfer coefficient, for the fluids and the operative conditions just discussed.

Recently new experimental heat transfer data during flow boiling inside a horizontal tube at quite high saturation temperature have been published. Greco and Vanoli (2005) measured the heat transfer coefficient of R134a during vaporization inside a plain tube at 17.5 °C and 28.6 °C. Cho and Kim (2007) presented measurements of carbon dioxide evaporating at 20 °C in smooth and microfin horizontal tubes. Silva Lima *et al.* (2009) reported measurements of flow boiling heat transfer coefficients of R134a inside a horizontal plain tube at 20 °C saturation temperature.

Table 1.1 presents some thermodynamics and thermo-physical properties for refrigerants R134a at 5 °C and 30 °C saturation temperature, R410A at 5 °C and 30 °C saturation temperature and carbon dioxide at -5 °C saturation temperature.

In the case of R410A, the reported saturation pressure is the average value between the bubble and the dew point at the same composition.

A higher saturation pressure results in high vapour density, low surface tension, high vapour viscosity and this yields flow boiling heat transfer and two-phase flow characteristics quite different from those of conventional data.

When evaporating CO_2 at -5 °C, the reduced pressure is 0.39, which is far higher as compared to the value of common halogenated refrigerants. For R134a, 30 °C saturation temperature corresponds to a reduced pressure value of 0.190, while a 0.072 reduced pressure is associated to 0 °C saturation temperature. In the case of R410A, 5 °C and 30 °C saturation temperature corresponds to 0.19 and 0.39 reduced pressure respectively.

Table 1.1. Thermo-physical and thermodynamics properties of R134a, R410A and CO_2 at different saturation temperature.

	R134a 5 °C	R134a 30 °C	R410A 5 °C	R410A 30 °C	CO_2 -5 °C
p_s [kPa]	350	770	935	1886	3046
p_r	0.086	0.190	0.191	0.385	0.392
M	102.03	102.03	72.585	72.585	44.01
ρ_l [kg/m^3]	1278	1187	1150	1033	956
ρ_v [kg/m^3]	17	38	36	77	83
ρ_l/ρ_v	74.61	31.64	32.06	77	83
μ_l [μPa s]	250.1	183.1	158.9	113.2	108.4
μ_v [μPa s]	10.9	11.9	12.9	15.0	14.3
μ_l/μ_v	22.92	15.38	12.30	7.57	7.58
λ_l [mW/(m K)]	89.81	78.99	106.72	91.55	116.50
λ_v [mW/(m K)]	11.95	14.34	12.85	16.70	18.17
λ_l/λ_v	7.51	14.34	12.85	5.48	6.41
σ [N/m]	0.01084	0.00742	0.00829	0.00460	0.00550

Thus, when evaporating at the same pressure, refrigerants have different thermo-physical and thermodynamics properties and even the role of heat transfer mechanisms can be quite different.

By performing a comparison at the same reduced pressure, quite similar values of the density ratio of liquid and vapour, viscosity ratio of liquid and vapour, thermal conductivity ratio of liquid and vapour and surface tension are observed.

Reduced pressure plays an important role in nucleate boiling heat transfer. Assuming spherical nuclei, the wall superheat required to the bubble formation can be expressed as:

$$T_{wall} > T_s + 2\frac{dT}{dp}\left(\frac{2\sigma}{a}\right) \tag{1.1}$$

$$T_{wall} > T_s + \frac{2\sigma T_s}{a\, h_{lv}\rho_v} \tag{1.2}$$

where σ is the surface tension, ρ_v the vapour density, h_{lv} the latent heat of evaporation and a the size of the nucleation sites. The expression (1.2) is obtained by applying the Clausius-Clapeyron equation.

As pressure increases, the surface tension and the slope of the saturation pressure decrease, while the vapour density increases; at the same wall superheat new smaller cavities can be activated on the heated surface, resulting in an augmentation of the nucleate boiling.

Gorenflo *et al.* (2004) reported the experimental measurements of heat transfer coefficients during pool boiling on a copper tube: the heat transfer coefficient of the tested fluid increases significantly with saturation pressure. Figure 1.4 shows a diagram by Gorenflo *et al.* (2004), where the effect of the saturation pressure is expressed in terms of reduced pressure. The reported heat transfer coefficients are normalized by the ones obtained for a 0.1 reduced pressure value; the heat flux is equal to 20 kW/m^2. The trend of experimental heat transfer coefficients against reduced pressure is independent of the type of fluid and the function F_p, which correlates the experimental coefficients is reported. The reduced heat transfer coefficient increases with the reduced pressure. At high evaporating pressure, the lower density ratio of liquid and vapour yields a smaller change in velocity for a fixed mass flux; thus a lower variation of the convective contribution occurs as the vapour quality increases. Moreover, the higher vapour density yields a lower vapour velocity and a lower convective contribution. This can result in the almost independent trend of heat transfer coefficient versus vapour quality, experimentally found for high pressure fluids.

At high saturation temperature, the lower convective contribution and liquid thermal conductivity can force the dry-out inception heat transfer coefficient to decrease, as experimentally observed by Silva Lima *et al.* (2009) in the case of flow boiling inside a plain tube.

Greco (2008) suggested how the decrease of the density ratio of liquid and vapour should also cause a lower shear stress, which leads to a larger effective liquid film thickness on the tube wall; this results in a lower suppression of the nucleate boiling. If a uniform thickness of liquid film is assumed around the tube perimeter, as the saturation temperature raises, the density ratio of liquid and vapour diminishes and the void fraction also decreases; hence, at the same vapour quality, a thicker liquid film will occur.

In the case of a plain tube, Wojtan *et al.* (2005a) experimentally measured the inception dry-out quality at much lower vapour qualities for R410A than for R22. The surface tension is lower for R410A than for R22 and they suggested that it is easier, for a lower surface tension, to entrain the liquid film into the high velocity vapour core and the dry-out inception occurs at lower vapour quality.

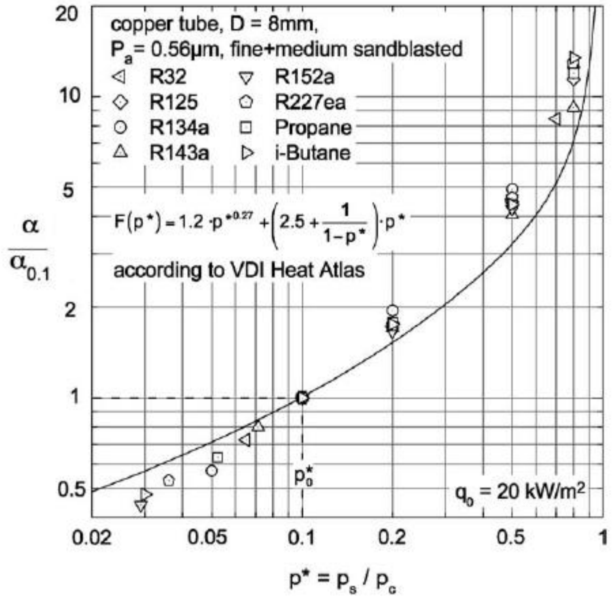

Figure 1.4. Reduced heat transfer coefficient vs. reduced pressure during pool boiling on a copper plain tube. The heat transfer coefficient is normalized by the one obtained with a reduced pressure value of 0.1. The heat flux is equal to 20 kW/m^2. Source: Gorenflo *et al.* (2004).

1.3 Literature review of experimental studies on heat transfer flow boiling

The measurement of the heat transfer coefficient during flow boiling inside horizontal tubes can be performed using different methods and measuring techniques. The type of heating source is a first way to classify the experimental works. The test section can be electrically heated, but hot water can also be used to provide the energy for the vaporization.

The heat transfer coefficient can be obtained from the heat flux exchanged in the test section and the measurement of the wall and saturation temperatures. In the case of water heated tubes, the Wilson plot technique can also be applied. Depending on the measuring technique adopted, the heat transfer coefficients reported in the open literature can be local or quasi local values, or even average coefficients along the heated tube length.

Table 1.2 and 1.3 report some recent experimental studies on in-tube vaporization of R134a, R410A and carbon dioxide inside plain and microfin tubes. The microfin tubes are made of copper and the main geometrical characteristics are summarized in Table 1.4: inner diameter at the root of the fins, height of the fins, number of fins, helix angle, apex angle and equivalent heat transfer length of the tube.

Eckels and Pate (1991) reported heat transfer coefficients of R134a, evaporating at 5 °C, 10 °C and 15 °C inside a plain tube. The mass velocity tested ranges from 125 kg/(m^2 s) to 400 kg/(m^2 s), while the inlet and outlet vapour quality was set to 0.10 and 0.90 respectively. The heat was transferred to the test section by water flowing in the annulus side and the Wilson plot technique was adopted for the data reduction. The heat transfer coefficient increases with both saturation temperature and mass flux.

Singh *et al.* (1996) presented the results of an experimental study on forced convective boiling of R134a inside a horizontal microfin tube at a saturation temperature around 20 °C. The test tube, 0.305 m long, was electrically heated. The heat transfer coefficients were obtained from the average value of the wall temperatures, which were measured in different axial positions. At a low value of mass flux, 50 kg/(m^2 s), the vapour quality does nor have any influence on the heat transfer coefficient. At this same condition, a wavy-stratified flow pattern was observed: the heat transfer is nucleate boiling dominated and any suppression of the nucleation appears as vapour quality increases. The heat transfer coefficient shows significant increase when mass velocity becomes greater than 100 kg/(m^2 s). The visual observations performed by the authors indicated as 100 kg/(m^2 s) was the transition value of mass flux for having a stratified flow.

Kim *et al.* (2002) experimentally investigated the heat transfer characteristics of R410A during vaporization inside smooth and microfin copper tubes as a function of saturation temperature, vapour quality, heat flux and mass velocity. For both the plain and microfin tubes, two different versions with outside diameters 9.52 and 7.0 mm were considered. The test sections were electrically heated and local values of heat transfer coefficients were obtained from the local measurements of the wall and saturation temperatures. With regard to the effect of evaporating pressure, the experimental results show that, when vapour quality is lower than about 0.6, the heat transfer coefficients decrease with the evaporating temperature for all the tubes tested; but, at higher quality values, the experimental coefficients merge together, regardless of the saturation temperature. Moreover, the coefficients measured for the smooth tubes show a lower dependence on the vapour quality as compared to the ones measured for the microfin tubes. Both in the plain and the enhanced tubes, heat transfer coefficients increase as the mass flux rises; however, it should be observed from Table 1.1 and 1.2 that only low values of mass velocity were tested by the authors.

Cieslinski and Targanski (2003) measured the heat transfer coefficient of R134a inside smooth and microfinned copper tubes at an average saturation temperature of 0 °C and mass flux between 250 and 500 kg/(m^2 s). The heat needed for the vaporization was provided by the water flowing in the annulus side of the test section. The measured coefficients were calculated from the general expression for the overall thermal resistance. During the tests, the inlet vapour quality was set to 0 ± 0.05 and the outlet quality was set to 0.7 ± 0.01. For both the smooth and the enhanced tube the heat transfer coefficient increases with the mass flux.

Yun *et al.* (2003) conducted heat transfer experimental tests of flow boiling of carbon dioxide in a smooth tube at saturation temperatures of 5 °C and 10 °C, mass velocity from 170 to 320 kg/(m^2 s) and heat flux from 10 to 20 kW/m^2.

The experimental heat transfer coefficient shows a decreasing trend versus vapour quality. For quality values between 0.2 and 0.5 the heat transfer coefficient is independent of mass velocity because nucleate boiling is dominant in this region, however, as vapour quality increases above 0.5, the heat transfer coefficient increases with the mass velocity because of convective evaporation.

Kim and Shin (2005) presented an experimental investigation of evaporative heat transfer in smooth and enhanced horizontal copper tubes at 15 °C saturation temperature. Five single-groove tubes and two cross-groove tubes were tested. The measuring sections were heated by hot water flowing in the surrounding annulus. The experimental coefficients reported were obtained by averaging the two values obtained using the modified Wilson plot technique and the wall temperature method. A small effect of vapour quality on the heat transfer coefficient is observed for the smooth tube and for some enhanced tube geometries.

Greco and Vanoli (2005) measured the heat transfer coefficients of R134a and R410A during flow boiling in a horizontal stainless steel smooth tube and investigated the effect of the evaporating pressure. The test section was 6 m long with an internal diameter of 6 mm and was uniformly heated by the Joule effect. Local heat transfer coefficients were obtained by measuring the wall temperature in eight different axial points along the tube. At the same value of mass velocity, around 370 kg/(m^2 s), the heat transfer coefficient presents a different trend versus vapour quality, as a function of the evaporating pressure. At low values of saturation pressure the heat transfer coefficient rises with the vapour quality; on the contrary in the case of high pressure a local minimum appears, since the heat transfer coefficient decreases at low values of vapour quality and then increases with vapour quality.

Schael and Kind (2005) presented flow pattern observations and measurements of the local heat transfer coefficient of carbon dioxide, evaporating in a horizontal copper microfin tube. They also reported measurements taken in a smooth tube to perform a comparison with data in microfin tube. The test section had an electrically heated length of 0.20 m. In the case of the microfin tube, with heat flux values around 60 kW/m^2 and high mass velocities, the heat transfer coefficient is almost independent of vapour quality. At the lowest mass velocity investigated, 75 kg/(m^2 s), the heat transfer coefficient decreases as the vapour quality increases. Contrary to the dependence observed for high heat fluxes, the heat transfer coefficient increases with vapour quality at low heat flux values. By increasing the mass velocity from 75 to 250 kg/(m^2 s), the heat transfer coefficient goes up significantly, but, by further increasing the mass flux to 500 kg/(m^2 s), the heat transfer coefficient decreases. Moreover, the heat transfer coefficient in smooth tube increases with vapour quality at low heat flux, but when heat flux is around 60 kW/m^2 it decreases as vapour quality increases.

Filho and Jabardo (2006) presented experimental measurements of the heat transfer coefficient for R134a in smooth, standard microfin and herringbone copper tubes of 9.52 mm outside diameter. Tape resistors, uniformly wrapped on the external surface of the tube, were used as heating source. The measured coefficients are average values along the test section. For a mass velocity value of 100 kg/(m^2 s), the heat transfer coefficient measured for the smooth tube remains essentially constant over the entire range of vapour quality; this is explained by the stratified flow pattern.

Table 1.2. Operative conditions of heat transfer experimental tests in plain tube

Authors	Fluid	T_{sat} [°C]	p_r	x	q [kW/m^2]	G [kg/(m^{2}s)]
Eckels and Pate (1991)	R134a	-15 ÷ 5	0.01 ÷ 0.26	0.1 ÷ 0.9[*]	-	20 ÷ 200
Kim *et al.* (2002)	R410A	-15 ÷ 5	0.01 ÷ 0.26	0.2 ÷ 0.8[**]	5 ÷ 15	70 ÷ 211
Cieslinski and Targanski (2003)	R134a	0	0.07	0 ÷ 0.7[*]	-	250 ÷ 500
Yun *et al.* (2003)	CO_2	5 ÷ 10	0.54 ÷ 0.61	0.05 ÷ 0.95[**]	10 ÷ 20	170 ÷ 320
Greco and Vanoli (2005)	R134a	0.95 ÷ 28.6	0.075 ÷ 0.18	0.1 ÷ 0.9[**]	15 ÷ 20.4	368 ÷ 377
Greco and Vanoli (2005)	R410A	-14.9 ÷ 13.5	0.098 ÷ 0.25	0 ÷ 1[**]	10 ÷ 20	363 ÷ 386
Kim and Shin (2005)	R410A	15	0.26	0.2 ÷ 0.8	11	140 ÷ 280
Schael and Kind (2005)	CO_2	5	0.54	0.1 ÷ 0.9	2 ÷ 64.5	75 ÷ 300
Filho and Jabardo (2006)	R134a	5	0.086	0.05 ÷ 0.9	5	100 ÷ 500
Cho *et al.* (2007)	CO_2	0 ÷ 20	0.47 ÷ 0.78	0 ÷ 1[**]	6 ÷ 20	212 ÷ 656
Gao *et al.* (2007)	CO_2	10	0.61	0.12 ÷ 0.55[***]	5 ÷ 30	200 ÷ 1300
Park and Hrnjak (2007)	R410A	-15 ÷ -30	0.06 ÷ 0.1	0.1 ÷ 0.8	5 ÷ 15	100 ÷ 400
Park and Hrnjak (2007)	CO_2	-15 ÷ -30	0.19 ÷ 0.31	0.1 ÷ 0.8	5 ÷ 15	100 ÷ 400
Zhao and Bansal (2007)	CO_2	-29 ÷ -30	0.19	0.1 ÷ 0.9[**]	12.6 ÷ 19.3	197 ÷ 231
Oh *et al.* (2008)	CO_2	-5 ÷ 5	0.61	0 ÷ 0.8[**]	10 ÷ 40	200 ÷ 500
Silva Lima *et al.* (2009)	R134a	5 ÷ 20	0.08 ÷ 0.14	0 ÷ 1	7.5 ÷ 17.5	300 ÷ 500

[*] Set vapour quality at inlet and outlet of test tube
[**] Vapour quality range estimated by the diagrams reported in the paper
[***] Inlet vapour quality

Table 1.3. Operative conditions of heat transfer experimental tests in microfin tube

Authors	Fluid	T_{sat} [°C]	p_r	x	q [kW/m^2]	G [kg/(m^{2}s)]
Singh *et al.* (1996)	R134a	20	0.14	0.05 ÷ 0.9[**]	5 ÷ 30	20 ÷ 200
Kim *et al.* (2002)	R410A	-15 ÷ 5	0.01 ÷ 0.26	0.2 ÷ 0.8[**]	5 ÷ 15	70 ÷ 211
Cieslinski and Targanski (2003)	R134a	0	0.07	0 ÷ 0.7[*]	-	250 ÷ 500
Kim and Shin (2005)	R410A	15	0.26	0.2 ÷ 0.8	11	205 - 215
Schael and Kind (2005)	CO_2	5	0.54	0.1 ÷ 0.9	4 ÷ 120	75 ÷ 500
Filho and Jabardo (2006)	R134a	5	0.086	0.05 ÷ 0.9	5	100 ÷ 500
Cho and Kim (2007)	CO_2	0 ÷ 20	0.47 ÷ 0.78	0 ÷ 1[**]	6 ÷ 20	212 ÷ 656
Gao *et al.* (2007)	CO_2	10	0.61	0.15 ÷ 0.85	5 ÷ 30	190 ÷ 770
Muller and Spindler (2006)	R134a	-20 ÷ 10	0.03 ÷ 0.10	0.1 ÷ 0.7	1÷ 15	25 ÷ 250
Hu *et al.* (2008)	R410A	5	0.26	0.2 ÷ 0.7[***]	5 ÷ 15	200 ÷ 400

[*] Set vapour quality at inlet and outlet of test tube
[**] Quality range estimated by the paper
[***] Inlet vapour quality

Table 1.4. Geometrical characteristics of microfin tubes

Authors	d_r [mm]	Fin Height [mm]	Fins Number	Helix Angle [°]	Apex Angle [°]	Heat transfer length [m]
Singh *et al.* (1996)	11.78	0.30	60	18	-	0.305
Kim *et al.* (2002)	8.92	0.12	60	25	-	3.0
Kim *et al.* (2002)	6.46	0.15	60	18	-	3.0
Cieslinski and Targanski (2003)	8.92	0.20	60	18	48	2.0
Kim and Shin (2005)			Several types of geometries			0.920
Schael and Kind (2005)	8.62	0.25	60	18	30°	0.2
Filho and Jabardo (2006)	8.92	0.20	82	18	33	1.5
Cho and Kim (2007)	4.4	0.15	60	18	-	5.0
Cho and Kim (2007)	8.92	0.12	40	25	-	5.0
Gao *et al.* (2007)	4.1*	0.11	40	12	40.5	0.9
Muller-Steinhagen and Spindler (2006)	8.95	0.24	55	15	20	1.0
Hu *et al.* (2008)	6.75	0.18	50	18	40	2.0

* Mean inner diameter

On the contrary, in the case of the microfin tube, the heat transfer coefficient increases with vapour quality in most of quality range; this trend is related to the presence of a thin liquid film promoted by the fins. As the mass flux increases to 200 kg/(m^2 s), the flow pattern in the smooth tube becomes annular and the heat transfer coefficient presents a trend similar to that observed for the microfin tube. When the mass velocity is equal to 500 kg/(m^2 s) a strange behaviour was observed for the standard microfin tube: the heat transfer coefficient increases until a vapour quality around 0.5, while for higher quality values the coefficient diminishes continuously with the quality.

Muller-Steinhagen and Spindler (2006) performed an experimental study on flow boiling heat transfer of R134a in a commercially copper microfin tube. The test section was 1 m long and electrically heated. Low mass velocities were investigated as it can be seen in Table 1.3. At 150 kg/(m^2 s) mass velocity, annular flow occurs and the heat transfer coefficient increases with vapour quality. When mass velocity is 25 kg/(m^2 s), the heat transfer coefficient shows a constant or decreasing trend versus vapour quality and the reason for it can be searched in the stratified flow pattern. Moreover, the increase in heat transfer is more pronounced in the mass flux range from 25 to 62.5 kg/(m^2 s) than in the range from 62.5 to 150 kg/(m^2 s): the flow regime changes from stratified or stratified wavy flow, visualized at 25 kg/(m^2 s), to intermittent flow with partial wetting of the upper part of the tube, observed at 62.5 kg/(m^2 s); annular flow finally occurs at mass velocity higher than 100 kg/(m^2 s).

Cho and Kim (2007) measured the heat transfer coefficient of carbon dioxide in smooth and microfin tubes of diameters 5 mm and 9.52 mm. Heating was transferred to the refrigerant by applying electric current directly to the test section. For both smooth and microfin tube, the heat transfer coefficient decreases as vapour quality increases, especially when high mass velocity and high heat flux occur.

Gao *et al.* (2007) performed heat transfer tests almost pure CO_2, evaporating at 10 °C inside a horizontal smooth and microfin tube. The smooth tube was a stainless steel tube with an inside diameter of 3 mm, while the microfin tube was a copper tube with a mean inside diameter of 3.04 mm. The oil circulation mass ratio was lower than 0.01 %. In the case of the smooth tube the local heat transfer coefficient decreases with the increase in vapour quality. For the microfin tube no influence of vapour quality on the heat transfer coefficient is observed when vapour quality is lower than 0.7. For both the tubes the heat transfer coefficient has a strong dependence on heat flux, at the same time it is independent of mass velocity: this implies that the process is nucleate boiling dominated. For the microfin tube, the effect of vapour quality on the heat transfer coefficient is not in agreement with those obtained by Cho and Kim (2007) at similar operating conditions.

Zhao and Bansal (2007) performed local heat transfer coefficient measurements of carbon dioxide in a smooth stainless steel tube at a saturation temperature around -30 °C. The test section was electrically heated to provide a uniform heat flux along the test tube. Thermocouples were installed at several axial locations along the tube to measure the local refrigerant and tube wall temperatures. The reported heat transfer coefficient increases with vapour quality until the inception of dryout and the highest coefficient is measured just before the dryout onset.

Park and Hrnjak (2007) experimentally investigated the heat transfer flow boiling of R410A and carbon dioxide in a plain horizontal copper tube at saturation temperatures around -15 °C and -30 °C. The test section has a heated length of 0.150 m while a secondary fluid, flowing in a brass jacket around the tube, was used as heating source. The measured coefficients were obtained from the measurement of the wall temperature in three different axial locations and the average coefficient along the tube was finally reported. They observed that, when evaporating at the same temperature, the heat transfer coefficient for carbon dioxide is nearly independent of vapour quality, whereas the heat transfer coefficient for R410A significantly increases with vapour quality. Data for carbon dioxide show a different trend as compared to the one reported by Zhao and Bansal (2007) at similar operating conditions. Moreover, at 400 kg/(m^2 s) and low values of vapour quality, CO_2 heat transfer coefficients are lower than those taken at 200 kg/(m^2 s) mass flux. On the contrary, R410A coefficients increase with mass velocity, showing a similar trend to the conventional HFC heat transfer data at low evaporating temperatures.

Hu *et al.* (2008) reported measurements of heat transfer coefficient for R410A inside a horizontal microfin tube, electrically heated by a tape wrapped around the outside of the tube. The mass velocity ranges from 200 to 400 kg/(m^2 s) and the heat flux varies between 7.5 and 15 kW/m^2. In the entire vapour quality range investigated, the heat transfer coefficient increases with vapour quality.

Oh *et al.* (2008) measured the heat transfer coefficient during flow boiling of carbon dioxide inside a horizontal stainless steel tube and performed a comparison with R134a and R22 data at the same test conditions. The test section was electrically heated. In the case of carbon dioxide, the heat transfer coefficient decreases as vapour quality increases, while, for R134a and R22, the heat transfer coefficient increases with vapour quality. They related the different trend of heat transfer coefficient versus vapour quality to the thermo-physical and thermodynamic properties.

Silva Lima *et al.* (2009) experimentally investigated the heat transfer during flow boiling of R134a inside a horizontal smooth tube at three saturation temperatures. At low vapour quality, in the slug regime, the heat transfer coefficient first decreases with the increasing of vapour quality. Nearby the slug to intermittent transition boundary, a local minimum is achieved by the heat transfer coefficient. After this minimum, the heat transfer coefficient increases with vapour quality until the dry-out inception. The particular trend of the heat transfer curve versus vapour quality is the result of the competition between nucleate and convective boiling mechanisms. Furthermore, in the low vapour quality region, the higher heat transfer coefficient always corresponds to that of the higher saturation temperature. As vapour quality increases, however, the difference between high and low saturation temperature heat transfer coefficients diminish and the curves intersect. After, the difference between the coefficients increases until the maximum value is reached and the higher heat transfer coefficient is achieved by the lower saturation temperature.

Figure 1.5 presents some discussed experimental data for R410A and carbon dioxide, evaporating inside a horizontal plain tube. The reported measurements are characterized by similar values of reduced pressure, mass velocity and heat flux. In particular the reduced pressure is 0.17 for data by Wang *et al.* (1998) and 0.19 for data by Kim *et al.* (2002), Park and Hrnjak (2007) and Zhao and Bansal (2007). Heat flux is around 15 kW/m^2 for data by Zhao and Bansal (2007) and 10 kW/m^2 for the other datasets; mass velocity is equal to 164 kg/(m^2 s) for data by Kim *et al.* (2002) and 200 kg/(m^2 s) in the case of the other datasets. The heat transfer coefficient seems almost independent of vapour quality for all the datasets with exception of the experimental coefficients by Zhao and Bansal (2007), which increase until the inception of dryout. Moreover, the experimental coefficients by Park and Hrnjak (2007) are higher than those by Zhao and Bansal (2007). It should be underlined that Park and Hrnjak (2007) performed the experimental measurements with 6.1 mm inside diameter copper tube, while the test section by Zhao and Bansal (2007) was a 4.57 mm inside diameter stainless steel tube.

In Figure 1.6 experimental heat transfer coefficients of R134a and R410A, measured by different researcher, during flow boiling in horizontal microfin tubes are compared. Again, datasets reported present similar values of reduced pressure, heat flux and mass velocity.

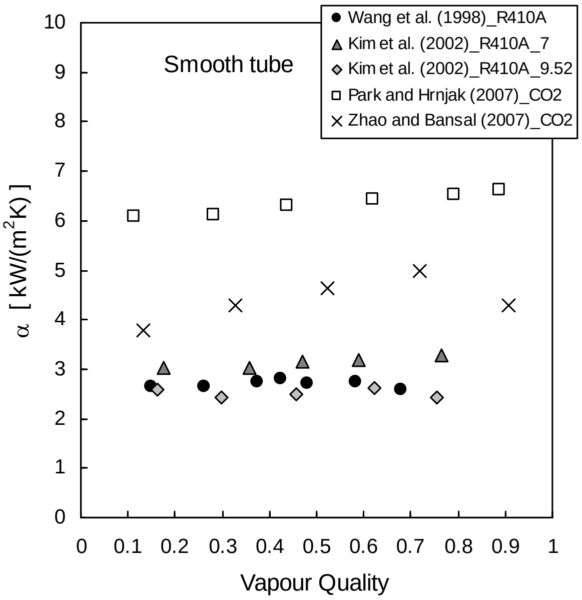

Figure 1.5. Heat transfer coefficient vs. vapour quality for R410A and CO_2 inside smooth tube: the reduced pressure is between 0.17 and 0.19, the heat flux is between 10 and 14 kW/m^2 and the mass velocity is between 164 and 200 kg/(m^2 s).

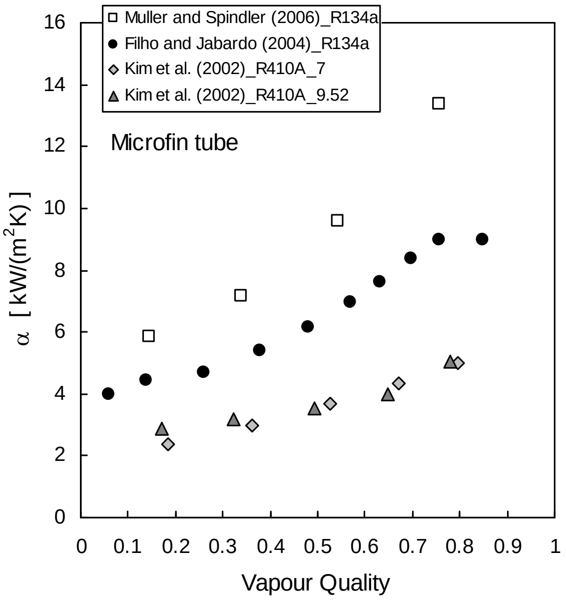

Figure 1.6. Heat transfer coefficient vs. vapour quality for R134a and R410A inside microfin tube: the reduced pressure is around 0.1, the heat flux is 5 kW/m^2 and the mass velocity ranges is between 150 and 200 kg/(m^2 s).

Data reported are published and available in the open literature. The heat flux is 5 kW/m^2; the reduced pressure is 0.09 for data by Filho and Jabardo (2004) and 0.10 for data by Kim *et al.* (2002), Muller-Steinhagen and Spindler (2006); mass velocity is 150 kg/(m^2 s) for data by Muller-Steinhagen and Spindler (2006), 164 kg/(m^2 s) for data by Kim *et al.* (2002) and 200 kg/(m^2 s) in the case of Filho and Jabardo (2004). Data by Kim *et al.* (2002) refer to 7.0 and 9.52 outside diameter tubes. Annular flow pattern was experimentally observed by the authors. The heat transfer coefficient increases with vapour quality independently of the refrigerant. The coefficients measured by Muller-Steinhagen and Spindler (2006) at 150 kg/(m^2 s) mass flux result higher as compared to the coefficients by Filho and Jabardo (2004) at 200 kg/(m^2 s) mass velocity, but the different test tubes and experimental facility must be considered in the comparison.

By Figure 1.5 and Figure 1.6, a similar trend of the experimental heat transfer coefficient against vapour quality is observed; measurements refer to different saturation temperature, but equal values of reduced pressure. At these same conditions quite similar fluids properties are observed for the compared refrigerants.

1.4 Prediction of heat transfer coefficient

Heat transfer predictive models for the estimation of the heat transfer coefficient during in-tube flow boiling can be classified in strictly empirical methods, superposition and asymptotic models and flow pattern based methods. Strictly empirical correlations are typically based on the heat transfer coefficient of liquid single-phase α_l, obtained with the Dittus and Boelter (1930) equation, and on dimensionless numbers:

$$\alpha = \alpha_l \, f(Bo, Fr, X_{tt}, ...) \tag{1.3}$$

Superposition models calculate the heat transfer coefficient as the sum of a nucleate boiling and a convective contribution:

$$\alpha = \alpha_{nb} + \alpha_{cv} \tag{1.4}$$

Generally, the nucleate boiling component is based on the pool boiling equation by Cooper (1985), while the convective term is based on Dittus and Boelter (1939) correlation for single-phase heat transfer. The nucleate boiling and the convective terms are corrected by appropriate boiling suppression factors and two-phase convection multipliers. In the case of enhanced tubes, the effect of fins on the convective and nucleate boiling contributes is also accounted for.

Asymptotic models calculate the heat transfer coefficient combining the nucleate boiling and the convective term as:

$$\alpha = \left(\alpha_{nb}^n + \alpha_{cv}^n\right)^{1/n} \tag{1.5}$$

where the nucleate boiling and the convective components are treated as in the superposition model.

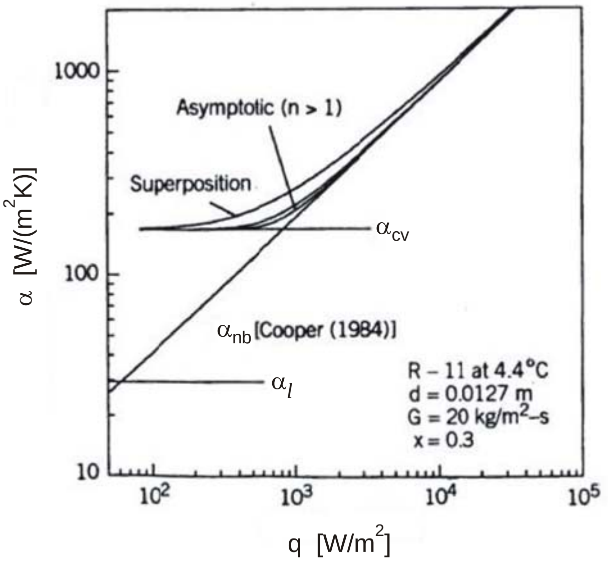

Figure 1.7. Webb and Gupte (1992): asymptotic and superposition models plotted in the form of heat transfer coefficient vs. heat flux.

Flow pattern based models are typically based on superposition or asymptotic methods, but the flow pattern characteristics are also taking into account.

Figure 1.7 shows the asymptotic and superposition models in the form of heat transfer coefficient versus vapour quality; the nucleate boiling heat transfer coefficient is in this case calculated with the Cooper (1984) equation. When n is greater than 1, the heat transfer coefficient curve is asymptotic with the limiting straight lines α_{nb} and α_{cv}. Thus, at a low heat flux the asymptote is the line of the fully convective heat transfer coefficient and the nucleate boiling contribution is negligible, but, at a high heat flux, the heat transfer coefficient curve tends to the line of nucleate boiling coefficient, which is the dominant mechanism. There is not theoretical basis for selection of the exponent n, and it is chosen to provide best fit of experimental data. If n is equal to 1, the total heat transfer coefficient is the sum of the two components and the superposition model is then obtained.

1.4.1 Heat transfer modelling in plain tube

In the case of smooth tube, four heat transfer predictive models are considered in the present thesis and compared with the heat transfer coefficients measured for R134a and R410A at saturation temperature around 30 °C and 40 °C. They are the models by Gungor and Winterton (1987), Liu and Winterton (1991), Kandlikar (1991) and Wojtan *et al.* (2005b). The methods by Gungor and Winterton (1987) and Liu and Winterton (1991) are superposition and asymptotic models, respectively. The Kandlikar (1991) predictive method is an empirical correlation, based on the correlation by Shah (1982). The Wojtan *et al.* (2005b) model is a flow pattern method based on the two-phase flow pattern diabatic map by Wojtan *et al.* (2005a).

In Figure 1.8, 1.9, 1.10, 1.11 the heat transfer coefficient calculated with the models by Gungor and Winterton (1987), Liu and Winterton (1991), Kandlikar (1991) and Wojtan *et al.* (2005b) are plotted against vapour quality for refrigerants at three saturation temperature, 5

°C, 20 °C and 40 °C. A 8 mm inside diameter plain tube has been used in the simulations. The mass flux has been set to 300 kg/(m^2 s) and the heat flux to 20 kW/m^2.

In model by Gungor and Winterton (1987), the vapour quality does not seem to have a great influence on heat transfer coefficient. At 5 °C saturation temperature the heat transfer coefficient increases a little with vapour quality, but at 40 °C evaporating temperature a slightly decreasing trend occurs.

In the case of Liu and Winterton (1991) and Wojtan *et al.* (2005b), the heat transfer coefficient increases with vapour quality for all the saturation temperatures considered. In the low vapour quality region the higher heat transfer coefficient occurs at the higher saturation temperature and the nucleate boiling represents the dominant contribution; but at high quality values the higher heat transfer coefficient is obtained with the lower saturation temperature. This trend was experimentally observed by Silva Lima *et al.* (2009) at similar operating conditions. In particular, the trend provided by Wojtan *et al.* (2005b) shows a reasonably agreement with the results by Silva Lima *et al.* (2009), whereas the local minimum experimentally observed is not reproduced by the model.

The heat transfer coefficient, calculated by Kandlikar (1991) at 5 °C evaporating temperature first decreases and then increases with vapour quality, with a local minimum at 0.2 vapour quality. At higher saturation temperatures a decreasing trend of heat transfer coefficient against vapour quality is observed.

A validation of the heat transfer modelling is required for high saturation temperatures and high reduced pressure, being the properties of the fluids quite different as compared to low evaporating temperatures.

Besides, new information must be obtained on the heat transfer prediction capability for high pressure fluids as R410A and CO_2. The models by Gungor and Winterton (1987), Liu and Winterton (1991) and Kandlikar (1991), have been often compared with heat transfer data for carbon dioxide, but further comparisons are required. New comparisons are expected for the recent flow pattern based model by Wojtan *et al.* (2005b), in particular with high reduced pressure heat transfer data.

A review of comparisons between heat transfer data and modelling, performed in the recent open literature, is presented; the accuracy of the models is evaluated reporting the *MAD* (mean absolute deviation) and the *MD* (mean deviation) values, which are defined in the nomenclature. The *MAD* parameter indicates the overall accuracy of a model; a positive value of *MD* indicates an overestimation of the experimental data, while a negative value indicates underestimation of experimental data.

Saitoh *et al.* (2007) compared the models by Gungor and Winterton (1987) and by Kandlikar (1991) with a database for R134a including measurements performed in horizontal tubes with inside diameter varying from 0.51 mm to 11 mm. Both the correlations did not agree well with the experimental data in the case of tubes with small diameters, where a overestimation above 30 % is observed. The *MAD* value found was 19.7 % for the Kandliklar (1991) correlation and 20.5 % for the model by Gungor and Winterton (1987).

Cho and Kim (2007) compared the experimental heat transfer coefficients, measured for carbon dioxide in 5 mm and 9.52 mm inside diameter horizontal tubes, with the predictive methods by Gungor and Winterton (1987), Kandlikar (1991) and Liu and Winterton (1987). The saturation temperature ranges from 0 °C to 20 °C. On the whole, the correlation by Kandlikar (1991) has a relatively good prediction as compared to the models by Gungor and Winterton (1987) and by Liu and Winterton (1991). In the case of 5 mm inside diameter tube, the coefficients calculated by Kandlikar (1991) present a trend versus vapour quality opposite to those of experimental data.

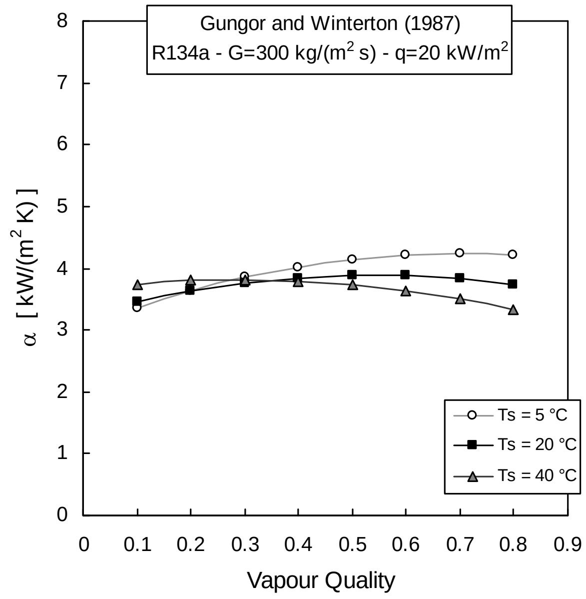

Figure 1.8. Heat transfer coefficient calculated by Gungor and Winterton (1987) vs vapour quality for R134a. The mass velocity is 300 kg/(m^2 s), the heat flux is 30 kW/m^2, and the saturation temperature is 5 °C, 20 °C and 40 °C.

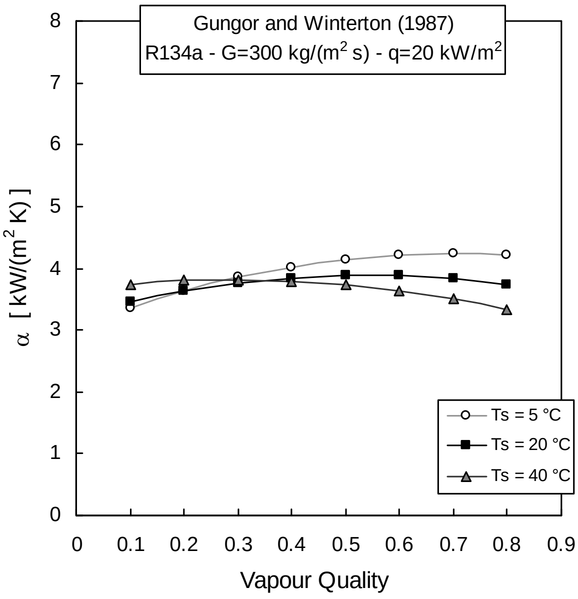

Figure 1.9. Heat transfer coefficient calculated by Liu and Winterton (1991) vs vapour quality for R134a. The mass velocity is 300 kg/(m^2 s), the heat flux is 30 kW/m^2, and the saturation temperature is 5 °C, 20 °C and 40 °C.

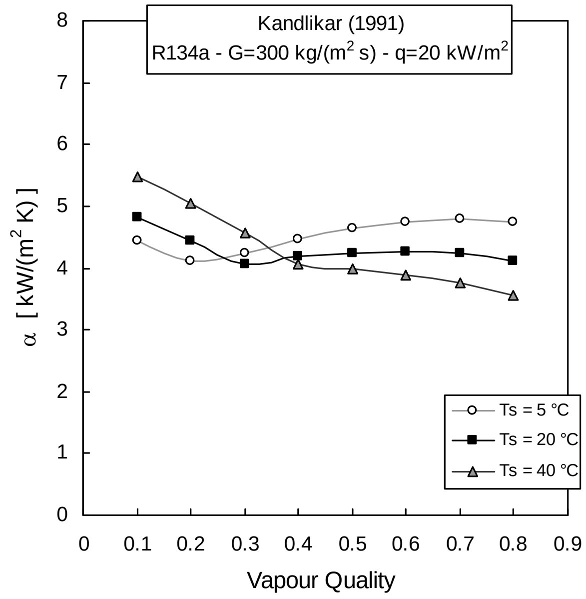

Figure 1.10. Heat transfer coefficient calculated by Kandlikar (1991) vs vapour quality for R134a. The mass velocity is 300 kg/(m^2 s), the heat flux is 30 kW/m^2, and the saturation temperature is 5 °C, 20 °C and 40 °C.

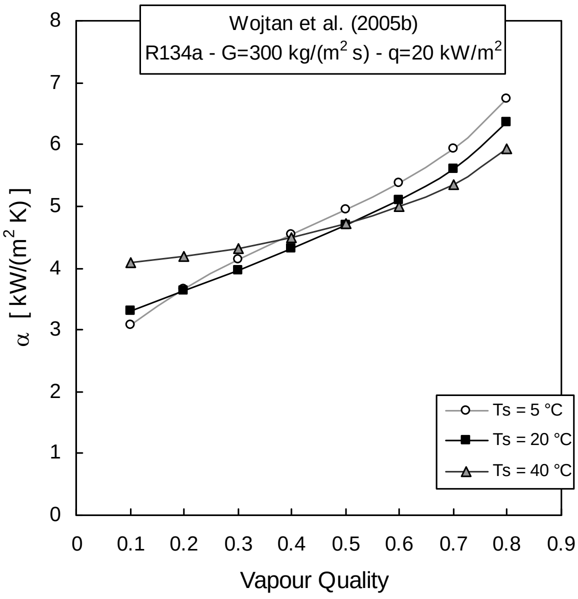

Figure 1.11. Heat transfer coefficient calculated by Wojtan et al. (2005b) vs vapour quality for R134a. The mass velocity is 300 kg/(m^2 s), the heat flux is 30 kW/m^2, and the saturation temperature is 5 °C, 20 °C and 40 °C.

Zhao and Bansal (2007) compared experimental heat transfer coefficients, taken at -30 °C saturation temperature, against the modelling. The model by Liu and Winterton (1991) provided a satisfactory agreement, within 20 %, with a *MAD* of 9.2 % and a *MD* of 0.4 %; in the case of the Kandlikar (1991) correlation larger deviations were found, with *MAD* of 16.8 % and *MD* of -15.8 %. They also compared these same models with experimental heat transfer coefficients by other authors and they observed as none of the correlations considered agreed with the experimental data. Their conclusion was that further information was needed to assess the accuracy of modelling.

Park and Hrnjiak (2007) compared the measured heat transfer coefficients for R410A and CO_2 with the models by Gungor and Winterton (1987) and by Liu and Winterton (1991). In the case of carbon dioxide data, both models underestimate the measurements, while an improvement of the prediction capability was observed for R410A.

Silva Lima *et al.* (2009) performed a comparison between new data for R134a, taken at saturation temperature between 5 and 20 °C, with the models by Liu and Winterton (1991) and Wojtan *et al.* (2005b). Liu and Winterton (1991) model yields the highest number of points within the ±30 % lines, whereas it provide some underestimation. The method by Wojtan *et al.* (2005b) also underestimates the experimental data, but, on the whole, it provides the highest accuracy. In particular, as compared to Liu and Winterton (1991), Wojtan *et al.* (2005b) shows higher accuracy in the low heat transfer coefficient region, typically constituted of slug flow pattern.

1.4.2. Heat transfer modelling in microfin tube

1.4.2.1 Koyama *et al.* (1995)

Koyama *et al.* (1995) presented a predictive correlation based on data of pure refrigerants R134a, R22 and R123 under the following conditions: mass velocity between 200 and 400 kg/(m^2 s), heat flux between 5 an 64 kW/m^2 and reduced pressure from 0.07 to 0.24. The heat transfer coefficient is based on the real inside area of the tube and it is obtained by the superposition of nucleate boiling and convective components:

$$\alpha = \alpha_{nb} + \alpha_{cv} \tag{1.6}$$

The convective term is obtained by multiplying the heat transfer coefficient for only liquid flow with a two-phase convection multiplier factor in the microfin tube:

$$\alpha_{cv} = \alpha_{lo} F \tag{1.7}$$

$$\alpha_{lo} = 0.028 \frac{\lambda_l}{d_i} \cdot Re_{lo}{}^{0.8} \cdot Pr^{0.4} \tag{1.8}$$

$$Re_{lo} = G(1-x)\frac{d_i}{\mu_l} \tag{1.9}$$

$$F = 1 + \frac{2}{X_{tt}^{0.8}} + \frac{0.8}{X_{tt}^{1.03}} \tag{1.10}$$

The term F was determined by observing that, for one value of X_{tt}, the ratio between the heat transfer coefficient and the only liquid heat transfer coefficient scatters in a range, that is related to the difference of nucleate boiling contribution. The experimental data, where the nucleate boiling component is considered to be fully suppressed are used to determine the two-phase convection multiplier factor in the microfin tube. The only liquid Reynolds number and the Nusselt number are based on the mean inner diameter of the tube, that is the diameter with which the cross sectional area of a smooth tube is equal to the cross sectional area of the microfin tube.

In the microfin tube the fin height is small and the fin efficiency is near unit. Therefore, all the inside surface area is effective for flow boiling heat transfer and the fin surface acts as the same as the base surface in nucleate boiling conditions. The microfin surface can be treated as a smooth surface with an area equal to that of the microfin tube. The nucleate boiling heat transfer coefficient is based on the real inner area of the tube and it is obtained from a modified pool boiling correlation for smooth tube. Pool experimental studies show that the departure bubble size in the microfin tube is smaller than the one in the smooth tube. Morepver, the fins yield an additional enhancement of the pool boiling heat transfer because of the increase of the surface area. These aspects are considered in different values of the constant C_1 and C_2 as compared to the smooth tube correlation

$$\alpha_{nb} = K^{0.745} S \ \alpha_{pb} \tag{1.11}$$

where K is the fraction between the nucleate boiling and the total heat flux and S is the suppression factor. The two term are calculated as a function of the bubble departure diameter and the equilibrium break-off diameter in the following manner:

$$K^{0.745} = \frac{1}{1 + 0.875\eta + 0.158\eta^2 - 0.159\eta^3 + 0.7907\eta^4} \tag{1.12}$$

$$\eta = \frac{\alpha_{cv}}{S\alpha_{pb}} \tag{1.13}$$

$$S = \frac{\left(1 - e^{-\xi}\right)}{\xi} \tag{1.14}$$

$$\xi = \frac{D_b \alpha_{cv}}{\lambda_l} \tag{1.15}$$

$$D_b = C_1 \left(\frac{\rho_l c_{p,l} T_s}{\rho_v h_{lv}} \right)^{1.25} \left(\frac{2\sigma}{g(\rho_l - \rho_v)} \right)^{0.5} \tag{1.16}$$

$$\alpha_{pb} = C_2 \cdot 207 \frac{\lambda_l}{D_{be}} \left(\frac{q \cdot D_{be}}{\lambda_l \cdot T_{sat}} \right)^{0.745} \left(\frac{\rho_v}{\rho_l} \right)^{0.581} \cdot Pr_l^{0.533} \tag{1.17}$$

$$D_{be} = 0.51\left[\frac{2\sigma}{g\ (\rho_l - \rho_v)}\right]^{0.5} \tag{1.18}$$

Figure 1.12 to 1.15 report some simulations performed for refrigerant R134a, which describes the effect of the parameters vapour quality, mass velocity, heat flux and saturation pressure on the model by Koyama *et al.* (1995). The input heat flux is based on the real inside heat transfer area and the mass velocity is referred to the mean inner diameter of the tube as just defined by Koyama *et al.* (1995). Refrigerant R134a has been considered, while the tube geometry has been assumed equal to those of the test microfin tube used in the experimental work.

A saturation temperature of 30 °C, mass velocity of 200 kg/(m^2 s) and heat flux of 20 kW/m^2 heat flux represents operative conditions typical for the experimental measurements and presented in this thesis. This same tube geometry and operative conditions will be assumed in the following to perform the simulations with the other models considered.

The total heat transfer coefficient, the nucleate boiling and the convective coefficients are shown in Figure 12 as function of the vapour quality; the heat transfer coefficient increases with the vapour quality.

The effect of mass velocity, heat flux and saturation pressure can be observed in Figure 1.13, 1.14, 1.15 for three different quality values, 0.2, 0.5 and 0.8.

At mass velocity under 100 kg/(m^2 s), a little effect of the vapour quality is observed, but as the mass velocity increases, the higher heat transfer coefficient occurs at 0.8 vapour quality due to the important convection contribution.

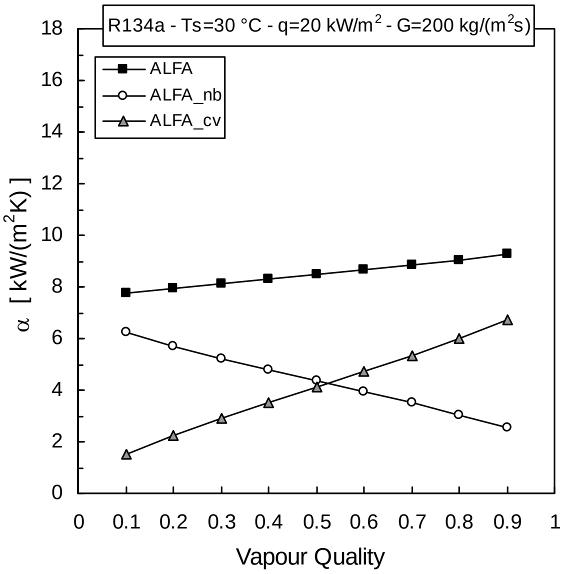

Figure 1.12. Model by Koyama *et al.* (1995): heat transfer coefficient vs. vapour quality. The saturation temperature is 30 °C, the mass velocity is 200 kg/(m^{2}s) and the heat flux is 20 kW/m^2. The heat transfer coefficient is based on the real inside area.

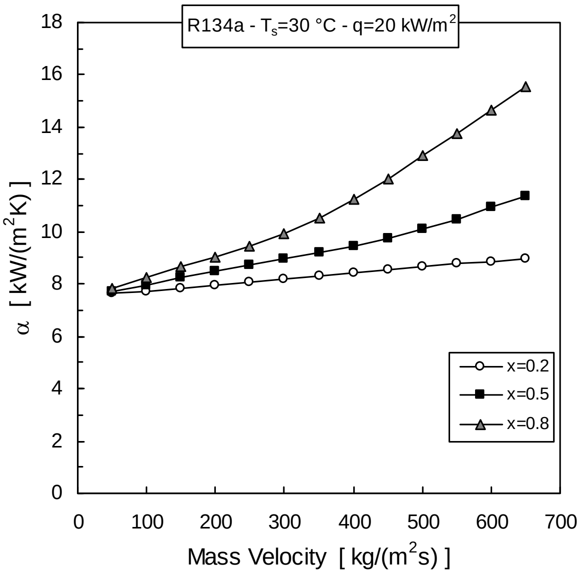

Figure 1.13. Model by Koyama *et al.* (1995): heat transfer coefficient vs. mass velocity. The saturation temperature is 30 °C, the heat flux is 20 kW/m^2 and the vapour quality is 0.2, 0.5, 0.8. The heat transfer coefficient is based on the real inside area.

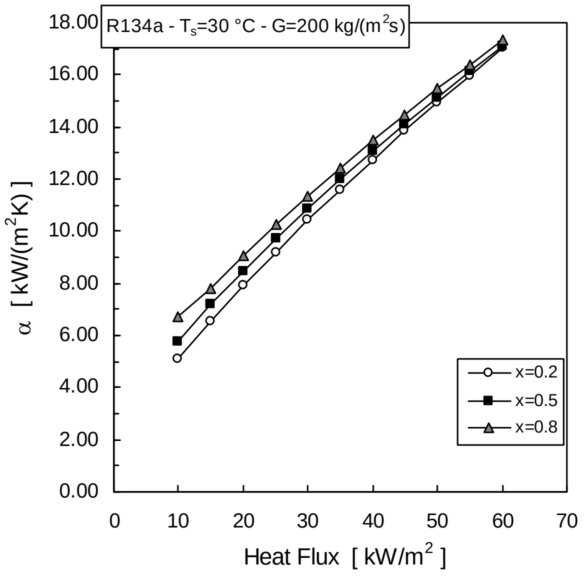

Figure 1.14. Model by Koyama *et al.* (1995): heat transfer coefficient vs. heat flux. The saturation temperature is 30 °C, mass velocity is 200 kg/(m^2 s) and the vapour quality is 0.2, 0.5, 0.8. The heat transfer coefficient is based on the real inside area.

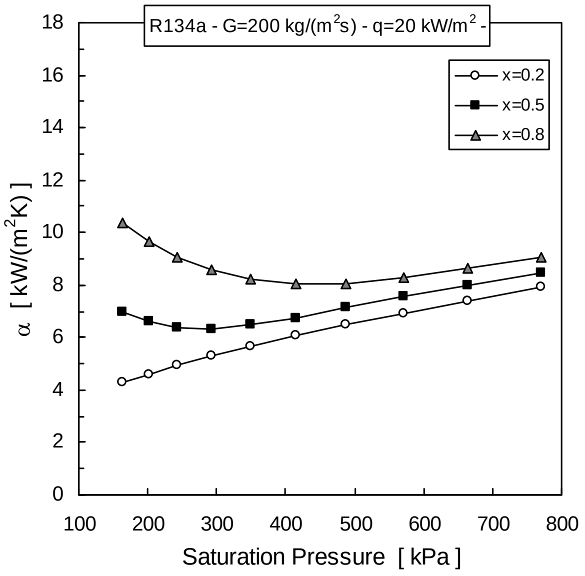

Figure 1.15. Model by Koyama *et al.* (1995): heat transfer coefficient vs. saturation pressure. The mass velocity is 200 kg/(m^2 s), the heat flux is 20 kW/m^2 and the vapour quality is 0.2, 0.5, 0.8. The heat transfer coefficient is based on the real inside area.

A strong effect of the heat flux appears by Figure 1.14; at high heat flux the heat transfer coefficient seems almost independent of the vapour quality and the heat transfer is nucleate boiling dominated.

By Figure 1.15, a significant effect of the vapour quality occurs at low vapour quality, but as the saturation pressure increases the curves merge regardless to vapour quality. At these same conditions, the thermo-physical thermodynamics yield an increasing of the nucleate boiling contribution while the convective mechanism becomes less important.

1.4.2.2 Thome *et al.* (1997)

The heat transfer model has been developed in the following range of operating conditions: vapour quality between 0.15 and 0.81, mass velocity between 100 and 501 kg/(m^2 s) and heat flux from 2 to 47 kW/m^2. The heat transfer method presents an asymptotic form and it is based on the inside surface area calculated with the diameter at the root of the fins:

$$\alpha = E_{mf}\left(\alpha_{nb}^3 + \alpha_{cv}^3\right)^{1/3} \tag{1.19}$$

The term α_{nb} is obtained by the Cooper (1984) nucleate pool boiling equation for pure fluids, where the heat flux is the total heat flux based on the effective internal surface area. The convective term is given by multiplying the convective flow boiling coefficient for plain tube with a convection enhancement factor for plain tubes:

$$\alpha_{cv} = \alpha_{cv,plain} E_{rb} \tag{1.20}$$

The convective coefficient for plain tube is calculated with the turbulent film flow model for annular flow presented by Kattan *et al.* (1998):

$$\alpha_{cv,plain} = C\,\mathrm{Re}_{l,film}^{m}\,\mathrm{Pr}_{l}^{0.4}\,\frac{\lambda_l}{\delta} \tag{1.21}$$

$$Re_{l,film} = \frac{4G(1-x)\delta}{(1-} \tag{1.22}$$

$$\varepsilon = \frac{x}{\rho_v}\left\{\left[\left(1+0.12(1-x)\right)\left(\frac{x}{\rho_v}+\frac{1-x}{\rho_l}\right)\right]+\left[1.18(1-x)\frac{\left(g\sigma(\rho_l-\rho_v)\right)^{0.25}}{G\rho_l^{0.5}}\right]\right\}^{-1} \tag{1.23}$$

$$\delta = D_r\,\frac{(1-\varepsilon)}{4} \tag{1.22}$$

where $Re_{l,film}$ is the liquid film Reynolds number, ε is the local void fraction determined with the Rouhani and Axelsson (1970) correlation and δ is the local thickness of the annular liquid film. The constant *C* is equal to 0.0133, while the constant *m* is equal to 0.69; they are obtained from an experimental database for five refrigerants (R123, R134a, R502, R402A, R404A) in plain tube.

The convection enhancement factor is given as:

$$E_{rb} = \left\{1+\left[2.64\,\mathrm{Re}_d^{0.036}\left(\frac{e}{D_r}\right)^{0.212}\left(\frac{p}{D_r}\right)^{-0.21}\left(\frac{\beta}{90}\right)^{0.29}\mathrm{Pr}^{-0.024}\right]^{7}\right\}^{1/7} \tag{1.24}$$

where Re_d is the only liquid Reynolds number:

$$\mathrm{Re}_d = \frac{G(1-x)d_r}{\mu_l} \tag{1.25}$$

Finally, the term E_{mf} account for two effects. The first is the action of the surface tension force in the microfin geometry, which draws the liquid from the convex surface to the concave region and enhances the feat transfer coefficient. Consequently, the nucleate boiling contribution in the model is underestimated an it is calculated with Cooper (1984) equation. The second aspect is that the convection film factor is for tubular flow, not film flow. Thus, the factor E_{mf} is calculated as:

$$E_{mf} = 1.89\left(\frac{G}{G_{ref}}\right)^{2} - 3.7\left(\frac{G}{G_{ref}}\right) + 3.02 \tag{1.26}$$

The reference mass velocity introduced in Eq. (1.25) to obtain a dimensionless expression is set to 500 kg/(m^2 s).

Some simulations have been performed to investigate the effect of vapour quality, mass velocity, heat flux and saturation temperature on the model by Thome *et al.* (1997).

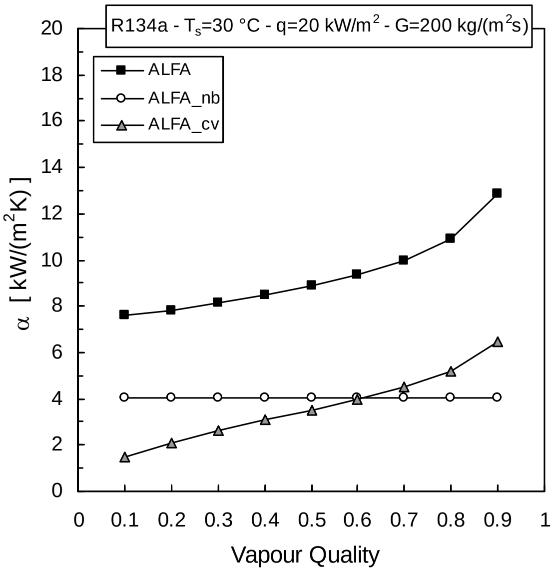

Figure 1.16. Model by Thome *et al.* (1997): heat transfer coefficient vs. vapour quality. The saturation temperature is 30 °C, the mass velocity is 200 kg/(m^{2}s) and the heat flux is 20 kW/m^2. The heat transfer coefficient is based on nominal inside surface area at the root fins diameter.

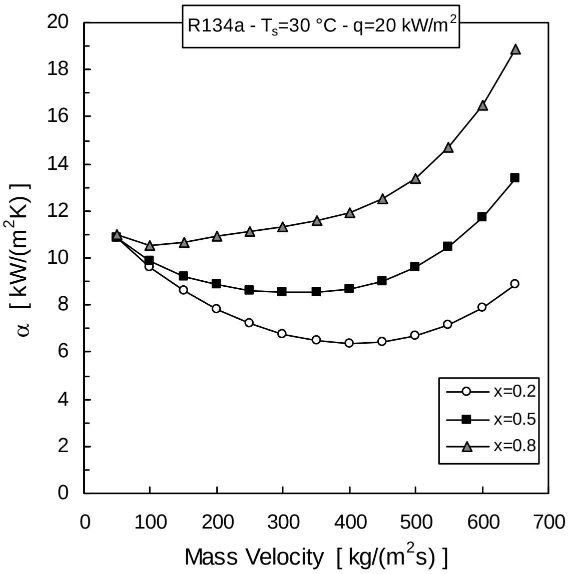

Figure 1.17. Model by Thome *et al.* (1997): heat transfer coefficient vs. mass velocity. The saturation temperature is 30 °C, the heat flux is 20 kW/m^2 and the vapour quality is 0.2, 0.5, 0.8. The heat transfer coefficient is based on nominal inside surface area at the root fins diameter.

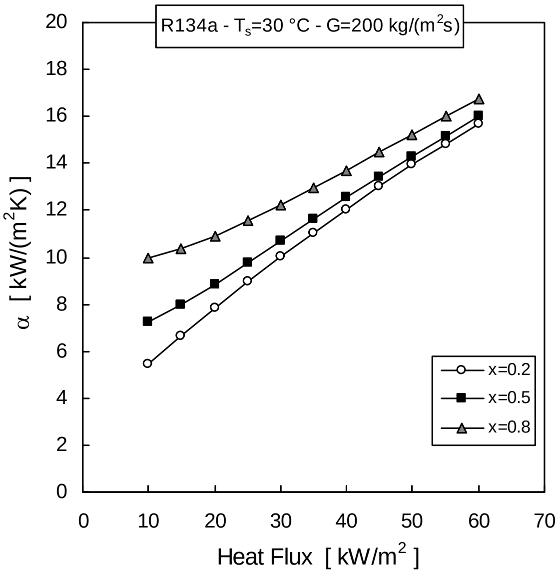

Figure 1.18. Model by Thome *et al.* (1997): heat transfer coefficient vs. heat flux. The saturation temperature is 30 °C, mass velocity is 200 kg/(m^2 s) and the vapour quality is 0.2, 0.5, 0.8. The heat transfer coefficient is based on nominal inside surface area at the root fins diameter.

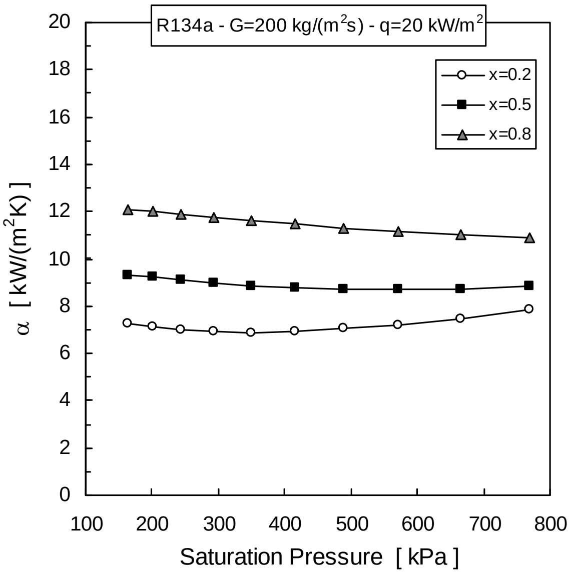

Figure 1.19. Model by Thome *et al.* (1997): heat transfer coefficient vs. saturation pressure. The mass velocity is 200 kg/(m^2 s), the heat flux is 20 kW/m^2 and the vapour quality is 0.2, 0.5, 0.8. The heat transfer coefficient is based on nominal inside surface area at the root fins diameter.

The heat flux used as input in the simulations is based on the real inside heat transfer area, but the heat transfer coefficient is referred to the inside surface area calculated with the diameter at the root of the fins.

Figure 1.16 reports the heat transfer coefficient calculated with the model by Thome *et al.* (1997) as a function of the vapour quality; the nucleate and the convective components are also presented. The nucleate boiling contribution is not suppressed with the increasing of vapour quality.

The effect of mass velocity is presented in Figure 1.17: the heat transfer coefficient increases with mass velocity for the entire quality range considered, but a greater effect of vapour quality occurs at higher mass velocity values. The heat transfer coefficient curves obtained at 0.2 and 0.5 vapour quality presents a local minimum at around 400 kg/(m^2 s) mass velocity and this is quite different from the trend observed for the other models.

In Figure 1.18 the heat transfer coefficient is plotted versus the heat flux for three vapour quality values, 0.2, 0.5, 0.8. As the heat flux increases the curves merge regardless the vapour quality and the process becomes nucleate boiling dominated; at 0.8 vapour quality, the heat transfer coefficient is higher again, because of the effect convective contribution in the high vapour quality region.

By Figure 1.19, the heat transfer coefficient is almost independent of saturation pressure and it increases with vapour quality for the entire vapour quality range reported.

1.4.2.3 Cavallini *et al.* (2006)

Cavallini *et al.* (2006) extended the predictive model by Cavallini *et al.* (1999) to very low values of mass velocity. A criteria based on the mass velocity is supplied by the authors for the transition between flow structures characterized by different dominant heat transfer mechanisms. The original model was based on available heat transfer data for several pure fluids, zeotropic and near-azeotropic mixtures of refrigerants. The experimental data bank, considered by the authors, includes a wide range of fluids and operative conditions, reported in detail in Cavallini *et al.* (1999) and Cavallini *et al.* (2006). For mass velocity values greater than 100 kg/(m^2 s) the model is equal to the original version by Cavallini *et al.* (1999), but when the mass velocity becomes lower than 100 kg/(m^2 s) a term due to the capillarity action is added

The heat transfer is the sum of the nucleate boiling, the convective and the capillarity components:

$$\alpha = \alpha_{nb} + \alpha_{cv} + \alpha_{cap} \tag{1.27}$$

When the mass velocity is lower than 100 kg/(m^{2}s) the capillary term α_{cap} is set equal to 0.

The nucleate boiling term is calculated with the Cooper equation, multiplied by a suppression factor *S* and a function of the fin tip tube diameter $F_1(d_i)$:

$$\alpha_{nb} = \alpha_{Cooper} S \; F_1(d_i) \tag{1.28}$$

$$S = A \; X_{tt}^{B} = A \left[\left(\frac{1-x}{x} \right)^{0.9} \left(\frac{\rho_G}{\rho_L} \right)^{0.5} \left(\frac{\mu_L}{\mu_G} \right)^{0.1} \right]^{B} \tag{1.29}$$

If $X_{tt} > 1$, then $X_{tt} = 1$. The factor $F_1(d_i)$ is calculated as:

$$F_1(d_i) = (d_0 / d_i)^C \tag{1.30}$$

where the reference diameter d_0 is set to 0.01 m.

In the Cooper (1984) equation the exponent of the heat flux is set equal to 0.67. Del Col *et al.* (2002) experimentally found a good agreement with the Cooper equation for plain surface data, but they found a lower exponent of the heat flux in the case of a microfin tube. In the present model the authors use the Cooper equation, because the exponent of the heat flux can be dependent on the microfin geometry.

Chamra and Webb (1995) found equal heat transfer coefficients for condensation and evaporation under the same operating conditions at vapour quality higher than 0.6 - 0.7. In these conditions Yoshida et al. (1988) observed that the fins were completely covered with liquid. Thus, the same type of equation that describes the forced convection condensation inside enhanced tubes can be used for forced convection evaporation. With reference to Cavallini *et al.* (1995), the convective term is expressed as follows:

$$\alpha_{cv} = \frac{\lambda_l}{d_i} Nu_{cv,smooth}\ R\ x^s (Bo \cdot Fr)^T F_2(d_i)^V F_3(G)^Z \tag{1.31}$$

where $Nu_{cv,plain}$ is the Nusselt number for evaporation in a plain tube and it is equal to the product of the all liquid Nusselt number Nu_{LO} and the two phase multiplier Φ :

$$Nu_{cv,plain} = Nu_{LO}\Phi = \left[0.023\left(\frac{Gd_i}{\mu_L}\right)^{0.8} \mathrm{Pr}_L^{\ 1/3}\right]\cdot\left\{\left[(1-x)+2.63x\left(\frac{\rho_L}{\rho_G}\right)^{0.5}\right]^{0.8}\right\} \tag{1.32}$$

The other parameters used in Eq. (1.30) are defined as follows:

$$Rx = \frac{\left[\dfrac{2h\ n_g\left(1-\sin(\alpha/2)\right)}{\pi\ d_i\cos(\alpha/2)}+1\right]}{\cos(\beta)} \tag{1.33}$$

$$Bo = \frac{g\rho_l h\ \pi\ d_i}{(8\sigma n_g)} \tag{1.34}$$

$$Fr = \frac{u_{vo}^2}{gd_i} \tag{1.35}$$

$$F_2(d_i) = \left(\frac{d_o}{d_i}\right)^{0.59} \tag{1.36}$$

$$F_3 = \left(\frac{G_0}{G}\right)^Z \tag{1.37}$$

with G_0 equal to 100 kg/(m^2 s).
The capillarity heat transfer coefficient is calculated as:

$$\alpha_{cap} = 0.332 \frac{\lambda_L}{h} \left(\frac{G h_{LG} \sin(\beta)}{q} \right)^{0.4326} F_g \tag{1.38}$$

If $G > 100$ kg/(m^{2}s) then

$$F_g = 0 \tag{1.39}$$

If $50 < G \leq 100$ kg/(m^2 s) then

$$F_g = 1 - \left(\frac{G}{G_0} \right)^3 \tag{1.40}$$

If $G \leq 50$ kg/(m^2 s) then

$$F_g = 1.75 \left(\frac{G}{G_0} \right) \tag{1.41}$$

In the case of zeotropic mixtures the heat transfer coefficients is:

$$\alpha = \left[\frac{1}{\alpha_f} + \left(\frac{\delta Q_{sv}}{\delta Q_t} \right) \frac{1}{\alpha_v} \right]^{-1} \tag{1.42}$$

where ($\delta Q_{sv}/\delta Q_t$) is the ratio between the sensible heat flow rate and the total heat flow rate, α_v is the heat transfer coefficient pertinent to the liquid film and α_v is the convective heat transfer coefficient of the vapour phase flowing alone in the duct. For mixtures with a maximum isobaric temperature glide the ratio ($\delta Q_{sv}/\delta Q_t$) becomes equal to:

$$\frac{\delta Q_{sv}}{\delta Q_t} = \frac{x c_{p,v} \Delta T}{\Delta h_m} \tag{1.43}$$

where ΔT is the glide temperature, x is the mean vapour quality and Δh_m is the enthalpy of isobaric vaporization of mixture. The heat transfer coefficient in the liquid film α_f can be calculated with Eq. (1.26) with the properties of the mixture (liquid and vapour at their equilibrium composition) correcting the nucleate boiling component for mass diffusion effect F_C:

$$\alpha_f = F_C \alpha_{nb} + \alpha_{cv} + \alpha_{cap} \tag{1.44}$$

$$F_C = \left[1 + \alpha_{fb,id} \frac{\Delta T}{q_{nb}} \left(1 - \exp(-\frac{q_{nb}}{\rho_l \Delta h_m \beta_l}) \right) \right]^{-1} \tag{1.45}$$

Table 1.5. Constants in Cavallini *et al.* (2006) model.

G [kg/(m^2 s)]		A	B	C	S	T	V	Z
$G < 500$	G > 100	1.36	0.36	0.38	2.14	-0.15	0.59	-3
	$G \leq 100$	1.36sin(β)	0.36(G/100)^4	0.38	2.14	-0.15	0.59	0.36
$G \geq 500$		1.36	0.36	0.38	2.14	-0.21	0.59	0.36

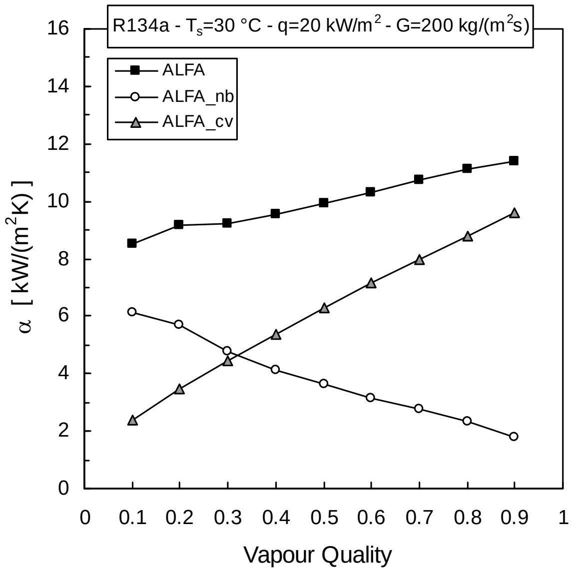

Figure 1.20. Model by Cavallini *et al.* (2006): heat transfer coefficient vs. vapour quality. The saturation temperature is 30 °C, the mass velocity is 200 kg/(m^{2}s) and the heat flux is 20 kW/m^2.

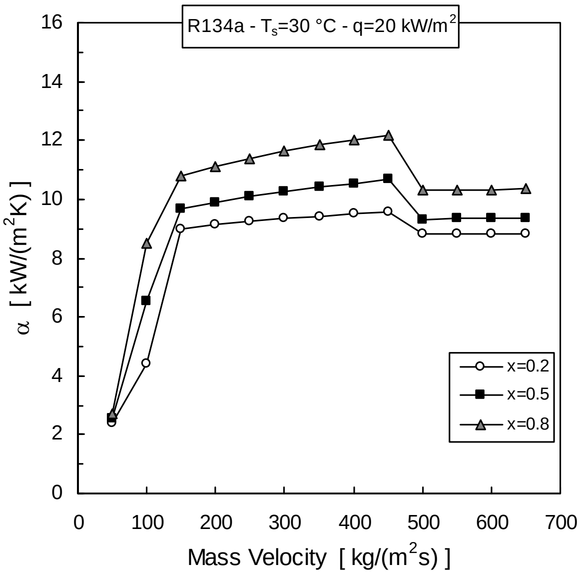

Figure 1.21. Model by Cavallini *et al.* (2006): heat transfer coefficient vs. mass velocity. The saturation temperature is 30 °C, the heat flux is 20 kW/m^2 and the vapour quality is 0.2, 0.5, 0.8.

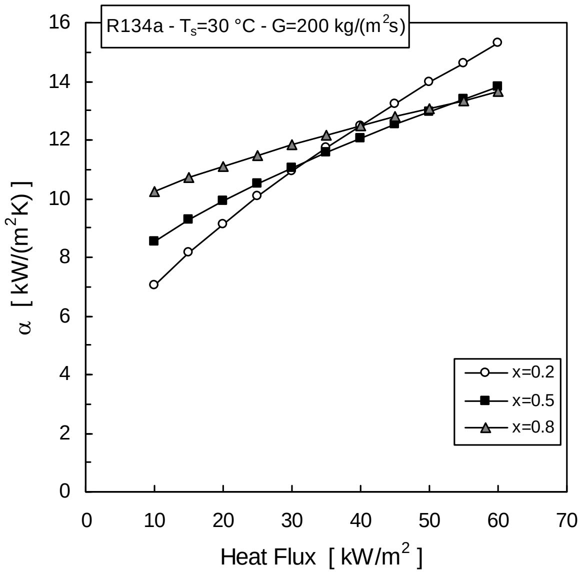

Figure 1.22. Model by Cavallini *et al.* (2006): heat transfer coefficient vs. heat flux. The saturation temperature is 30 °C, mass velocity is 200 kg/(m^{2}s) and the vapour quality is 0.2, 0.5, 0.8.

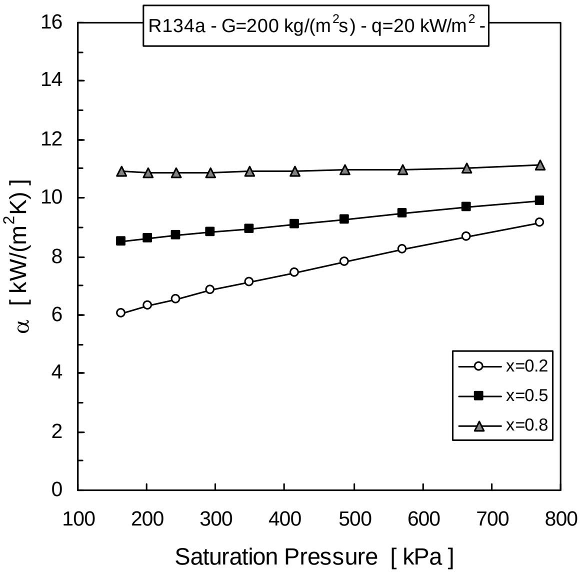

Figure 1.23. Model by Cavallini *et al.* (2006): heat transfer coefficient vs. saturation pressure. The mass velocity is 200 kg/(m^{2}s), the heat flux is 20 kW/m^2 and the vapour quality is 0.2, 0.5, 0.8.

The term $\alpha_{fb,id}$ is the ideal heat transfer coefficient calculated with the pure refrigerant flow boiling correlation. For the mass transfer coefficient β_l a value 0.0003 m/s was suggested by Thome (1996).

Some simulations performed with the Cavallini *et al.* (2006) predictive method are reported from Figure 1.20 to Figure 1.23, in order to evaluate the effect of the parameters vapour quality, mass velocity, heat flux and evaporating pressure. The nucleate boiling and the convective components are also drawn in Figure 1.20, while the capillarity term does not give any contribution at 200 kg/(m^2 s) mass velocity.

From the graph in Figure 1.21, the heat transfer coefficient rises abruptly with the mass velocity until 100 kg/(m^2s); for mass velocity values higher than 100 kg/(m^2 s) the heat transfer coefficient increases more slowly as a function of the mass flux. At mass velocities higher than 500 kg/(m^2 s), the heat transfer coefficient is lower as compared to mass fluxes less than 500 kg/(m^2 s).

At low heat flux, the vapour quality has a significant effect on the heat transfer coefficient and the convective mechanism seems to be the main heat transfer mechanism. At the heat fluxes around 60 kW/m^2 the nucleate boiling provides the higher contribution. The heat transfer coefficient calculated at 0.5 and 0.8 vapour quality assumes similar values and it is lower as compare to the coefficient calculated at 0.2 vapour quality: a suppression of the nucleate boiling mechanism occurs as the vapour quality increases (Figure 1.22).

When the saturation pressure is low a strong effect of the vapour quality is observed by Figure 1.23, but, as the saturation pressure increases, the nucleate boiling contribution raises and the heat transfer coefficient curves calculated for the three different vapour quality values ten to merge.

1.4.2.4 Chamra and Mago (2007)

Chamra and Mago (2007) compared the model by Cavallini *et al.* (1999) with R134a and R22 heat transfer data: in the case of R134a they did not found a satisfactory agreement, while the model was successful in predicting R22 experimental datasets. Thus, they introduced new empirical constants in the method by Cavallini *et al.* (1999). New constants were determined by using a large database of pure refrigerants and mixtures, covering a range of saturation temperatures typical for the conventional applications of the air-conditioning and refrigeration industry. Data for R410A were not included in their data bank. The new constants for pure fluid and fluids mixture are reported in Table 1.6.

According to Cavallini *et al.* (1999), the two phase heat transfer coefficient for pure refrigerants is given as the sum of the nucleate boiling and the convective component:

$$\alpha = \alpha_{nb} + \alpha_{cv} \tag{1.46}$$

In the case of the zeotropic mixtures, the same procedure as by Cavallini *et al.* (1999) is followed, introducing the new empirical constants for fluids mixture; but, in the case of the correction factor F_C, the pure fluid constants are used to calculate the coefficient $\alpha_{fb,id}$.

Some simulations have been performed with the Chamra and Mago model (2007) for R134a and presented in Figure 1.24 - 1.27. The effect of vapour quality, mass velocity, heat flux and saturation pressure is shown. By Figure 1.24, the importance of the nucleate boiling component is diminished as compared to Cavallini *et al.* (2006), while the contribute of the convective mechanism is increased; for quality values greater than 0.5 the nucleate boiling contribution is quite negligible as compared to the convective term.

Table 1.6. Constans in Chamra and Mago (2007) model

	A	B	C	S	T	V	Z
Pure fluid	1.5160	1.1610	-1.7640	2.6220	-0.2158	0.5927	0.0582
Fluids mixture	0.7098	1.2040	3.3010	0.8317	0.1578	-1.0780	0.0582

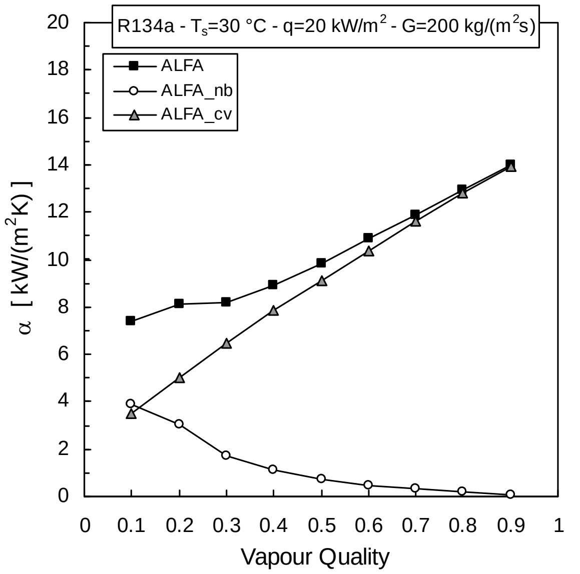

Figure 1.24. Model by Chamra and Mago (2007): heat transfer coefficient vs. vapour quality. The saturation temperature is 30 °C, the mass velocity is 200 kg/(m^2 s) and the heat flux is 20 kW/m^2.

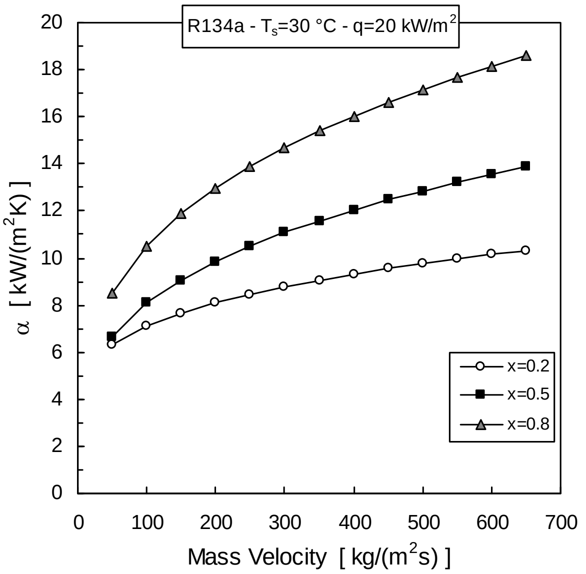

Figure 1.25. Model by Chamra and Mago (2007): heat transfer coefficient vs. mass velocity. The saturation temperature is 30 °C, the heat flux is 20 kW/m^2 and the vapour quality is 0.2, 0.5, 0.8.

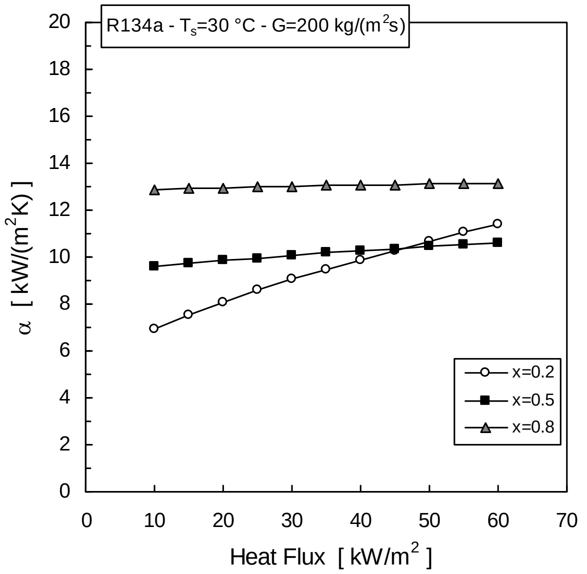

Figure 1.26. Model by Chamra and Mago (2007): heat transfer coefficient vs. heat flux. The saturation temperature is 30 °C, mass velocity is 200 kg/(m^2 s) and the vapour quality is 0.2, 0.5, 0.8.

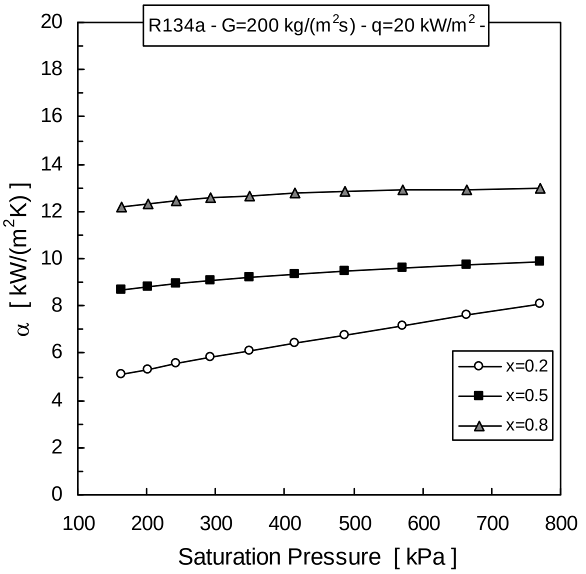

Figure 1.27. Model by Chamra and Mago (2007): heat transfer coefficient vs. saturation pressure. The mass velocity is 200 kg/(m^2 s), the heat flux is 20 kW/m^2 and the vapour quality is 0.2, 0.5, 0.8.

The heat transfer coefficient by Chamra and Mago (2007) is plotted as a function of mass velocity in Figure 1.25: when the mass velocity is under 100 kg/(m^2 s), no effect of vapour quality appears at low quality values; as the mass velocity increases above 100 kg/(m^2 s), a significant effect of vapour quality can be observed.

Figure 1.26 shows the heat transfer coefficient as a function of the vapour quality; at low heat flux, the heat transfer coefficient increases with vapour quality, but at high heat flux, around 60 kW/m^2, the heat transfer coefficient calculated at 0.2 vapour quality is higher than the coefficient calculated at 0.5 vapour quality, because of the importance of the nucleate boiling mechanism. At 0.8 vapour quality the highest heat transfer coefficient occurs, due to the suppression of the boiling mechanism and the increasing of the convective contribution.

By comparing Figure 1.23 and Figure 1.27, one can conclude that effect of saturation pressure is lower in Chamra and Mago (2007) as compared to Cavallini *et al.* (2006).

1.4.2.5 Hamilton *et al.* (2008)

Hamilton *et al.* (2008) correlated a data bank of measured convective boiling Nusselt numbers in the form of the product of several dimensionless variables, following the procedure presented by Cooper (1984). The calculated Nusselt number is based on the hydraulic diameter and the heat transfer coefficient is based on the actual inner surface area of the tube:

$$Nu = \frac{\alpha\ d_h}{\lambda_l} \tag{1.47}$$

$$Nu = 482.18\,\mathrm{Re}_{lo}^{0.3}\,\mathrm{Pr}^{C_1}\left(\frac{p_r}{p_c}\right)^{C_2} Bo^{C_3}\left(-\log_{10}\frac{p_r}{p_c}\right)^{C_4} M_w^{C_5}\,1.1^{C_6} \tag{1.48}$$

$$C_1 = 0.51x \tag{1.49}$$

$$C_2 = 5.57x - 5.21x^2 \tag{1.50}$$

$$C_3 = 0.54 - 1.56x + 1.42x^2 \tag{1.51}$$

$$C_4 = -0.81 - 12.56x + 11.00x^2 \tag*{(1.51)}$$

$$C_5 = -0.25 - 0.035x^2 \tag{1.53}$$

$$C_6 = \frac{(T_{LV} - T_{MV})[279.8(z_v - z_l) - 4298(T_d - T_b)/T_s]}{T_s} \tag{1.54}$$

The term M_w is the molecular mass of the refrigerant normalized by the molecular mass of hydrogen. The temperatures T_d and T_b are the dew point and bubble point temperature of the mixture, respectively, evaluated at the local saturated pressure and overall composition. The temperatures T_{LV} and T_{MV} are the temperatures of the least volatile component and the most volatile component evaluated at the saturation pressure of mixture, respectively.

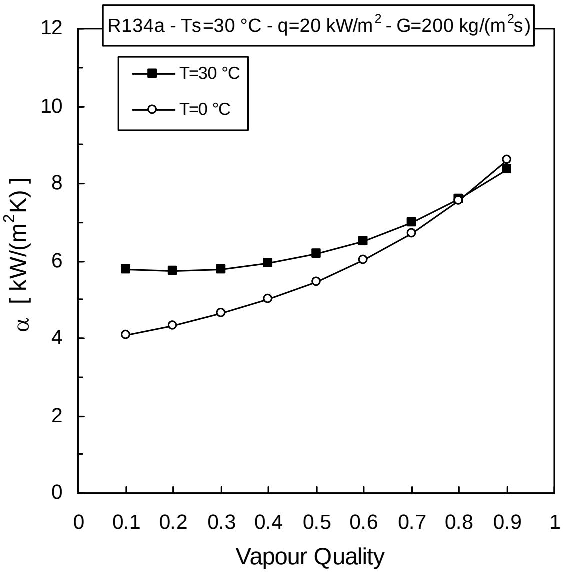

Figure 1.28. Model by Hamilton *et al.* (2008): heat transfer coefficient vs. vapour quality. The mass velocity is 200 kg/(m^2 s), the heat flux is 20 kW/m^2 and the saturation temperature is 0 and 30 °C. The heat transfer coefficient is based on the actual inner surface area.

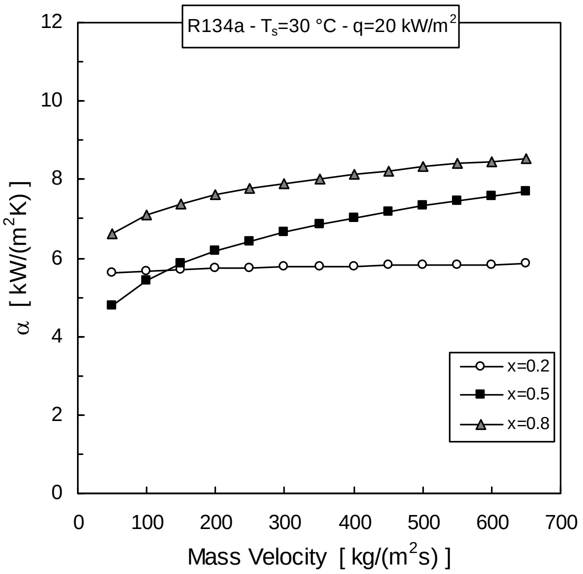

Figure 1.29. Model by Hamilton *et al.* (2008): heat transfer coefficient vs. mass velocity. The saturation temperature is 30 °C, the heat flux is 20 kW/m^2 and the vapour quality is 0.2, 0.5, 0.8. The heat transfer coefficient is based on the actual inner surface area.

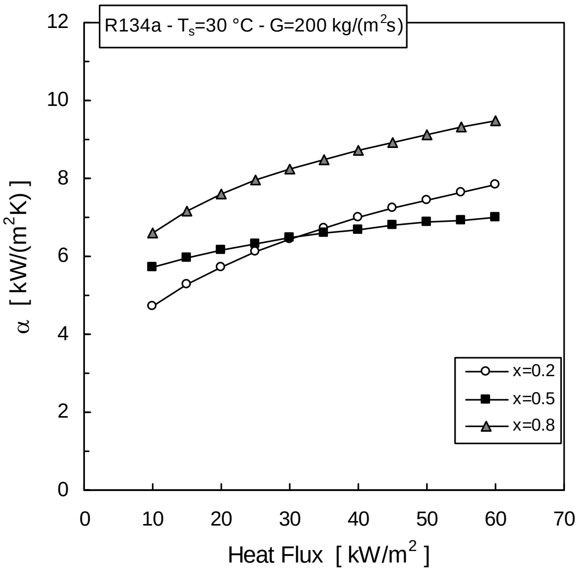

Figure 1.30. Model by Hamilton *et al.* (2008): heat transfer coefficient vs. heat flux. The saturation temperature is 30 °C, mass velocity is 200 kg/(m^2 s) and the vapour quality is 0.2, 0.5, 0.8. The heat transfer coefficient is based on the actual inner surface area.

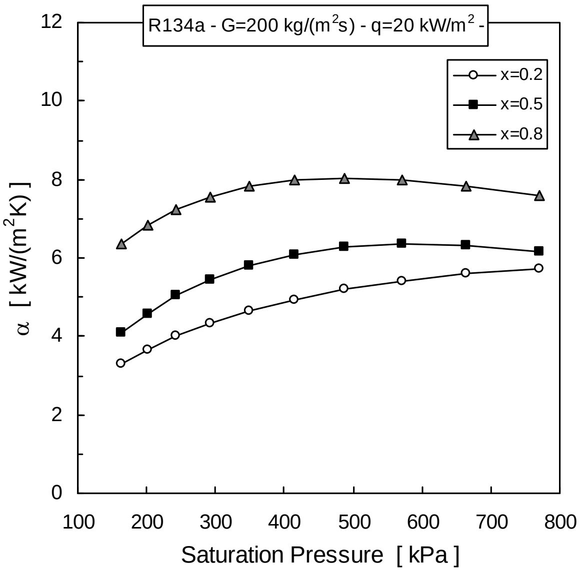

Figure 1.31. Model by Hamilton *et al.* (2008): heat transfer coefficient vs. saturation pressure. The mass velocity is 200 kg/(m^2 s), the heat flux is 20 kW/m^2 and the vapour quality is 0.2, 0.5, 0.8. The heat transfer coefficient is based on the actual inner surface area.

The mass fraction of the vapour, z_v, and that of the liquid, z_l, are evaluated at the saturation pressure and local thermodynamic quality, while the overall composition is the all liquid or all vapour value. The constant C_6 is set 0 for pure refrigerants, but it can also set to zero in the case of near-azeotropic mixtures because of the negligible influence of the composition difference between vapour and liquid phases.

Figure 1.28 reports the heat transfer coefficient calculated with Hamilton *et al.* (2008) against vapour quality for R134a at 0 °C and 30°C saturation temperature. In the low vapour quality region the heat transfer coefficient calculated at 30° C is higher than that calculated at 0 °C, because the nucleate boiling contribution is higher. As the vapour quality increases, the two coefficient curves tend to merge and the convective mechanism provides the main contribution.

Figure 1.29 - 1.31 present the effect of mass velocity, heat flux and saturation pressure for three different values of vapour quality, 0.2, 0.5 and 0.8. By Figure 1.23, for mass velocity under 100 kg/(m^2 s), the heat transfer coefficient calculated at 0.2 vapour quality results higher as compared to the coefficient calculated at 0.5 vapour quality. As vapour quality increases to 0.8 the highest heat transfer coefficient occurs, probably because of the combined effect of the convective mechanism and the nucleate boiling suppression. At high mass velocity the convective mechanism seems to provide the main contribution and the heat transfer coefficient increases with vapour quality.

In Figure 1.30 the effect of heat flux is reported. When the heat flux is lower than around 30 kW/m^2, the heat transfer coefficient increases with vapour quality, but at higher heat flux values the process becomes nucleate boiling dominated for vapour quality under 0.5.

Saturation pressure seems to play a lower role as compared to mass velocity and heat flux, as it can be seen from Figure 1.31.

CHAPTER 2

EXPERIMENTAL APPARATUS AND MEASURING PROCEDURE

2.1 Experimental apparatus

The measurements of heat transfer coefficient and pressure drop have been performed on the experimental apparatus, set up within the two-phase heat transfer laboratory of the Dipartimento di Fisica Tecnica of the University of Padova. The test facility is set up to perform test runs during vaporization and condensation. Only the flow boiling set up will be explained in the following. A schematic view of the experimental apparatus is reported in Figure 2.1. The test facility consists of two loops: the refrigerant and the water loop. In the first loop, the refrigerant is pumped as sub-cooled liquid in the pre-heater, where it is heated and in some cases partially evaporated to achieve the desired vapour quality at the inlet of the test section. The refrigerant enters the tube side of the test section at a known mass velocity and vapour quality and then it is vaporized. Both the pre-heater and the test section are coaxial tube in tube heat exchangers, in which the refrigerant, flowing inside the tube, is heated and vaporized by hot water flowing in the annulus. After, the two-phase mixture leaves the test section and goes to a braised plate type condenser, where it is fully condensed and sub-cooled by ground water. A bladder accumulator, connected to a nitrogen bottle and a pressure regulator, are installed in the refrigerant loop: the refrigerant pressure can be controlled, by varying the charge of nitrogen on the accumulator. The pump is a magnetically coupled variable speed gear pump, oil free, which allows to control independently the refrigerant flow.

The vapour quality at the inlet of the test section is determined by the heat extracted in the pre-heater, by varying the water temperature and flow rate. The heat transfer rate in the test section is also controlled by acting on the water temperature and flow rate. Magnetic type flow meters, by Endress-Hauser, are used to measure the water flow rate.

The temperature of the hot water, entering the pre-heater and the test section is controlled by a secondary water circuit, where an electrical heater supplies the water with the power transferred to the refrigerant. A scheme of the hot water circuit is provided in Figure 2.2. The water back from the test section, the pre-heater and the electrical boiler are mixed together in a storage tank, where the temperature is maintained constant. The electrical heater has 22 kW power, which can be adjusted by a PID controller to ensure the set temperature in the water tank; from the storage, water is then directly pumped to the primary loop. If two different water temperatures are required in the primary loop, a second electrical heater can be used to heat the water flow rate just before arriving to the refrigerant circuit. Ground water, cooled in some cases by a chiller, is used when the water temperature in the storage tank must be lowered. A by-pass system is adopted to vary the water flow rate.

The test section, reported in Figure 2.3, is divided in three parts: a pre-conditioning section, 0.60 m long, the measuring section, 0.30 m long, and a post-section, 0.20 m long, which drives the refrigerant to the outlet of the test tube.

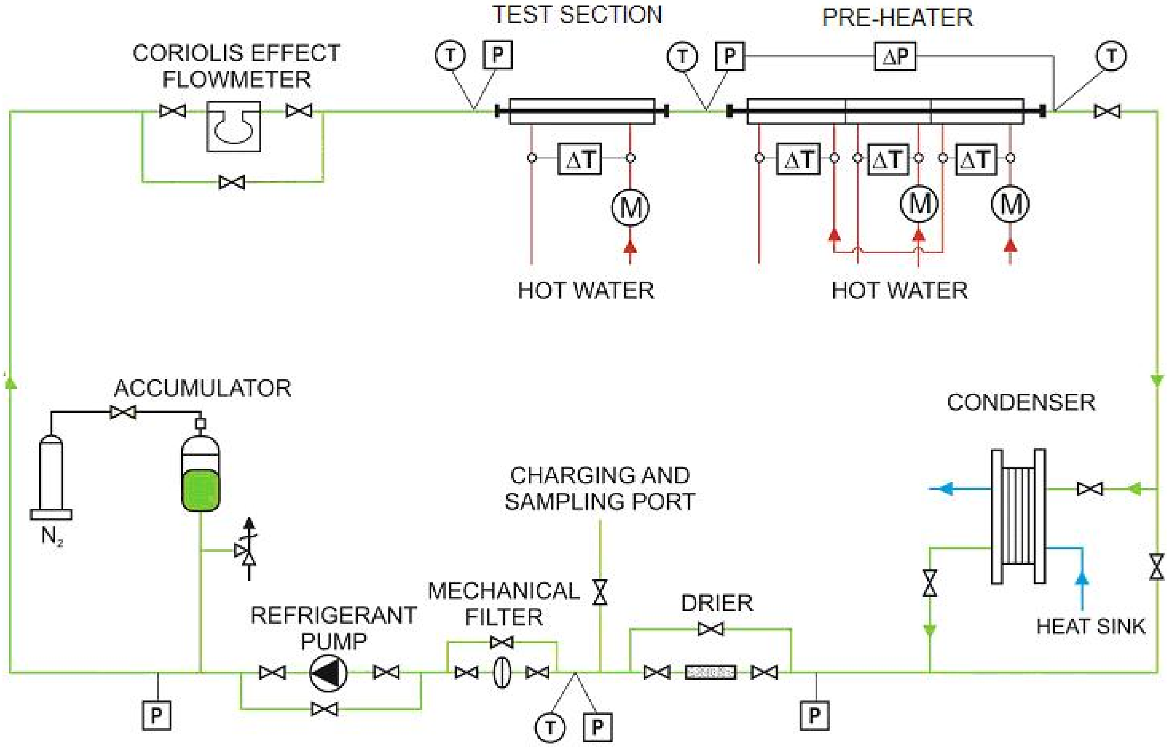

Figure 2.1. Schematic view of the experimental test rig.

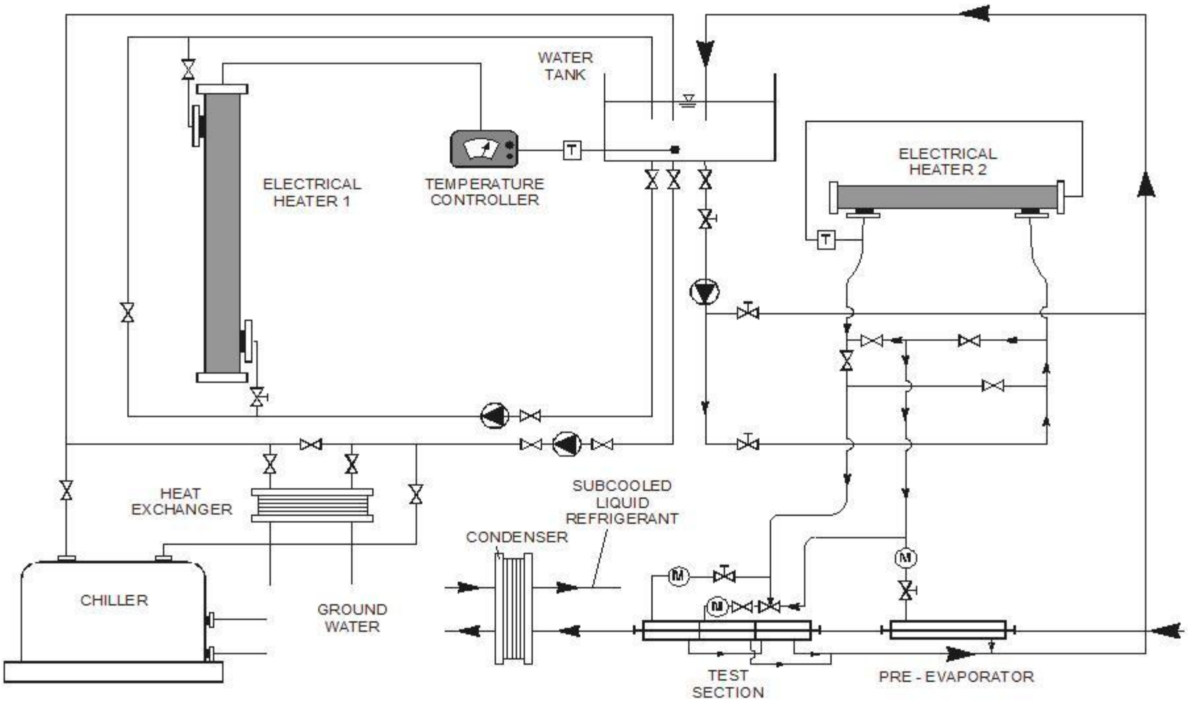

Figure 2.2. Schematic view of the hot water loop.

In the pre-conditioning section the refrigerant flow achieves a fully developed flow regime and a final adjustment of vapour quality can be performed. The middle part is the measuring section, where the heat transfer coefficient is measured. The test section is obtained using a single 1.4 m long inner microfin tube and three separated heating water jackets.

The water temperature and flow rate entering the pre-conditioning and the measuring sections can be independently controlled. The inner tube, which is the test tube, is a microfin tube with 60 fins, with 0.23 mm fin height, 13° helix angle and 43° apex angle; the fin tip is smoothed as it can be observed by the enlarged image reported in Figure 2.4. The geometrical characteristics of the microfin test section are described in detail in Figure 2.5 and Table 2.1.

The test section is instrumented with copper-constantan (type T) thermocouples, embedded in its wall, to measure the surface temperature. The thermocouples are located in the middle point of each section and they are inserted and soldered circumferentially into four equidistant axial grooves (Figure 2.4).

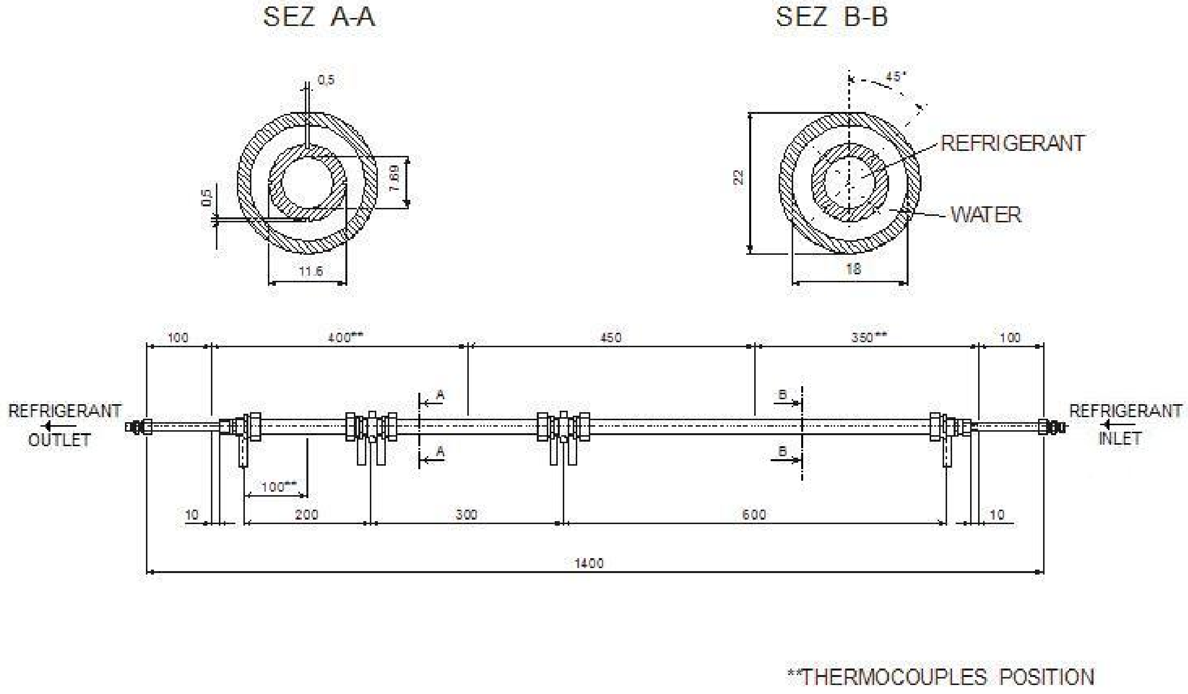

Figure 2.3. Experimental test section. The cross-section of the pre-conditioning and the measuring sections are also reported.

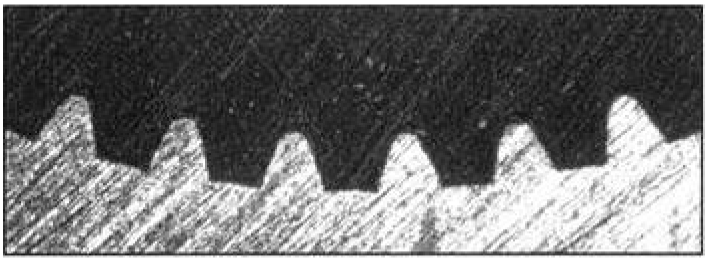

Figure 2.4. Enlarged image of the micro-fins.

Table 2.1. Geometrical characteristics of the test section

Outside diameter [mm]	11.6
Inside diameter at fin tip [mm]	7.69
Total length [mm]	1400
Pre-conditioning section length [mm]	600
Measuring section length [mm]	300
Post-section length [mm]	200
Fins number	60
Fin height [mm]	0.23
Apex angle [°]	43
Helix angle [°]	13

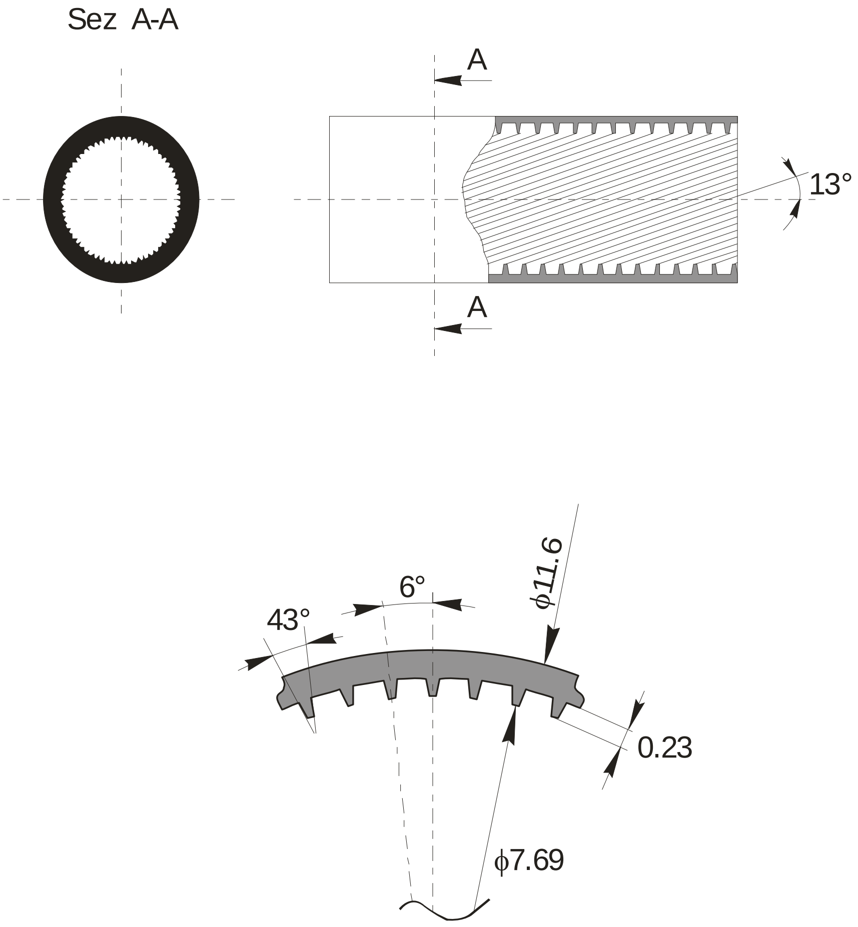

Figure 2.5. Geometrical characteristics of the microfin tube.

The water temperature change in each section is measured by a four junction copper-constantan thermopile, inserted into appropriate adiabatic mixing chambers, where copper-constantan thermocouples are also inserted to measure the water temperature. A metal helix is wounded around the outside surface of the test tube, inside the annulus, in order to avoid stratification in the water flow and to get high heat transfer coefficient on the water side, with reasonable values of water temperature decrease.

A digital Rosemount pressure transducer is connected to a manometric tap to measure the vapour pressure upstream the microfin tube. Pressure drop along the entire length of the microfin tube is measured by a digital Endress-Hauser pressure transducer, connected to two manometric taps upstream and downstream the test tube.

Refrigerant temperatures at the inlet and the outlet of test section are measured by means of adiabatic sectors, with thermocouples inserted into both the refrigerant flow and the tube wall. Refrigerant temperature at the inlet and outlet of the pre-heater are also measured, as well as the inlet and outlet water temperature and the water temperature change. The water side temperature measurements are performed by means of mixing chambers, again.

The refrigerant mass flow rate is measured by a Coriolis effect Micromotion mass flow meter inserted downstream of the pump.

A picture of the test section is reported in Figure 2.6; as it can be observed, much careful have been paid to insulate the test section and the water pipes connecting the test section and the mixing chambers, where water temperature is measured, in order to minimize the heat flow rate dispersed to the surrounding ambient.

The measured parameters are acquired, analyzed and stored. The data acquisition system consists of a Keithley Digital Multimeter DM 196, a Keithley Switch System MOD. 7001 and a personal computer running the LabView 4.0 software. The list of sensors and parameters acquired is reported in Table 2.2.

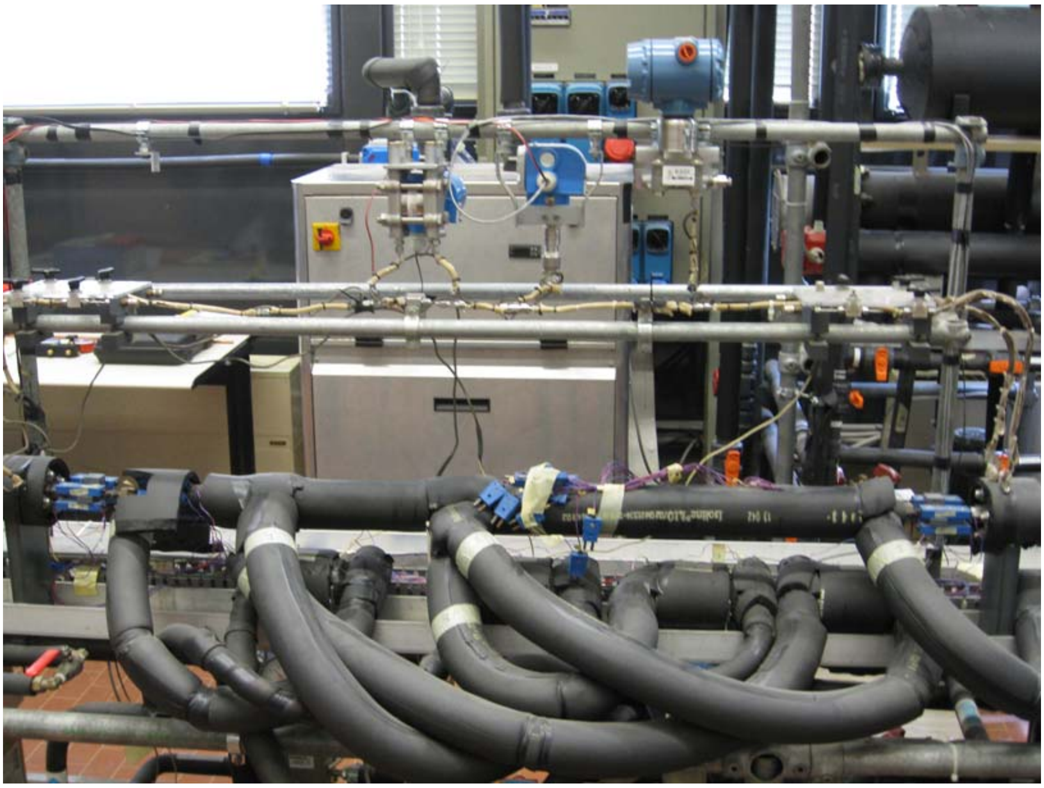

Figure 2.6. Experimental test section.

Table 2.2. Sensors and parameters measured.

Sensor	Channel recording	Unit	Measured parameter
Thermocouple	7	°C	Refrigerant temperature - Inlet pre-heater
Thermocouple	8	°C	Refrigerant temperature Inlet pre-heater
Thermocouple	9	°C	Refrigerant temperature Inlet pre-heater
Thermocouple	10	°C	Refrigerant temperature Inlet test section
Thermocouple	11	°C	Refrigerant temperature - Inlet test section
Thermocouple	12	°C	Refrigerant temperature -Inlet test section
Thermocouple	13	°C	Wall temperature - Pre-conditioning section
Thermocouple	14	°C	Wall temperature - Pre-conditioning section
Thermocouple	15	°C	Wall temperature - Pre-conditioning section
Thermocouple	16	°C	Wall temperature - Pre-conditioning section
Thermocouple	17	°C	Wall temperature – Post-section
Thermocouple	18	°C	Wall temperature – Post-section
Thermocouple	19	°C	Wall temperature – Post-section
Thermocouple	20	°C	Wall temperature – Post-section
Thermocouple	21	°C	Water temperature – Inlet pre-conditioning section
Thermocouple	22	°C	Water temperature – Outlet measuring section
Thermocouple	23	°C	Water temperature – Inlet measuring section
Thermocouple	30	°C	Wall temperature – Measuring section
Thermocouple	31	°C	Wall temperature – Measuring section
Thermocouple	32	°C	Wall temperature – Measuring section
Thermocouple	33	°C	Wall temperature – Measuring section
Coriolis effect flow meter	41	Kg/min	Refrigerant mass flow rate
Differential pressure transducer	43	mbar	Refrigerant pressare drop – Test section
Pressure transducer	44	bar	Refrigerant pressure – Inlet pre-heater
Magnetic flow meter	45	l/h	Water flow rate – Measuring section
Magnetic flow meter	46	l/h	Water flow rate – Pre-heater
Magnetic flow meter	49	l/h	Water flow rate – Measuring section
Pressure transducer	50	bar	Refrigerant pressure – Inlet test section
Thermocouple	53	°C	Refrigerant temperature – Outlet test section
Thermocouple	54	°C	Refrigerant temperature – Outlet test section
Thermocouple	55	°C	Refrigerant temperature – Outlet test section
Thermocouple	56	°C	Air ambient temperature
Thermocouple	57	°C	Water temperature – Inlet post-section
Thermocouple	58	°C	Water temperature – Outlet post-section
Thermocouple	59	°C	Water temperature – Inlet pre-heater
Thermopile	63	°C	Water temperature difference – Pre-heater
Thermopile	64	°C	Water temperature difference – Preconditioning section
Thermopile	65	°C	Water temperature difference – Post-section
Thermopile	66	°C	Water temperature difference – Measuring section
Pressure transducer	67	°C	Atmospheric pressure

2.2 Measuring technique and data reduction

The measured heat transfer coefficients are quasi-local values; this means that the vapour quality change across the measuring section is small, lower to 0.20.

The experimental heat transfer coefficient is determined by the ratio of the heat flux, transferred to refrigerant, and the difference between the wall and the saturation temperature:

$$\alpha = \frac{Q}{A(T_{wall} - T_s)} \tag{2.1}$$

The heat flow rate, *Q*, is obtained by a thermal balance on the water side and it is given by the measurement of the water flow rate and the water temperature difference across the measuring section. The heat dispersed from hot water to the surrounding air has been evaluated by specific tests, reported in 2.3, and it is considered in the determination of the heat flow rate transferred to the refrigerant in the various heat transfer sectors. The wall temperature is the average value obtained by the four thermocouple readings, inserted in the middle point of the measuring section. The saturation temperature is reduced by the local measurement of the refrigerant pressure. The inlet refrigerant pressure and the pressure drop across the entire tube length are measured, thus the saturation pressure at the measuring point is obtained by a linear interpolation of the pressure readings at the inlet and the outlet of the test section.

The vapour quality, entering the measuring section, is given by an energy balance performed on the pre-heater and the first sector of the test section.

$$x_{in,S2} = \frac{Q_{pre} + Q_{S1} - m_r\left(h_{l,sott} - h_{l,s}\right)}{m_r h_{lv}} \tag{2.2}$$

where Q_{pre} and Q_{S1} are the heat flow rate exchanged in the pre-heater and in the first sector of the test section, respectively, obtained by the side water measurements; m_r is the refrigerant mass flow rate, and $h_{l,sott}$, h_{ls}, and h_{lv} are sub-cooled liquid enthalpy, the liquid saturate enthalpy and the latent heat of evaporation.

An energy balance is performed in the measuring section to determine the vapour quality change:

$$\Delta x_2 = \frac{\dot{Q}_{S2}}{\dot{m}_r h_{lv}} \tag{2.3}$$

The vapour quality at the middle of the measuring section is finally obtained as:

$$x_2 = x_{in,S2} + \frac{\Delta x_2}{2} \tag{2.4}$$

The data reduction procedure has been implemented program, written in Fortran 90 language. All the thermo-physical and thermodynamics properties are given by RefProp7.0 software.

Test runs have been performed with refrigerant R134a and R410A. The second fluid is a quasi-azeotropic mixture of R125 (50 %) and R32 (50 %), with a glide temperature around 0.1 °C. Thus, due to the very low glide temperature, in the saturate region, R410A properties are evaluated at the average temperature between bubble and dew point corresponding to the measured pressure.

Test runs have been performed paying attention to have a water temperature difference in each heat transfer sector greater than 1 °C to obtain a reasonable accuracy in the measurement of the heat flux exchanged. Besides, to perform a quasi-local measurement, the water temperature difference in the measuring section was maintained lower than 2 °C, to get a low variation of the wall temperature profile along the measuring sector.

During test runs, each measurement is obtained as the average value of 10 readings. The experimental uncertainty of the measured parameters has been lead following the method provided by the ISO ("Guide to the expression of the experimental uncertainty, ISO, 1999"), which distinguishes between type A and type B uncertainty. Type B uncertainty is proper of the sensor and it is generally provided by the manufacturer. The type B uncertainty of the sensors used here is reported in Table 2.3. All thermocouples have been calibrated using a bath with a Kaye reference thermometer (accuracy 0.02 °C). Type A uncertainty is due to the measurement and it is obtained as the standard deviation of the mean of the ten readings taken for each measurement:

$$u_A = \sqrt{\frac{\sum_i (x_i - \bar{x})^2}{N(N-1)}} \tag{2.5}$$

where N is the number of readings.

The standard uncertainty is obtained by the combination of the two uncertainty components:

$$u = \sqrt{u_A^2 + u_B^2} \tag{2.6}$$

where u_A and u_B are the type A and type B uncertainty, respectively. When a parameter R is the result of independent m independent measurements x_i, the law of combined uncertainties is applied to evaluate the standard uncertainty:

$$R = f(x_1, x_2, ..., x_m) \tag{2.7}$$

$$u_R = \sqrt{\sum_i \left(\frac{\partial R}{\partial x_i}\right)^2 u_i^2} \tag{2.8}$$

where u_i is the standard uncertainty associated at each independent measurement and it is determined by Eq. (2.6). The final uncertainty is expanded to a confidence level of 95 %, by multiplying the standard uncertainty u_R by a coverage factor equal to 2.

Table 2.3. Type B uncertainty for sensors (95% confidence level).

Thermocouples	± 0.05 °C
Thermopile	± 0.05 °C
Water Flow meter	1 %
Refrigerant Mass Flow meter	0.4 %
Pressure transducer	±1 kPa
Differential pressure transducer	±200 Pa

2.3 Calibration of the test rig

Preliminary tests have been lead to check the calibration of the test rig. First of the calibration of all the sensors used for experimental tests has been checked. After, three different tests have been performed: a measurement of the heat dispersed from the heat transfer sections (test section and pre-heater) toward the ambient air, an energy balance on the heat transfer sectors (pre-heater and test section) and a check of the agreement between the saturation temperature measured from the pressure and the saturation temperature directly measured with the thermocouples.

The measurement of heat flow rate dispersed to the ambient air have been performed for all the heat transfer sectors, the pre-heater, the pre-conditioning section, the measuring section and the post-section. This is because, water is introduced in the heat transfer sections at quite high temperature in order to vaporize the refrigerant at 30 °C and 40 °C. This test has been performed, by making under vacuum the inner side of the heat transfer sections and then introducing water flow rate at different temperatures, ranging between the ambient air temperature up to around 60 °C, which represents the maximum value reached during vaporization test runs. The heat flow rate dispersed from the water to the surrounding air is then obtained from the measurement of the water flow rate and the temperature difference along the considered sector. The ambient air temperature is also measured, thus for each heat transfer sector a correlation is experimentally established between the heat flow rate dispersed from water to air and the difference between the men water temperature inside the sector and the ambient air temperature. In Figure 2.7 for instance the measurements performed to determine the heat dispersed in the measuring section is reported.

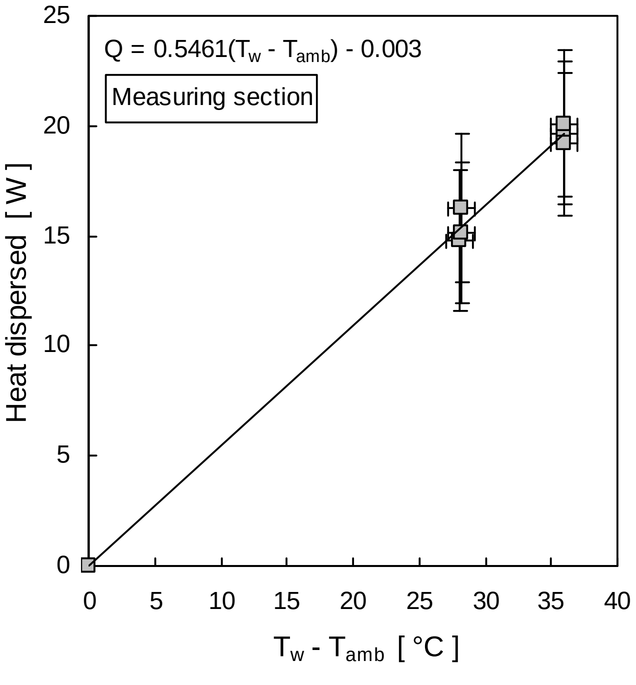

Figure 2.7. Heat flow rate dispersed as a function of the difference between the water and ambient air temperature: measuring section.

Therefore, in the reduction of experimental data, the heat flow rate transferred from water to the refrigerant is obtained by subtracting the heat flow rate dispersed toward the ambient from the heat flow rate provided by the water side thermal balance.

For each heat transfer section, an energy balance has been performed on the water and refrigerant side, respectively; the values obtained have been compared and a satisfactory agreement within 2.5 % is obtained.

The saturation temperature measured by the pressure and that directly measured by the thermocouples during adiabatic two-phase flow are compared. For R134a the two values differ less than 0.15 °C at high mass velocity. Higher deviations are found at low vapour quality and are probably related to non equilibrium in the flow and local sub-cooling at the inlet.

CHAPTER 3

EXPERIMENTAL MEASUREMENTS OF HEAT TRANSFER COEFFICIENT IN A MICROFIN TUBE

3.1 Experimental results for R134a

The experimental measurements of the heat transfer coefficient during flow boiling of R134a inside the microfin tube are here presented. Test runs has been performed at 30 °C and 40 °C saturation temperature, mass velocity from 80 to 600 kg/(m^2 s) and heat flux from 14 to 83.5 kW/m^2; vapour quality is between 0.1 and 0.99. The experimental data sets are reported in Table 3.1 - 3.12, where the measured values of saturation temperature, mass velocity, heat flux, vapour quality and heat transfer coefficient are provided. The experimental uncertainty, at 95 % confidence level, is indicated for heat transfer coefficient $U(\alpha)$ and vapour quality $U(x)$. During test runs, heat flux has been kept constant within ±2 % as compared to the average value, at high heat fluxes (42 - 83.5 kW/m^2); a larger deviation, around ±8.5 %, is sometimes observed at the lower heat flux investigated, 14 kW/m^2. Mass velocity varies within ±2.5 % at 80 and 100 kg/(m^2 s) and within ±1 % at higher mass velocities. Saturation temperature is within around ±1 °C. Larger deviations are sometimes observed, especially under dry-out regime, due to the more unstable flow conditions. The average percentage uncertainty of the heat transfer coefficient is between ±5 % and ±8.5 %, before the onset of dryout; the higher uncertainty values are observed around the dry-out quality inception. The experimental uncertainty of vapour quality is also higher near the dry-out region.

Table 3.1. Heat transfer experimental results for R134a in microfin tube: T_s = 30 °C, G = 600 kg/(m^2 s), q = 42.4 kW/m^2.

T_s [°C]	G [kg/(m^2 s)]	q [kW/m^2]	x	α [W/(m^2 K)]	$U(x)$	$U(\alpha)$ [W/(m^2 K)]
29.7	599	42.5	0.16	11231	0.003	962
29.8	598	43	0.17	11362	0.003	962
29.6	598	42.9	0.29	11193	0.004	797
29.6	599	42.6	0.29	10962	0.004	781
29.6	603	41.5	0.42	11164	0.007	798
29.6	603	42	0.42	11197	0.007	790
29.8	598	43.2	0.63	11869	0.008	856
29.8	598	42.6	0.63	11683	0.008	837
29.7	598	41.5	0.75	12556	0.009	985
29.7	597	42.4	0.75	12782	0.009	1005

Table 3.2. Heat transfer experimental results for R134a in microfin tube: T_s = 30 °C, G = 600 kg/(m^2 s), q = 58.9 kW/m^2.

T_s [°C]	G [kg/(m^2 s)]	q [kW/m^2]	x	α [W/(m^2 K)]	U(x)	U(α) [W/(m^2 K)]
29.7	601	58.7	0.19	12554	0.003	822
29.7	600	59	0.19	12666	0.003	827
29.7	600	58.7	0.19	12600	0.003	823
29.8	600	58.1	0.30	12259	0.006	821
29.9	600	58.8	0.31	12585	0.006	845
29.9	599	60.2	0.32	12705	0.006	839
29.8	601	59.3	0.42	12707	0.007	839
29.8	600	59.2	0.43	12581	0.007	826
30	600	57.8	0.57	13026	0.008	773

Table 3.3. Heat transfer experimental results for R4134a in microfin tube: T_s = 30 °C, G = 600 kg/(m^2 s), q = 83.5 kW/m^2.

T_s [°C]	G [kg/(m^2 s)]	q [kW/m^2]	x	α [W/(m^2 K)]	U(x)	U(α) [W/(m^2 K)]
30.1	604	83	0.10	15197	0.004	814
30	604	83.3	0.10	15217	0.004	815
29.9	601	83.4	0.23	14536	0.003	749
29.9	600	83.5	0.23	14456	0.003	741
29.7	598	84	0.30	14134	0.004	721
29.7	597	84.2	0.30	14256	0.004	729
29.4	601	83.8	0.31	14187	0.004	717
29.4	600	83.8	0.31	14150	0.004	716
30	600	83.4	0.43	14292	0.006	764
30	600	83.5	0.44	14209	0.006	733
30	600	83.1	0.44	14097	0.006	726
29.8	598	83.5	0.57	14418	0.008	747
29.8	599	82.8	0.57	14277	0.008	743
29.9	599	82.7	0.58	14415	0.008	759
29.8	596	83.5	0.64	14635	0.008	741
29.8	596	84	0.64	14605	0.008	734

Table 3.4. Heat transfer experimental results for R134a in microfin tube: T_s = 30 °C, G = 400 kg/(m^2 s), q = 22.3 kW/m^2.

T_s [°C]	G [kg/(m^2 s)]	q [kW/m^2]	x	α [W/(m^2 K)]	U(x)	U(α) [W/(m^2 K)]
29.6	400	20.8	0.19	9243	0.004	492
29.6	400	21.2	0.19	9354	0.004	517
30.4	400	22.3	0.27	10426	0.005	614
30.4	400	22.5	0.28	10490	0.005	622
30.2	397	21.9	0.37	9858	0.009	386
29.7	402	22.7	0.46	10509	0.008	580
29.7	402	22.7	0.47	10454	0.008	569
30.7	400	20.7	0.57	10297	0.010	700
30.3	401	21.7	0.59	10378	0.010	558
30.3	402	21.7	0.59	10395	0.010	602
30.2	401	21.8	0.59	10340	0.010	588
30.4	400	22.3	0.77	12213	0.010	651
30.4	400	22.3	0.77	12366	0.010	664
30.3	400	23.7	0.77	12371	0.010	672
29.8	398	21.8	0.80	12148	0.012	711
29.8	398	21.4	0.80	12316	0.012	961
30.3	402	23.9	0.95	16966	0.012	1127
30.4	402	23.7	0.95	16755	0.012	1094
30.4	401	23.3	0.95	16643	0.012	1112
30.4	402	22.9	0.95	17314	0.012	1179
30.4	402	24.1	0.97	6741	0.012	695
30.4	402	23.8	0.97	7896	0.012	691

Table 3.5. Heat transfer experimental results for R134a in microfin tube: T_s = 30 °C, G = 400 kg/(m^2 s), q = 28.5 kW/m^2.

T_s [°C]	G [kg/(m^2 s)]	q [kW/m^2]	x	α [W/(m^2 K)]	U(x)	U(α) [W/(m^2 K)]
30	402	27.9	0.10	9692	0.006	474
31.1	402	29.3	0.10	10091	0.006	501
30.1	402	27.7	0.11	10339	0.004	658
30.6	401	27.8	0.16	10508	0.004	544
30.4	399	28.3	0.24	10442	0.006	504
30.5	397	27.7	0.24	10472	0.007	571
30.3	398	28.7	0.39	10661	0.008	443
29.5	397	29.6	0.45	10975	0.008	440
30.2	399	27.6	0.60	10976	0.009	480
30.2	400	28.2	0.61	11074	0.009	491
30.4	398	29.1	0.76	11914	0.010	564
30.4	398	27.4	0.77	11722	0.010	545
30.4	399	28.5	0.81	12575	0.011	602
30.5	399	28.8	0.81	12696	0.011	608
30.7	401	29.1	0.91	15277	0.012	952
30.7	399	29.9	0.91	15797	0.013	1115
30.6	401	29.3	0.91	15366	0.013	833
30.1	400	28.1	0.97	4462	0.012	301
29.1	399	30	0.97	3202	0.011	130
29.1	399	30.9	0.98	2720	0.011	146
29.1	399	28.8	0.98	2490	0.011	138

Table 3.6. Heat transfer experimental results for R134a in microfin tube: T_s = 30 °C, G = 400 kg/(m^2 s), q = 43.2 kW/m^2.

T_s [°C]	G [kg/(m^2 s)]	q [kW/m^2]	x	α [W/(m^2 K)]	U(x)	U(α) [W/(m^2 K)]
29.7	402	43.1	0.24	11439	0.005	687
29.6	402	44.2	0.25	11656	0.005	701
28.7	403	43.1	0.38	11590	0.005	439
28.8	403	44.5	0.39	11669	0.005	429
29.4	402	45.1	0.42	11878	0.006	429
30	400	41.9	0.57	11966	0.009	499
30	399	42.8	0.57	11838	0.008	447
30	400	42.3	0.57	12027	0.010	511
30.1	399	41.7	0.58	11807	0.008	440
30.1	399	45.6	0.70	12821	0.011	461
30.1	398	46.7	0.71	12996	0.011	485
29.6	399	41.3	0.83	14184	0.012	1445
29.6	399	41.4	0.83	14239	0.012	1434
29.6	400	42.2	0.87	15231	0.017	1508
29.6	400	41.9	0.87	15128	0.020	2397
29.6	400	42.4	0.94	11410	0.012	1043
29.6	400	41.4	0.94	10739	0.012	964

Table 3.7. Heat transfer experimental results for R134a in microfin tube: T_s = 30 °C, G = 200 kg/(m^2 s), q = 14.9 kW/m^2.

T_s [°C]	G [kg/(m^2 s)]	q [kW/m^2]	x	α [W/(m^2 K)]	U(x)	U(α) [W/(m^2 K)]
29.2	201	14.9	0.13	7721	0.012	489
29.2	201	15.1	0.13	7828	0.012	498
30.1	201	14.6	0.19	8376	0.007	567
30.1	201	14.9	0.19	8389	0.007	549
30.7	200	15.1	0.41	9345	0.0008	649
30.8	200	14.7	0.41	9270	0.008	622
30.8	200	14.9	0.42	9357	0.008	626
30.8	199	15.4	0.55	9768	0.009	677
30.8	199	15.8	0.56	9929	0.009	674
30.8	200	15.6	0.56	9921	0.009	698
30.5	201	13.6	0.76	13023	0.011	1203
30.7	202	14.4	0.77	13570	0.011	1228
30.7	202	14.4	0.78	13336	0.012	1219
31	202	14.8	0.93	16730	0.012	1651
31.1	202	14.6	0.94	17089	0.013	1892
31	202	14.8	0.94	17425	0.013	1849
31	202	15.3	0.95	17787	0.013	2036
31.2	202	13.6	0.98	7258	0.013	1194
30.9	202	14.5	0.98	8535	0.013	1057
30.8	202	13.5	0.98	5022	0.012	755
30.7	202	12.2	0.99	3738	0.013	497

Table 3.8. Heat transfer experimental results for R134a in microfin tube: T_s = 30 °C, G = 200 kg/(m^2 s), q = 22.3 kW/m^2.

T_s [°C]	G [kg/(m^2 s)]	q [kW/m^2]	x	α [W/(m^2 K)]	U(x)	U(α) [W/(m^2 K)]
30.5	202	22.2	0.17	9229	0.007	441
30.5	202	22.5	0.18	9464	0.007	637
30.5	202	22.5	0.18	9139	0.007	435
30.7	202	22.2	0.24	9401	0.012	497
30.7	202	22	0.24	9341	0.012	502
30.3	202	22.2	0.27	9309	0.013	464
31	200	22.1	0.38	10949	0.007	648
31	200	22.1	0.38	10896	0.007	649
30.2	201	22.4	0.47	10211	0.008	520
30.2	200	22.3	0.47	10251	0.008	534
30.7	200	20.9	0.60	11039	0.011	595
30.7	199	21.6	0.60	11313	0.011	648
30.4	199	22.2	0.75	12110	0.016	660
30.5	198	22.4	0.76	12665	0.016	711
30.1	200	23.2	0.82	13207	0.018	737
30.1	199	22.7	0.83	13097	0.018	720
30.2	200	23	0.84	13281	0.018	755
30.4	200	22.3	0.91	14650	0.018	860
30.4	200	22.7	0.91	14747	0.018	922
31	202	22.3	0.94	12493	0.016	681
31	202	22.4	0.94	12674	0.015	679
31	202	22.6	0.95	12514	0.015	658
31	202	23	0.95	12585	0.015	663
31	202	22.9	0.96	12791	0.016	721
30.5	202	22.5	0.96	12133	0.016	629
30.5	202	21.8	0.97	11352	0.016	615

Table 3.9. Heat transfer experimental results for R134a in microfin tube: T_s = 30 °C, G = 200 kg/(m^2 s), q = 42.4 kW/m^2.

T_s [°C]	G [kg/(m^2 s)]	q [kW/m^2]	x	α [W/(m^2 K)]	U(x)	U(α) [W/(m^2 K)]
30	202	42	0.22	12361	0.006	999
30	200	42.1	0.22	12154	0.006	968
30	200	42.4	0.40	12901	0.010	1007
30	200	42.5	0.40	12865	0.010	1000
29.9	202	41.9	0.57	12780	0.009	1105
29.9	202	42	0.57	12455	0.009	1055
30	201	42.8	0.70	13298	0.010	1152
30	201	42.9	0.70	13338	0.010	1160
30.1	203	42.2	0.77	14443	0.011	1265
30.1	202	42.5	0.78	14429	0.010	1251
30	201	42.5	0.83	15199	0.012	1387
30	201	42.3	0.84	15270	0.012	1405
30.2	201	42.4	0.88	15793	0.014	1593
30.2	201	42.4	0.88	15606	0.014	1576
30	200	42	0.90	13380	0.017	1473
30	199	41.8	0.91	13362	0.018	1433

Table 3.10. Heat transfer experimental results for R134a in microfin tube: T_s = 42 °C, G = 200 kg/(m^2 s), q = 14.1 kW/m^2.

T_s [°C]	G [kg/(m^2 s)]	q [kW/m^2]	x	α [W/(m^2 K)]	U(x)	U(α) [W/(m^2 K)]
42.7	202	12.6	0.17	9187	0.014	741
42.5	203	12.6	0.23	9448	0.014	729
42.5	202	14.2	0.23	10072	0.014	814
42	202	13	0.34	10228	0.009	861
42	202	13.6	0.35	10095	0.009	782
42.8	202	12.8	0.54	10653	0.015	866
42.8	202	14.1	0.55	11024	0.015	854
42.9	201	14.3	0.55	11023	0.015	867
42.8	201	13.4	0.56	10608	0.015	818
41.6	201	15.2	0.77	12522	0.013	916
42.1	201	14.8	0.80	12925	0.013	1034
42.1	201	15.3	0.81	13106	0.012	1022
41.8	201	14.6	0.81	12466	0.016	1189
41.8	201	15.3	0.81	13681	0.017	1246
41.8	201	14.7	0.81	13137	0.016	991
42	201	13.4	0.89	14749	0.016	1371
42	201	13.5	0.91	14657	0.016	1377
42	201	14.7	0.92	15565	0.016	1429
42.1	201	14.5	0.92	15394	0.016	1385
42.5	202	14.9	0.96	14585	0.016	1327
42.5	201	11.6	0.98	5742	0.016	865
42.5	201	11.9	0.98	4528	0.016	712
42.6	201	11.3	0.99	4723	0.016	644

Table 3.11. Heat transfer experimental results for R134a in microfin tube: T_s = 30 °C, G = 100 kg/(m^2 s), q = 14.7 kW/m^2.

T_s [°C]	G [kg/(m^2 s)]	q [kW/m^2]	x	α [W/(m^2 K)]	U(x)	U(α) [W/(m^2 K)]
30.4	101	14.2	0.16	5457	0.009	374
39.4	101	14.5	0.16	5623	0.009	360
30.6	101	13.9	0.20	5390	0.013	341
30.6	101	14.1	0.20	5485	0.013	348
30.6	101	14.3	0.20	5539	0.013	346
29.8	100	14.2	0.25	5542	0.011	355
29.9	100	14.3	0.26	5632	0.011	356
29.9	100	14.4	0.26	5627	0.011	356
29.9	98	13.9	0.26	5641	0.013	383
30.9	101	15.2	0.26	5763	0.013	351
30.9	101	15.4	0.27	5798	0.013	344
30	101	14.9	0.33	5632	0.013	359
30	101	15.1	0.34	5583	0.013	350
30.5	101	14.8	0.36	6535	0.013	434
30	102	15.8	0.36	6316	0.01	380
30.5	100	15	0.36	6552	0.014	429
30	102	16	0.37	6534	0.010	357
30	102	15.4	0.37	6214	0.010	356
30.5	100	15	0.37	6630	0.014	436
30.3	101	14.7	0.47	6852	0.019	468
30.3	101	14.9	0.48	6768	0.019	458
30.4	102	15	0.48	6812	0.019	447
29.8	102	14.3	0.53	7749	0.012	524
29.9	101	15	0.54	7830	0.015	508
30	101	15.3	0.55	7829	0.013	506
30	100	14.9	0.61	7379	0.014	502
30	100	14.4	0.61	7351	0.014	510
29.9	102	14.2	0.63	7426	0.024	524
29.9	102	14.1	0.63	7414	0.025	520
29.9	102	14.4	0.63	7504	0.025	520
30.5	102	13.9	0.75	8434	0.017	619
30.5	102	14	0.76	8440	0.016	599
30.5	100	14.9	0.83	8750	0.016	616
30.5	100	15.3	0.83	8771	0.016	602
30.8	102	14.6	0.87	9602	0.019	691
30.8	102	14.9	0.90	9936	0.021	723
30.5	100	14.7	0.90	9087	0.018	652
30.6	100	15.7	0.92	10558	0.018	760
30.6	100	14.9	0.93	10190	0.018	716
30.6	100	14.9	0.93	10258	0.018	730
30.9	102	15	0.97	6886	0.017	602

Table 3.12. Heat transfer experimental results for R134a in microfin tube: T_s = 30 °C, G = 100 kg/(m^2 s), q = 21.5 kW/m^2.

T_s [°C]	G [kg/(m^2 s)]	q [kW/m^2]	x	α [W/(m^2 K)]	U(x)	U(α) [W/(m^2 K)]
30	101	22	0.16	7013	0.008	336
30.1	101	22.2	0.19	6981	0.010	330
30.1	101	22	0.19	6933	0.010	330
30.4	101	21.4	0.25	6770	0.011	337
30.4	101	21.6	0.25	6787	0.011	332
30.7	101	21.6	0.30	6929	0.016	332
30.7	101	22	0.30	7052	0.016	334
30.7	102	21.7	0.43	7482	0.012	375
30.7	101	22.2	0.43	7599	0.012	371
30.5	101	21.1	0.50	7451	0.014	422
30.5	101	20.8	0.50	7462	0.014	430
30.7	102	21.5	0.64	9187	0.017	455
30.7	102	21.5	0.64	9180	0.017	449
30.8	102	21.6	0.64	9140	0.017	444
30.8	101	20.6	0.70	9139	0.019	533
30.8	101	21.2	0.72	9362	0.019	543
30.1	101	22.1	0.72	10861	0.014	692
30.1	101	22.1	0.73	10686	0.014	654
30.7	102	22	0.77	10475	0.030	597
30.7	102	22.1	0.77	10325	0.030	586
29.9	101	20.9	0.80	11171	0.016	719
30	101	20.4	0.82	11369	0.016	688
29.8	99	20.6	0.88	11303	0.016	647
30.6	101	21.3	0.89	10047	0.023	582
29.7	99	21.7	0.89	11128	0.016	633
30.6	101	21.6	0.90	9968	0.023	566
30.6	101	21.7	0.90	9907	0.023	555
30.7	101	21.2	0.90	10192	0.024	597
30.6	101	21.5	0.91	10288	0.024	588
30.7	101	21.7	0.95	10586	0.026	601
30.8	101	20.9	0.96	9273	0.024	549
30.8	101	20.2	0.96	8620	0.026	557
30.8	101	20.8	0.97	9842	0.026	574
30.8	101	19.4	0.98	8105	0.026	545

Table 3.13. Heat transfer experimental results for R134a in microfin tube: T_s = 31 °C, G = 80 kg/(m^{2}s), q = 14.7 kW/m^2.

T_s [°C]	G [kg/(m^2 s)]	q [kW/m^2]	x	α [W/(m^2 K)]	U(x)	U(α) [W/(m^2 K)]
31.44	80	14.1	0.20	5202	0.01	340
31.48	81	13.9	0.20	5156	0.01	337
31.51	81	14	0.21	5212	0.01	335
31.49	81	14.4	0.21	5146	0.01	327
30.66	81	14.4	0.21	5235	0.01	336
30.62	81	14.5	0.21	5276	0.01	334
30.63	81	14.2	0.21	5154	0.01	331
30.97	81	15.9	0.26	5547	0.012	357
30.86	81	14.5	0.32	5040	0.01	308
30.88	81	14.7	0.32	4994	0.01	310
30.97	81	14.7	0.38	4995	0.014	335
30.99	81	15	0.38	5119	0.014	329
30.97	81	15	0.38	5030	0.013	317
30.76	82	14.8	0.42	5206	0.017	337
30.76	81	14.8	0.42	5247	0.018	335
30.78	81	15.2	0.43	5250	0.018	335
30.88	81	14	0.49	5472	0.016	352
30.88	81	14.7	0.49	5602	0.016	386
30.88	81	14	0.49	5502	0.016	351
30.87	81	14	0.55	5623	0.025	367
30.88	81	14.4	0.56	5792	0.026	374
30.89	81	14.4	0.57	5726	0.025	364
30.88	81	14.9	0.64	6264	0.018	402
30.9	81	15	0.65	6346	0.018	407
31.37	81	14.3	0.71	6438	0.025	421
31.38	81	14.6	0.71	6501	0.026	427
31.41	81	14.5	0.72	6440	0.026	414
31.41	82	14.3	0.72	6514	0.025	435
31.16	82	15.5	0.77	7058	0.025	444
31.13	81	15.2	0.78	6895	0.026	436
31.08	81	14.9	0.79	7145	0.024	466
31.06	81	15.1	0.79	7076	0.024	461
31.07	81	15.2	0.80	7113	0.024	460
30.93	81	15.7	0.82	7448	0.029	458
30.92	81	15.6	0.85	7536	0.031	467
31.14	81	14.6	0.85	7799	0.029	527
30.93	81	15.7	0.87	7679	0.03	476
31.12	81	14.7	0.87	7927	0.029	531
31.14	81	14.8	0.87	8101	0.029	540
31.12	81	14.8	0.88	7956	0.029	528

The measured heat transfer coefficient is plotted in Figure 3.1 as a function of vapour quality for 30 °C saturation temperature, 14.7 kW/m^2 heat flux and mass velocity from 80 to 200 kg/(m^2 s). When mass velocity is 80 and 100 kg/(m^2 s) and vapour quality is lower than around 0.3, the heat transfer coefficient does not raise either with mass velocity and vapour quality: the heat transfer may be nucleate boiling dominated. At 80 kg/(m^2 s), a local minimum of heat transfer coefficient can be observed at around 0.35 vapour quality. But, at vapour quality values higher than 0.3, the heat transfer coefficient increases with vapour quality until the onset of dry-out. When mass velocity is increased to 200 kg/(m^2 s), the heat transfer coefficient is higher also at low vapour quality as compared to test runs at lower mass velocity; moreover, the trend of heat transfer coefficient is continuously increasing with vapour quality until dry-out. The different behaviour observed at low vapour quality at 200 kg/(m^2 s) as compared to the other two data sets may be related to a change in the flow pattern.

In Figure 3.2 the effect of mass velocity is investigated, by comparing the heat transfer coefficients measured at 30° C saturation temperature, around 22 kW/m^2 heat flux and mass velocity from 100 to 400 kg/(m^2 s). When mass velocity is increased from 100 to 200 kg/(m^2 s), the heat transfer coefficient significantly raises for the entire vapour quality range. But, by further increasing mass flux to 400 kg/(m^2 s), the heat transfer coefficient does not increase. The heat transfer coefficient curves merge together at high vapour quality. At around 0.8 vapour quality, the heat transfer coefficient curves at 200 and 400 kg/(m^2 s) mass velocity intersect; after this point, the maximum heat transfer coefficient is achieved by the higher mass velocity.

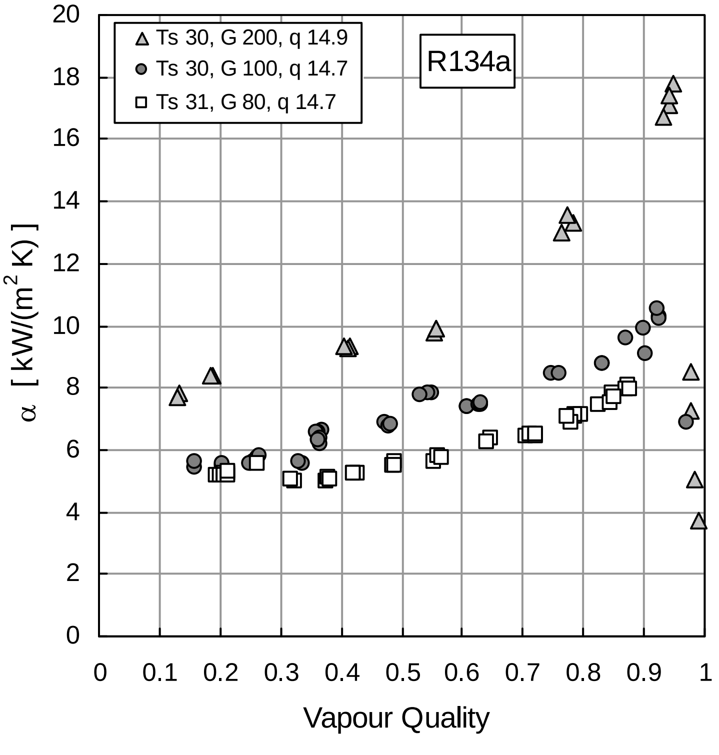

Figure 3.1. Experimental heat transfer coefficient vs. vapour quality for R134a: saturation temperature is around 30 °C, heat flux is 14.7 kW/m^2 and mass velocity is 80, 100 and 200 kg/(m^2 s).

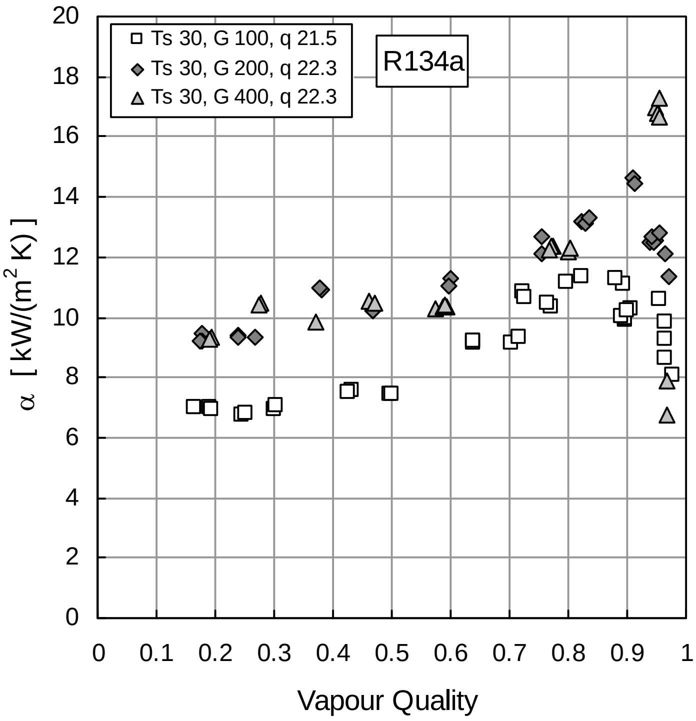

Figure 3.2. Experimental heat transfer coefficient vs. vapour quality for R134a: saturation temperature is around 30 °C, heat flux is around 22 kW/m^2 and mass velocity is 100, 200 and 400 kg/(m^2 s).

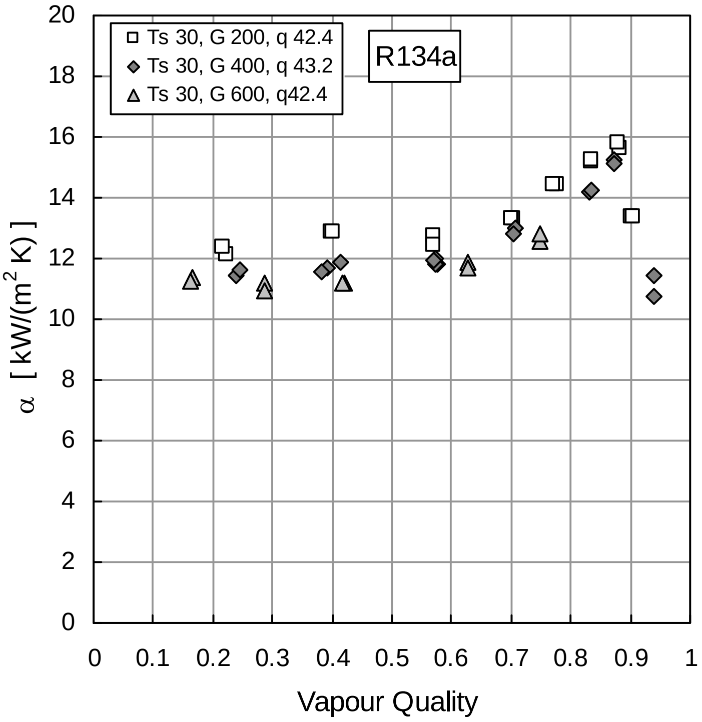

Figure 3.3. Experimental heat transfer coefficient vs. vapour quality for R134a: saturation temperature is 30 °C, heat flux is around 42 kW/m^2 and mass velocity is 200, 400 and 600 kg/(m^2 s).

Figure 3.3 reports the heat transfer coefficient against vapour quality for mass velocity from 200 to 600 kg/(m^2 s), heat flux around 43 kW/m^2 and 30 °C saturation temperature. Up to around 0.7 vapour quality, the heat transfer coefficient does not raise with vapour quality and mass velocity and the process may be nucleate boiling dominated. At 400 and 600 kg/(m^2 s), the heat transfer coefficient is slightly lower as compared to 200 kg/(m^2 s).

The effect of mass velocity on heat transfer coefficient is investigated in Figure 3.4 - 3.6, where the heat transfer coefficient is plotted as a function of mass velocity for a low, medium and high vapour quality. From Figure 3.4 and Figure 3.5, the heat transfer coefficient increases with mass velocity, when *G* is lower than 200 kg/(m^2 s). At 22 kW/m^2 heat flux, by increasing mass velocity from 200 to 400 kg/(m^2 s), the heat transfer coefficient does not raise (Figure 3.5). At 43 kW/m^2 heat flux, the heat transfer coefficient slightly decreases when mass velocity increases from 200 to 600 kg/(m^2 s), as it can be observed in Figure 3.7; moreover, the heat transfer coefficient is not significantly affected by vapour quality and the process is nucleate boiling dominated.

Schael and Kind (2005) found, for carbon dioxide evaporating at 0.54 reduced pressure, heat transfer coefficient increasing with mass velocity up to 250 kg/(m^2 s); but, as mass velocity further increases to 500 kg/(m^2 s), the heat transfer coefficient decreases. Experimental results by Bogart and Thors (1999) show a significant increase of heat transfer coefficient when mass velocity is increased from 50 to 150 kg/(m^2 s), while at higher mass velocities the increase in heat transfer coefficient is lower. Muller-Steinhagen and Spindler (2006) also reported a great increase of heat transfer coefficient in the mass velocity range between 25 and 150 kg/(m^2 s), inlet vapour quality around 0.3 and heat flux from 1000 to 15000 W/m^2.

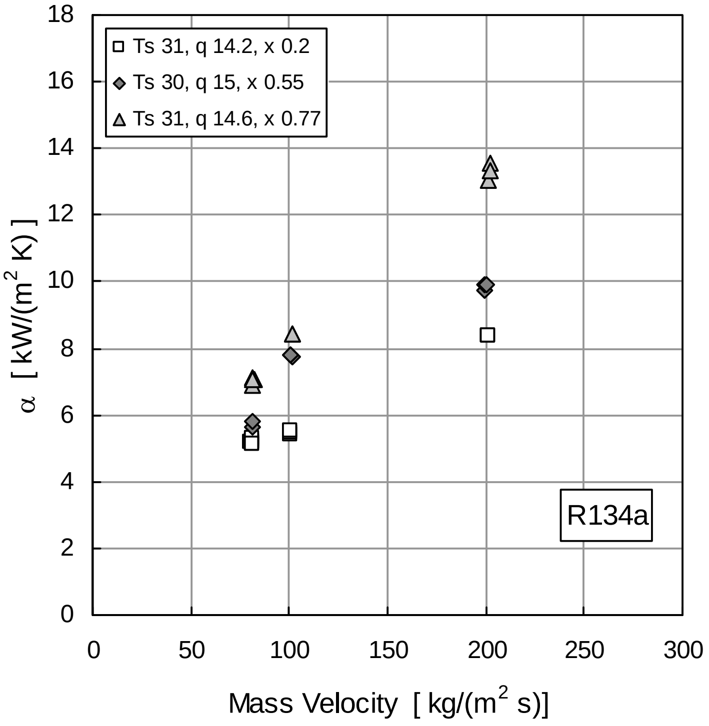

Figure 3.4. Experimental heat transfer coefficient vs. mass velocity for R134a: saturation temperature is around 30 °C, heat flux between 14 an 15 kW/m^2 and vapour quality is 0.2, 0.55 and 0.77.

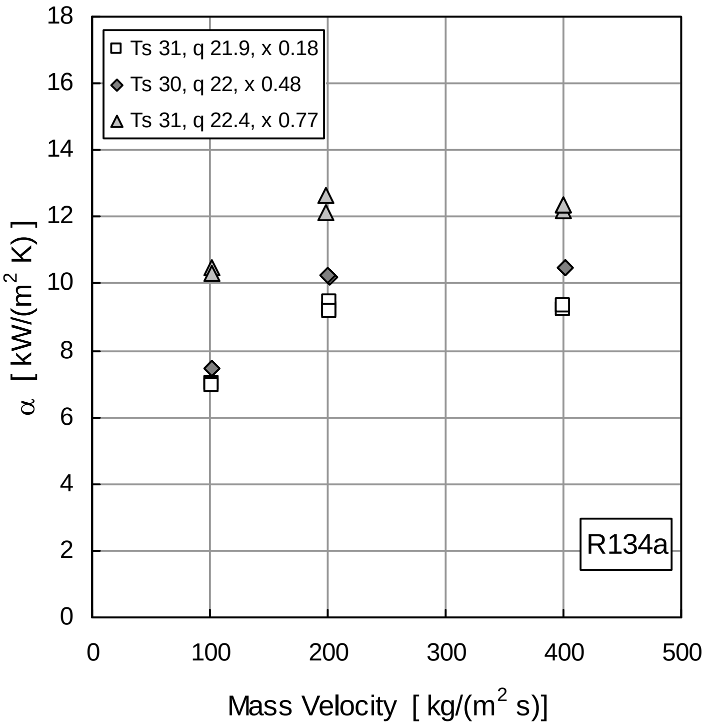

Figure 3.5. Experimental heat transfer coefficient vs. mass velocity for R134a: saturation temperature is around 30 °C, heat flux is around 22 kW/m^2 and vapour quality is 0.18, 0.48 and 0.77.

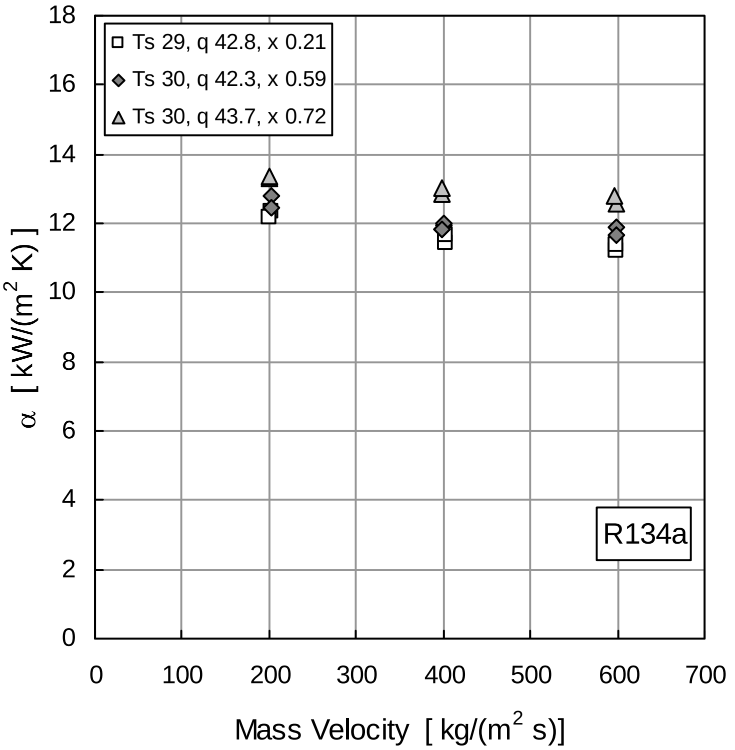

Figure 3.6. Experimental heat transfer coefficient vs. mass velocity for R134a: saturation temperature is around 30 °C, heat flux is around 43 kW/m^2 and vapour quality is 0.2, 0.55 and 0.77.

The effect of heat flux on heat transfer coefficient is investigated in the following part.

Figure 3.7 presents the experimental heat transfer coefficient against vapour quality for 30 °C saturation temperature, 200 kg/(m^2 s) mass velocity and heat flux from 14.9 to 42.4 kW/m^2. At 14.9 kW/m^2 heat flux, the heat transfer coefficient continuously increases with vapour quality. But, as heat flux is increased to 22.3 kW/m^2, the heat transfer coefficient is independent of vapour quality up to around 0.3 vapour quality; after it begins to increase with vapour quality. At the higher heat flux, 42.4 kW/m^2, the heat transfer coefficient is almost independent of vapour quality up to 0.6 vapour quality; after it abruptly raises until the onset of dry-out. This flat trend of heat transfer coefficient is probably related to the dominance of the nucleate boiling mechanism, which is greater at high heat fluxes. By comparing the heat transfer coefficient at 14.9 and 22.3 kW/m^2, the effect of heat flux appears at medium and low vapour qualities; at around 0.8 vapour quality, the heat transfer coefficient curves intersect and then the higher heat transfer coefficient is achieved by the lower heat flux, while dry-out first occurs at 22.3 kW/m^2. At 42.4 kW/m^2 heat flux, the heat transfer coefficient is always higher as compared to the one measured at 22.3 kW/m^2, but in this case the heat flux is two times higher. However, as vapour quality increases, the three heat transfer coefficient curves tend to merge and intersect at vapour quality between 0.8 and 0.9.

In Figure 3.8, the heat transfer coefficient is plotted as a function of vapour quality for the following conditions: saturation temperature of 30 °C, mass velocity of 100 kg/(m^2 s) and heat flux equal to 14.7 and 21.4 kW/m^2. The heat transfer coefficient measured at 21.5 kW/m^2 is always higher than the coefficient at 14.7 kW/m^2 on all the vapour quality range. Moreover, different to 200 kg/(m^2 s), the heat transfer coefficient at 14.7 kW/m^2 is independent of vapour quality at quality values under around 0.35. The different behaviour observed at 100 kg/(m^2 s) mass velocity may be attributed to the two-phase flow pattern which influences the role of the heat transfer mechanisms.

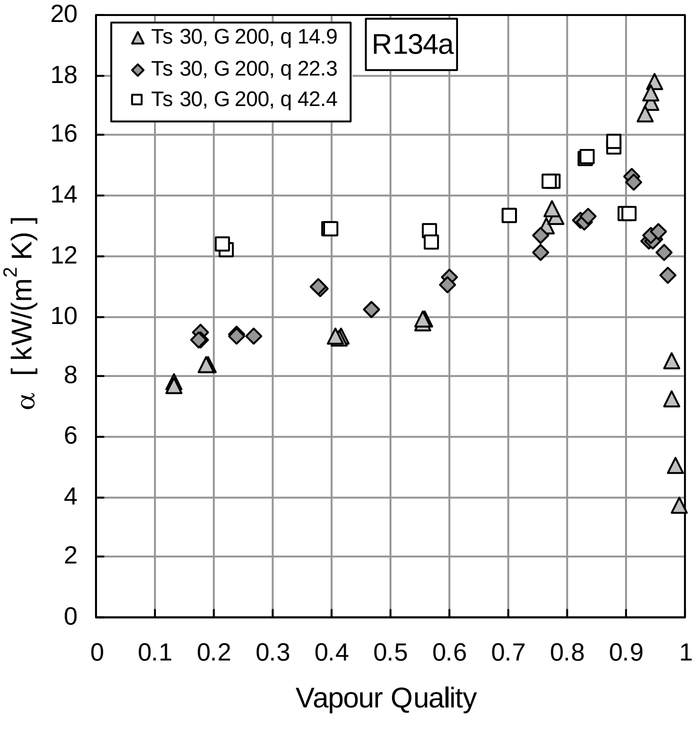

Figure 3.7. Experimental heat transfer coefficient vs. vapour quality for R134a: saturation temperature is around 30 °C, mass velocity is 200 kg/(m^2 s) and heat flux is 14.9, 22.3 and 42.4 kW/m^2.

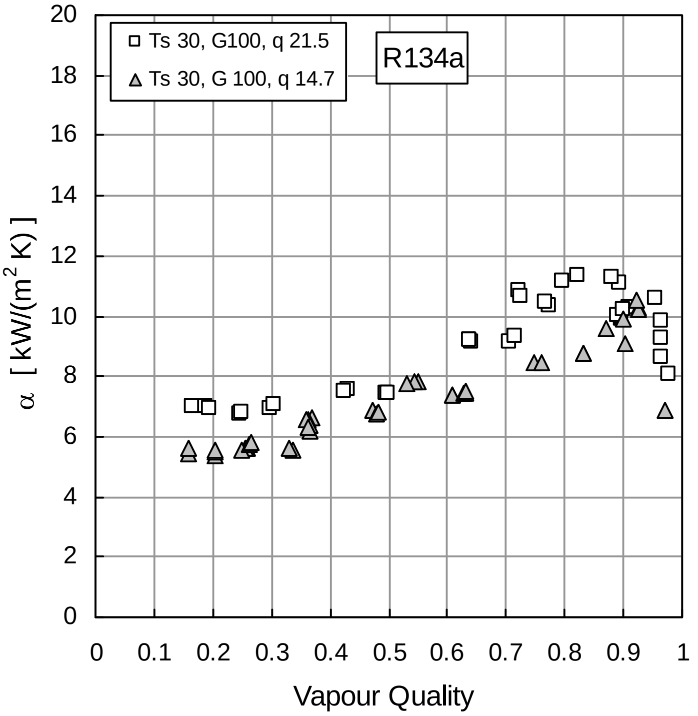

Figure 3.8. Experimental heat transfer coefficient vs. vapour quality for R134a: saturation temperature is 30 °C, mass velocity is 100 kg/(m^2 s) and heat flux is 14.7 and 21.5 kW/m^2.

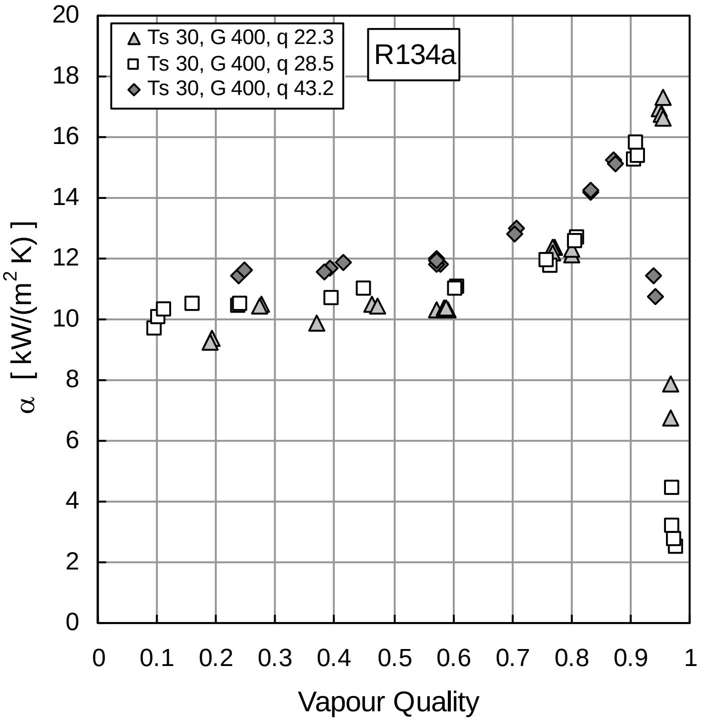

Figure 3.9. Experimental heat transfer coefficient vs. vapour quality for R134a: saturation temperature is 30 °C, mass velocity is 400 kg/(m^2 s) and heat flux is 22.3, 28.5 and 43.2 kW/m^2.

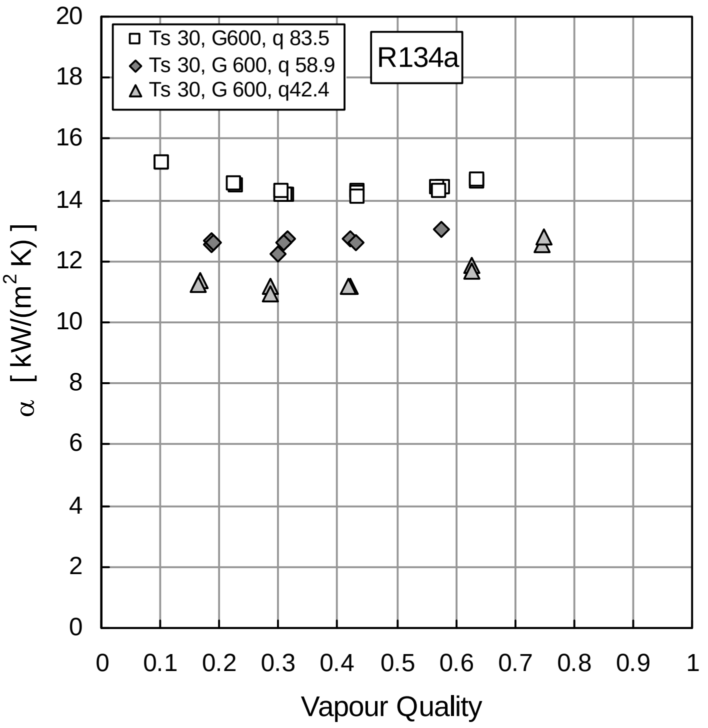

Figure 3.10. Experimental heat transfer coefficient vs. vapour quality for R134a: saturation temperature is 30 °C, mass velocity is 600 kg/(m^2 s) and heat flux is 42.4, 58.9 and 83.5 kW/m^2.

Figure 3.9 compares the heat transfer coefficient measured at 30 °C saturation temperature, 400 kg/(m^2 s) mass velocity and heat flux from 22.3 to 43.2 kW/m^2. In all the tests, the heat transfer coefficient is almost independent of vapour quality up to around 0.7 vapour quality; after this point, it abruptly increases with vapour quality. A clear effect of heat flux on the onset of dry-out is observed; as heat flux increases from 22.3 to 43.2 kW/m^2, dry-out occurs at lower vapour quality.

In Figure 3.10, the experimental heat transfer coefficients taken at high mass velocity, 600 kg/(m^2 s) and high heat fluxes, from 42.4 to 83.5 kW/m^2, are plotted as a function of vapour quality; the saturation temperature is around 30 °C. The effect of heat flux is observed on the entire vapour quality range investigated. For the higher heat flux, 83.5 kW/m^2, a local minimum of heat transfer coefficient is observed at around 0.4 vapour quality, and this may be attributed to competition between nucleate and convective boiling. The presence of this minimum is not observed for the other two test runs, probably because a measurement of heat transfer coefficient is not available for vapour quality around 0.1.

The heat transfer coefficient is plotted as a function of heat flux in Figure 3.11, for 200 and 600 kg/ (m^2 s) mass velocity and low vapour quality. The trend obtained is in agreement with the power law ($\alpha = C\, q^n$) by the Cooper (1984) equation for pool boiling. The experimental points have been interpolated and the best fit curve is reported in the graph; the value of the exponent n obtained is 0.37, which is lower than the value 0.67 suggested by Cooper (1984) for pool boiling in plain tube. Del Col *et al.* (2002) measured the pool boiling heat transfer coefficient for a plain and a microfin DX-75 surface and they found the same dependence of heat flux as given by Cooper (1984). They correlated the experimental points and obtained a value of the exponent *n* equal to 0.67 and 0.39 for the plain and the enhanced surface, respectively. Schael and Kind (2005) also reported the heat transfer coefficient as a function of heat flux for smooth and microfin tube, in the case of carbon dioxide evaporating at 0.54 reduced pressure, 0.5 vapour quality and mass velocity between 75 and 300 kg/(m^2 s). Their data also show the same dependence on heat flux as given by Cooper (1984) and the exponent *n*, experimentally found, varies between 0.5 and 0.55 for the smooth tube and between 0.4 and 0.55 for the microfin tube.

The influence of saturation temperature is discussed in Figure 3.12, where the heat transfer coefficient is plotted as a function of vapour quality for a saturation temperature of 30.5 °C and 42 °C. When vapour quality is lower than around 0.6, the heat transfer coefficient at 42 °C saturation temperature is higher, because of the greater nucleate boiling heat transfer which occurs at high reduced pressure. At 0.8 vapour quality the heat transfer coefficient curves intersect and the maximum heat transfer coefficient is achieved at 30.5 °C saturation temperature. This is because, as saturation temperature raises, vapour density increases and vapour velocity decreases, resulting in a lower convective heat transfer mechanism; in addition the liquid thermal conductivity diminishes as saturation temperature increases.

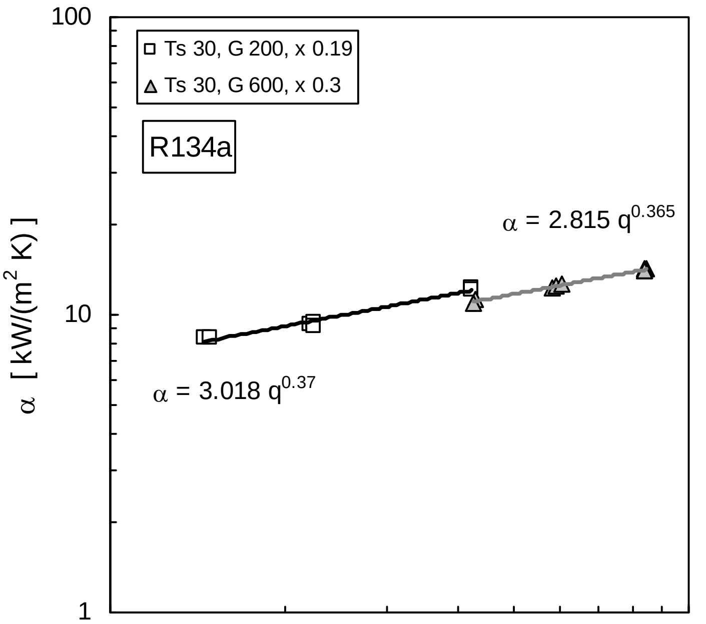

Figure 3.11. Experimental heat transfer coefficient vs. vapour quality for R134a: saturation temperature is 30 °C, mass velocity is 600 kg/(m^2 s) and heat flux is 42.4, 58.9, 83.5 kW/m^2. The diagram is in log - log scale.

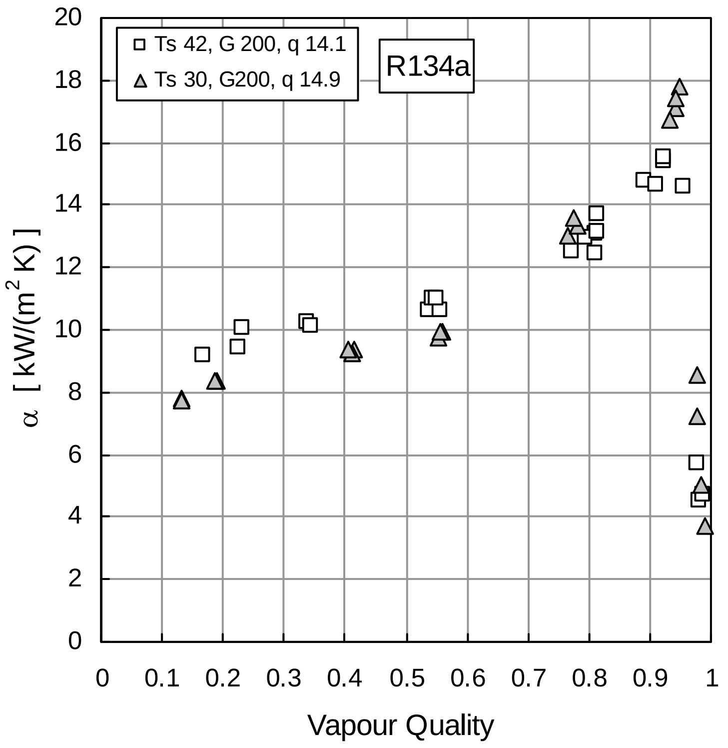

Figure 3.12. Experimental heat transfer coefficient vs. vapour quality for R134a: saturation temperature is 30 and 42 °C, mass velocity is 200 kg/(m^2 s) and heat flux is 14.9 and 14.1 kW/m^2.

3.2 Experimental results for R410A

The experimental measurements of heat transfer coefficient in microfin tube for R410A are reported in this section. Test runs have been performed at 30 °C and 40 °C saturation temperature. The effect of the main operative parameters have been here investigated, considering the following experimental conditions: vapour quality between 0.17 and 1, mass velocity equal to 200, 400 and 600 kg/(m^2 s) and heat flux around 22 and 44 kW/m^2. The experimental results are summarized in Table 3.13 - 3.18, where the measured values of saturation temperature, mass velocity, heat flux and heat transfer coefficient are reported. The expanded uncertainty (95% confidence level) of the transfer coefficient and vapour quality is reported. For each data set, the measured heat fluxes are within ±4.5 % as compared to the average value, while the measured mass velocities are within ±2 %. The percentage experimental uncertainty varies between 5 % and 8 %, before the onset of dry-out; under dry-out regime, the heat transfer coefficient has a higher uncertainty, from 8 % to 12 %.

Table 3.13. Heat transfer experimental results for R410 in microfin tube: T_s = 30 °C, G = 200 kg/(m^2 s), q = 44.1 kW/m^2.

T_s [°C]	G [kg/(m^2 s)]	q [kW/m^2]	x	α [W/(m^2 K)]	U(x)	U(α) [W/(m^2 K)]
30.30	205	43.6	0.18	16925	0.006	935
30.28	205	44.0	0.19	17031	0.006	934
30.43	200	43.7	0.37	18364	0.008	1159
30.43	200	43.9	0.37	18631	0.008	1185
30.38	200	43.7	0.46	18692	0.008	1034
30.31	200	43.6	0.46	18526	0.008	1031
30.39	205	43.4	0.58	19469	0.011	1126
30.34	205	43.5	0.58	19470	0.011	1121
30.32	202	44.6	0.72	19784	0.014	1196
30.31	202	45.1	0.72	20108	0.013	1180
30.34	200	43.6	0.85	20823	0.015	1257
30.47	200	45.0	0.85	19965	0.009	1056
30.25	200	45.4	0.89	19237	0.011	939
30.18	200	45.2	0.90	18220	0.011	1361
30.33	200	43.8	0.92	17484	0.010	1217
30.38	201	42.3	0.94	11435	0.014	1406
30.72	200	43.5	0.95	9763	0.012	1139

Table 3.14. Heat transfer experimental results for R410A in microfin tube: T_s = 30 °C, G = 400 kg/(m^2 s), q = 44.2 kW/m^2.

T_s [°C]	G [kg/(m^2 s)]	q [kW/m^2]	x	α [W/(m^2 K)]	U(x)	U(α) [W/(m^2 K)]
30.28	399	45.4	0.17	18791	0.005	1025
30.30	399	42.1	0.27	17975	0.007	910
29.95	399	43.9	0.46	17988	0.007	889
30.24	400	44.6	0.61	19571	0.008	986
30.08	398	44.2	0.73	19883	0.009	869
29.72	395	44.2	0.80	19694	0.012	1093
30.21	395	43.9	0.82	20252	0.011	1141
30.28	401	43.4	0.87	19971	0.010	988
30.19	403	44.4	0.90	20801	0.010	1011
30.35	403	45.4	0.94	20754	0.010	1065
29.96	402	42.8	0.95	19374	0.011	1436
30.02	404	40.5	0.97	7057	0.012	603

Table 3.15. Heat transfer experimental results for R410A in microfin tube: T_s = 30 °C, G = 400 kg/(m^2 s), q = 21.4 kW/m^2.

T_s [°C]	G [kg/(m^2 s)]	q [kW/m^2]	x	α [W/(m^2 K)]	U(x)	U(α) [W/(m^2 K)]
30.10	406	21.5	0.21	13688	0.005	798
30.00	406	21.0	0.21	13206	0.005	786
30.34	399	20.9	0.41	13525	0.008	844
30.10	398	21.2	0.42	13466	0.008	851
30.37	400	20.9	0.61	13207	0.009	855
30.21	398	21.8	0.75	15614	0.010	1066
30.16	399	21.9	0.75	15506	0.010	1036
30.20	398	21.7	0.81	15442	0.010	1018
30.19	399	21.9	0.81	15405	0.010	1010
30.24	398	21.6	0.88	15628	0.011	1080
30.38	400	21.1	0.89	15418	0.011	1024
30.39	400	20.9	0.90	15312	0.011	1022
30.15	402	21.6	0.93	16210	0.011	1078
30.15	401	22.0	0.94	16988	0.012	1259
30.32	400	21.4	0.96	17535	0.011	1265
30.30	402	21.2	0.99	4261	0.012	395
30.34	403	16.8	1.00	3025	0.012	352

Table 3.16. Heat transfer experimental results for R410A in microfin tube: T_s = 30 °C, G = 600 kg/(m^2 s), q = 44.2 kW/m^2.

T_s [°C]	G [kg/(m^2 s)]	q [kW/m^2]	x	α [W/(m^2 K)]	U(x)	U(α) [W/(m^2 K)]
30.22	602	43.5	0.20	18121	0.005	985
30.05	601	44.1	0.21	18140	0.005	986
30.24	599	43.7	0.34	17940	0.006	940
30.19	603	45.5	0.46	18215	0.007	974
30.17	603	45.4	0.46	18048	0.007	956
30.11	598	44.7	0.62	17996	0.008	948
30.13	598	44.6	0.62	17830	0.008	949
30.06	600	43.8	0.74	19545	0.009	992
30.03	599	43.6	0.75	19687	0.009	1009
30.04	605	43.7	0.80	19530	0.010	1052
29.96	604	43.8	0.80	19444	0.010	1001

Table 3.17. Heat transfer experimental results for R410A in microfin tube: T_s = 40 °C, G = 400 kg/(m^{2}s), q = 21.1 kW/m^2.

T_s [°C]	G [kg/(m^2 s)]	q [kW/m^2]	x	α [W/(m^2 K)]	U(x)	U(α) [W/(m^2 K)]
39.95	397	21.5	0.17	15637	0.004	962
39.93	397	21.6	0.17	15547	0.004	965
39.95	397	21.1	0.30	15387	0.006	960
39.95	398	21.0	0.31	15308	0.006	951
39.90	396	20.9	0.42	14749	0.009	956
39.92	396	21.1	0.43	14950	0.009	941
39.75	400	20.7	0.62	14361	0.009	903
39.79	399	21.2	0.74	14958	0.010	934
39.77	399	21.0	0.74	14863	0.010	940
39.98	399	20.7	0.83	15657	0.011	1982
39.82	399	21.8	0.85	16284	0.011	1101
39.83	399	21.0	0.91	15974	0.013	1134
39.83	399	21.0	0.91	16328	0.013	1179
39.90	400	21.5	0.95	17520	0.015	1308
39.89	400	20.9	0.95	17065	0.015	1282
39.80	398	20.9	0.97	16331	0.015	1247
39.82	400	20.6	0.97	16468	0.015	1611
39.88	400	19.6	0.98	5161	0.014	497
39.74	400	19.9	0.99	4346	0.014	325

Table 3.18. Heat transfer experimental results for R410A in microfin tube: T_s = 40 °C, G = 200 kg/(m^2 s), q = 21 kW/m^2.

T_s [°C]	G [kg/(m^2 s)]	q [kW/m^2]	x	α [W/(m^2 K)]	U(x)	U(α) [W/(m^2 K)]
40.39	201	21.0	0.57	17572	0.015	1403
40.43	202	20.8	0.57	17626	0.016	1451
40.14	201	21.9	0.71	17255	0.016	1313
40.21	201	21.5	0.74	17361	0.016	1419
40.05	202	21.4	0.81	16823	0.016	1258
40.03	202	21.4	0.81	16788	0.016	1246
40.09	202	20.3	0.92	17560	0.017	1377
40.20	203	20.5	0.94	17545	0.023	1447
40.03	204	20.8	0.96	14119	0.017	1244
40.04	203	20.0	0.97	12205	0.018	1496

Figure 3.13 reports the effect of vapour quality and mass velocity on heat transfer coefficient for a heat flux value of 44 kW/m^2. The mass velocity is equal to 200, 400 and 600 kg/(m^2 s). At 200 kg/(m^2 s) mass velocity, the heat transfer coefficient increases with vapour quality until up to dry-out. When mass velocity is 400 kg/(m^2 s) and 600 kg/(m^2 s) and vapour quality is lower than 0.5, the heat transfer coefficient seems to be quite independent of vapour quality; but, at higher vapour qualities the heat transfer coefficient increases until dry-out. Mass velocity does not seem to have influence on heat transfer coefficient, suggesting that the process is nucleate boiling dominated. However, when mass flux is 200 kg/(m^2 s), the onset of dry-out occurs at lower vapour quality as compared to test run at G = 400 kg/(m^2 s).

Schael and Kind (2005) found heat transfer coefficient almost independent of the vapour quality, in the case of carbon dioxide evaporating inside a microfin tube at high heat flux; at 500 kg/(m^2 s), they measured lower heat transfer coefficients as compared to 250 kg/(m^2 s) mass velocity. Gao *et al.* (2007) observed as the heat transfer coefficient of carbon dioxide at 10 °C saturation temperature, was independent of the vapour quality and mass velocity; in their study mass velocity varies between 190 and 770 kg/(m^2 s) and heat flux is equal to 20 kW/m^2.

In Figure 3.14 the heat transfer coefficient is plotted against vapour quality; saturation temperature is 30 °C, mass velocity is 400 kg/(m^2 s), and heat flux is around 21 and 44 kW/m^2. When heat flux is 44 kW/m^2, the transfer coefficient is higher over the entire vapour quality range, showing a strong dependence on heat flux: this confirms the dominant role of the nucleate boiling mechanism at high reduced pressure. When heat flux is 44 kW/m^2, the onset of dry-out occurs at lower vapour quality as compared to the case of q = 21 kW/m^2.

Different from the present experimental results, Kim *et al.* (2002) found an enhancement of heat transfer coefficient with heat flux only at low vapour qualities; but, at high quality values the coefficients merge regardless of the heat flux. Their measurements refer to a saturation temperature of -5 °C and 164 kg/(m^2 s) mass velocity. When R410A evaporating at -5 °C, the reduced pressure corresponds to 0.14, while 0.39 reduced pressure is associated to 30 °C saturation temperature: this implies a greater nucleate boiling contribution for the present data as compared to the measurements by Kim *et al.* (2002). Moreover, in the case of carbon dioxide evaporating at 10 °C (0.61 reduced pressure), Gao *et al.* (2007) found a strong effect of the heat flux on all the vapour quality range, up to the inception of the dry-out.

Figure 3.15 shows the effect of saturation temperature on the heat transfer coefficient. For both 30 °C and 40 °C evaporating temperature, the heat transfer coefficient presents a local minimum, since the heat transfer coefficient decreases at low values of vapour quality and then increases with vapour quality. This same trend was also observed for test characterized by 30 °C saturation temperature, 400 kg/(m^2 s) mass velocity and 44 kW/m^2 heat flux. By Figure 3.15, at vapour quality values lower than about 0.7, the heat transfer coefficients at 40 °C saturation temperature are higher as compared to the ones measured at 30 °C, because of the higher reduced pressure which increases the nucleate boiling mechanism; but, at high vapour qualities, the heat transfer coefficients merge regardless of the reduced pressure. The effect of the evaporating pressure obtained here is similar to the one found by Kim *et al.* (2002) for R410A.

At the end, the new heat transfer data for R410A at high saturation pressure have shown some agreement with the heat transfer behaviour of carbon dioxide inside microfin tube. As discussed in section 1.2, this can be explained by the high saturation temperature of the present data, which yields thermo-physical and thermodynamics properties quite different from those of conventional R410A heat transfer data.

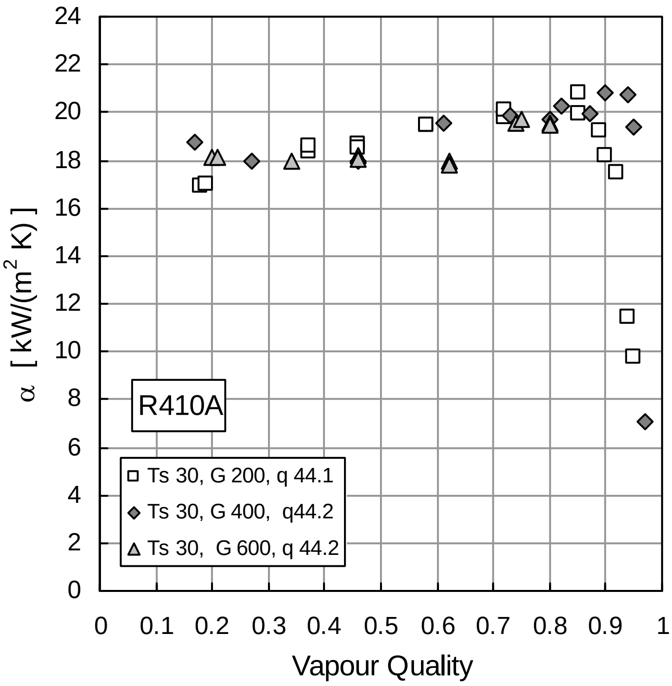

Figure 3.13. Experimental heat transfer coefficient vs. vapour quality for R410A: saturation temperature is 30 °C, heat flux is around 44 kW/m^2, mass velocity is 200, 400 and 600 kg/(m^2 s).

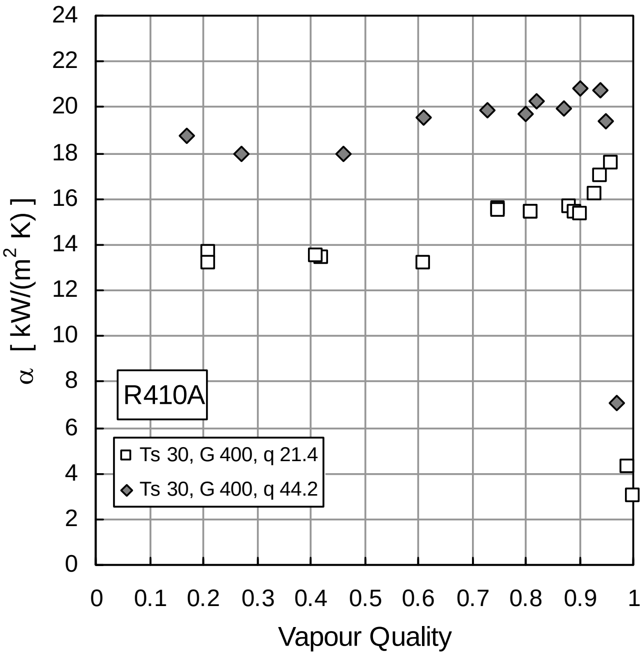

Figure 3.14. Experimental heat transfer coefficient vs. vapour quality for R410A: saturation temperature is around 30 °C, mass velocity is 400 kg/(m^2 s) and heat flux is 21.4 and 44.2 kW/m^2.

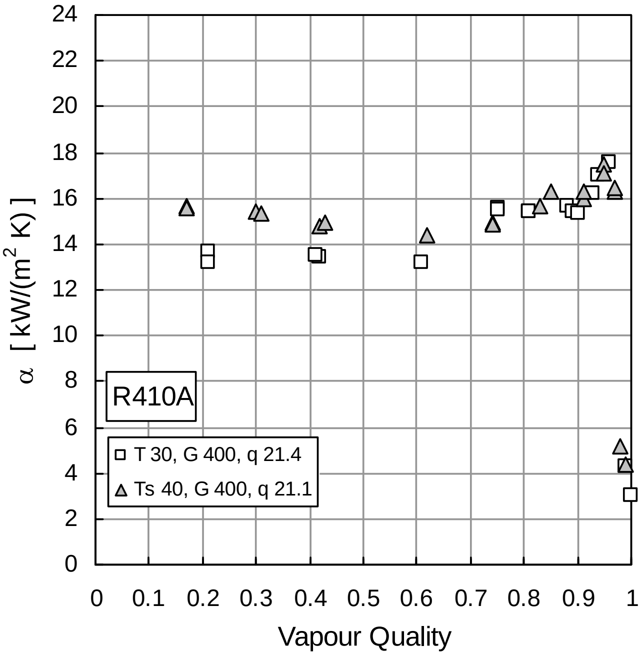

Figure 3.15. Experimental heat transfer coefficient vs. vapour quality: mass velocity is around 400 kg/(m^2 s), heat flux is around 21 kW/m^2, and saturation temperature is 30 °C and 40 °C.

3.3 Comparison between R134a and R410A heat transfer coefficients

The experimental measurements of heat transfer coefficients for R134a and R410A in microfin tube are here compared. Comparison is performed at 30 °C saturation temperature and heat flux around 42 - 44 kW/m^2. For R134a, the reduced pressure is 0.19, while in the case of R410A it is equal to 0.385 and this yields quite different thermodynamic and thermo-physical properties for the two fluids.

Figures 3.16, 3.17 and 3.18 report the measured heat transfer coefficients as a function of vapour quality at 200, 400 and 600 kg/(m^2 s) mass velocity. A quite similar trend of heat transfer coefficient versus vapour quality is observed for test runs at 200 and 600 kg/(m^2 s), except at higher quality values, just before the inception of dry-out, where the heat transfer coefficient for R134a abruptly increases as compared to R410A. At 600 kg/(m^2 s), a local minimum for heat transfer coefficient is observed in the case of R410A, while a flat trend occurs for R134a: this may be attributed to the different reduced pressure, which results in a different competition between nucleate boiling and convective mechanisms.

The dry-out inception vapour quality for the two fluids is in agreement within the experimental uncertainty of the measurement.

On the whole, the heat transfer coefficients measured for R410A are higher than R134a coefficients over the entire vapour quality range; the increase in heat transfer obtained with R410A varies from 40 to 60 %; this difference diminishes at the higher vapour qualities.

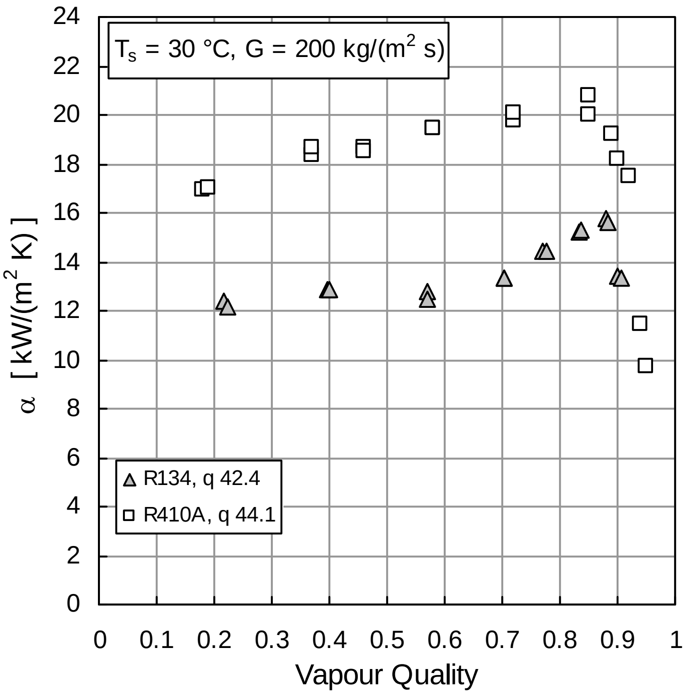

Figure 3.16. Experimental heat transfer coefficient vs. vapour quality: comparison between R134a and R410A experimental data. The saturation temperature is 30 °C, mass velocity is 200 kg/(m^2 s) and heat flux is 42.4 kW/m^2 for R134a and 44.1 kW/m^2 for R410A.

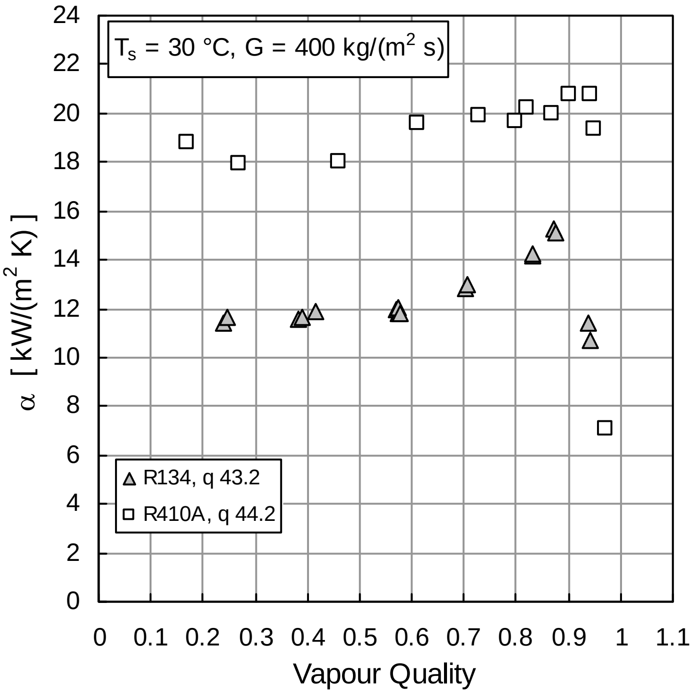

Figure 3.17. Experimental heat transfer coefficient vs. vapour quality: comparison between R134a and R410A experimental data. The saturation temperature is 30 °C, mass velocity is 400 kg/(m^2 s) and heat flux is 43.2 kW/m^2 for R134a and 44.2 kW/m^2 for R410A.

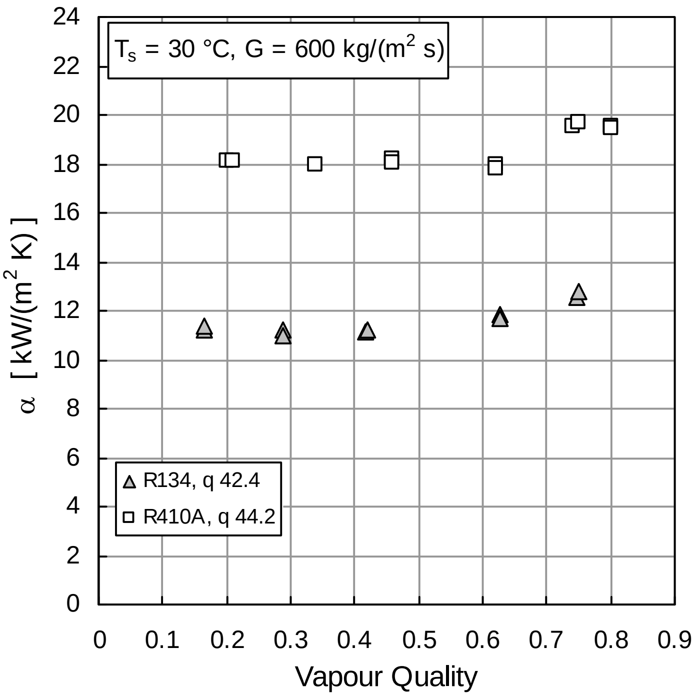

Figure 3.18. Experimental heat transfer coefficient vs. vapour quality: comparison between R134a and R410A experimental data. The saturation temperature is 30 °C, mass velocity is 600 kg/(m^2 s) and heat flux is 42.4 kW/m^2 for R134a and 44.2 kW/m^2 for R410A.

CHAPTER 4

COMPARISON OF HEAT TRANSFER COEFFICIENTS IN A MICROFIN TUBE WITH PREDICTIVE MODELS

4.1 Introduction to comparison between experimental data and models

In this chapter the new measurements of the heat transfer coefficient during flow boiling of R134a and R410A at high saturation temperature inside the microfin are compared with the predictive models by Koyama *et al.* (1995), Thome *et al.* (1999), Cavallini *et al.* (2006), Chamra and Mago (2007) and Hamilton *et al.* (2008). In the comparison, the heat transfer area based on the diameter at the fin tip has been used to define the heat transfer coefficient; mass velocity also refer to the diameter at the fin of the tip. This choice is in agreement with the convention adopted in the reduction of the experimental heat transfer coefficient. Thus, much care has been paid in the use of the models by Koyama *et al.* (1995), Thome *et al.* (1997) and Hamilton *et al.* (2008), where heat transfer coefficient is based on a different surface area. For R134a, 266 experimental data have been considered and used in the comparison with the models, while 68 experimental data have been used for R410A. Data taken under dry-out regime are not considered here, because the models can not predict those conditions.

In the case of R134a, the experimental database includes heat transfer coefficients measured at mass velocity under 100 kg/(m^2 s), where the heat transfer mechanisms can be quite different from those at higher mass fluxes. The validity range of the models by Koyama *et al.* (1995) will be here extended to mass velocities lower than 100 kg/(m^2 s). In the case of the Cavallini *et al.* (2006) method, there is need to assess the part of the correlation which predicts the heat transfer coefficients at the mass velocity lower than 100 kg/(m^2 s). Finally, the models by Chamra and Mago (2007) and by Hamilton *et al.* (2008) are quite recent; therefore, the present investigation can provide new information on their accuracy, when used at high saturation temperature. Hamilton *et al.* (2008) correlation can be used for mass velocity down to 70 kg/(m^2 s).

In the case of R410A, further work is required to assess the prediction capability of models. Refrigerant R410A is a high pressure fluid, with thermodynamics and thermo-physical properties quite different as compared to other HFC fluids; moreover, present experimental data refer to high reduced pressure.

Some mathematical indicators are used to assess the prediction capability of the models:

- mean absolute deviation: $$MAD = \frac{\sum_{i=1}^{n} \left| e_p \right|}{n} \quad [\%]$$

- mean deviation: $$MD = \frac{\sum_{i=1}^{n} e_p}{n} \quad [\%]$$

− standard deviation: $$SD = \sqrt{\frac{\sum_{i=1}^{n}(e_p - MD)^2}{n-1}} \qquad [\%]$$

where e_p is the percentage error defined as:

− $$e_p = \frac{\alpha_{cal} - \alpha_{\exp}}{\alpha_{\exp}} 100 \qquad [\%]$$

The absolute mean deviation provides a global information on the accuracy of the predictive method. A low value of *MAD* corresponds to high accuracy of the model. A positive value of the mean deviation, *MD*, indicates an overestimation of the experimental data, while a negative value indicates an underestimation of the measurement. Finally, a low value of the standard deviation means that the error provided by the model is not affected by any particular parameter as vapour quality, reduced pressure, mass velocity and heat flux.

4.2 Comparison between calculated and measured heat transfer coefficient for R134a

4.2.1 Koyama *et al.* (1995)

The results obtained by the comparison between the model by Koyama *et al.* (1995) and R134a data is reported Table 4.1 and in Figure 4.1, where the calculated values are plotted against the measured values for all experimental data sets. Calculated heat transfer coefficients strongly overestimates the experimental data for all the operative conditions investigated here, in particular at high mass velocity and high heat flux.

Table 4.1. Comparison between experimental heat transfer coefficients for R134a in microfin tube and model by Koyama *et al.* (1995): percentage values of *MAD*, *MD* and *SD*.

T_s [°C]	G [kg/(m^2 s)]	q [kW/m^2]	*MAD* [%]	*MD* [%]	*SD* [%]
31	80	14.7	95.8	95.8	23.5
30.3	100	14.7	70.3	70.3	26.8
30.4	100	21.5	73.6	73.6	29.5
30.5	200	14.9	26.1	19.6	25
30.5	200	22.3	47.9	47.9	15.5
30	200	42.4	80.1	80.1	13
30.2	400	22.3	61.4	61.4	13.3
30.3	400	28.5	77.1	77.1	12.3
29.7	400	43.2	106.8	106.8	15.6
29.7	600	42.4	127.3	127.3	15.1
29.8	600	58.9	146.1	146.1	4.2
29.8	600	83.5	170.2	170.2	4.3
42.2	200	14.1	21.7	21.7	11.5
	All data		79.8	79.4	19.4

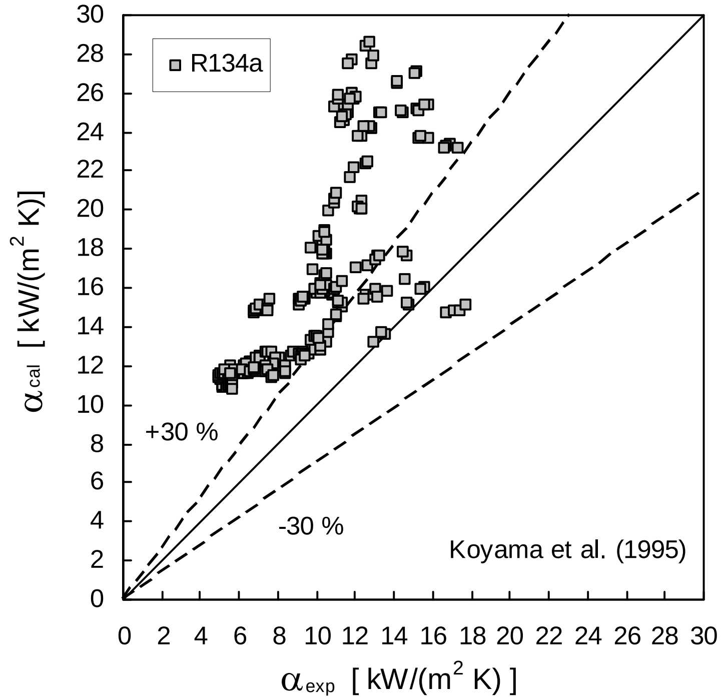

Figure 4.1. Calculated vs measured heat transfer coefficient for R134a. The calculated values are obtained with the model by Koyama *et al.* (1995). The ± 30 error lines are reported.

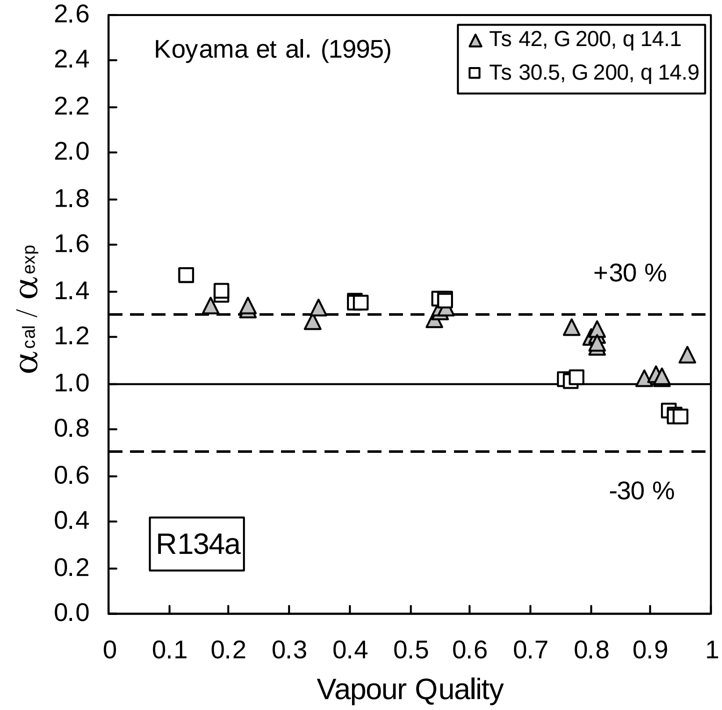

Figure 4.2. Ratio between calculated and experimental heat transfer coefficient vs. vapour quality for R134a. The calculated coefficients are obtained with the model by Koyama *et al.* (1995). Saturation temperature is 30.5 and 42 °C, mass velocity is 200 kg/(m^2 s) and heat flux is 14.1 and 14.9 kW/m^2.

Cavallini *et al.* (1998) compared the model by Koyama *et al.* (1995) with a large number of data at saturation temperature lower than the present one and also found a strong overestimation of the experimental data. Some improvement in the prediction capability is observed at $G = 200$ kg/(m^2 s) and q around 14 kW/m^2. For these same conditions, the ratio between calculated and experimental heat transfer coefficient is reported in Figure 4.2 as function of vapour quality; reduced pressure does not seem to have a great effect on the prediction capability.

4.2.2 Thome *et al.* (1997)

The comparison between R134a experimental heat transfer coefficients and the model by Thome *et al.* (1997) is presented. In Table 4.2, the percentage values of *MAD*, *MD* and *SD* are reported for each data set and for the entire R134a database.

At mass velocity 80 and 100 kg/(m^2 s), experimental and calculated values show a very satisfactory agreement, within ± 30 % for all data. This is observed in detail in Figure 4.3 and 4.4, where the ratio between calculated and measured heat transfer coefficient is around the unit for the entire vapour quality range: any particular trend versus vapour quality is observed, and neither the prediction capability is affected by other parameters as confirmed by the low value of standard deviation.

But, as mass velocity is increased to 200, 400 and 600 kg/(m^2 s) some degradation of the prediction capability occurs, as it can be seen in Figure 4.5, 4.6 and 4.7. The ratio between calculated and experimental heat transfer coefficient shows a clear dependence on vapour quality, and high values of standard deviation are found for these data sets. At low vapour quality values, the model underestimates the experimental heat transfer coefficient, while at high vapour quality some overprediciton is found. This trend increases at high mass velocity, and shows that the model is not able to catch the experimental trend of heat transfer coefficient versus vapour quality and mass velocity.

Table 4.2. Comparison between experimental heat transfer coefficients for R134a in microfin tube and model by Thome *et al.* (1997): percentage values of *MAD*, *MD* and *SD*.

T_s [°C]	G [kg/(m^2 s)]	q [kW/m^2]	*MAD* [%]	*MD* [%]	*SD* [%]
31	80	14.7	13.1	13.1	5.1
30.3	100	14.7	4.3	-1	5.6
30.4	100	21.5	8.5	-2.5	9.9
30.5	200	14.9	22.3	-22.3	9.8
30.5	200	22.3	22.6	-22.6	10.1
30	200	42.4	20.1	-20.1	5.4
30.2	400	22.3	14.1	-6.1	18.3
30.3	400	28.5	20.8	-15.8	22.6
29.7	400	43.2	13.9	-13.9	11.4
29.7	600	42.4	30.9	25.3	27.4
29.8	600	58.9	4.4	12	14.4
29.8	600	83.5	13.7	5.8	7.2
42.2	200	14.1	27.9	-27.1	13.2
	All data		15.4	-4.8	12.2

It has been reported in section 1.4.2 as the heat transfer coefficient calculated with the model by Thome *et al.* (1997) continuously increases with vapour quality, because the nucleate boiling term is not suppressed at quality values. This trend of the calculated coefficient is quite different from that experimentally found for instance at 200, 400 and 600 kg/(m^2 s) and heat flux around 42 kW/m^2, where the heat transfer coefficient is almost independent of vapour quality up to 0.7 vapour quality and then abruptly increases for higher qualities.

In Figure 4.8 the effect of saturation pressure can be evaluated; by comparing data sets at 30.5 and 42 °C, saturation pressure does not provided any significant influence on the prediction capability.

The global comparison between calculated and measured heat transfer coefficient is reported in Figure 4.9 for R134a: for most of points the agreement between calculated and experimental coefficients is within ±30 %, with a little general underestimation around 5 %.

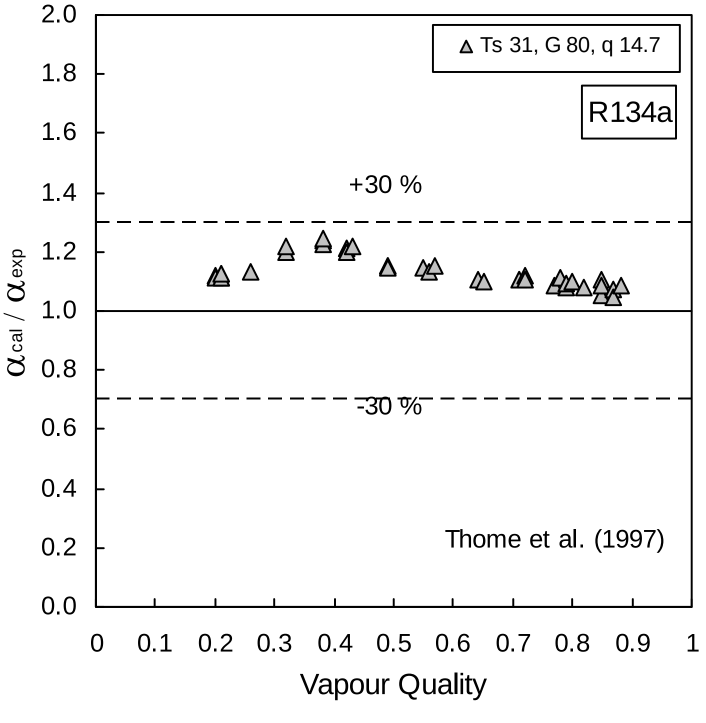

Figure 4.3. Ratio between calculated and experimental heat transfer coefficient vs. vapour quality for R134a. The calculated coefficients are obtained with the model by Thome *et al.* (1997). Saturation temperature is 31 °C, mass velocity is 80 kg/(m^2 s) and heat flux is 14.7 kW/m^2. The ±30 % error lines are reported.

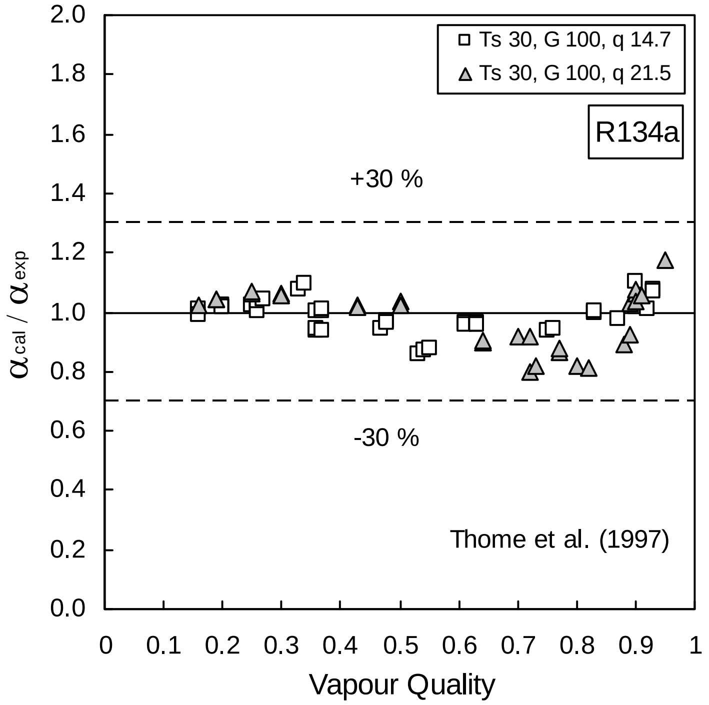

Figure 4.4. Ratio between calculated and experimental heat transfer coefficient vs. vapour quality for R134a. The calculated coefficients are obtained with the model by Thome *et al.* (1997). Saturation temperature is 30 °C, mass velocity is 100 kg/(m^2 s) and heat flux is 14.7 and 21.5 kW/m^2. The ±30 % error lines are reported.

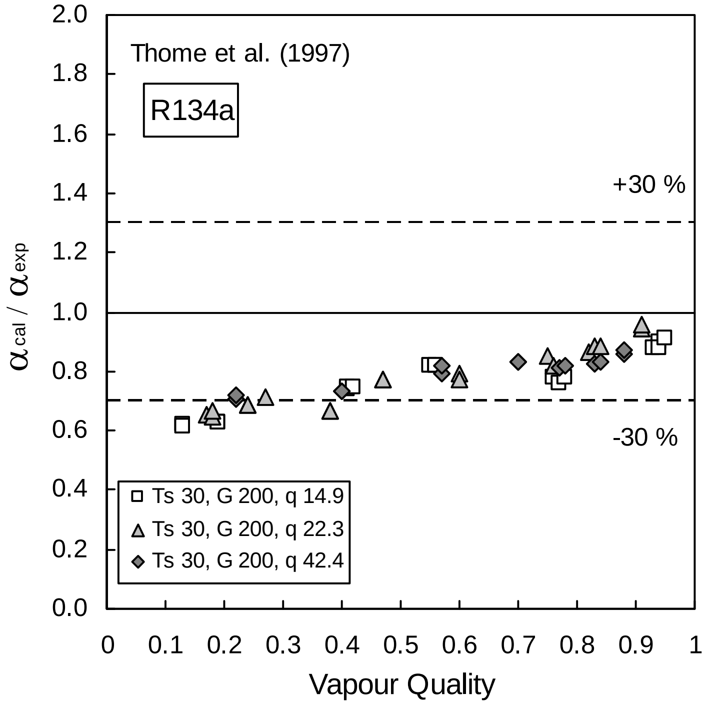

Figure 4.5. Ratio between calculated and experimental heat transfer coefficient vs. vapour quality for R134a. The calculated coefficients are obtained with the model by Thome *et al.* (1997). Saturation temperature is 30 °C, mass velocity is 200 kg/(m^2 s) and heat flux is 14.9, 22.3, 42.4 kW/m^2. The ±30 % error lines are reported.

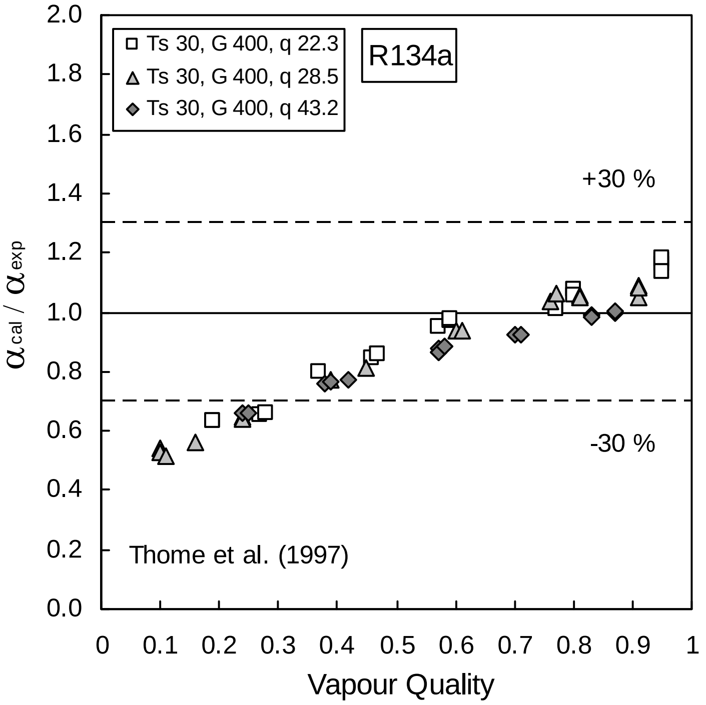

Figure 4.6. Ratio between calculated and experimental heat transfer coefficient vs. vapour quality for R134a. The calculated coefficients are obtained with model by Thome *et al.* (1997). Saturation temperature is 30 °C, mass velocity is 400 kg/(m^2 s) and heat flux is 22.3, 28.5, 43.2 kW/m^2. The ±30 % error lines are reported.

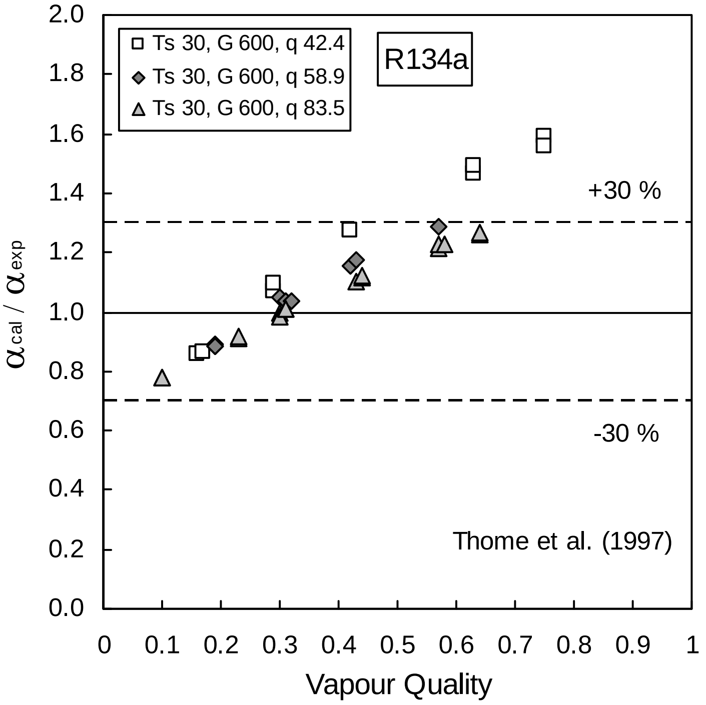

Figure 4.7. Ratio between calculated and experimental heat transfer coefficient vs. vapour quality for R134a. The calculated coefficients are obtained with the model by Thome *et al.* (1997). Saturation temperature is 30 °C, mass velocity is 600 kg/(m^2 s) and heat flux is 42.4, 58.9, 83.5 kW/m^2. The ±30 % error lines are reported.

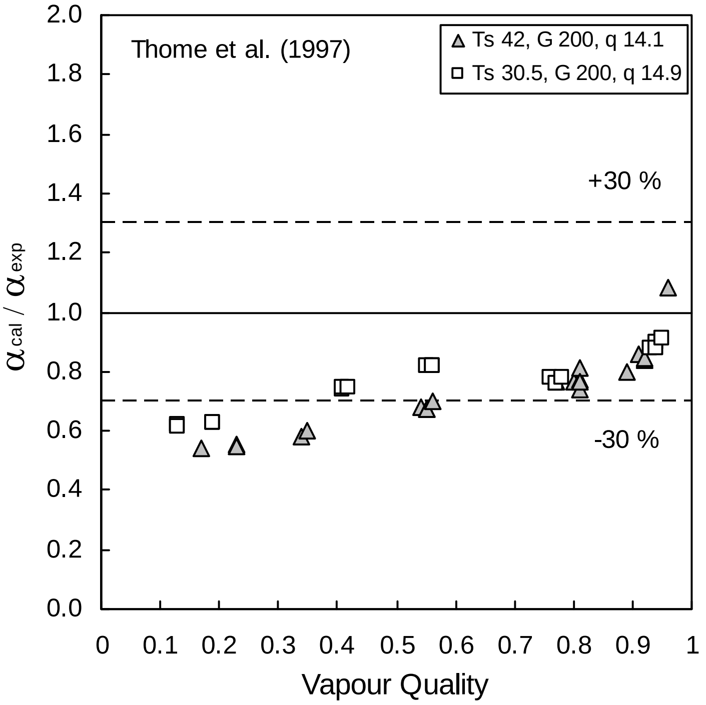

Figure 4.8. Ratio between calculated and experimental heat transfer coefficient vs. vapour quality for R134a. The calculated coefficients are obtained with the model by Thome *et al.* (1997). Saturation temperature are 30.5 and 42 °C, mass velocity is 200 kg/(m^2 s) and heat flux is 14.1 and 14.9 kW/m^2. The ±30 % error lines are reported.

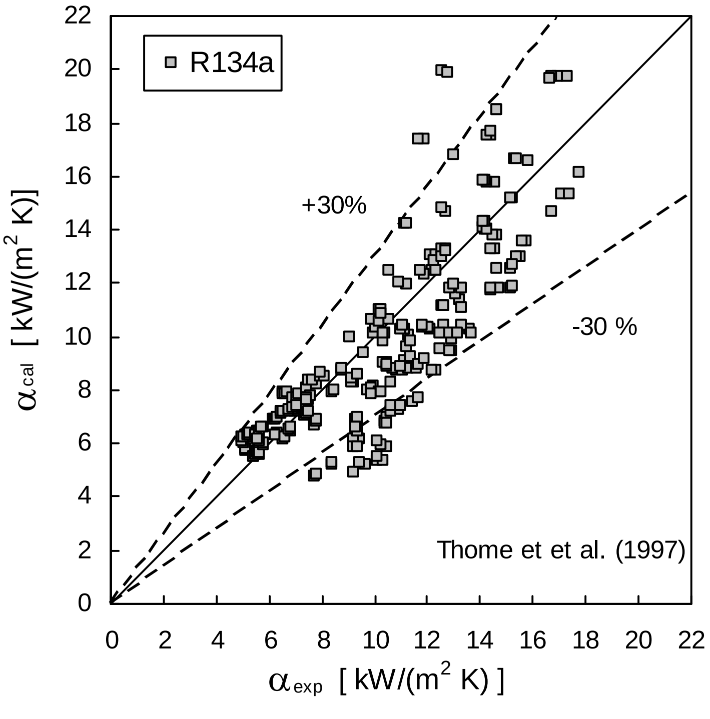

Figure 4.9. Calculated vs measured heat transfer coefficient for R134a. The calculated values are obtained with the model by Thome *et al.* (1997). The ±30 % error lines are reported.

4.2.3 Cavallini *et al.* (2006)

The model by Cavallini *et al.* (2006) is compared with new heat transfer coefficients for R134a and R410A in microfin tube. This predictive method is the only among the superposition and asymptotic models considered here, which accounts for the different heat transfer mechanisms, which occur at low mass velocity. For data sets with mass velocity 80 and 100 kg/(m^2 s), the previous version of the model, by Cavallini *et al.* (1999), is also applied; in this version the capillarity term is not considered and the same method is used both for high and low mass velocities. At mass velocity higher than 100 kg/(m^2 s), the two predicting procedures are the same.

Table 4.3 reports the percentage values of mean absolute deviation, mean deviation and standard deviation, obtained with the models by Cavallini *et al.* (1999) for test runs at mass velocity 80 and 100 kg/(m^2 s). In Table 4.4 the values of *MAD*, *MD* and *SD*, obtained by Cavallini *et al.* (2006) predictive method for all the test runs are reported.

Figure 4.10 compares the prediction capability of the models by Cavallini *et al.* (1999) and Cavallini *et al.* (2006) for mass velocity of 80 kg/(m^2 s) and heat flux of 14.7 kW/m^2; the saturation temperature is 30 °C. Cavallini *et al.* (1999) strongly overpredicts, over 30 %, for the entire vapour quality range; on the contrary, Cavallini *et al.* (2006) underestimates around 30 % the experimental data. On the whole, Cavallini *et al.* (2006) shows a better accuracy, with a *MAD* value of 29.7 %, as compared to Cavallini *et al.* (1999), which provides a *MAD* value of 44.9 %.

Table 4.3. Percentage values of *MAD*, *MD* and *SD* for R134a data sets with mass velocity 80 and 100 kg/(m^2 s): models by Cavallini *et al.* (1999) and Cavallini *et al.* (2006).

T_s [°C]	*G* [kg/(m^2 s)]	*q* [kW/m^2]	*MAD* [%]	*MD* [%]	*SD* [%]
31	80	14.7	44.9	44.9	11
30.3	100	14.7	25	24.9	13.4
30.4	100	21.5	14.8	12.2	15

Table 4.4. Comparison between experimental heat transfer coefficients for R134a in microfin tube and model by Cavallini *et al.* (2006): percentage values of *MAD*, *MD* and *SD*.

T_s [°C]	*G* [kg/(m^2 s)]	*q* [kW/m^2]	*MAD* [%]	*MD* [%]	*SD* [%]
31	80	14.7	29.7	-29.7	5.7
30.3	100	14.7	12.5	-12.5	8
30.4	100	21.5	20.2	-20.2	8.4
30.5	200	14.9	13.7	-13.7	14.2
30.5	200	22.3	8.3	-6.1	8.4
30	200	42.4	9.4	-8.5	8
30.2	400	22.3	8.2	-3.6	12
30.3	400	28.5	6.6	0.7	8.6
29.7	400	43.2	9.1	4.8	8.4
29.7	600	42.4	6.7	3.8	7.5
29.8	600	58.9	10.8	10.8	6.6
29.8	600	83.5	10.9	10.9	2.1
42.2	200	14.1	15.6	-15.6	7.4
	All data sets		15.3	-11.3	16.9

The accuracy of the models by Cavallini *et al.* (1999) and Cavallini *et al.* (2006) at mass velocity 100 kg/(m^2 s) and two heat fluxes, 14.7 and 21.5 kW/m^2, can be evaluated by the graphs of Figure 4.11 and 4.12, respectively.

By Figure 4.11, Cavallini *et al.* (1999) overpredicts above 30% at vapour quality under 0.4, but, as vapour quality increases an improvement of the prediction capability is observed. Moreover this model shows higher accuracy at the greater heat flux, 21.5 kW/m^2, as also indicated by the *MAD* values reported in Table 4.1. On the contrary, the model by Cavallini *et al.* (2006) tends to underestimate the measured heat transfer coefficients, in particular at low vapour quality. Different from Cavallini *et al.* (1999), the method by Cavallini *et al.* (2006) is more accurate at the lower heat flux, 14.7 kW/m^2. By comparing the values of standard deviation found with the two methods, one can see as the prediction capability of Cavallini *et al.* (2006) is less affected by the operative parameters as compared to Cavallini *et al.* (1999).

On the whole, at mass velocities 80 and 100 kg/(m^2 s) and heat flux 14.7 kW/m^2, Cavallini *et al.* (2006) shows higher accuracy, but at G = 100 kg/(m^2 s) and q = 21.5 kW/m^2 the lower *MAD* value is provided by Cavallini *et al.* (1999).

Figure 4.13 reports the ratio between calculated and measured heat transfer coefficient as a function of vapour quality for 200 kg/(m^2 s) mass velocity and three heat fluxes, 14.9, 22.3 and 42.4 kW/m^2; the saturation temperature is around 30 °C, again. The calculated coefficients show a very satisfactory agreement with the experimental values; only at high vapour quality, above 0.7, the model tends to underestimates a little the experimental value.

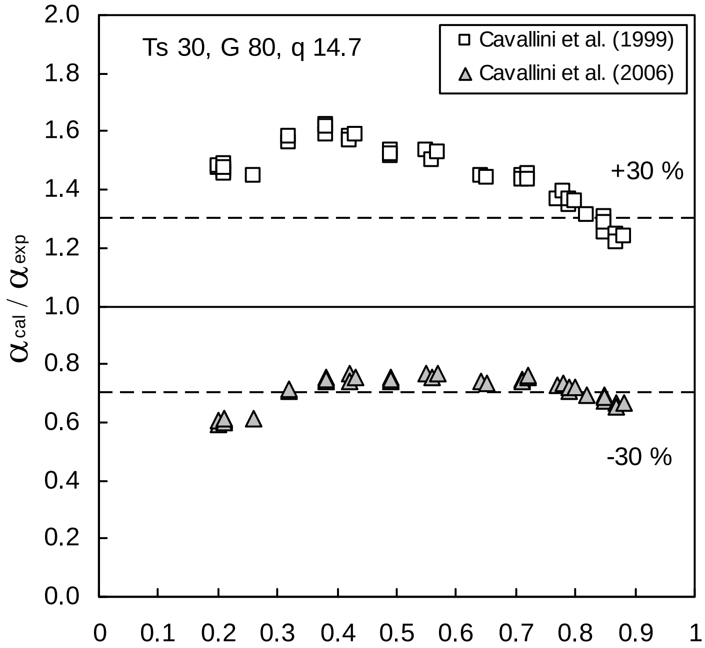

Figure 4.10. Ratio between calculated and experimental heat transfer coefficient vs. vapour quality for R134a. The calculated coefficients are obtained with the model by Cavallini *et al.* (1999) and by Cavallini *et al.* (2006). Saturation temperature is 30 °C, mass velocity is 80 kg/(m^2 s) and heat flux is 14.7 kW/m^2. The ±30 % error lines are reported.

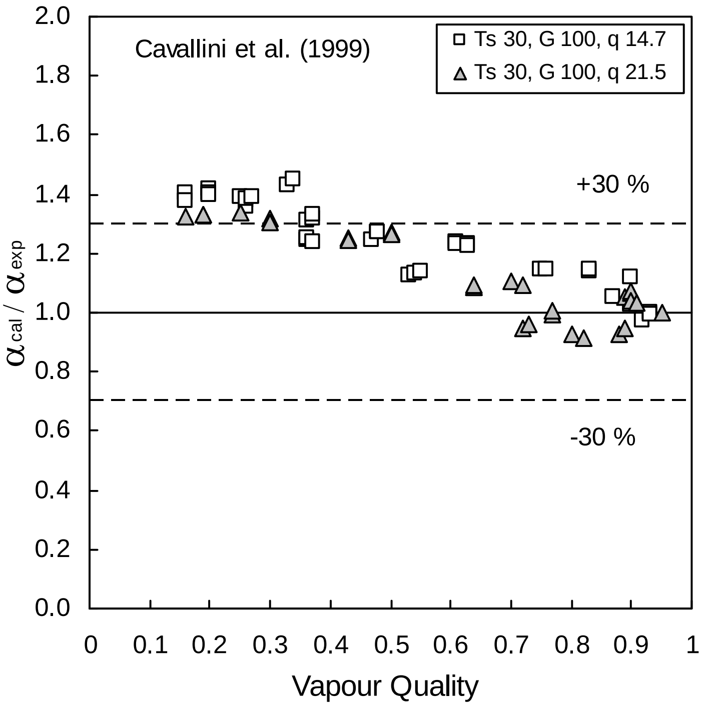

Figure 4.11. Ratio between calculated and experimental heat transfer coefficient vs. vapour quality for R134a. The calculated coefficients are obtained with the model by Cavallini *et al.* (1999). Saturation temperature is 30 °C, mass velocity is 100 kg/(m^2 s) and heat flux is 14.7 and 21.5 kW/m^2. The ±30 % error lines are reported.

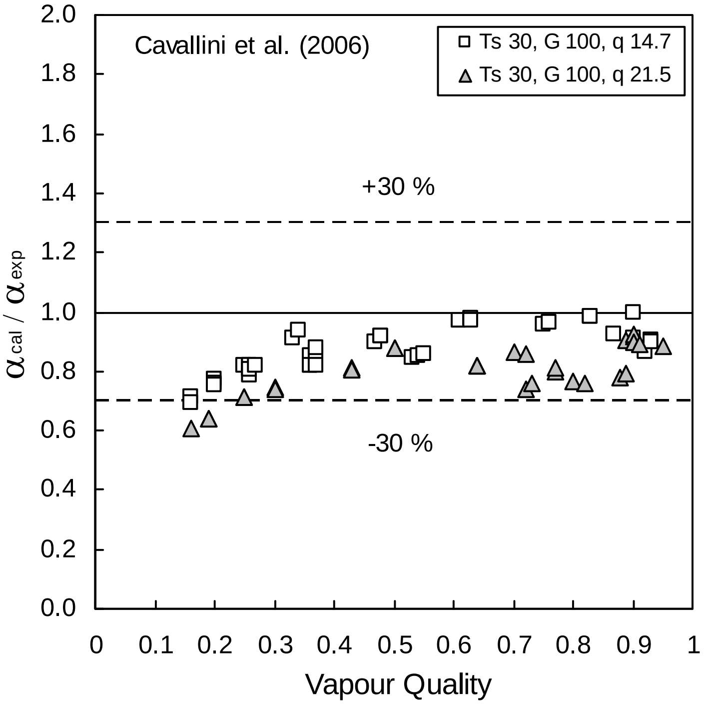

Figure 4.12. Ratio between calculated and experimental heat transfer coefficient vs. vapour quality for R134a. The calculated coefficients are obtained with the model by Cavallini *et al.* (2006). Saturation temperature is 30 °C, mass velocity is 100 kg/(m^2 s) and heat flux is 14.7 and 21.5 kW/m^2. The ±30 % error lines are reported.

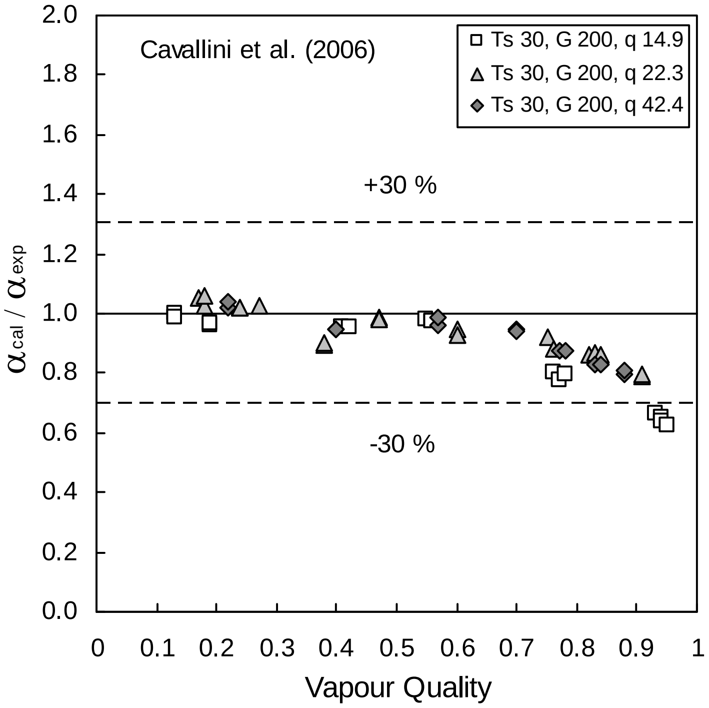

Figure 4.13. Ratio between calculated and experimental heat transfer coefficient vs. vapour quality for R134a. The calculated coefficients are obtained with the model by Cavallini *et al.* (2006). Saturation temperature is 30 °C, mass velocity is 200 kg/(m^2 s) and heat flux is 14.9, 22.3, 42.4 kW/m^2. The ±30 % error lines are reported.

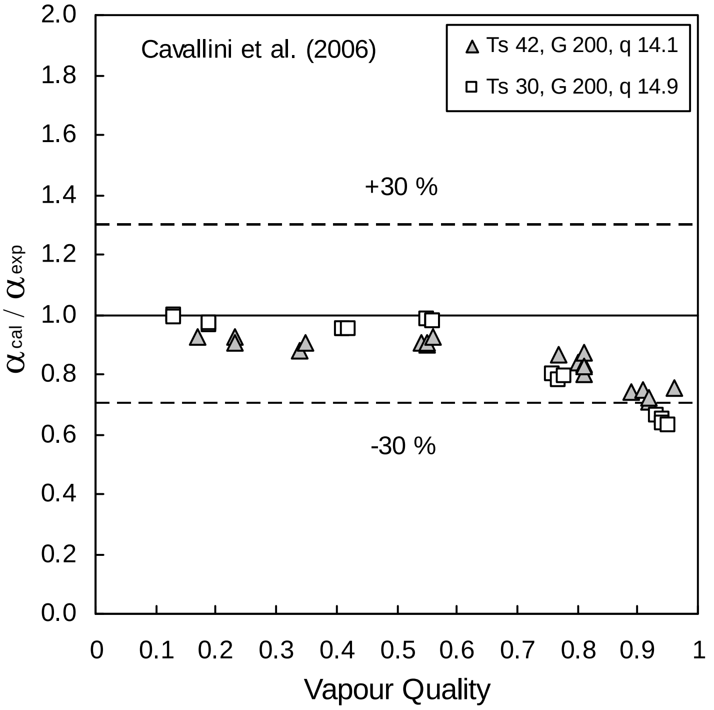

Figure 4.14. Ratio between calculated and experimental heat transfer coefficient vs. vapour quality for R134a. The calculated coefficients are obtained with the model by Cavallini *et al.* (2006). Saturation temperature is around 30 and 42 °C, mass velocity is 200 kg/(m^2 s) and heat flux is 14.9 and 14.1 kW/m^2. The ±30 % error lines are reported.

The effect of saturation pressure is investigated in Figure 4.14, where the ratio of calculated and measured heat transfer coefficient is plotted as a function of vapour quality at 200 kg/(m^2 s) mass velocity, and heat flux around 14 kW/m^2. For both the test runs reported the trend of $\alpha_{cal}/\alpha_{exp}$ is very similar.

The ratio between calculated and experimental heat transfer coefficient is plotted in Figure 4.15 against vapour quality for 30 °C saturation temperature, 400 kg/(m^2 s) mass velocity and heat flux from 22.3 to 43.2 kW/m^2. For vapour quality under 0.8, great accuracy is observed in the prediction of the experimental heat transfer coefficient; however, as vapour quality increases above 0.8, the model underestimates the experimental heat transfer coefficient, again. In Figure 4.16 the ratio between calculated and measured heat transfer coefficient is reported as a function of vapour quality; saturation temperature is 30 °C, mass velocity is 600 kg/(m^2 s) and heat flux goes from 42.4 to 83.5 kW/m^2. All points fall within 30 % error lines. Some overprediction is observed at low vapour quality, but the ration between calculated and experimental value decreases as vapour quality increases.

A more comprehensive understanding of the prediction capability provided by the model can be obtained by the graphs reported in Figure 4.17 and 4.18, where the calculated and the experimental heat transfer coefficients are plotted as a function of vapour quality. It can be observed as the model is not able to catch the abrupt increase in heat transfer coefficient at high vapour quality, just before the onset of dry-out. By comparing in Figure 4.17 test runs at 200 and 600 kg/(m^2 s), the model is able to predict the effect of mass velocity on heat transfer coefficient experimentally found. On the contrary, by Figure 4.18, for a fixed vapour quality the calculated heat transfer coefficient is higher at 400 kg/(m^2 s) than at 200 kg/(m^2 s), while higher coefficients have been measured at 200 kg/(m^2 s).

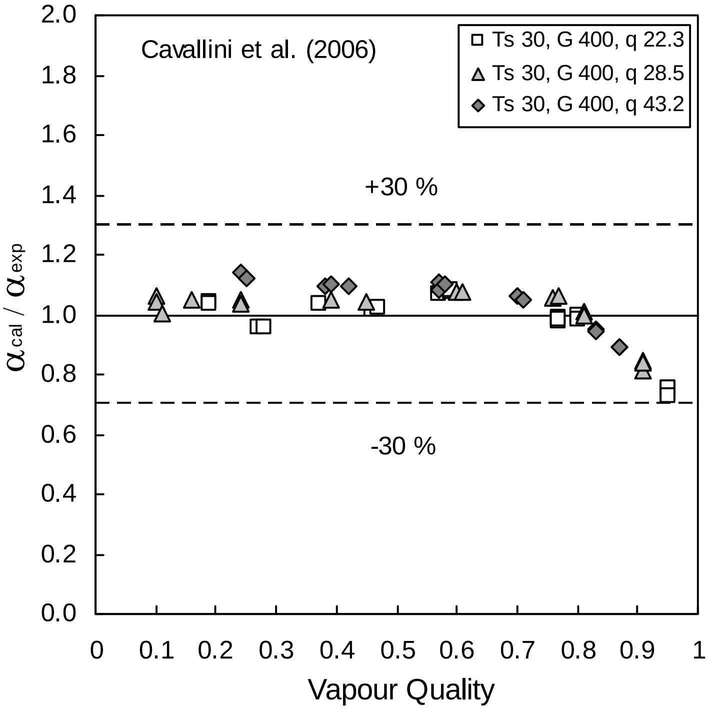

Figure 4.15. Ratio between calculated and experimental heat transfer coefficient vs. vapour quality for R134a. The calculated coefficients are obtained with the model by Cavallini *et al.* (2006). Saturation temperature is 30 °C, mass velocity is 400 kg/(m^2 s) and heat flux is 22.3, 28.5, 43.2 kW/m^2. The ±30 % error lines are reported.

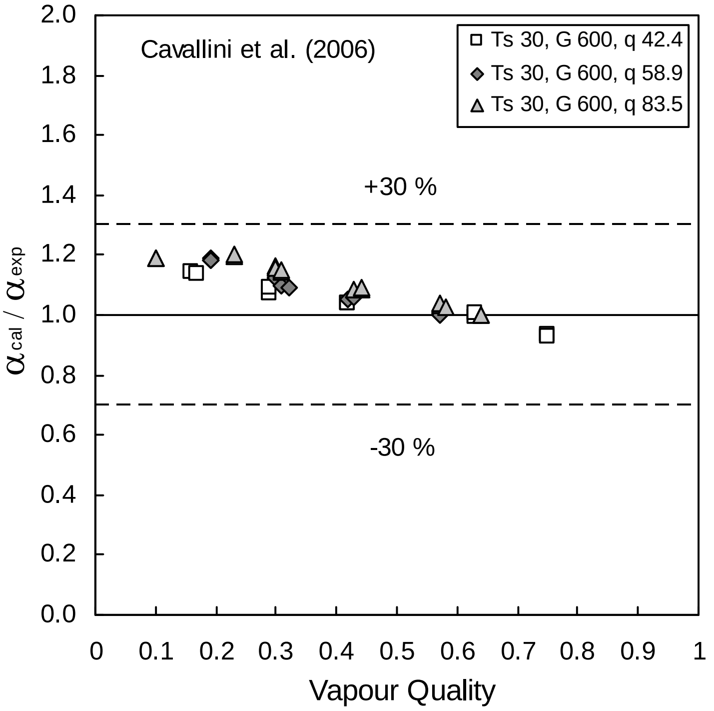

Figure 4.16. Ratio between calculated and experimental heat transfer coefficient vs. vapour quality for R134a. The calculated coefficients are obtained with the model by Cavallini *et al.* (2006). The saturation temperature is 30 °C, mass velocity is 400 kg/(m^2 s) and heat flux is 22.3, 28.5 and 42.4 kW/m^2. The ±30 % error lines are reported.

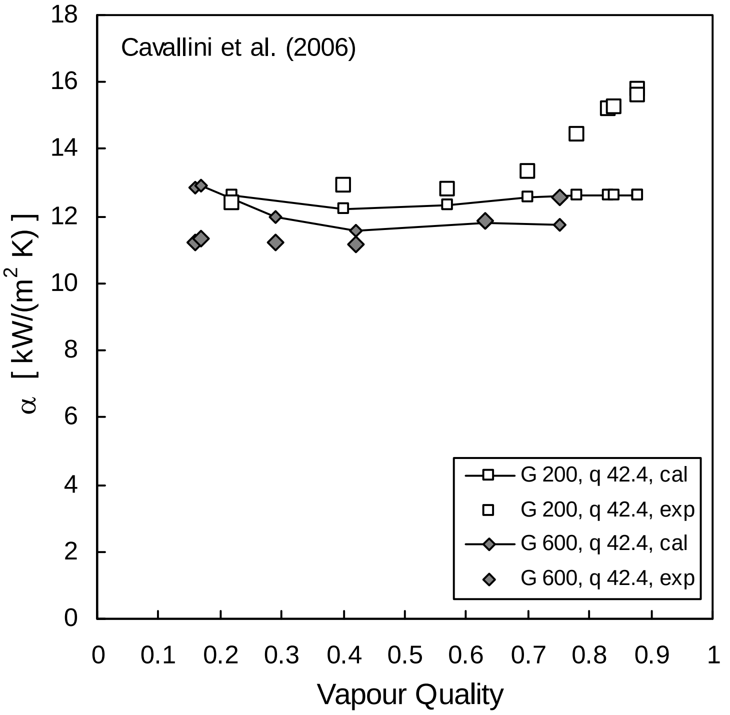

Figure 4.17. Experimental and calculated heat transfer coefficient vs. vapour quality for R134a. The calculated coefficients are obtained with the model by Cavallini *et al.* (2006). Saturation temperature is 30 °C, mass velocity is 200 and 600 kg/(m^2 s) and heat flux is around 42.4 kW/m^2.

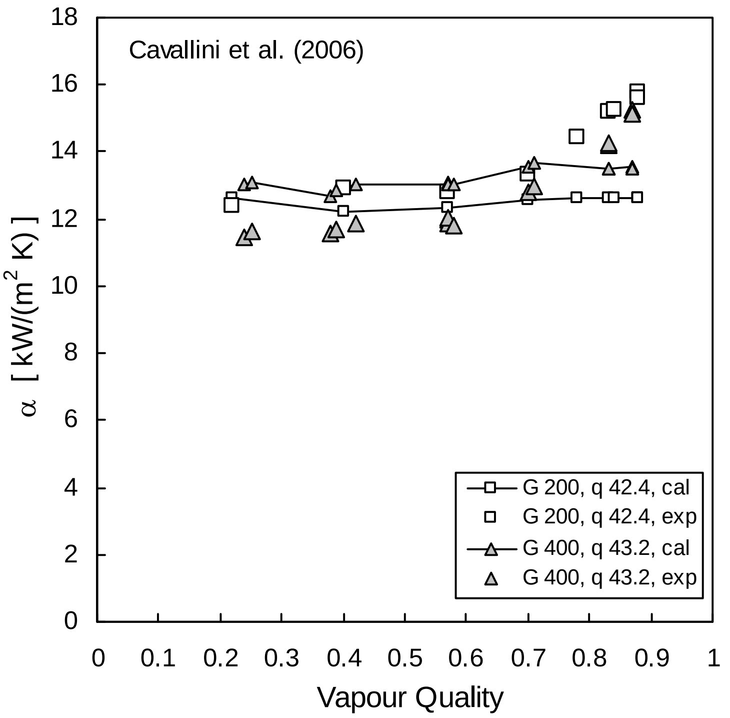

Figure 4.18. Experimental and calculated heat transfer coefficient vs. vapour quality for R134a. The calculated coefficients are obtained with the model by Cavallini *et al.* (2006). Saturation temperature is 30 °C, mass velocity is 200 and 400 kg/(m^2 s) and heat flux is around 43 kW/m^2.

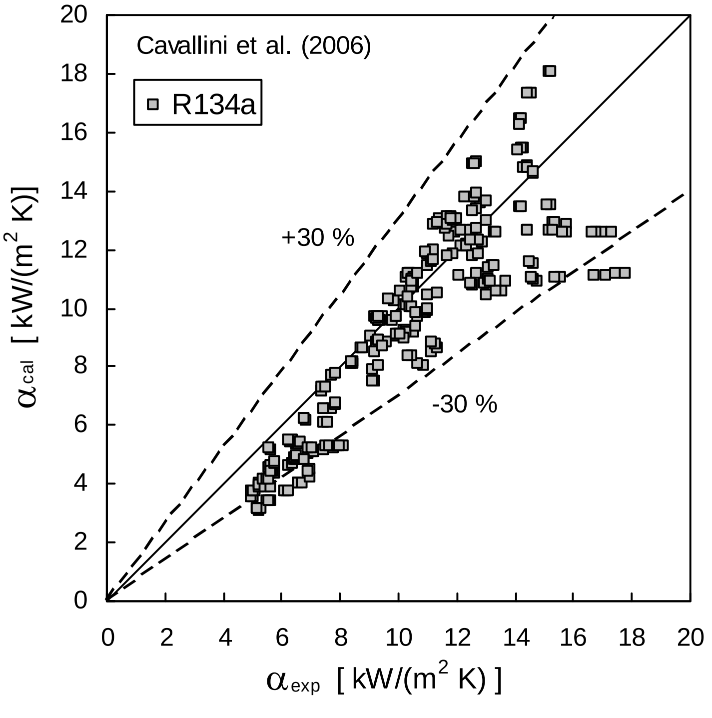

Figure 4.19. Calculated vs measured heat transfer coefficient for R134a. The calculated values are obtained with the model by Cavallini *et al.* (2006). The ±30 % error lines are reported.

4.2.4 Chamra and Mago (2007)

The experimental heat transfer coefficients for R134a are compared with the model by Chamra and Mago (2007) in this section. Table 4.5 reports percentage values of *MAD*, *MD* and *SD*, resulting from the comparison.

At 80 kg/(m^2 s) mass velocity, the model overestimates above 30 % the experimental heat transfer coefficients; Chamra and Mago (2007) also observed as their model provided some overprediction when compared with data at mass velocity lower than 100 kg/(m^2 s). When mass velocity is increased to 100 kg/(m^2 s), the accuracy of the model significantly improves, as it can be observed by comparing Figure 4.20 and 4.21. Some overpredition occurs for test run taken at 14.7 kW/m^2, but at 21.5 kW/m^2 heat flux high accuracy is observed, with a *MAD* value of 6 %. Moreover, at 100 kg/(m^2 s) mass velocity, the ratio of calculated and experimental heat transfer coefficient does not show any particular dependence of vapour quality and a low standard deviation is obtained. Therefore, at those conditions, the model satisfactory reproduces the experimental trend of heat transfer coefficient versus vapour quality. When mass velocity is further increased to 200 kg/(m^2 s), the calculated and experimental heat transfer coefficients are in agreement within ±30 %, again. By comparing the three test runs at G = 200 kg/(m^2 s) reported in Figure 4.22, some underestimation of experimental data is found at vapour quality lower than 0.5, in particular for the higher heat flux. At 400 and 600 kg/(m^2 s) a reasonable good prediction capability is observed at vapour quality under around 0.4, but, as vapour quality increases, the model tends to overestimate the experimental heat transfer coefficient.

Any significant effect of the reduced pressure is found on the prediction capability of the model (see Figure 4.25).

Table 4.5. Comparison between experimental heat transfer coefficients for R134a in microfin tube and model by Chamra and Mago. (2007): percentage values of *MAD*, *MD* and *SD*.

T_s [°C]	G [kg/(m^2 s)]	q [kW/m^2]	*MAD* [%]	*MD* [%]	*SD* [%]
31	80	14.7	32.1	32.1	7.1
30.3	100	14.7	15.9	15.9	5.5
30.4	100	21.5	6	4	6.4
30.5	200	14.9	8.4	-6.8	7
30.5	200	22.3	6.4	-5.2	6.2
30	200	42.4	14.6	-14.6	5.7
30.2	400	22.3	16.2	14.9	13.1
30.3	400	28.5	14.5	10.8	14.7
29.7	400	43.2	10.1	8	8.4
29.7	600	42.4	21.6	21.6	12.9
29.8	600	58.9	6.3	6.3	4.8
29.8	600	83.5	4.5	1.4	0.7
42.2	200	14.1	5.8	-5.2	5.7
	All data sets		15	10.1	7.9

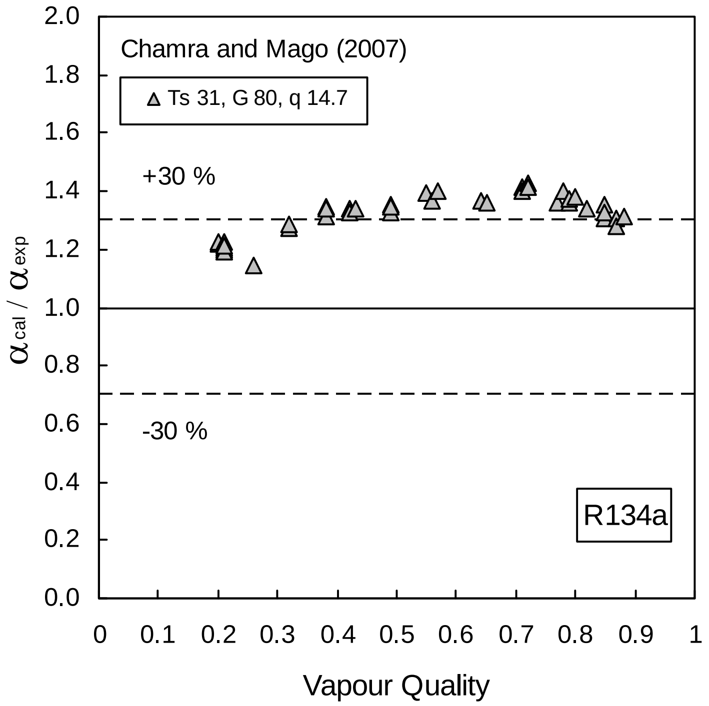

Figure 4.20. Ratio between calculated and experimental heat transfer coefficient vs. vapour quality. The calculated coefficients are obtained with the model by Chamra and Mago *et al.* (2007). Saturation temperature is 30 °C, mass velocity is 80 kg/(m^2 s) and heat flux is 14.7 kW/m^2. The ±30 % error lines are reported.

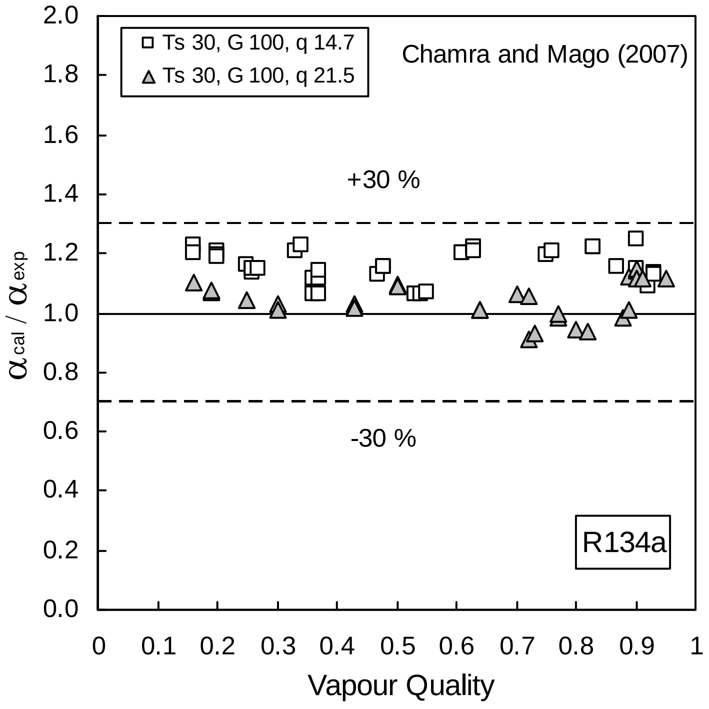

Figure 4.21. Ratio between calculated and experimental heat transfer coefficient vs. vapour quality. The calculated coefficients are obtained with the model by Chamra and Mago (2007). Saturation temperature is 30 °C, mass velocity is 100 kg/(m^2 s) and heat flux is 14.7 and 21.5 kW/m^2. The ±30 % error lines are reported.

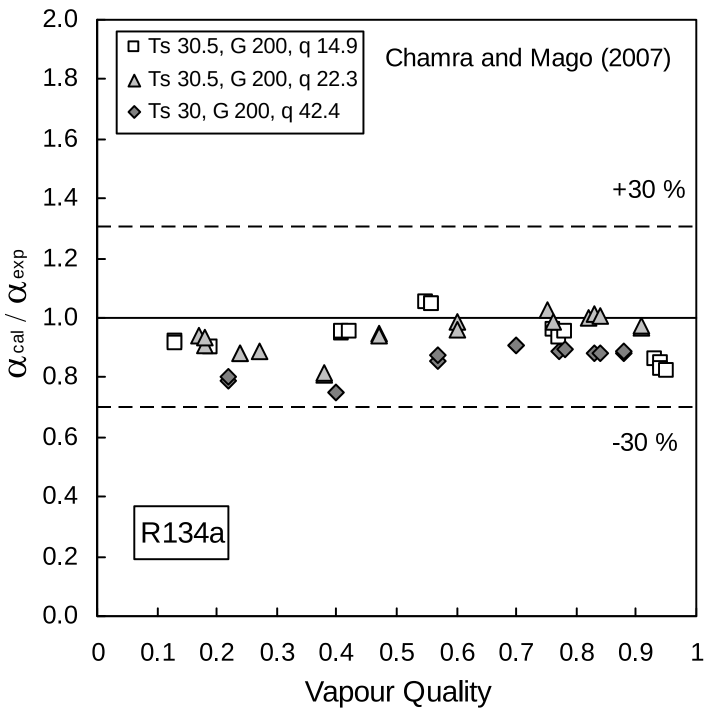

Figure 4.22. Ratio between calculated and experimental heat transfer coefficient vs. vapour quality. The calculated coefficients are obtained with the model by Chamra and Mago (2007). Saturation temperature is 30 °C, mass velocity is 200 kg/(m^2 s) and heat flux is 14.9, 22.3, 42.4 kW/m^2. The ±30 % error lines are reported.

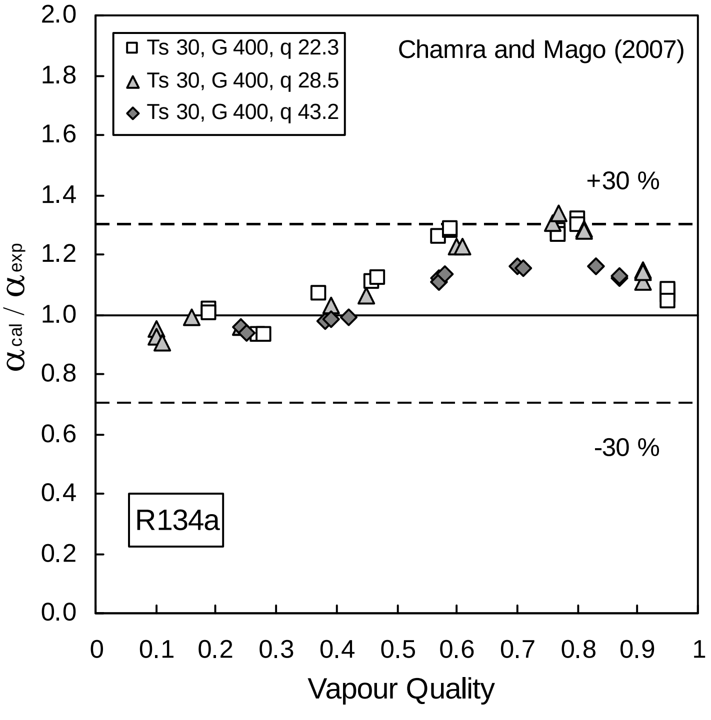

Figure 4.23. Ratio between calculated and experimental heat transfer coefficient vs. vapour quality. The calculated coefficients are obtained with the model by Chamra and Mago (2007). Saturation temperature is 30 °C, mass velocity is 400 kg/(m^2 s) and heat flux is 22.3, 28.5 and 43.2 kW/m^2. The ±30 % error lines are reported.

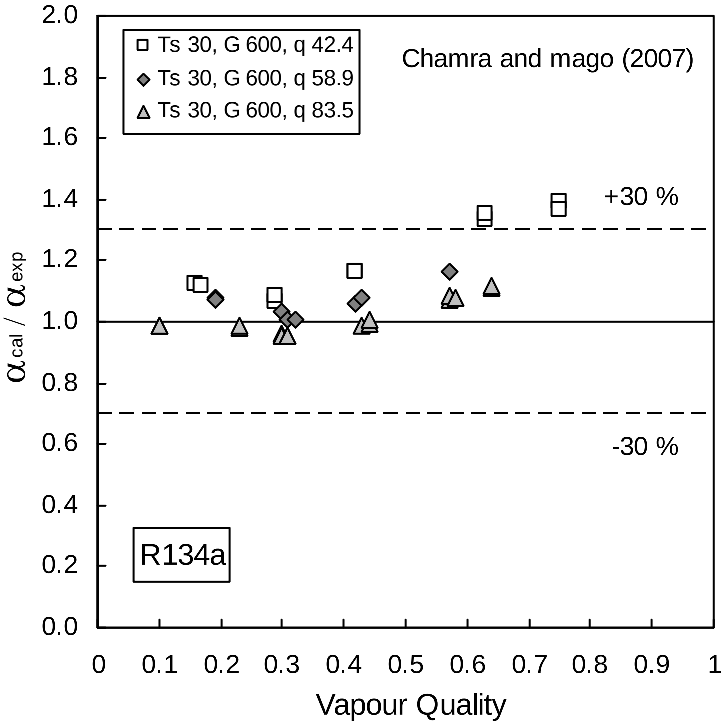

Figure 4.24. Ratio between calculated and experimental heat transfer coefficient vs. vapour quality. The calculated coefficients are obtained with the model by Chamra and Mago (2007). Saturation temperature is 30 °C, mass velocity is 600 kg/(m^2 s) and heat flux is 42.4, 58.9 and 83.5 kW/m^2. The ±30 % error lines are reported.

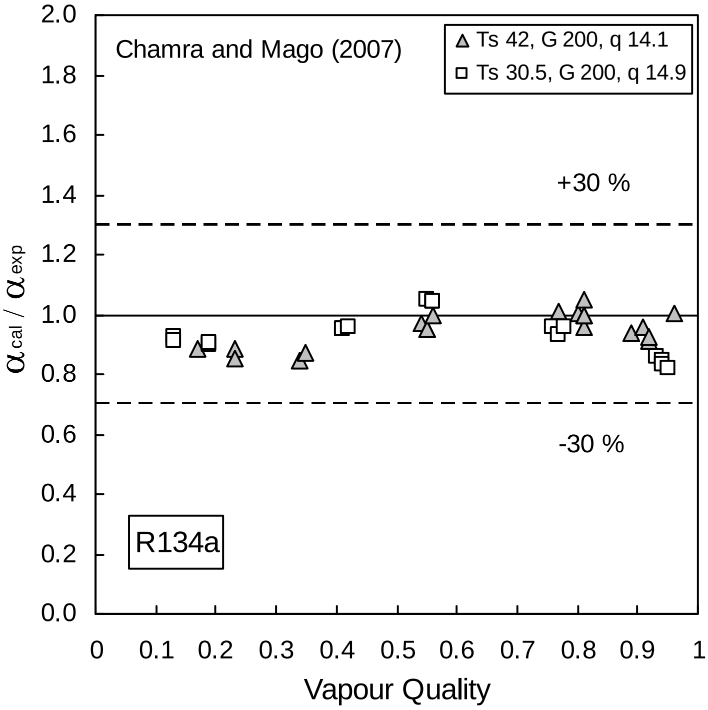

Figure 4.25. Ratio between calculated and experimental heat transfer coefficient vs. vapour quality. The calculated coefficients are obtained with the model by Chamra and Mago (2007). Saturation temperature are around 30 °C and 42 °C, mass velocity is 200 kg/(m^2 s) and heat flux is 14.9 and 14.1 kW/m^2. The ±30 % error lines are reported.

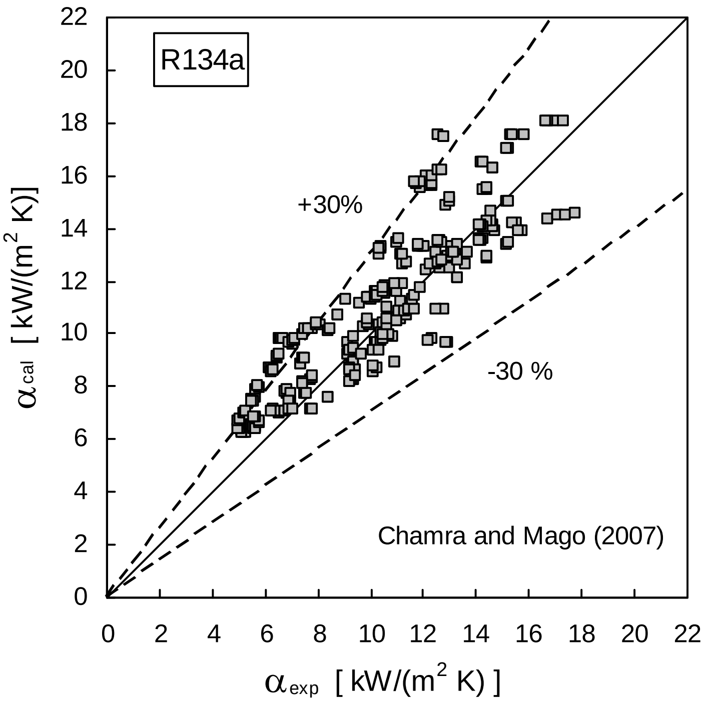

Figure 4.26. Calculated vs measured heat transfer coefficient for R134a. The calculated values are obtained with the model by Chamra and Mago (2007). The ±30 % error lines are reported.

4.2.5 Hamilton *et al.* (2008)

The results obtained by the comparison between the experimental measurements of the heat transfer coefficient and the values predicted by Hamilton *et al.* (2008) are here presented and discussed. In Table 4.6 the values of *MAD*, *MD* and *SD* obtained for each data set and for the entire database collected for R134a are reported. Figure 4.27 - 4.33 show the ratio of calculated and experimental heat transfer coefficient as a function of vapour quality for all the test runs performed.

When mass velocity is lower than 100 kg/(m^2 s), the model strongly overestimates experimental data, but as mass velocity increases above 100 kg/(m^2 s), the accuracy of the model becomes significantly higher. Moreover, at 100 kg/(m^2 s), the model does not seem able to predict the experimental trend of heat transfer coefficient versus vapour quality, because the ratio $\alpha_{cal}/\alpha_{exp}$ presents a local minimum (Figure 4.28). Besides higher values of standard deviation are found as compared to Thome *et al.* (1997), Cavallini *et al.* (2006) and Chamra and Mago (2007).

For test runs at 200, 400, 600 kg/(m^2 s) satisfactory values of *SD* have been found, which means a little dependence of the prediction capability by the operative parameters. Only at G = 600 kg/(m^2 s) and q = 42.4 kW/m^2, some dependence on vapour quality is observed. However, except for low mass velocity, the predicted heat transfer coefficients agree with the experimental values within ±30 % (Figure 4.33).

Moreover, different from the other models, some effect of the saturation pressure on heat transfer coefficient is observed here, because test runs performed at similar mass velocity and heat flux present a different ratio of calculated and measured coefficient at low vapour quality, where nucleate boiling is the main heat transfer mechanism. On the contrary the same prediction capability occurs at high vapour quality, where convection heat transfer becomes important.

Table 4.6. Comparison between experimental heat transfer coefficients for R134a in microfin tube and model by Hamilton *et al.* (2008): percentage values of *MAD*, *MD* and *SD*.

T_s [°C]	G [kg/(m^2 s)]	q [kW/m^2]	*MAD* [%]	*MD* [%]	*SD* [%]
31	80	14.7	62	62	7.1
30.3	100	14.7	42.1	42.1	14.4
30.4	100	21.5	30	30	15.5
30.5	200	14.9	11.9	-0.7	13.4
30.5	200	22.3	6.7	5.7	5.1
30	200	42.4	11.9	5.5	6.9
30.2	400	22.3	14.1	11.6	10.7
30.3	400	28.5	13.5	13.5	7.4
29.7	400	43.2	14.9	14.9	3.8
29.7	600	42.4	22.9	22.9	8.2
29.8	600	58.9	12.6	12.6	2.9
29.8	600	83.5	8.2	8.2	0.7
42.2	200	14.1	15	-15	5
	All data sets		27.5	24.5	9.9

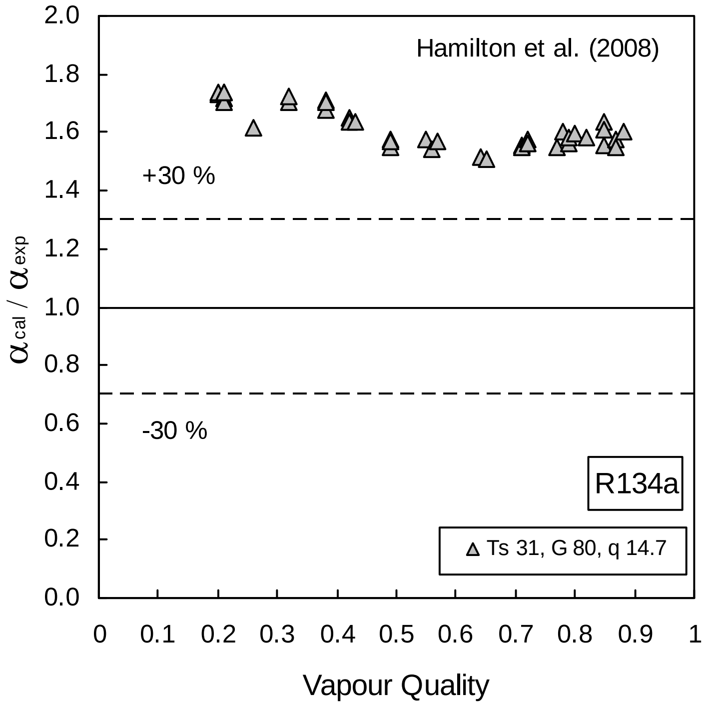

Figure 4.27. Ratio between calculated and experimental heat transfer coefficient vs. vapour quality. The calculated coefficients are obtained with the model by Hamilton *et al.* (2008). Saturation temperature is 30 °C, mass velocity is 80 kg/(m^2 s) and heat flux is 14.7 kW/m^2. The ±30 % error lines are reported.

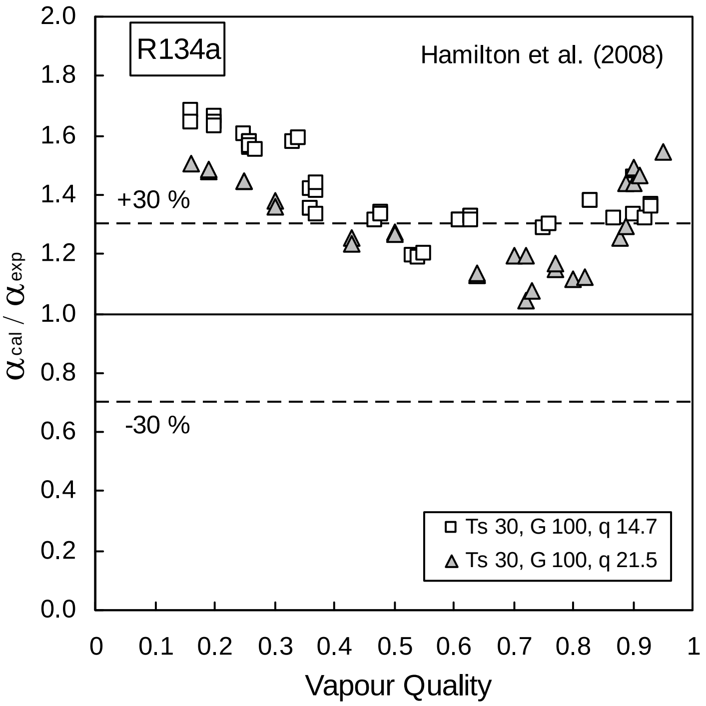

Figure 4.28. Ratio between calculated and experimental heat transfer coefficient vs. vapour quality. The calculated coefficients are obtained with the model by Hamilton *et al.* (2008). Saturation temperature is 30 °C, mass velocity is 100 kg/(m^2 s), heat flux is 14.7 and 21.5 kW/m^2. The ±30 % error lines are reported.

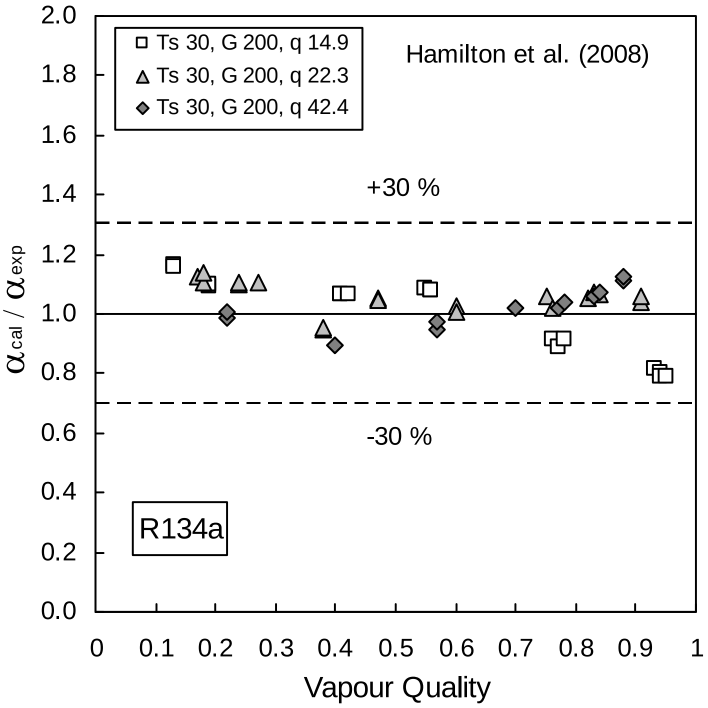

Figure 4.29. Ratio between calculated and experimental heat transfer coefficient vs. vapour quality. The calculated coefficients are obtained with the model by Hamilton *et al.* (2007). Saturation temperature is 30 °C, mass velocity is 200 kg/(m^2 s) and heat flux is 14.9, 22.3 and 42.4 kW/m^2. The ±30 % error lines are reported.

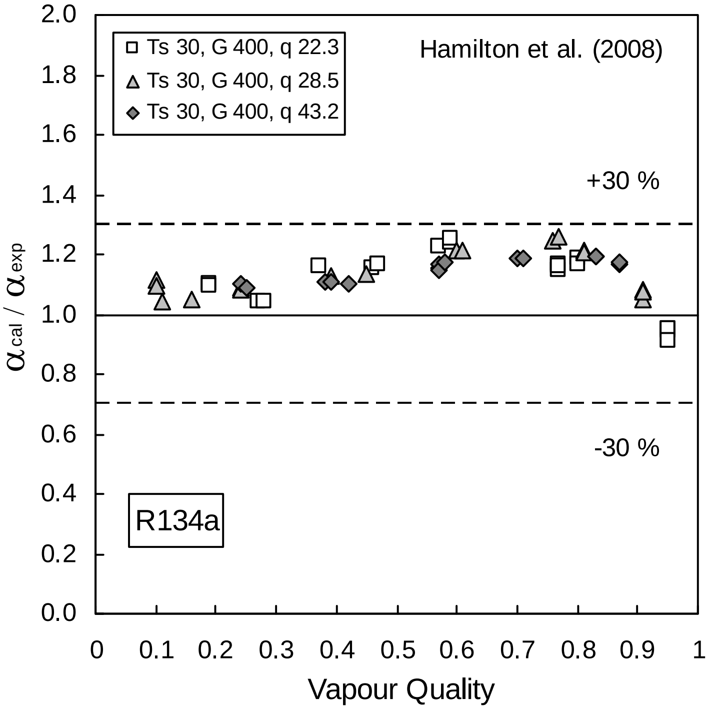

Figure 4.30. Ratio between calculated and experimental heat transfer coefficient vs. vapour quality. The calculated coefficients are obtained with the model by Hamilton *et al.* (2008). Saturation temperature is 30 °C, mass velocity is 400 kg/(m^2 s) and heat flux is 22.3, 28.5 and 43.2 kW/m^2. The ±30 % error lines are reported.

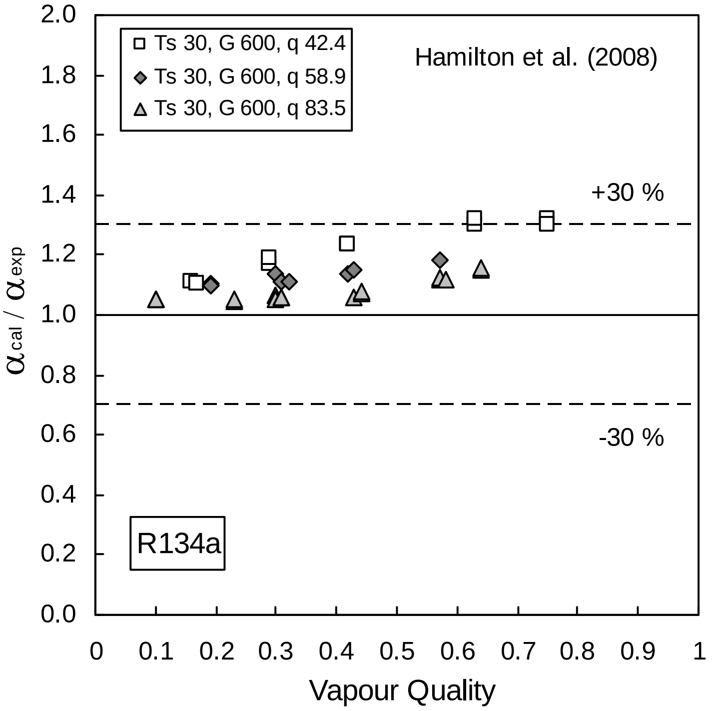

Figure 4.31. Ratio between calculated and experimental heat transfer coefficient vs. vapour quality. The calculated coefficients are obtained with the model by Hamilton *et al.* (2008). Saturation temperature is 30 °C, mass velocity is 600 kg/(m^2 s), heat flux is 42.4, 58.9 and 83.5 kW/m^2. The ±30 % error lines are reported.

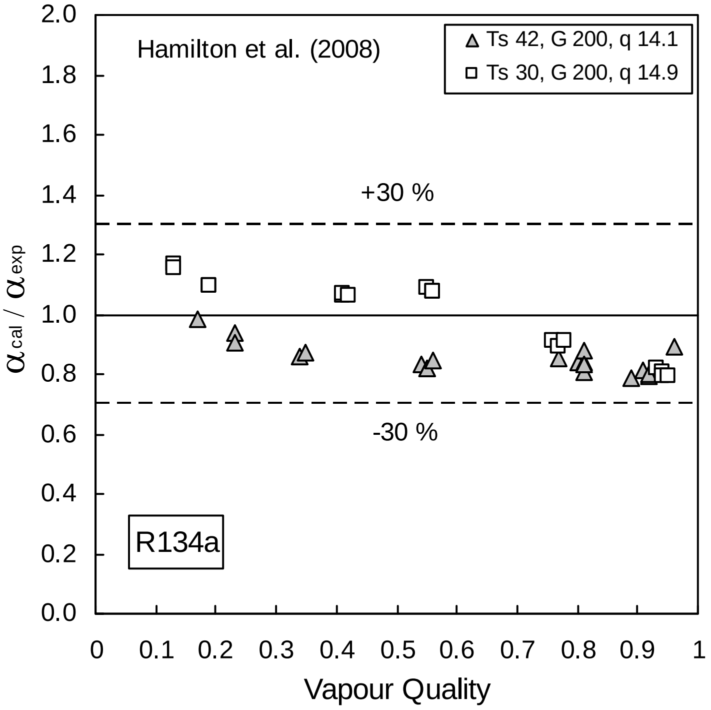

Figure 4.32. Ratio between calculated and experimental heat transfer coefficient vs. vapour quality. The calculated coefficients are obtained with the model by Hamilton *et al.* (2008). Saturation temperature are 30 °C and 42 °C, mass velocity is 200 kg/(m^2 s) and heat flux is 14.1 and 14.9 kW/m^2. The ±30 % error lines are reported.

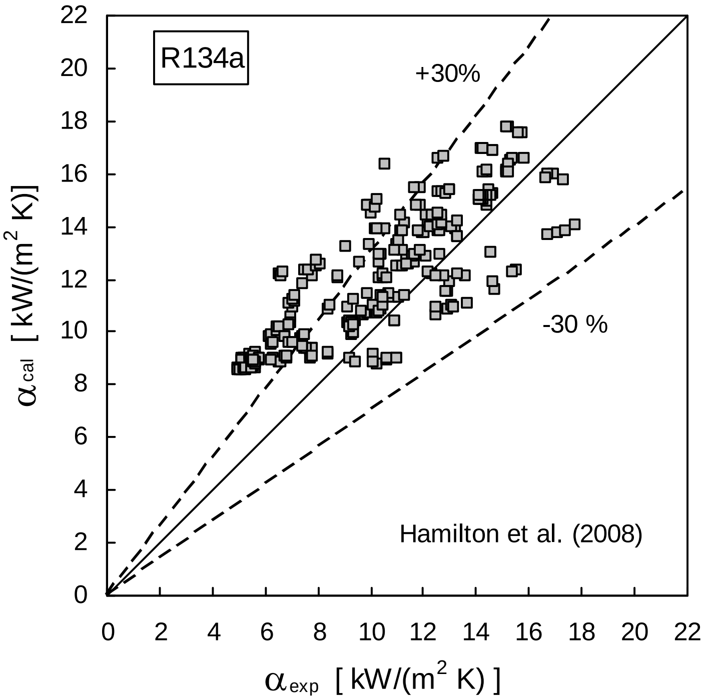

Figure 4.33 Calculated vs measured heat transfer coefficient for R134a. The calculated values are obtained with the model by Hamilton *et al.* (2008). The ±30 % error lines are reported.

4.3. Comparison between calculated and measured heat transfer coefficient for R410A

4.3.1 Koyama *et al.* (1995)

The model by Koyama *et al.* (1995) is here compared with new data for R410A at high saturation temperature. Table 4.7 reports the value of *MAD*, *MD* and *SD* obtained by the comparison. As already found for R134a, the model also provides a strong overestimation of R410A experimental data. The calculated heat transfer coefficient is plotted against the measured value in Figure 4.34: no data agree within ±30.

Table 4.7. Comparison between experimental heat transfer coefficients for R410A in microfin tube and model by Koyama *et al.* (1995): percentage values of *MAD*, *MD* and *SD*.

T_s [°C]	G [kg/(m^2 s)]	q [kW/m^2]	*MAD* [%]	*MD* [%]	*SD* [%]
30.3	200	43.9	89.8	89.8	9.3
30.2	400	21.4	70	70	6.4
30.2	400	44	95.9	95.9	3.7
30.1	600	44	111.9	111.9	8.3
40.2	200	21.1	56	56	5.2
39.9	400	21.2	83.2	83.2	9.7
	All data sets		84.5	84.5	7.4

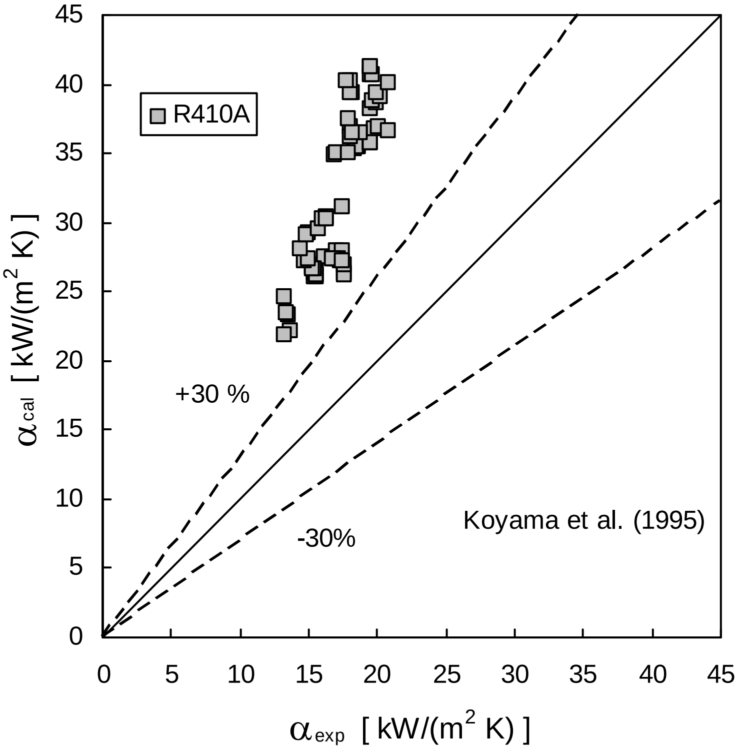

Figure 4.34. Calculated vs measured heat transfer coefficient for R410A. The calculated values are obtained with the model by Koyama *et al.* (1999). The ±30 % error lines are reported.

4.3.2 Thome *et al.* (1997)

The results of the comparison between the model by Thome *et al.* (1997) and the new experimental heat transfer coefficients for R410A is presented in this section. The value of *MAD*, *MD* and *SD* are finally reported in Table 4.8 for the different data sets and for the entire data bank collected for R410A.

In Figure 4.35, the ratio between calculated and experimental heat transfer coefficient is plotted as a function of vapour quality for 30 °C saturation temperature. When mass velocity is 200 kg/(m^2 s), the error provided by the model is almost constant with vapour quality, as also indicated by the low value of standard deviation obtained. On the contrary, for the other data sets the prediction capability shows an evident dependence on vapour quality: at low vapour quality, the calculated coefficients underestimate the measured values, but as vapour quality increases the deviation between calculated and experimental coefficient diminishes; for high vapour quality, some overprediciton is provided in the case of G = 400 kg/(m^2 s) with q = 21.2 kW/m^2 and G = 600 kg/(m^2 s) with q = 44 kW/m^2.

At 40 °C saturation temperature and 400 kg/(m^2 s) mass velocity, the model underestimates the measured heat transfer coefficient at low vapour quality, but the error decreases as vapour quality increases (Figure 4.36); the model is not able to catch the experimental trend of heat transfer coefficient against vapour quality, again.

In Figure 4.37 the calculated heat transfer coefficient is plotted versus the measured heat transfer coefficient: most of calculated coefficients are in agreement with the experimental values within ±30 %, but a general underprediction is observed, confirmed by a mean deviation of -16.6%.

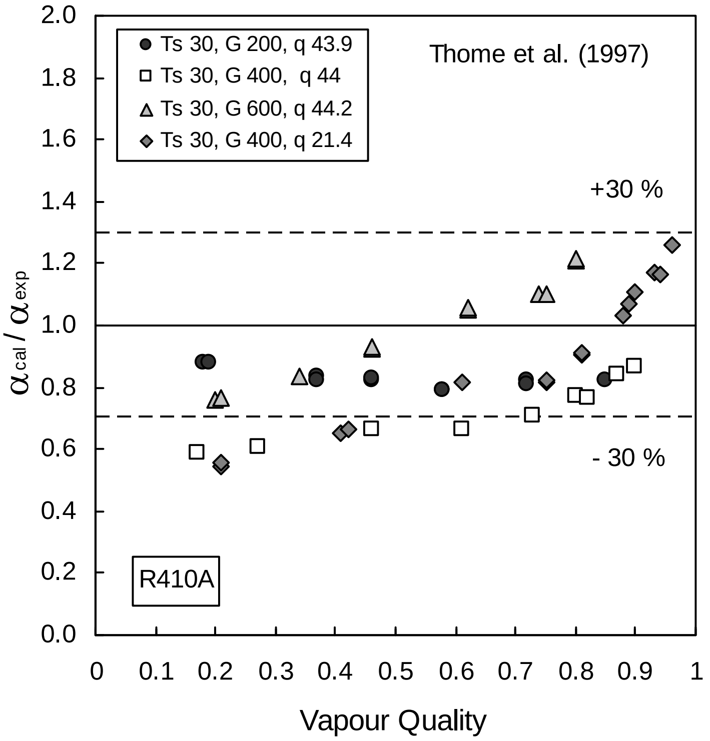

Figure 4.35. Ratio between calculated and experimental heat transfer coefficient vs. vapour quality for R410A. The calculated coefficients are obtained by Thome *et al.* (1997). Saturation temperature is 30 °C, mass velocity is 200, 400 and 600 kg/(m^2 s) and heat flux is around 21 and 44 kW/m^2. The ±30 % error lines are reported.

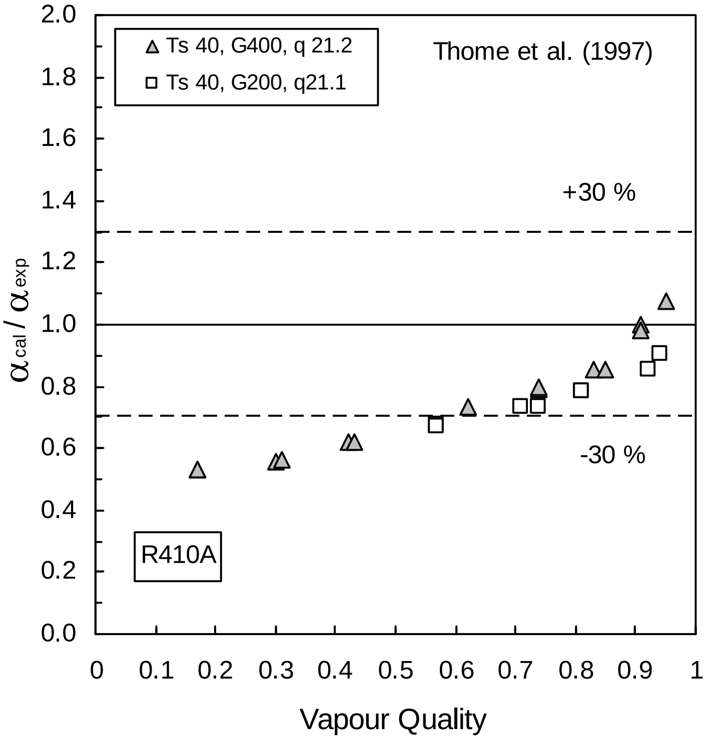

Figure 4.36. Ratio between calculated and experimental heat transfer coefficient vs. vapour quality for R410A. The calculated values are obtained by Thome *et al.* (1997). Saturation temperature is 40 °C, mass velocity is 200 and 400 kg/(m^2 s), heat flux is around 21 kW/m^2. The ±30 % error lines are reported.

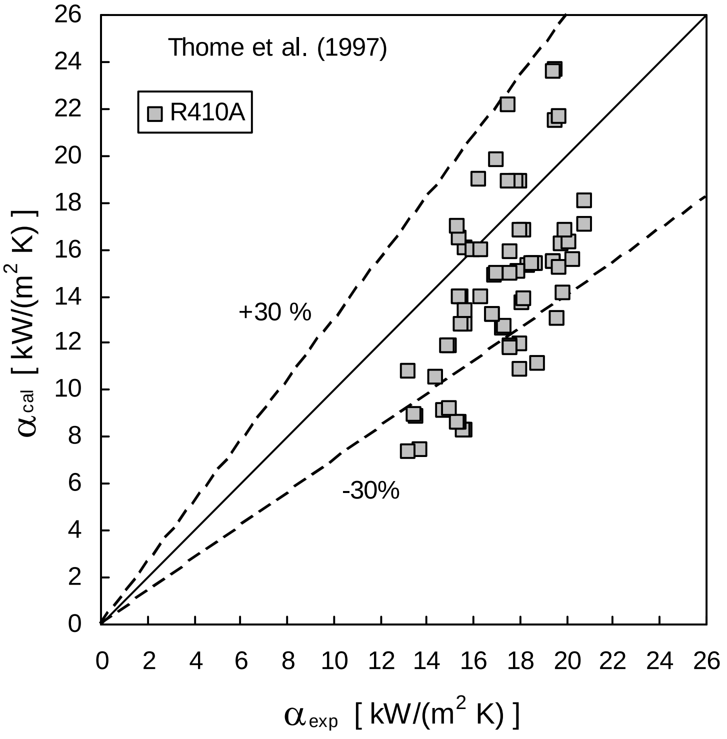

Figure 4.37. Calculated vs measured heat transfer coefficient for R410A. The calculated values are obtained with the model by Thome *et al.* (1999). The ±30 % error lines are also reported.

Table 4.8. Comparison between experimental heat transfer coefficients for R410A in microfin tube and model by Thome *et al.* (1997): percentage values of *MAD*, *MD* and *SD*.

T_s [°C]	*G* [kg/(m^2 s)]	*q* [kW/m^2]	*MAD* [%]	*MD* [%]	*SD* [%]
30.3	200	43.9	17.2	-17.2	2.8
30.2	400	21.4	20.7	-10	23
30.2	400	44	27.9	-27.9	9.9
30.1	600	44	13.8	-0.5	16.3
40.2	200	21.1	23.2	-23.2	8.2
39.9	400	21.2	26	-24.9	18.6
	All data sets		21.4	-16.6	15.4

4.3.3 Cavallini *et al.* (2006)

The model by Cavallini *et al.* (2006) is here compared with new heat transfer coefficients for R410A in microfin tube. The results of the comparison are summarized in Table 4.9, where the values of mean absolute deviation, mean deviation and standard deviation are reported. On the whole, the model by Cavallini *et al.* (2006) provides a satisfactory agreement with experimental data, with a little oveprediction around 4%.

In the case of data taken at 30 °C, the ratio between calculated and experimental coefficient decreases as the vapour quality increases, and the model does not catch the experimental trend of heat transfer coefficient versus vapour quality (Figure 4.39). For instance in Figure 4.40, the calculated and experimental heat transfer coefficients are plotted as a function of vapour quality for 400 kg/(m^2 s) mass velocity, 21.4 and 44 kW/m^2 heat flux; the saturation temperature is 30 °C. As it can be observed, the experimental coefficient increases at higher quality values; on the contrary the calculated heat transfer coefficient continuously decreases as vapour quality increases. However, the predicted coefficients agree with the measured values within ±30 %.

In Figure 4.41, the ratio of calculated and measured heat transfer coefficient is plotted against vapour quality at 40 °C saturation temperature. At 200 kg/(m^2 s), and vapour quality lower than around 0.6 the deviation between calculated and experimental value is almost independent of vapour quality; this trend was also observed at the same heat flux at 30 °C saturation temperature.

Table 4.9. Comparison between experimental heat transfer coefficients for R410A in microfin tube and model by Cavallini *et al.* (2006): percentage values of *MAD*, *MD* and *SD*.

T_s [°C]	*G* [kg/(m^2 s)]	*q* [kW/m^2]	*MAD* [%]	*MD* [%]	*SD* [%]
30.3	200	43.9	10.6	3.6	13.6
30.2	400	21.4	9.4	7.4	8.9
30.2	400	44	9.3	2.6	11.7
30.1	600	44	10.6	4.6	11.3
40.2	200	21.1	12.3	11.2	8.1
39.9	400	21.2	8.5	-8.5	3.8
	All data sets		10.3	4.6	9.7

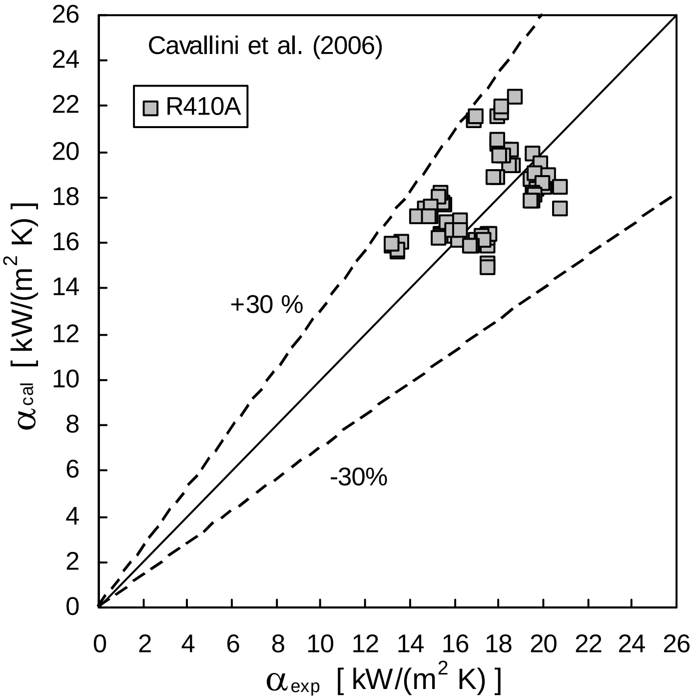

Figure 4.38. Calculated vs measured heat transfer coefficient for R410A. The calculated values are obtained with the model by Cavallini *et al.* (2006). The ±30 % error lines are reported.

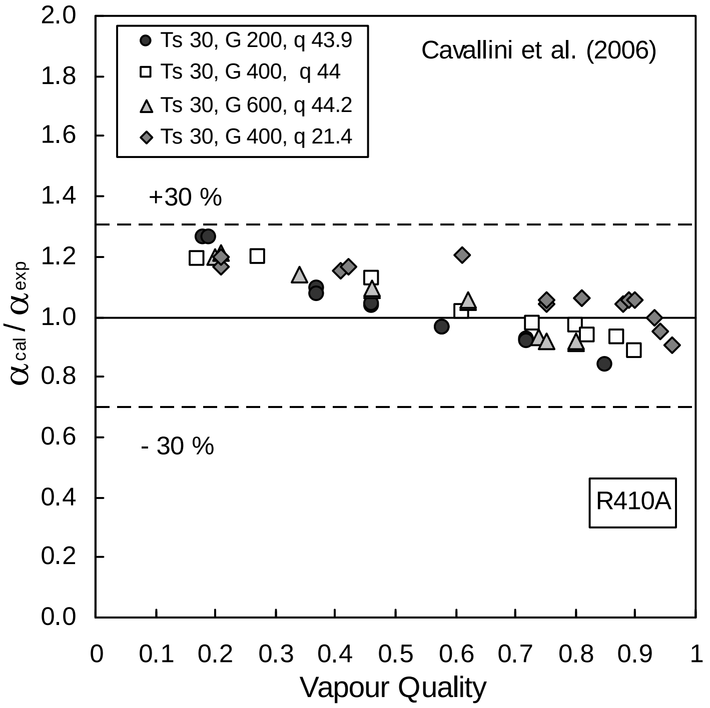

Figure 4.39. Ratio between calculated and experimental heat transfer coefficient vs. vapour quality for R410A. The calculated values are obtained with the model by Cavallini *et al.* (2006). Saturation temperature is 30 °C, mass velocity is 200, 400, 600 kg/(m^2 s) and heat flux is 21.2 and around 44 kW/m^2. The ±30 % error lines are reported.

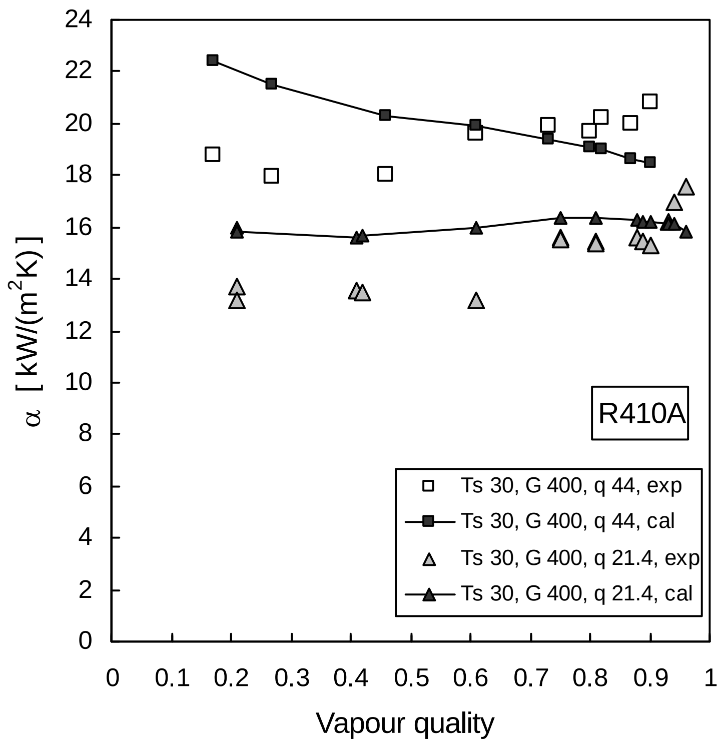

Figure 4.40. Experimental and calculated heat transfer coefficient vs. vapour quality. The calculated values are obtained with the model by Cavallini *et al.* (2006). The saturation temperature is 30 °C, mass velocity is 400 kg/(m^2 s) and heat flux is 21.4 and 44 kW/m^2.

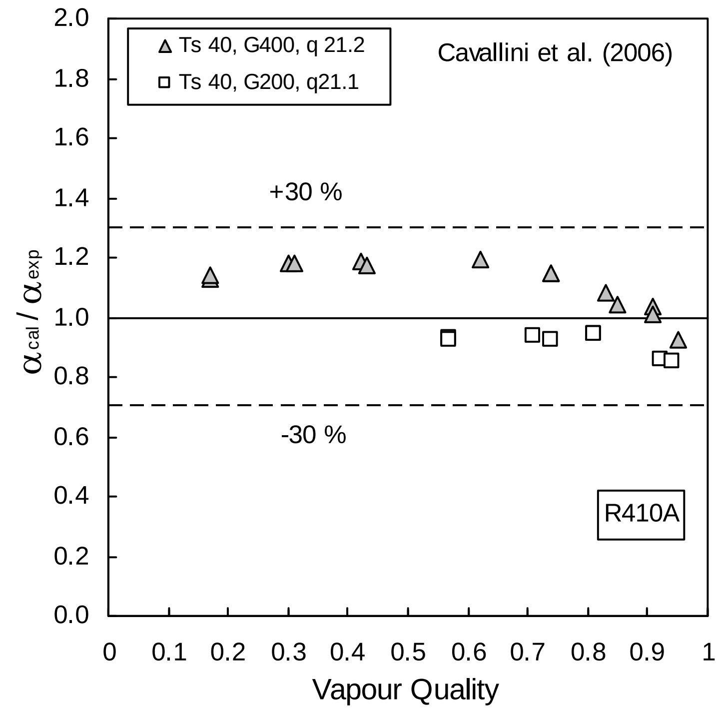

Figure 4.41. Ratio between calculated and experimental heat transfer coefficient vs. vapour quality for R410A. The calculated values are obtained with the model by Cavallini *et al.* (2006). The saturation temperature is 40 °C, mass velocity is 200 and 400 kg/(m^2 s), heat flux is around 21 kW/m^2. The ±30 % error lines are reported.

4.3.4 Chamra and Mago (2007)

The results of the comparison between the model by Chamra and Mago (2007) and the R410A experimental heat transfer coefficients are reported in this section. The model has been here used, adopting the empirical constants for pure fluids; R410A present a low temperature glide, around 0.1 °C.

Table 4.10 shows the values of *MAD*, *MD* and *SD*, obtained by the comparison. By Figure 4.42, most of calculated heat transfer coefficients agree with the experimental values within ±30 %, with a mean deviation of 12.5 %.

In Figure 4.43 and Figure 4.44 the ratio between calculated and experimental heat transfer coefficient is plotted as a function of the vapour quality for saturation temperature around 30 and 40 °C, respectively. For both the temperatures investigated, some overprediction is observed at 400 kg/(m^2 s) mass velocity and 21 kW/m^2 heat flux and high values of vapour quality, where the error can exceed 30 %. For this same conditions, the calculated and experimental heat transfer coefficient are plotted as a function of vapour quality in Figure 4.45. The model provides a strong overestimation above all at higher vapour qualities, because of the high convective contribution calculated by the model (see Figure 1.24 in section 1.4.4).

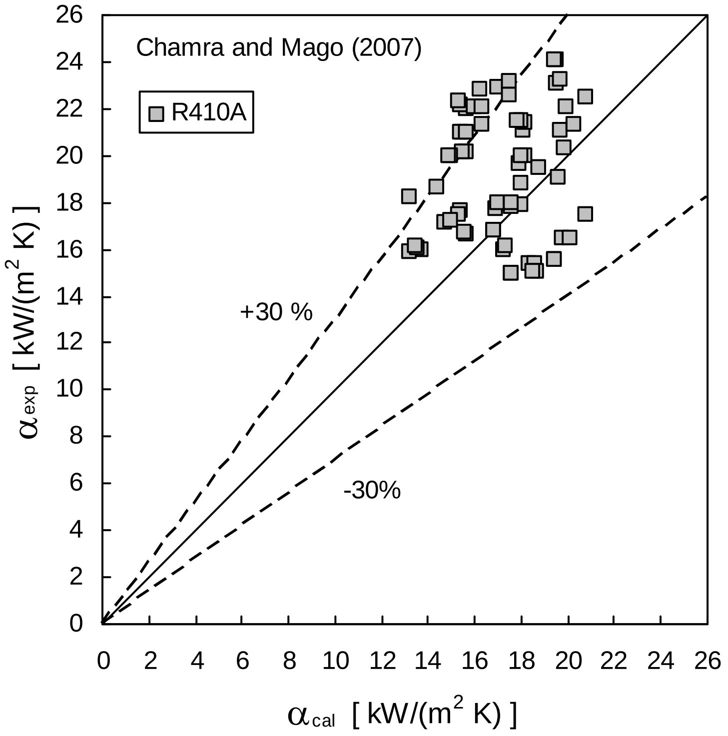

Figure 4.42. Calculated vs measured heat transfer coefficient for R410A. The calculated values are obtained with the model by Chamra and Mago (2007). The ±30 % error lines are reported.

Table 4.10. Comparison between experimental heat transfer coefficients for R410A in microfin tube and model by Chamra and Mago (2007): percentage values of *MAD*, *MD* and *SD*.

T_s [°C]	*G* [kg/(m^2 s)]	*q* [kW/m^2]	*MAD* [%]	*MD* [%]	*SD* [%]
30.3	200	43.9	15.8	-14	9.5
30.2	400	21.4	32	32	9.5
30.2	400	44	5	4.2	4.2
30.1	600	44	17	17	5
40.2	200	21.1	6.1	-5.1	7.1
39.9	400	21.2	24.1	24.1	11.1
	All data sets		18.8	12.5	8.3

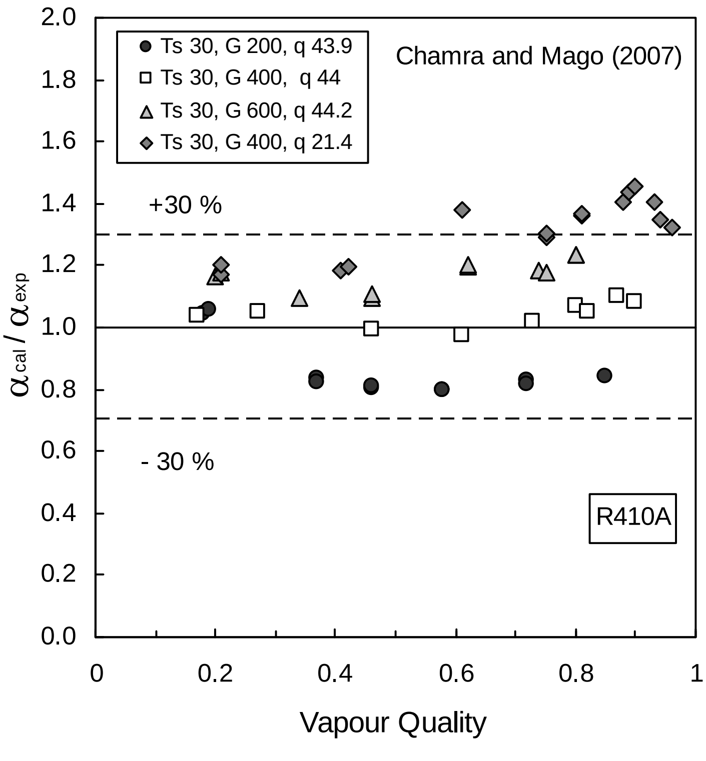

Figure 4.43. Ratio between calculated and experimental heat transfer coefficient vs. vapour quality for R410A. The calculated coefficients are obtained with the model by Chamra and Mago (2007). The saturation temperature is 30 °C, mass velocity is from 200 to 600 kg/(m^2 s) and heat flux is around 21 and 44 kW/m^2.

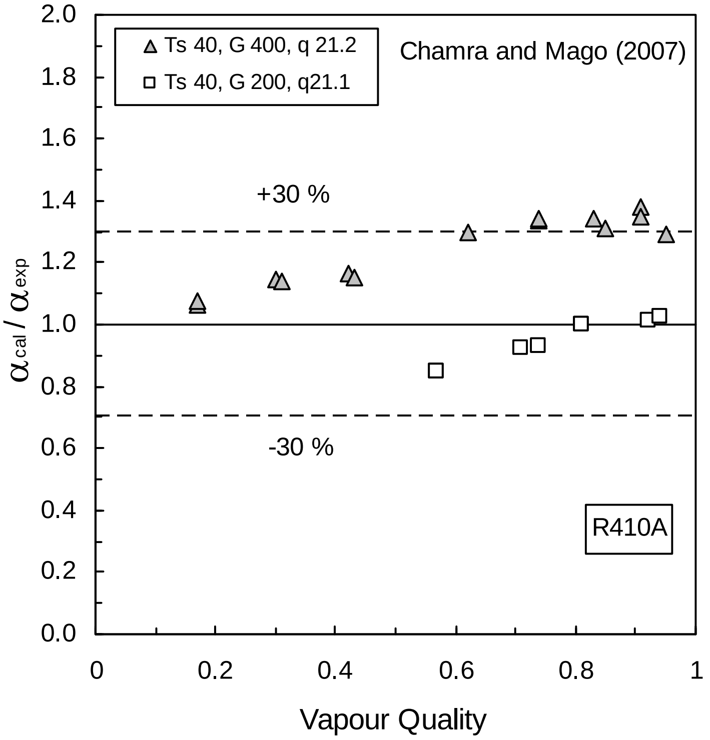

Figure 4.44. Ratio between calculated and experimental heat transfer coefficient vs. vapour quality for R410A. The calculated values are obtained by Chamra and Mago (2007). Saturation temperature is 40 °C, mass velocity is 200 and 400 kg/(m^2 s), heat flux is 21 kW/m^2.

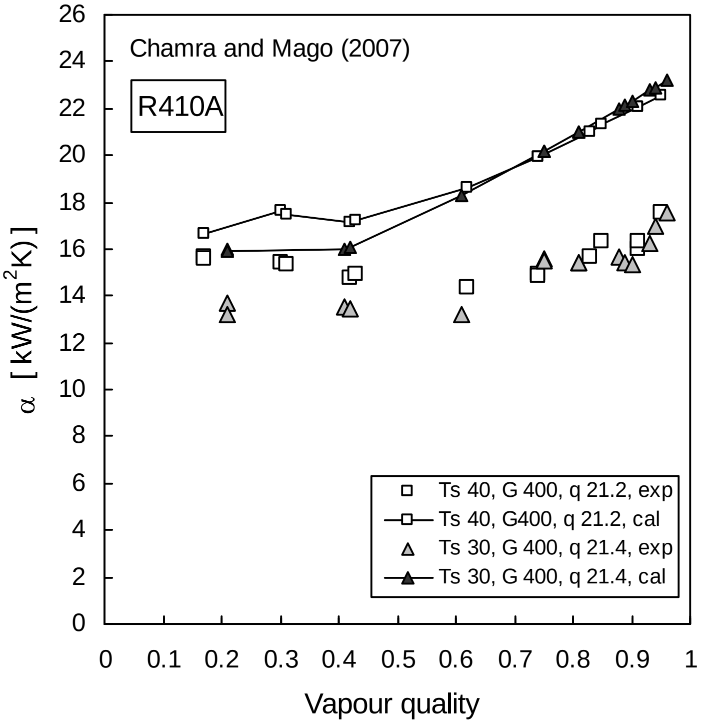

Figure 4.45. Experimental and calculated heat transfer coefficient vs. vapour quality. The calculated values are obtained with the model by Chamra and Mago (2007). Saturation temperature is 30 °C and 40 °C, mass velocity is 400 kg/(m^2 s) and heat flux is around 21 kW/m^2.

4.3.5 Hamilton *et al.* (2008)

The prediction capability of the model by Hamilton *et al.* (2008) against new data for R410A are here investigated. Figure 4.46 presents the calculated heat transfer coefficient against the experimental heat transfer coefficient. A very poor accuracy is provided by the model, which strongly underestimates all experimental data.

For each data set the percentage values of *MAD*, *MD* and *SD* are reported in Table 4.11: when comparing data sets taken at 30 °C and 40 °C saturation temperature, a further degradation of the prediction capability occurs when reduced pressure increases. By also considering the quite satisfactory behaviour of this model against R134a data, one could be suggest as the model is not able to predict data at very high reduced pressure.

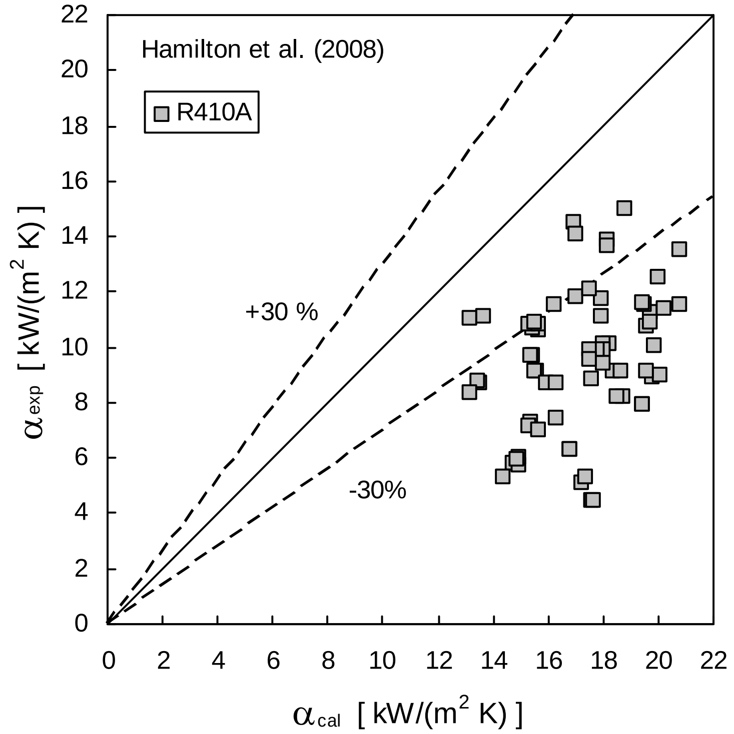

Figure 4.46. Calculated vs measured heat transfer coefficient for R410A. The calculated values are obtained with the model by Hamilton *et al.* (2008). The ±30 % error lines are reported.

Table 4.4. Comparison between experimental heat transfer coefficients for R134a in microfin tube and model by Hamilton *et al.* (2008): percentage values of *MAD*, *MD* and *SD*.

T_s [°C]	G [kg/(m^2 s)]	q [kW/m^2]	*MAD* [%]	*MD* [%]	*SD* [%]
30.3	200	43.9	47	-47	16.1
30.2	400	21.4	32.1	-32.1	7.1
30.2	400	44	40.4	-40.4	7.1
30.1	600	44	39.5	-39.5	8.
40.2	200	21.1	63.6	-63.6	11
39.9	400	21.2	49.8	-49.9	10.9
	All data sets		44.5	-44.5	10.3

4.4 Assessment of the models in enhanced tube

In this section a final assessment of the prediction capability of the models is performed, by comparing the values of *MAD* (mean absolute deviation), *MD* (mean deviation), and *SD* (standard deviation) obtained for refrigerant R134a and R410A. The model by Koyama *et al.* (1995) is not considered because of the high inaccuracy provided both for R134a and R410A.

Figure 4.47 reports the values of *MAD* and *MD* obtained for the entire database collected for R134a: the model by Chamra and Mago (2007) presents the higher accuracy, with a *MAD* of 10.1 % and a *MD* of 7.9 %. Cavallini *et al.* (2006) provides underestimation as compared to Thome *et al.* (1997).

In Figure 4.48 the models are compared only for mass velocity 80 and 100 kg/(m^2 s). When compared at low mass velocity the model by Thome *et al.* (1997) is the more accurate; this can be expected since the validity range of this model is goes from 100 to 500 kg/(m^2 s).

The models are finally compared only at mass velocity from 200 to 600 kg/(m^2 s) in Figure 4.49. At these conditions, the model by Cavallini *et al.* (2006) and by Chamra and Mago (2007) provide the better accuracy. Hamilton *et al.* (2008) also provides a satisfactory prediction capability, with the lowest standard deviation. On the contrary, the accuracy provided Thome *et al.* (1997) significantly degrades.

Figure 4.49 compares the mean absolute deviation and the mean deviation of the models when experimental data of R410A are considered. It is underlined that mass velocity ranges in this case from 200 to 600 kg/(m^2 s). Cavallini *et al.* (2006) is the most acuurate among the models compared here. Thome *et al.* (1999) gives values of *MAD* and *MD* similar to those obtained for R134a at mass velocity between 200 and 600 kg/(m^2 s). A strong degradation of the prediction capability by Hamilton *et al.* (2008) is observed and it may be related to the high reduced pressure of R410A data.

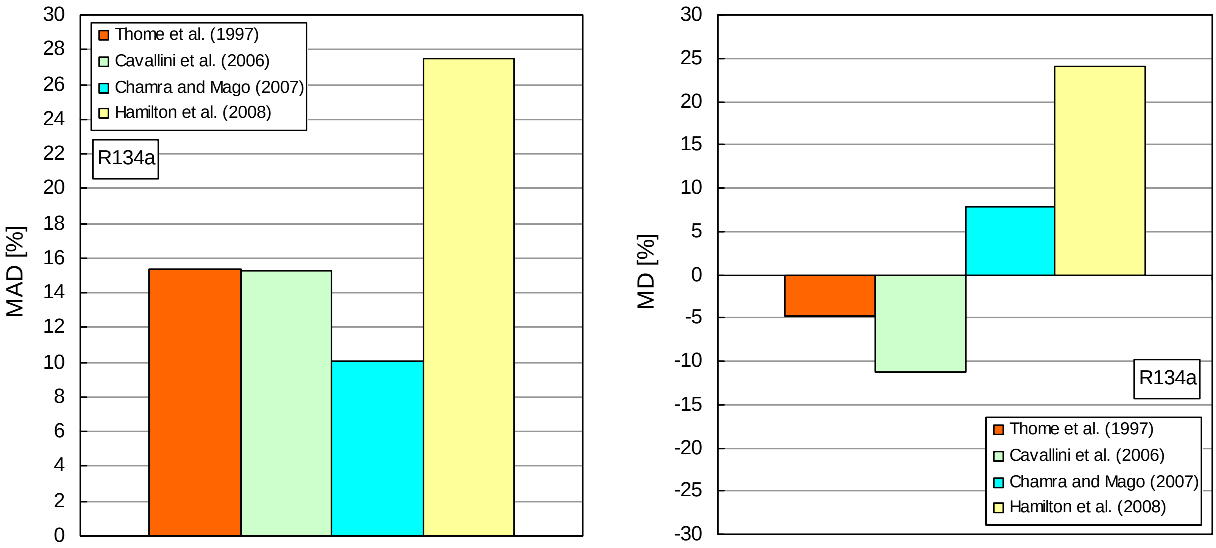

Figure 4.47. Values of *MAD* (mean absolute deviation) and *MD* (mean deviation) for R134a database: models by Thome *et al.* (1997), Cavallini *et al.* (2006), Chamra and Mago (2007) and Hamilton *et al.* (2008).

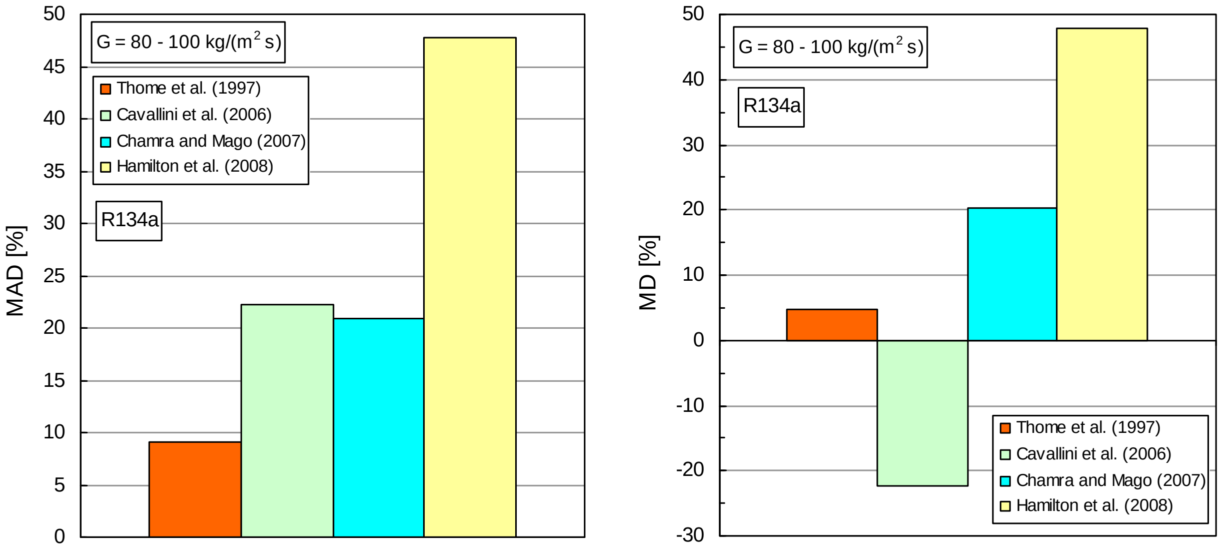

Figure 4.48. Values of *MAD* (mean absolute deviation) and *MD* (mean deviation) for R134a data at mass velocity 80 and 100 kg/(m^2 s): models by Thome *et al.* (1997), Cavallini *et al.* (2006), Chamra and Mago (2007) and Hamilton *et al.* (2008).

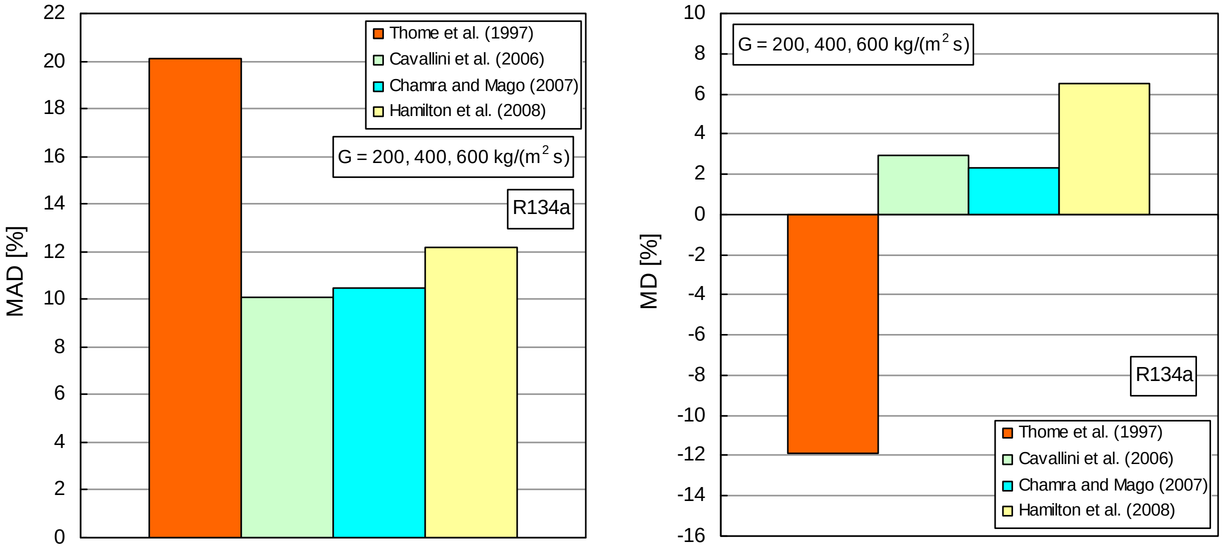

Figure 4.49. Values of *MAD* (mean absolute deviation) and *MD* (mean deviation) for R134a data at mass velocity from 200 to 600 kg/(m^2 s): models by Thome *et al.* (1997), Cavallini *et al.* (2006), Chamra and Mago (2007) and Hamilton *et al.* (2008).

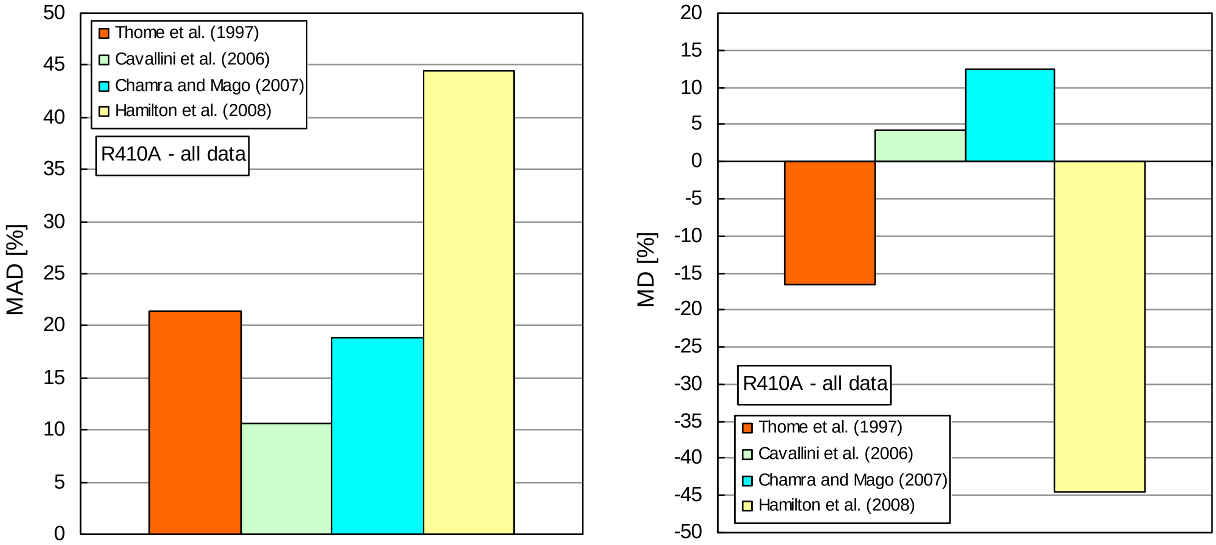

Figure 4.50. Values of *MAD* (mean absolute deviation) and *MD* (mean deviation) for R410A database: models by Thome *et al.* (1997), Cavallini *et al.* (2006), Chamra and Mago (2007) and Hamilton *et al.* (2008).

CHAPTER 5

COMPARISON WITH HEAT TRANSFER DATA IN SMOOTH TUBE

5.1 Introduction to heat transfer data in smooth tube

Heat transfer data for R134a and R410A during flow boiling inside a horizontal smooth tube at high saturation temperature are here discussed and used to perform a comparison with the experimental heat transfer coefficients measured for the microfin tube. Heat transfer coefficients in plain tube was measured in the same experimental apparatus, used for tests in microfin tube. Thus, only a brief description of the smooth tube test section and of the reduction of the heat transfer coefficient is given in the following.

The test section, reported in Figure 5.1, consists of a counter flow tube in tube heat exchanger, in which the refrigerant flowing inside the tube is heated and vaporized by hot water flowing in the annulus side. The test section is divided into two different parts: a pre-conditioning section around 300 mm long, where the refrigerant flow, under vaporization, achieves a fully developed flow regime, and the measuring section, around 1 m long, in which the heat transfer coefficient is measured. This structure is obtained using a single 1.6 m long inner tube and two separate heating water jackets, connected in series on the water side. The inner tube, which is the test tube, is a commercial plain copper tube, with 8 mm inside diameter. It is instrumented with eight copper-constantan (type T) thermocouples embedded in its wall to measure the surface temperature. The thermocouples are inserted and soldered into four equidistant axial grooves. Four thermocouples are located 100 mm past the inlet of the measuring section. The other four thermocouples are located 100 mm before the outlet.

The water temperature change in the test tube is measured by a four junction copper-constantan thermopile inserted into appropriate mixing chambers, where thermocouples are also introduced to measure the water temperature. A metal helix is wound around the test tube inside the annulus, in order to avoid stratification in the water flow and to get high heat transfer coefficient on the water side, together with appropriate values for the water temperature decrease.

Two digital strain gauge pressure transducers (absolute and differential transducers) are connected to manometric taps to measure the vapour pressure upstream and downstream of the test tube. Refrigerant temperatures at inlet and outlet of the test section are measured by means of adiabatic sections, with thermocouples inserted into both the refrigerant flow and the tube wall.

The heat flow rate transferred in the test tube is derived from an enthalpy balance on the heating water side. The average heat transfer coefficient is obtained from the equation:

$$\frac{Q}{A} = \alpha \frac{\left(T_{w1} - T_{w2}\right)}{\ln\left(\dfrac{T_{w1} - T_s}{T_{w2} - T_s}\right)} \tag{5.1}$$

where Q is the heat flow rate exchanged in the tube, A is the heat transfer surface area, T_s is the mean saturation temperature, T_{w1} and T_{w2} are the wall temperatures at inlet and outlet. Experimental heat transfer coefficients are reduced from the measured values of saturation temperature and wall temperature. The saturation temperature is obtained from the pressure and it is compared to the refrigerant temperature directly measured in the adiabatic sections before and after the test section. When saturated refrigerant flows in the tube, saturation temperature determined from the pressure and directly measured refrigerant temperature was compared. For pure fluid R134a, the two values differed by less than 0.1 °C at high mass velocity. Higher deviation occurred at low vapour quality, and are probably due to non-equilibrium in the flow and local sub-cooling at the inlet of the test section.

Experimental data of heat transfer coefficient measured for R134a and R410A are reported here. On the whole, five data sets for R134a and two data sets for R410A are considered. For each data set, the average operative conditions range are reported in Table 5.1.

For both R134a and R410A data, the average experimental uncertainty of the heat transfer coefficient, at 95 % confidence level, is around 6.5 %, while the experimental uncertainty of vapour quality is around ± 0.01.

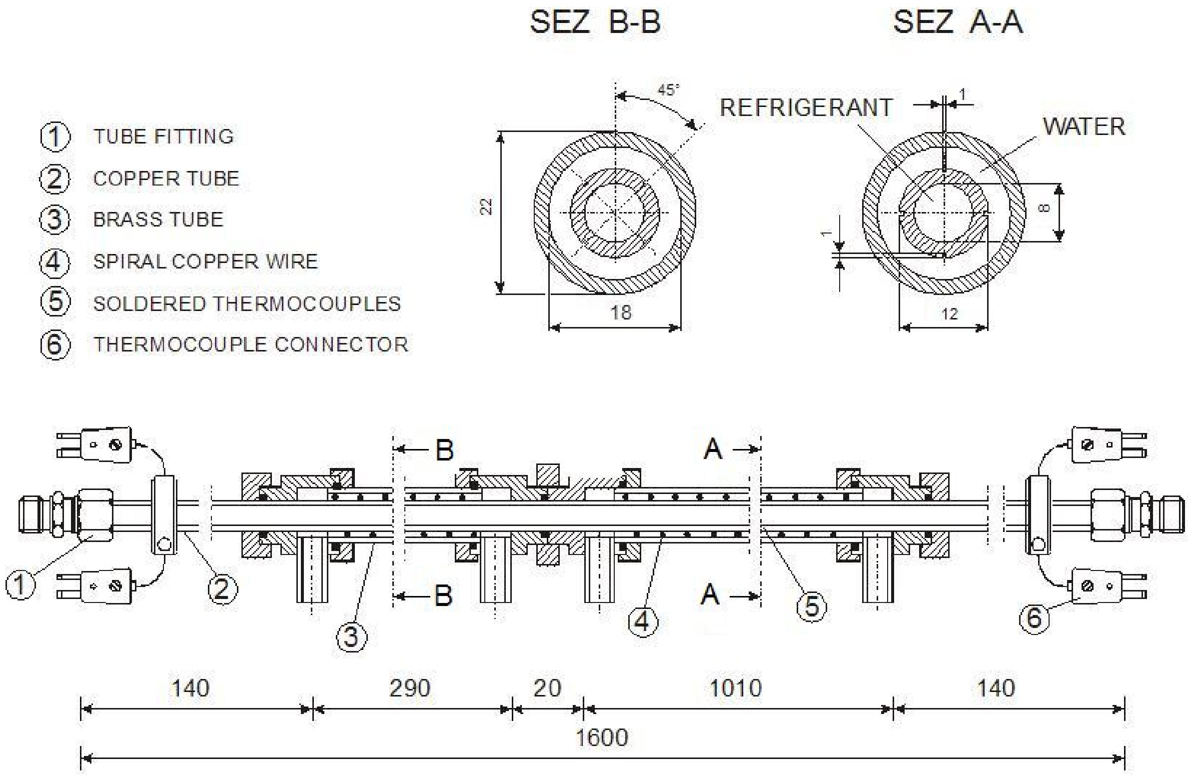

Figure 5.1. Experimental test section in smooth tube.

Table 5.1. Experimental data sets in smooth tube

	T_s [°C]	p_r	x	G [kg/(m^2 s)]	q [kW/m^2]
R134a	43	0.271	0.11 – 0.84	400	26.6
R134a	45	0.286	0.18 – 0.80	200	13.7
R134a	44	0.278	0.07 – 0.30	400	13.7
R134a	43	0.271	0.11 – 0.58	600	30
R134a	31	0.198	0.08 – 0.87	400	28.6
R410A	42	0.518	0.12 – 0.83	400	24
R410A	40	0.494	0.19 – 0.95	200	15

5.2 Experimental heat transfer coefficients in smooth tube

Experimental heat transfer coefficients for R134a are plotted in Figure 5.2 and 5.3 as a function of vapour quality.

Data at saturation temperature between 43 and 45 °C are reported and compared in Figure 5.2. The heat transfer coefficient is approximately constant up to 0.6 vapour quality, no matter what the mass velocity and heat flux conditions are. Recently experimental data of R134a at saturation temperature from 5 °C to 20 °C have been reported by Silva Lima *et al.* (2009). In their work the trend of experimental heat transfer coefficient versus vapour quality becomes more flat when saturation temperature increases.

For the test runs performed at 400 kg/(m^2 s) and 26.6 kW/m^2 average heat flux, the heat transfer coefficient shows an abrupt decreases at 0.85 vapour quality, due to the dry-out of the liquid film at the wall.

The strong effect of heat flux on the heat transfer coefficient is evidenced by comparing data sets at same mass velocity but different heat flux.

In the test runs at G 200 - q 13.7 and G 400 - q 26.6 there is a local minimum, since the heat transfer coefficient decreases at low values of vapour quality and then increases with vapour quality. The presence of this minimum is the result of the competition between nucleate and convective boiling mechanisms and was also noted by Silva Lima *et al.* (2009). As vapour quality increases the flow pattern is expected to be annular type, the liquid film thickness decreases and the vapour velocity increases. Both phenomena promote heat transfer increase.

By comparing the R134a test runs at 400 and 600 kg/(m^2 s), which have been performed at similar values of heat flux, one can see that heat transfer coefficients increase with mass velocity and the heat transfer coefficient increase, due to mass velocity, depends on the vapour quality, showing a stronger effect of the convective mechanism at higher mass velocity.

In Figure 5.3 heat transfer coefficients at similar values of mass velocity and heat flux but different saturation temperature are compared. At vapour quality lower than around 0.4, heat transfer coefficients at 43 °C saturation temperature are higher than heat transfer coefficients at 31.5 °C saturation temperature. This is due to the higher nucleate boiling contribution which occurs at higher reduced pressure. At higher quality values, the heat transfer coefficients at 43 °C and at 31.5 °C merge together regardless of saturation temperature.

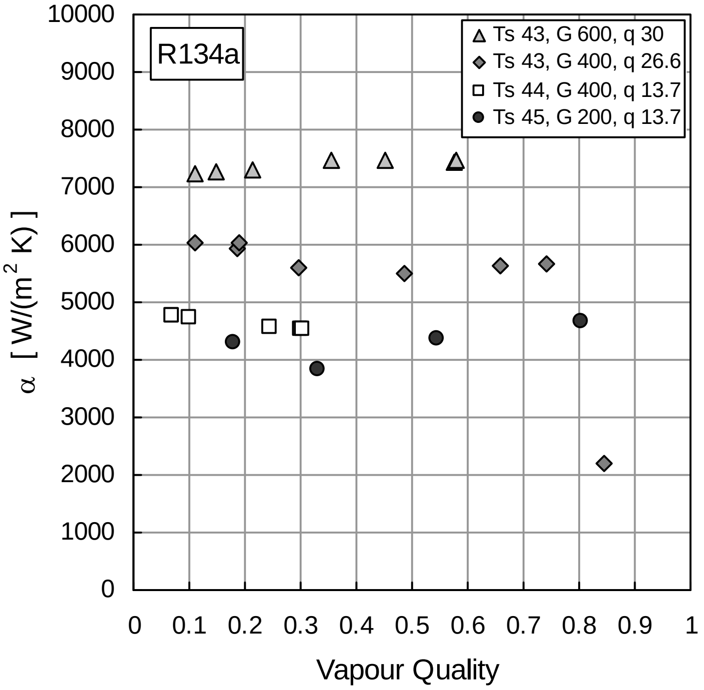

Figure 5.2. Heat transfer coefficient vs. vapour quality for R134a in smooth tube. Saturation temperature varies from 43 to 45 °C, mass velocity is 200, 400, 600 kg/(m^2 s) and heat flux is between 13.7 and 30 kW/m^2.

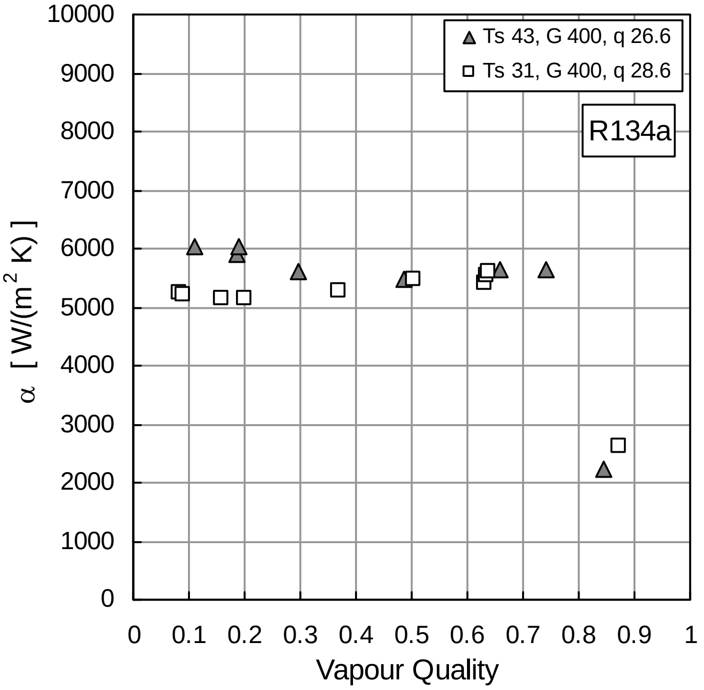

Figure 5.3. Heat transfer coefficient vs. vapour quality for R134a in smooth tube. Saturation temperature is 31.5 and 43 °C, mass velocity is 400 kg/(m^2 s) and the heat flux is 28.6 and 26.6 kW/m^2.

Data of heat transfer coefficient for R410A at around 40 °C saturation temperature are reported in Figure 5.4; the results refer to two values of mass velocity and heat flux. As compared to R134a data, the experimental heat transfer coefficient diminishes when vapour quality increases, for the entire range. This trend is not usual for halogenated refrigerants, where an increase of the heat transfer with vapour quality is usually expected. Nevertheless, this trend is similar to what one measured for high pressure fluid carbon dioxide, reported for instance by Yun *et al.* (2003) and Oh *et al.* (2008). Both the papers have shown that the effect of mass velocity on the heat transfer coefficient of carbon dioxide is negligible at low vapour quality, up to 0.4, while the heat transfer if heat flux dependent, suggesting that the nucleate boiling mechanism is dominant in this region. For carbon dioxide, the drop in heat transfer coefficient is due to the large dominance of nucleate boiling at low vapour qualities and to partial dry-out of the liquid film. The dominance of nucleate boiling at low qualities is caused by the thermo-physical properties of the fluid, such as a low surface tension and a low liquid to vapour density ratio. The effect of thermodynamics and thermo-physical properties on heat transfer mechanisms has been discussed in detail in section 1.2.

The difference on heat transfer coefficient between the two test runs observed in Figure 5.4 is manly due to the different heat fluxes at low vapour quality, while at higher vapour quality both heat flux and mass flux may play a role since the rise of mass velocity provides an enhancement of convective evaporation.

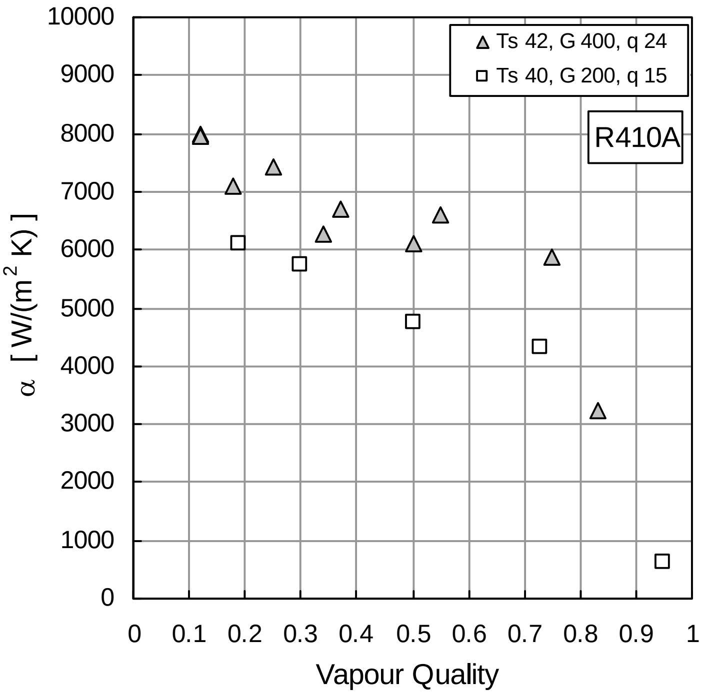

Figure 5.4. Heat transfer coefficient vs. vapour quality for R410A in smooth tube. The saturation temperature is 40 and 42 °C, the mass velocity is 200 and 400 kg/(m^2 s) and the heat flux is 24 and 15 kW/m^2.

5.3 Comparison of heat transfer coefficients in smooth tube with predictive models

Four well known models have been chosen for comparison with data in plain tube. They are the models by Gungor and Winterton (1987), Kandlikar (1991), Liu and Winterton (1991) and Wojtan *et al.* (2005b). These models have been presented in section 1.4.1. In the correlation by Kandlikar a value of the fluid parameter equal to 1.63 is adopted for R134a, while a value of 3.3 is used in the case of R410A as suggested by Wattelet *et al.* (1994). The comparison have been performed for all the data points presented in section 5.2, excluding the tests with dry-out and mist flow regimes for which those methods, except the one by Wojtan *et al.* (2005b), can not be applied. On the whole, 34 experimental data for R134a and 13 data for R410A has been used in the comparison. Table 5.2 reports the mean absolute deviation, the mean deviation and the standard deviation obtained from the comparison between experimental and calculated heat transfer coefficients for R134a and R410A data sets.

The model by Gungor and Winterton (1987) underestimates the experimental data both for R134a and R410A. In Figure 5.6 the ratio between the heat transfer coefficient calculated by Gungor and Winterton (1987) and the experimental value is plotted as a function of vapour quality. The prediction capability is not affected by any parameter (vapour quality, mass velocity, heat flux, reduced pressure), as suggested by the low value of standard deviation obtained for both data sets. On the average the underprediction is around 20 %.

The Kandlikar correlation (1991) predicts most of experimental data within ±30 % with a low mean deviation, but it is not able to catch the trend of experimental heat transfer coefficient versus vapour quality, as it can be observed in Figure 5.7. A high value of standard deviation is found both for R134a and R410A.

In Figure 5.9 the heat transfer coefficient calculated by Liu and Winterton (1991) model is plotted against the experimental heat transfer coefficient; the model provides a better accuracy for R134 than for R410A. However, for R410A, it does not reproduce the trend of the experimental heat transfer coefficient versus vapour quality and the standard deviation is quite high.

By comparing Figure 5.9 and Figure 5.11, Wojtan *et al.* (2005b) shows a similar behaviour as the Liu and Winterton (1991) correlation; but, a greater dependence of the prediction capability on vapour quality is observed in Figure 5.12 both for R134a and R410A, whereas it is a flow pattern based method.

Table 5.2. Comparison between experimental data and models: percentage values of *MAD, MD, SD*.

	R134a			R410A		
	MAD [%]	*MD* [%]	*SD* [%]	*MAD* [%]	*MD* [%]	*SD* [%]
Gungor and Winterton (1987)	21.2	-21.2	10.5	19.2	-19.2	9.6
Kandlikar (1991)	14.7	-4.4	18.7	24.8	18.4	23.8
Liu and Winterton (1991)	14.2	-14	9	18.6	16.3	16.6
Wojtan *et al.* (2005b)	16.4	-12.3	14	21.6	20.9	18

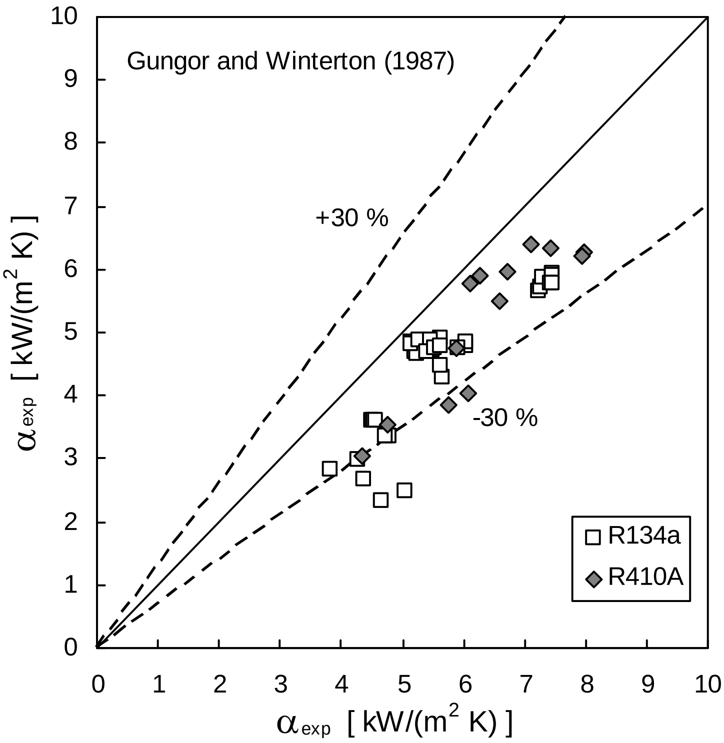

Figure 5.5. Calculated vs. experimental heat transfer coefficient. The calculated coefficients are obtained by Gungor and Winterton (1987). The ±30 % error lines are reported.

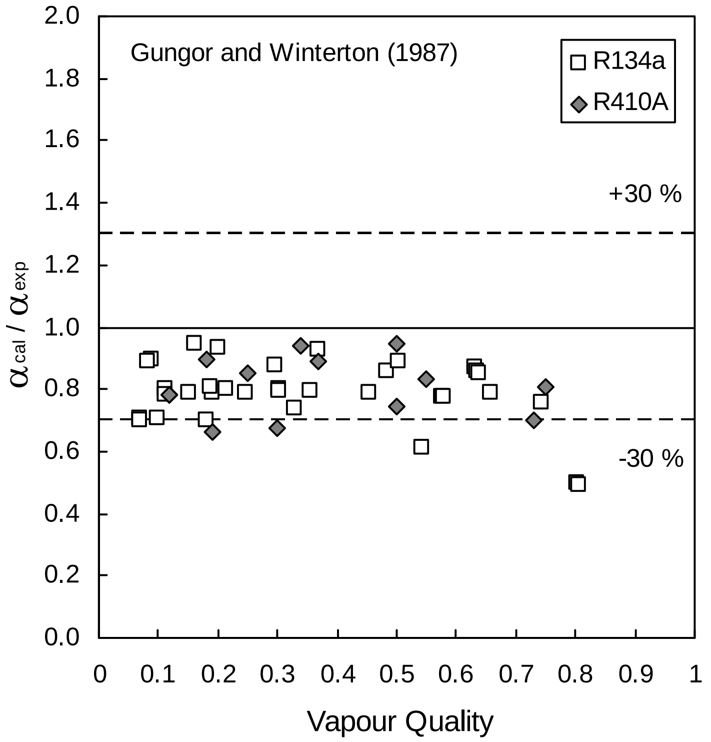

Figure 5.6. Ratio between calculated and experimental heat transfer coefficient vs. vapour quality. The calculated values are obtained by Gungor and Winterton (1987). The ±30 % error lines are reported.

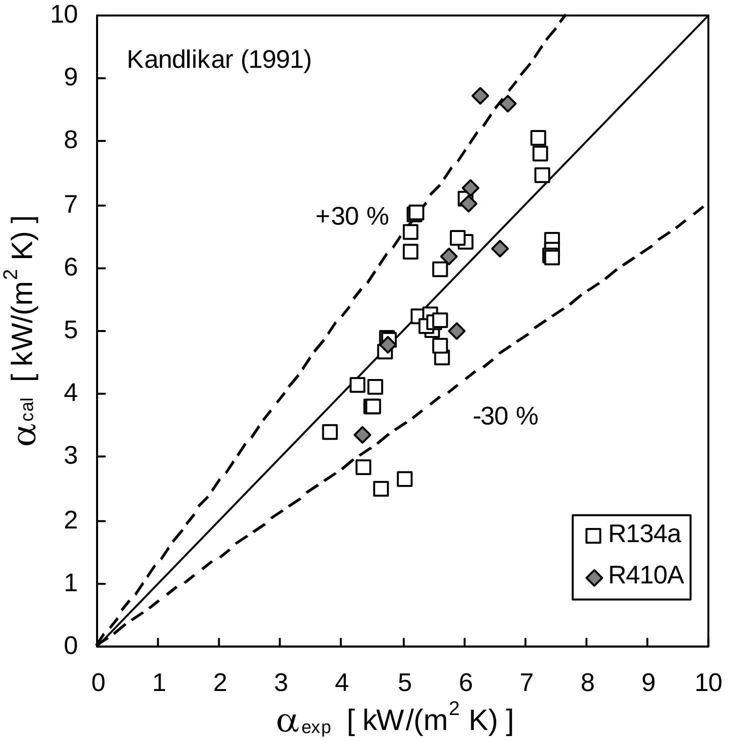

Figure 5.7. Calculated vs. experimental heat transfer coefficient. The calculated coefficients are obtained by Kandlikar (1991). The ±30 % error lines are reported.

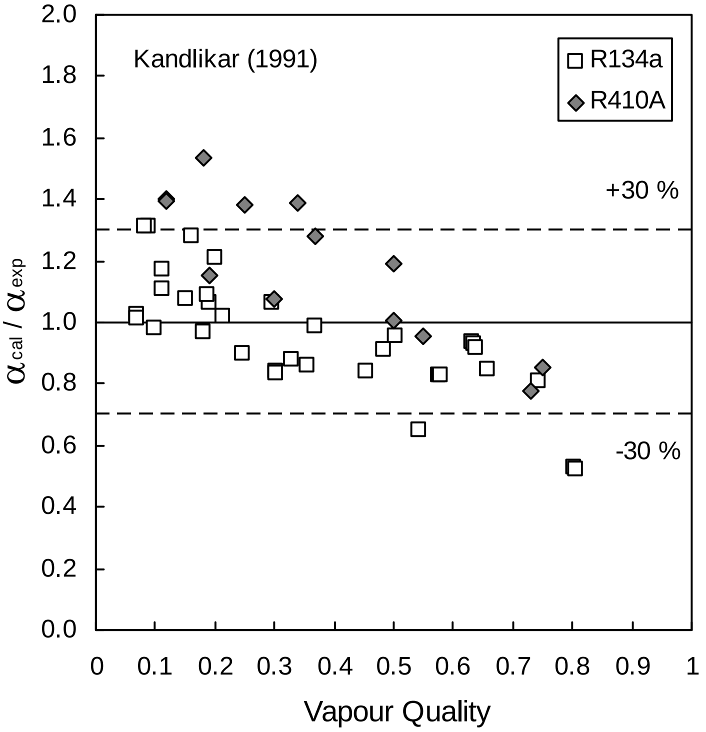

Figure 5.8. Ratio between calculated and experimental heat transfer coefficient vs. vapour quality. The calculated values are obtained by Kandlikar (1991). The ±30 % error lines are reported.

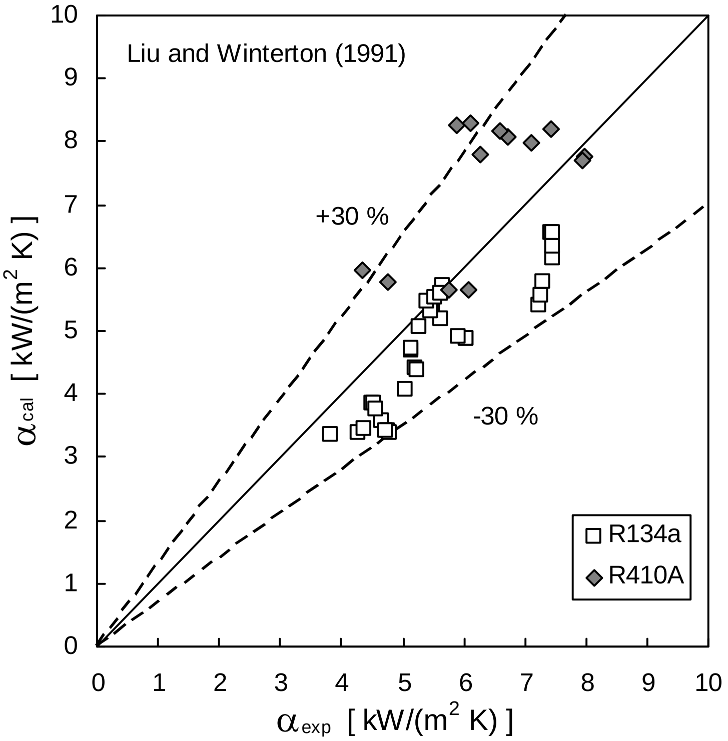

Figure 5.9. Calculated vs. experimental heat transfer coefficient. The calculated coefficients are obtained by Liu and Winterton (1991). The ±30 % error lines are reported.

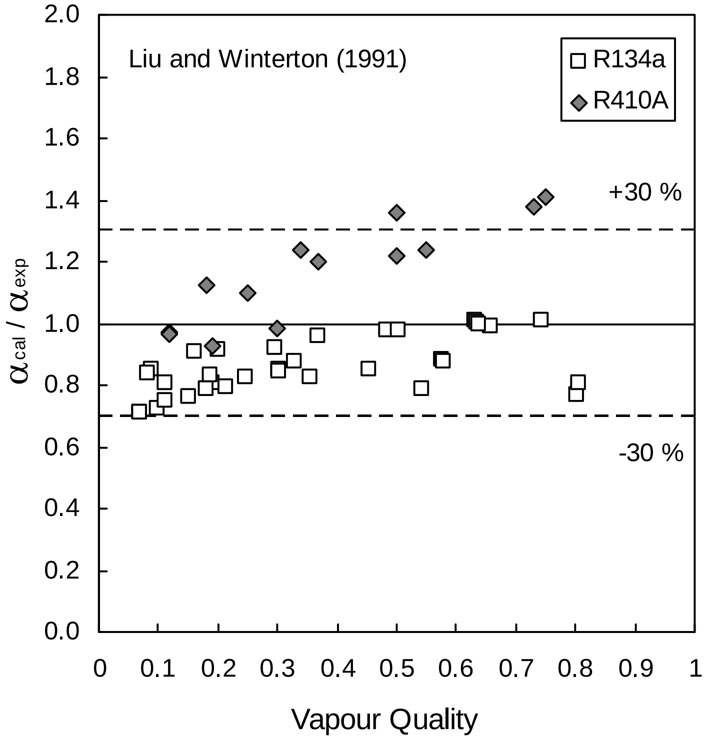

Figure 5.10. Ratio between calculated and experimental heat transfer coefficient vs. vapour quality. The calculated values are obtained by Liu and Winterton (1991). The ±30 % error lines are reported.

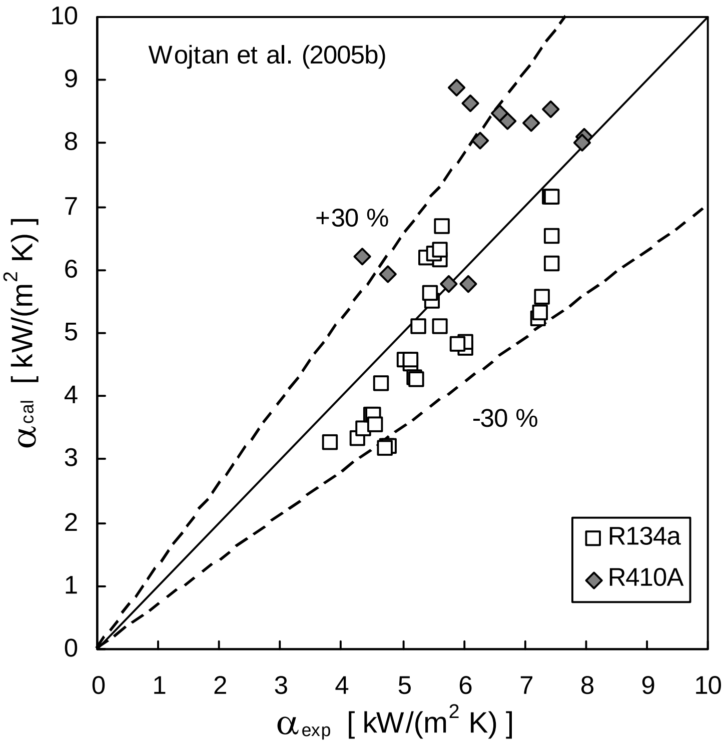

Figure 5.11. Ratio between calculated and experimental heat transfer coefficient vs. vapour quality. The calculated values are obtained by Wojtan *et al.* (2005b). The ±30 % error lines are reported.

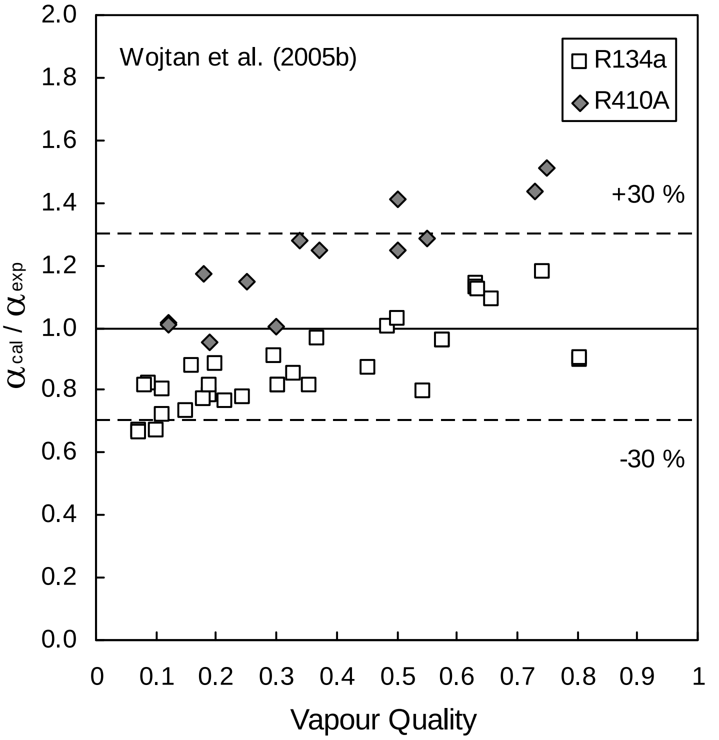

Figure 5.12. Ratio between calculated and experimental heat transfer coefficient vs. vapour quality. The calculated values are obtained by Wojtan *et al.* (2005b). The ±30 % error lines are reported.

5.4 Comparison between heat transfer coefficients in microfin and smooth tube

The heat transfer coefficients for R134a measured in microfin tube are compared with the heat transfer coefficients in smooth tube in Figure 5.13 and 5.14. When comparing data at around 30 °C saturation temperature, 400 kg/(m^2 s) mass velocity and 28.5 kW/m^2 heat flux, the heat transfer coefficients in microfin and smooth tube show the same trend up to 0.6 vapour quality and the heat transfer coefficient in microfin tube is about 2 times the coefficient in smooth tube. It should be noted that the enhancement in heat transfer area is equal to 1.8 as compared to the surface area of a plain tube of inside diameter equal to the diameter at fin tip. When vapour quality is around 0.8, dry-out occurs in the case of the plain tube; on the contrary the heat transfer coefficient in microfin tube abruptly increases and dry-out occurs at much higher vapour quality, as reported in Figure 5.13.

Data at saturation temperature around 40 °C, 200 kg/(m^2 s) mass velocity and around 14 kW/m^2 heat flux are plotted as a function of vapour quality in Figure 5.14. The heat transfer coefficient in microfin tube continuously increases with vapour quality; this behaviour is different from smooth tube data, where a quite flat trend versus vapour quality is observed, due to the competition between nucleate boiling and convective mechanisms. Besides, the presence of the fins should be enlarge the region of annular regime at lower vapour quality and this probably influences the role of the heat transfer mechanisms and the trend of heat transfer coefficient. When vapour quality is around 0.2, the heat transfer coefficient in microfin tube is about 2.3 times higher as compared to the plain tube, but at vapour quality around 0.8 the heat transfer coefficient in microfin tube is 2.7 times the coefficient in smooth tube.

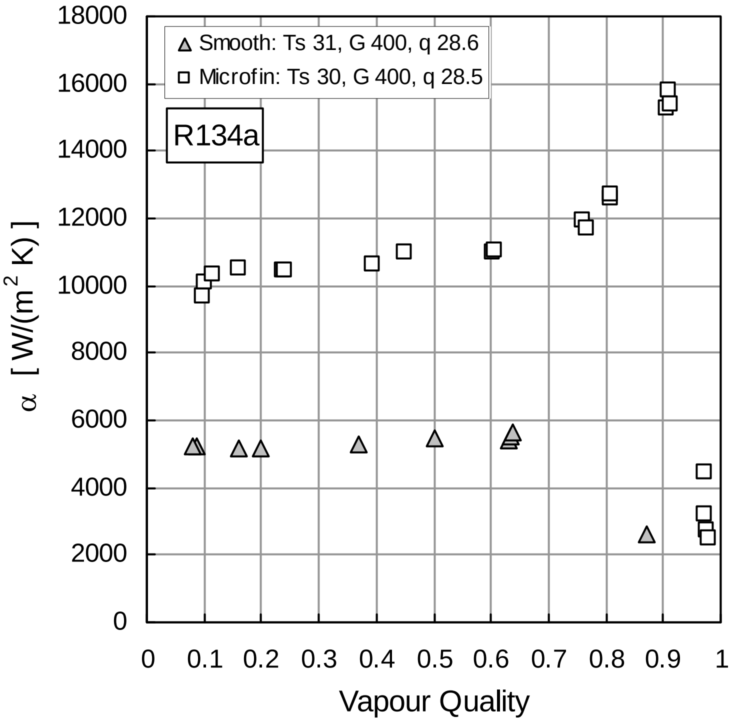

Figure 5.13. Heat transfer coefficient vs. vapour quality: comparison between R134a data in microfin and smooth tube. Saturation temperature is 30 °C, mass velocity is 400 kg/(m^2 s) and heat flux is around 28.5 kW/m^2.

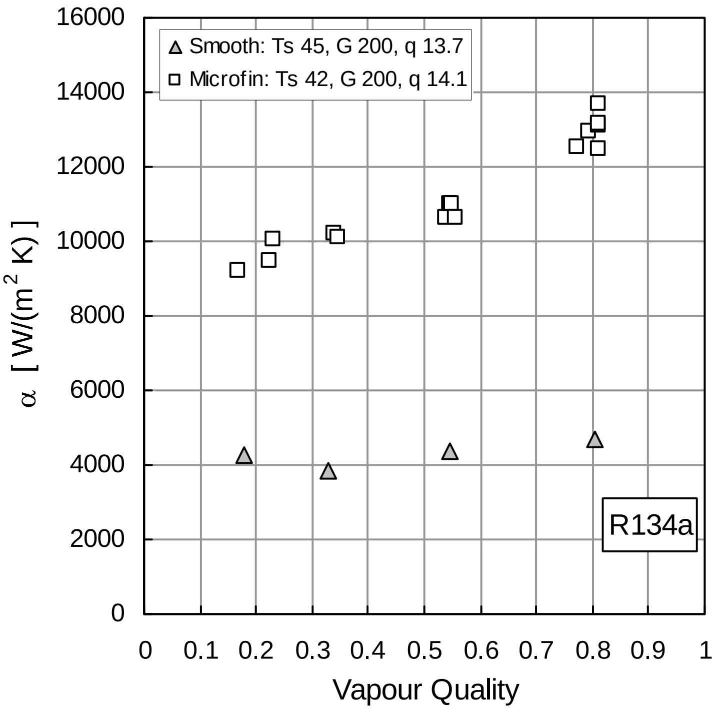

Figure 5.14. Heat transfer coefficient vs. vapour quality: comparison between R134a data in microfin and smooth tube. Saturation temperature is 42 °C and 45 °C, mass velocity is 200 kg/(m^2 s) and heat flux is around 14 kW/m^2.

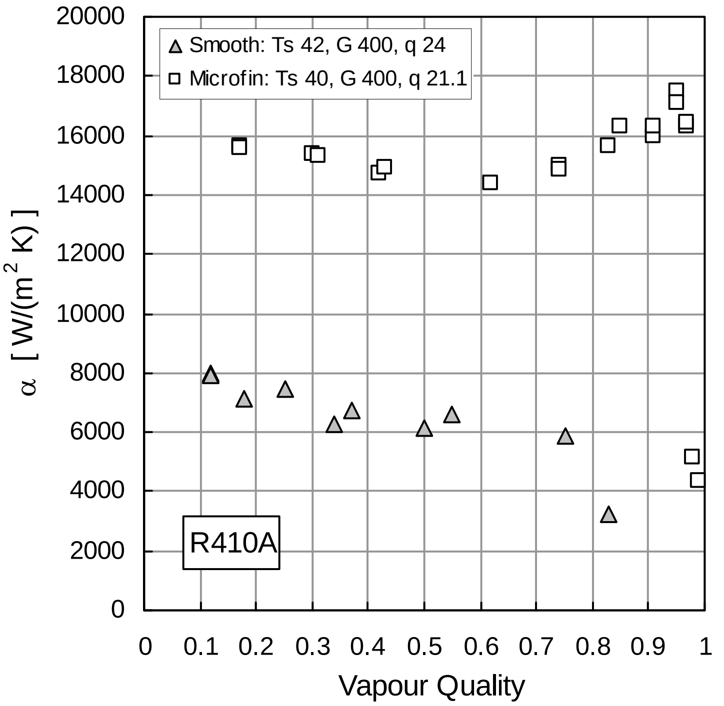

Figure 5.15. Heat transfer coefficient vs. vapour quality: comparison between R410A data in microfin and smooth tube. Saturation temperature is 40 °C and 42 °C, mass velocity is 400 kg/(m^2 s) and heat flux is around 21.1 and 24 kW/m^2.

Heat transfer coefficients in microfin and smooth tube are compared for R410A at saturation temperature around 40 °C, mass velocity 400 kg/(m^2 s) and heat flux around 28.5 kW/m^2 (Figure 5.15). For vapour quality up to 0.5, the heat transfer coefficient decreases as vapour quality increases both for the microfin and the smooth tube. At around 0.5 vapour quality, a local minimum for the heat transfer coefficient is observed in the case of the microfin tube; after this minimum the heat transfer coefficient increases with vapour quality up to the inception of dry-out. On the contrary, the hat transfer coefficient in smooth tube continues to diminish. Due to the high reduced pressure, the process may be nucleate boiling dominated in the low quality region; but, as vapour quality increases partial dry-out occurs in the smooth tube, while the convective mechanism takes place in the microfin tube and yields the increase of heat transfer coefficient with vapour quality. On the whole, the heat transfer coefficient in microfin tube is about two times higher as compared to the one in smooth tube.

CHAPTER 6

DISCUSSION ON TWO-PHASE FLOW PATTERN DURING FLOW BOILING AND PREDICTION OF DRY-OUT

6.1 Comparison of flow boiling data in smooth tube with Wojtan *et al.* (2005a) diabatic two-phase flow pattern map

The development of two-phase flow pattern maps is a key aspect to improve the understanding of the role of heat transfer mechanisms during in-tube flow boiling.

Kattan *et al.* (1998) first presented a diabatic two-phase flow pattern map in coordinates mass velocity versus vapour quality for refrigerants under evaporating conditions in horizontal plain tubes. The map was developed from a database of five different fluids (R134a, R123, R402A, R404A and R502), covering a wide range of mass velocities and vapour qualities.

Thome and El Hajal (2002) upgraded the Kattan *et al.* (1998) map, by observing as mass velocity influenced the position of the transition curves between flow regimes. In particular the strongest effect of mass velocity was observed for the transition from stratified-wavy to intermittent flow, for vapour quality below 0.1, where the transition curve goes up with increasing mass velocity; this divergence becomes less significant as vapour quality increases. Wojtan *et al.* (2005a) introduced several important modifications to the more recent version of the flow pattern map by Kattan *et al.* (1998), based on new measurements of dynamic void fraction. They subdivided the stratified-wavy region into three sub-zones: slug, a mixing of slug and stratified-wavy and stratified-wavy regions. Dynamic void fraction measurements were performed for R22 at mass velocity from 70 to 200 kg/(m^2 s) and for R410A for mass velocity from 70 to 300 kg/(m^2 s). Furthermore, annular to dry-out and dry-out to mist flow transition curves were added and integrated into the new flow pattern map, based on new heat transfer experimental measurements for R22 and R410A under partial dry-out and mist flow conditions. Heat transfer coefficients, obtained at mass velocities from 300 to 700 kg/(m^2 s) and initial heat flux from 7.5 to 57.5 kW/m^2, were used to find the annular to dry-out and dry-out to mist flow transition curves. An example of the new map by Wojtan *et al.* (2005a) is reported in Figure 6.1, for R22 evaporating at 5 °C saturation temperature, 2.1 kW/m^2 heat flux and 100 kg/(m^2 s) mass velocity; the corresponding flow regimes are also reported for each region. The map is built for one value of saturation temperature, heat flux and mass velocity.

Experimental flow boiling data for R134a and R410A in smooth tube at high saturation temperature are here plotted in the diabatic two-phase flow pattern map by Wojtan *et al.* (2005a). For each test run, the experimental heat transfer coefficient against vapour quality is also reported in order to discuss the relationship between the behaviour in heat transfer and the predicted flow pattern. Experimental data under dry-out regime are here reported in the map with a different marker as compared to data before dry-out, in order to check the prediction capability of the dry-out regime.

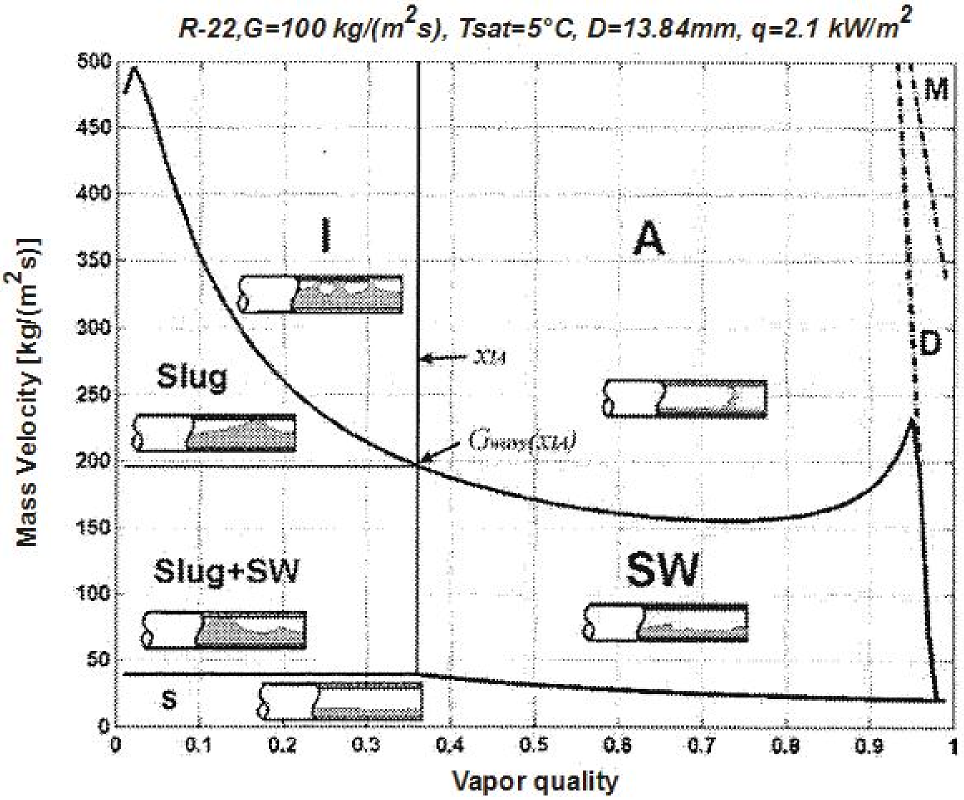

Figure 6.1. Wojtan *et al.* (2005a) diabatic two-phase flow pattern map during flow boiling of R22 inside a horizontal plain tube of diameter 13.84 mm. Saturation temperature is 5 °C, mass velocity is 100 kg/(m^2 s) and heat flux is 2.1 kW/m^2. Source: Wojtan *et al.* (2005a).

In Figure 6.2 flow boiling data for R134a in smooth tube at around 30 °C saturation temperature, 400 kg/(m^2 s) mass velocity and 29 kW/m^2 heat flux are plotted in the map by Wojtan *et al.* (2005a). For this condition, the heat transfer coefficient as a function of vapour quality is plotted in Figure 6.3. When vapour quality is below 0.4, the trend of heat transfer coefficient versus vapour quality is first slightly decreasing up to 0.2 vapour quality and then increasing; intermittent flow regime is predicted by Wojtan *et al.* (2005a) map. When vapour quality increases above 0.4, the flow pattern changes from intermittent to annular and heat transfer coefficient grows with vapour quality. Dryout is successfully predicted by the map.

In Figure 6.4, R134a data in plain tube at 45 °C saturation temperature, 200 kg/(m^2 s) mass velocity and 13.7 kW/m^2 heat flux are plotted in the flow pattern map. By Figure 6.5, the experimental trend of heat transfer coefficient versus vapour quality presents a local minimum at around 0.3 vapour quality, which corresponds to slug to intermittent transition boundary in the flow pattern map by Wojtan *et al.* (2005a). This is in agreement with the experimental results for R134a in smooth tube by Silva Lima *et al.* (2009), who systematically measured a local minimum of heat transfer coefficient in the slug region or nearby the slug to intermittent transition boundary. Indeed, in their data, the local minimum moves from the slug region to the slug to intermittent transition boundary as saturation temperature is increased from 5 °C to 20 °C.

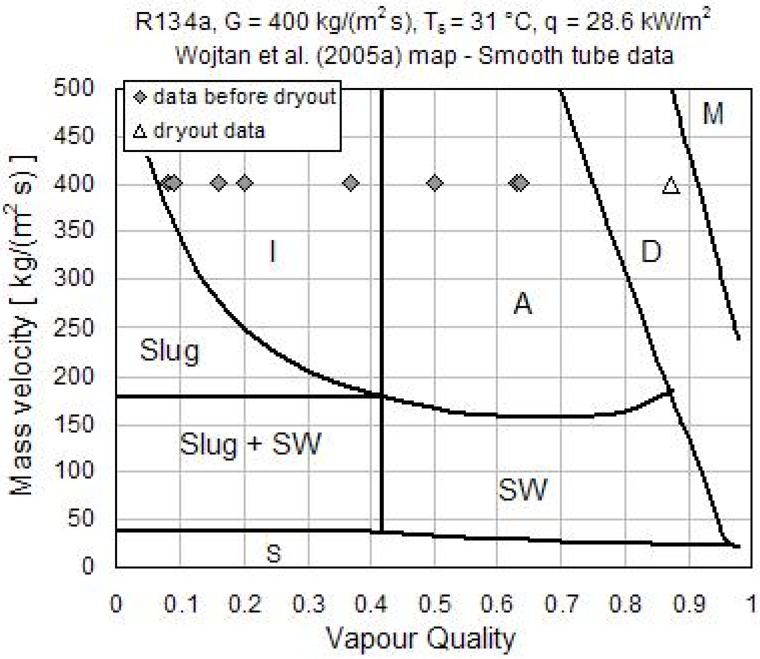

Figure 6.2 Experimental flow boiling data for R134a in smooth tube and flow pattern map by Wojtan *et al.* (2005a). The average saturation temperature is 31 °C, mass velocity is 400 kg/(m^2 s) and the average heat flux is 28.6 kW/m^2. Dryout data are identified by the triangular marker.

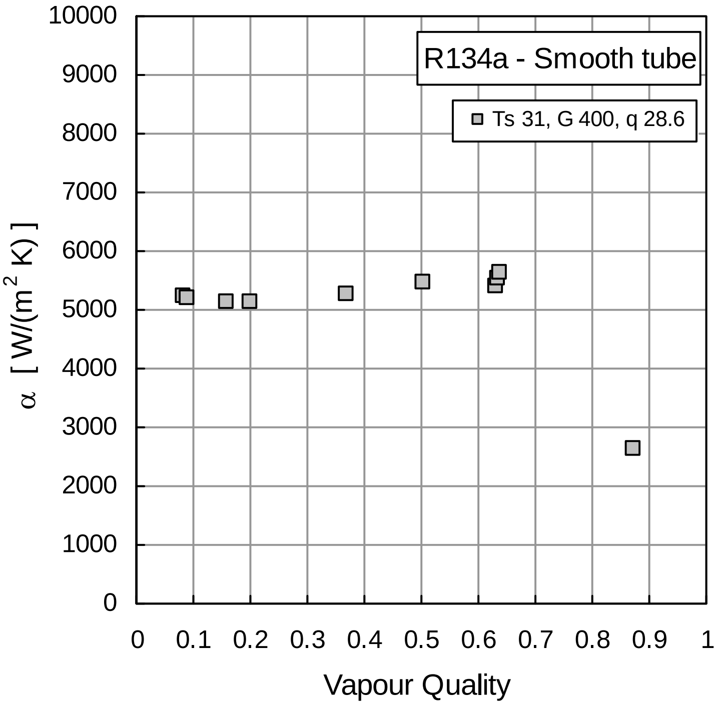

Figure 6.3. Experimental heat transfer coefficient for R134a in smooth tube vs. vapour quality. The average saturation temperature is 31 °C, mass velocity is 400 kg/(m^2 s) and heat flux is 28.6 kW/m^2.

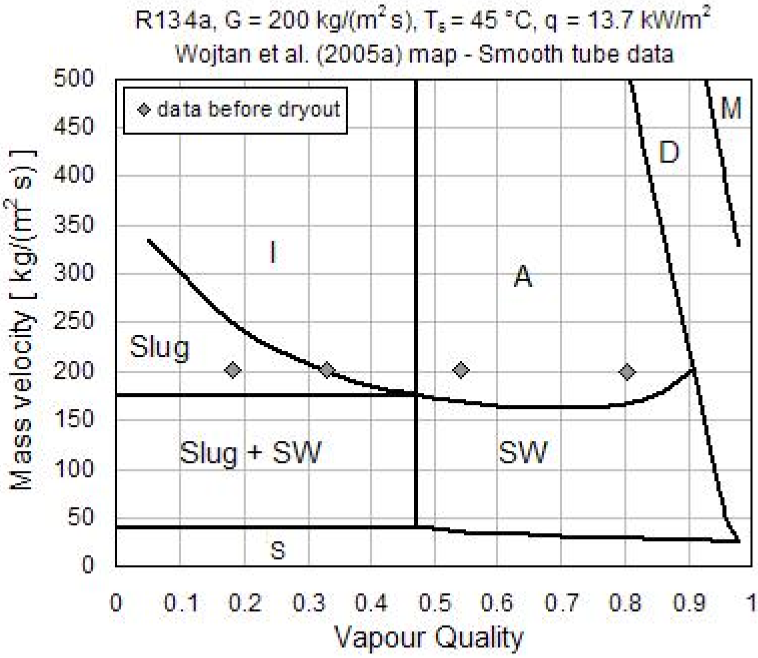

Figure 6.4 Experimental flow boiling data for R134a in smooth and flow pattern map by Wojtan *et al.* (2005a). The average saturation temperature is 45 °C, mass velocity is 200 kg/(m^2 s) and heat flux is 13.7 kW/m^2.

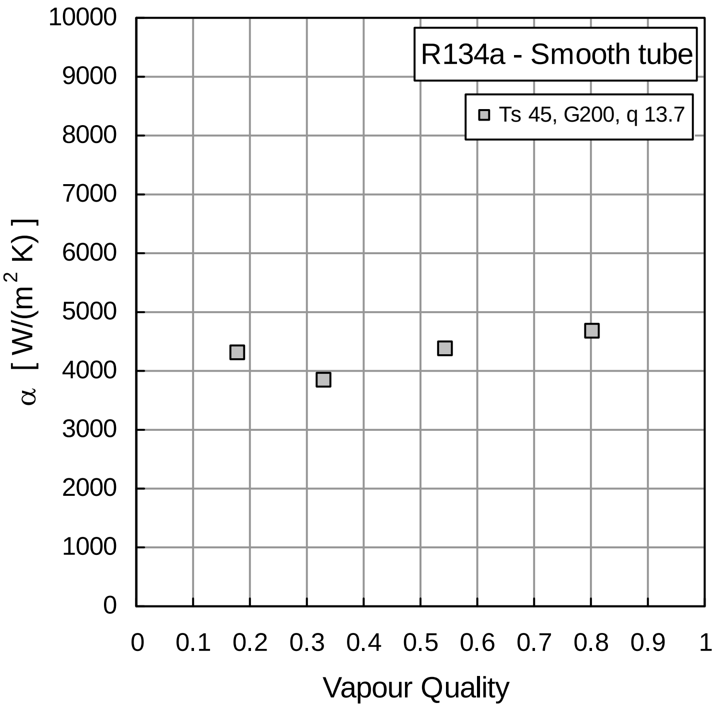

Figure 6.5. Experimental heat transfer coefficient for R134a in smooth tube vs. vapour quality. Saturation temperature is 45 °C, mass velocity is 200 kg/(m^2 s) and heat flux is 13.7 kW/m^2.

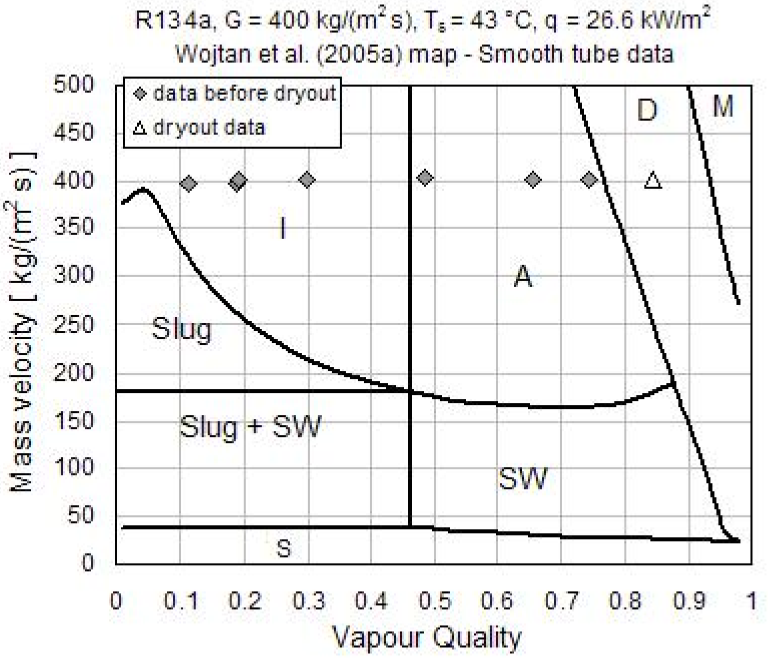

Figure 6.6. Experimental flow boiling data for R134a in smooth tube and flow pattern map by Wojtan *et al.* (2005a). The average saturation temperature is 43 °C, mass velocity is 400 kg/(m^2 s) and the average heat flux is 26.6 kW/m^2. Dryout data are identified by the triangular marker.

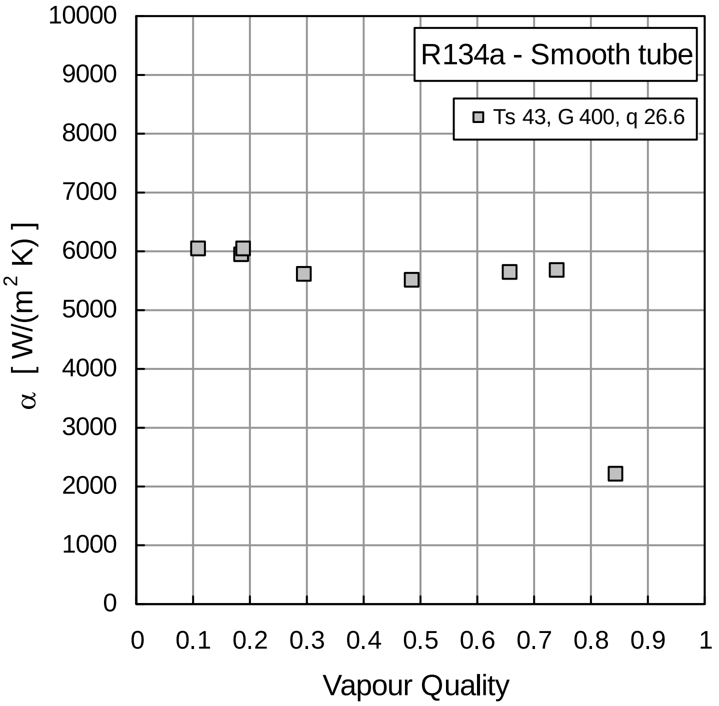

Figure 6.7. Experimental heat transfer coefficient for R134a in smooth vs. vapour quality. Saturation temperature is 43 °C, mass velocity is 400 kg/(m^2 s) and heat flux is 26.6 kW/m^2.

Figure 6.6 reports flow boiling data in smooth tube for R134a at around 43 °C saturation temperature, 400 kg/(m^2 s) mass velocity and 26.7 kW/m^2. The corresponding heat transfer coefficients are plotted as a function of vapour quality in Figure 6.7; the higher heat transfer coefficient occurs at the lower vapour quality, below 0.2, which corresponds to intermittent flow in the map. After 0.2 vapour quality, the heat transfer coefficient first decreases and then slightly increases with vapour quality; transition from intermittent to annular flow pattern is predicted at 0.46 vapour quality. Dryout is successfully estimated by the map, again.

Flow boiling experimental data for R410A inside smooth tube are plotted in the map by Wojtan *et al.* (2005a) in Figure 6.8 and 6.10. Transition boundary from intermittent to annular flow pattern is predicted by the map at 0.56 vapour quality. Thus, most of present experimental data fall within intermittent flow pattern, but this does not seem to be in agreement with the experimental heat transfer results (Figure 6.9 and Figure 6.11). For instance, when flow pattern changes from intermittent to annular, no difference is observed in the trend of heat transfer coefficient against vapour quality.

Some disagreement in the prediction of transition boundary between intermittent to annular flow was observed by Park and Hrnjak (2005), who compared experimental visualizations of flow boiling of R410A and CO_2 at 0.1 and 0.3 reduced pressure (-15 °C saturation temperature), respectively, with the diabatic two-phase flow pattern map by Wojtan *et al.* (2005a). In their work, intermittent flow pattern is predicted by the map, when annular flow is experimentally observed, in particular in the case of carbon dioxide.

It must be also said that data at high reduced pressure as the same as the ones investigated in the present study were not used to develop this map. Moreover, the trend of heat transfer coefficient versus vapour quality, observed here for R410A, was also found by other authors in the case of flow boiling of carbon dioxide inside a plain tube, and this may be attributed to similar thermodynamic and thermo-physical properties.

Sun and Groll (2002) investigated the flow pattern and the heat transfer mechanisms, when carbon dioxide evaporates inside a horizontal tube. By analyzing CO_2 properties, they suggested that annular flow is the predominant flow pattern, except when mass velocity is lower than 200 kg/(m^2 s); consequently annular flow takes place earlier as compared to other refrigerants. As vapour quality increases, the high entrainment mechanism of liquid droplets in the vapour core yields a thinner liquid film in the upper part of the tube, resulting in an incomplete liquid film and early dry-out.

Yun *et al.* (2003) also suggested that, in the case of CO_2, intermittent flow exists at very low vapour quality and the process is nucleate boiling dominated; as vapour quality increases, an unstable annular flow pattern appears due to the liquid droplet entrainment from the liquid film.

Cheng *et al.* (2006) proposed a modification of the diabatic flow pattern map by Wojtan *et al.* (2005) for carbon dioxide; by comparing the modified version with the original map, the transition boundary from intermittent to annular flow and from annular to dry-out regime moves to lower vapour quality, as it can be seen by Figure 6.12.

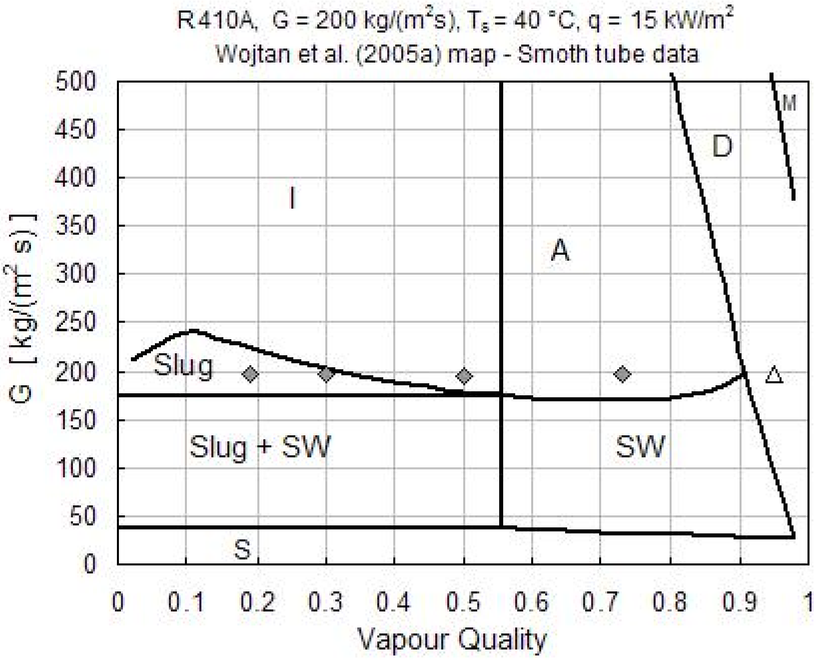

Figure 6.8. Experimental flow boiling data for R410A in smooth tube and flow pattern map by Wojtan *et al.* (2005a). The average saturation temperature is 40 °C, mass velocity is 200 kg/(m^2 s) and heat flux is 15 kW/m^2. Dry-out is identified by the triangular marker.

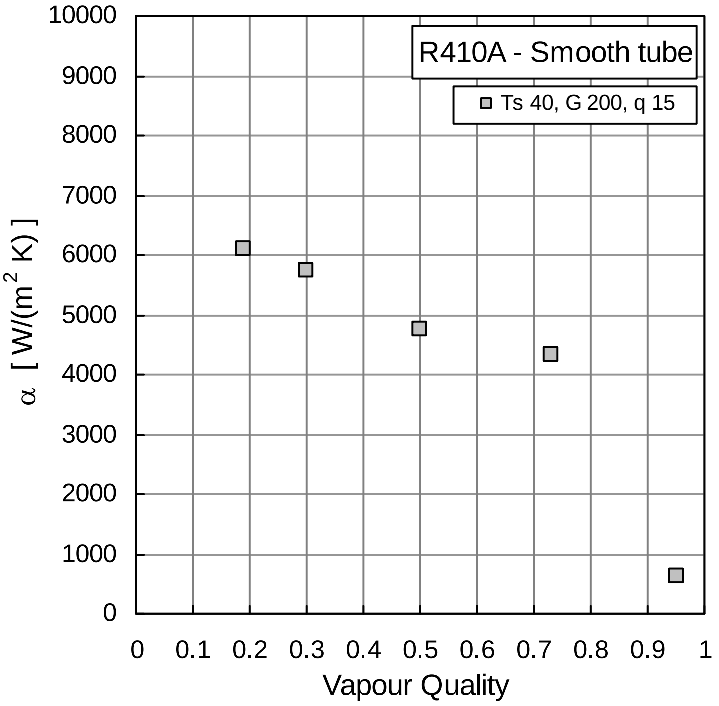

Figure 6.9. Experimental heat transfer coefficient for R410A in smooth tube vs. vapour quality. Saturation temperature is 40 °C, mass velocity is 200 kg/(m^2 s) and heat flux is 15 kW/m^2.

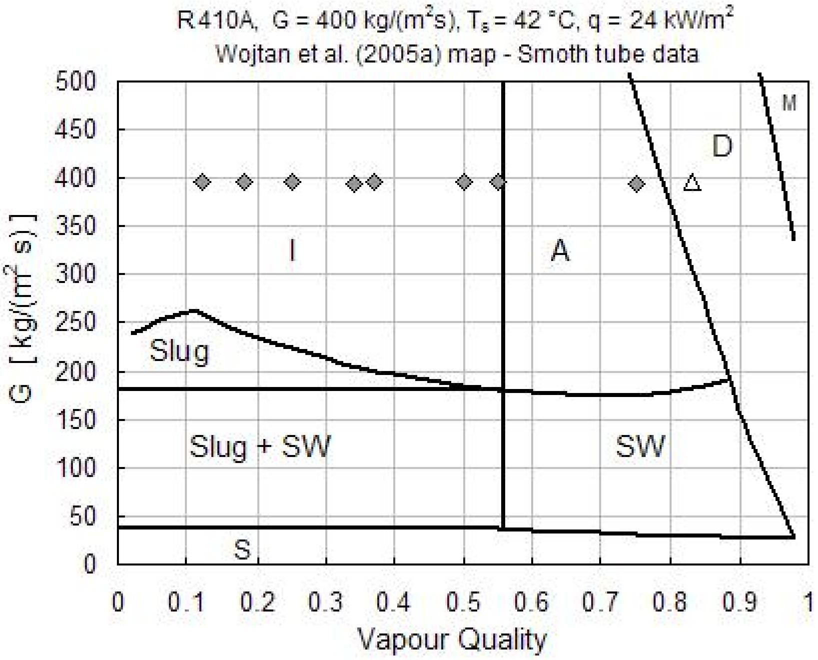

Figure 6.10. Experimental flow boiling data for R410A in smooth tube and flow pattern map by Wojtan *et al.* (2005a). The average saturation temperature is 42 °C, mass velocity is 400 kg/(m^2 s) and the average heat flux is 24 kW/m^2. Dry-out is identified by the triangular marker.

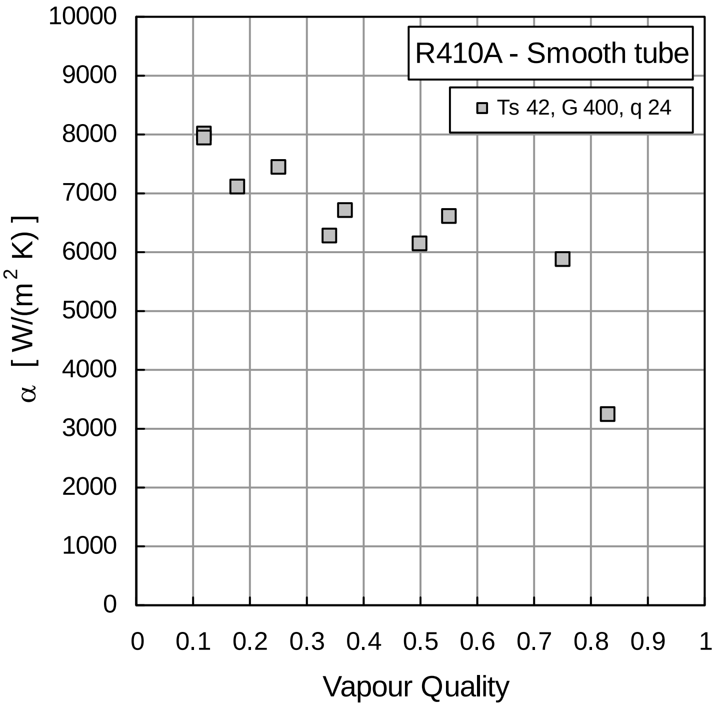

Figure 6.11. Experimental heat transfer coefficient for R410A in smooth tube vs. vapour quality. Saturation temperature is around 42 °C, mass velocity is 400 kg/(m^2 s) and heat flux is 24 kW/m^2.

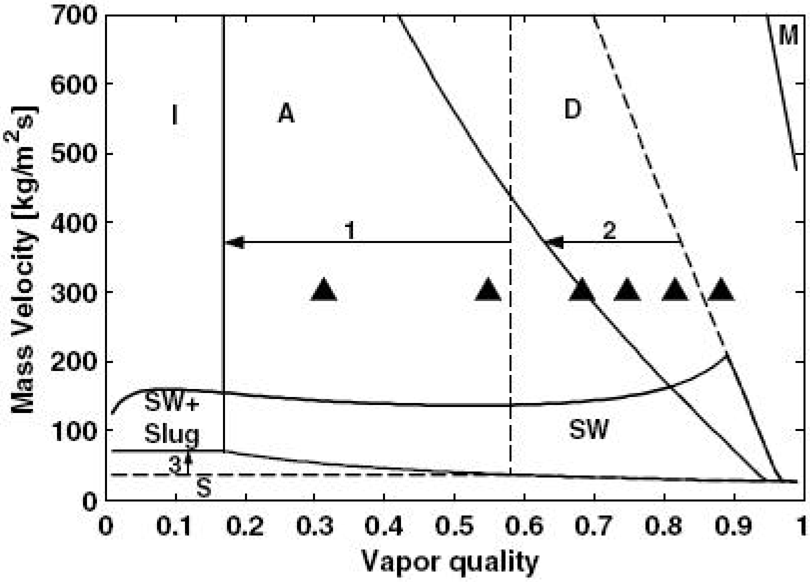

Figure 6.12. Flow pattern transition boundary (solid lines) for CO_2 and flow pattern transition boundaries by Wojtan *et al.* (2005a) compared to CO_2 experimental data by Yun *et al.* (2003). Arrow 1 shows the change of intermittent to annular transition boundary, arrow 2 shows the change of annular to dryout transition boundary and arrow 3 shows the change of slug and stratified-wavy to stratified-wavy transition boundary. Source: Cheng *et al.* (2006)

6.2 Comparison with annular-stratified transition boundary for condensation in microfin tube

The investigation of two-phase flow pattern during flow boiling in a microfin tube can contribute to improve the understanding of the role of heat transfer mechanisms. In the case of a smooth tube, it has been observed as the change in flow pattern yields a change of the behaviour during heat transfer. In a microfin tube, the presence of the fins modifies the two-phase flow pattern and this can result for instance in a different trend of heat transfer coefficient versus vapour quality. This was observed, when heat transfer data in plain and microfin tube were compared.

Experimental investigations, available in the open literature, on two-phase flow pattern during in-tube flow boiling suggest that in a microfin tube an enlargement of the annular flow regime occurs as compared to a smooth tube. For instance, Yu *et al.* (2002) performed visual observations during flow boiling of R134a inside a smooth and a microfin tube and they reported the experimental observations in a G - x plane. As compared to a plain tube, the transition boundaries from intermittent flow to annular flow and from stratified flow to annular flow occur in the microfin tube at lower vapour quality and mass velocity.

Lucchini *et al.* (2009) compared visual observations, performed during flow boiling of R134a in a smooth and a microfin tube at 5 °C saturation temperature and heat flux from 6 to 15 kW/m^2, with the diabatic two-phase flow pattern map by Kattan *et al.* (1998). They observed as in the case of the microfin tube, for a fixed mass velocity, the transition between intermittent to annular flow occurs at lower vapour quality; thus, by increasing mass velocity, the transition line is shifted toward lower quality values and could be approximately represented by a straight line with negative slope. Moreover, the transition between annular to wavy flow generally takes place at lower mass velocities as compared to the smooth tube.

Doretti *et al.* (2005) experimentally observed the two-phase flow patterns, during condensation inside horizontal smooth and microfin tubes at 40 °C saturation temperature; they correlated the transition from annular to stratified flow to the dimensionless parameter J_G. Visual observations were performed for R134a and R410A. For all the fluids investigated, with vapour quality around 0.5 and different values of mass velocity, the transition always occurs at J_G around 2.5 for the smooth tube and J_G around 1.5 for the microfin tube. If the two-phase flow pattern is described in a map in coordinates J_G - X_{tt}, the transition curve from stratified to annular flow for the microfin tube can be described by the following equation:

$$J_G^T = \left[\left(\frac{7.5}{4.3 X_{tt}^{1.111} + 1} \right)^{-3} + 1.6^{-3} \right]^{-1/3} \tag{6.1}$$

where X_{tt} is the parameter of Martinelli, defined as:

$$X_{tt} = \left(\frac{\mu_l}{\mu_v} \right)^{0.1} \left(\frac{\rho_v}{\rho_l} \right)^{0.5} \left(\frac{1-x}{x} \right)^{0.9} \tag{6.2}$$

By considering the expression of the parameter J_G, one can plot the transition curve by Doretti *et al.* (2005) in a plane in coordinates G - x:

$$J_G = \frac{x\, G}{\left[g\ d\ \rho_v (\rho_l - \rho_v) \right]^{0.5}} \tag{6.3}$$

Figure 6.13 reports in a plane in coordinates mass velocity versus vapour quality, the transition curve during condensation inside a microfin tube at 30 °C saturation temperature as given by Eq. 6.1; some test runs during flow boiling in microfin tube for R134 at 30 °C saturation temperature, mass velocity from 80 to 400 kg/(m^2 s) and heat flux around 15 and 22 kW/m^2 are also reported. Data under dry-out regime are not reported in the graph. The transition boundary by Doretti *et al.* (2005) predicts stratified flow regime for test runs at 80 and 100 kg/(m^2 s) over the entire quality range.

In Figure 6.14 - 6.17, the same microfin data sets reported in Figure 6.13 are plotted in the map by Wojtan *et al.* (2005a). The map underpredicts the dry-out regime for all the test runs. For data at 80 and 100 kg/(m^2 s), the map predicts slug - stratified-wavy flow at vapour quality below 0.4 and stratified-wavy flow at higher vapour quality.

At mass velocity 400 kg/(m^2 s), annular flow is predicted by Wojtan *et al.* (2005a) at vapour quality higher than around 0.4. This is quite different from Figure 6.13, where annular flow is predicted for all the flow boiling data. Experimental visual observations by Lucchini *et al.* (2009) for R134a at mass velocity around 200 kg/(m^2 s), heat flux 15 kW/m^2 and saturation temperature 5 °C, show as annular flow takes place at vapour quality below 0.3. But, as reported in Figure 6.13 and Figure 6.16, annular flow is predicted at around 0.4 in both the cases.

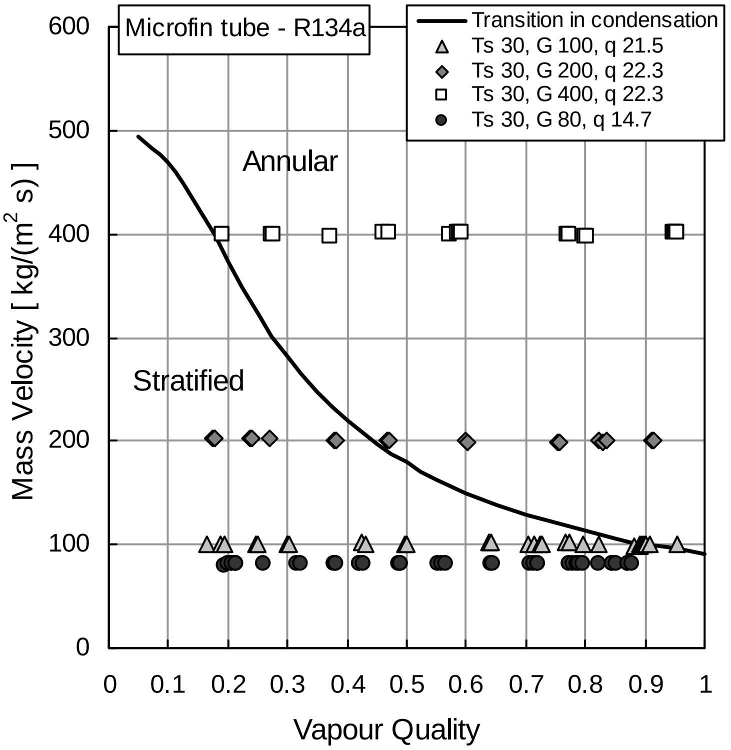

Figure 6.13. Mass velocity vs. vapour quality: annular to stratified transition boundary for condensation in microfin tube by Doretti *et al.* (2005) and experimental flow boiling data in microfin tube for R134a. Saturation temperature is around 30 °C, heat flux is around 15 and 22 kW/m^2 and mass velocity is 80, 100, 200 and 400 kg/(m^2 s).

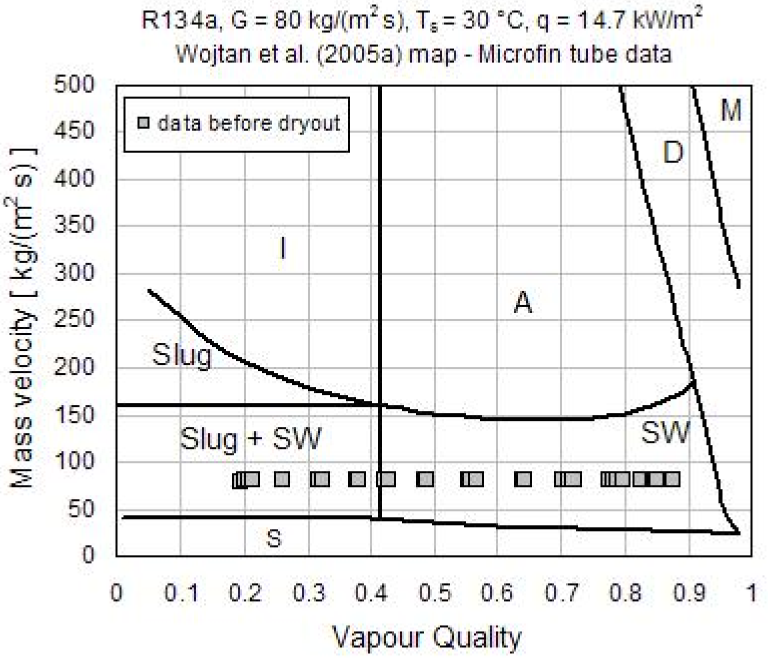

Figure 6.14. Experimental flow boiling data for R134 in microfin tube and flow pattern map by Wojtan *et al.* (2005a). The average saturation temperature is 30 °C, mass velocity is 80 kg/(m^2 s) and the average heat flux is 14.7 kW/m^2.

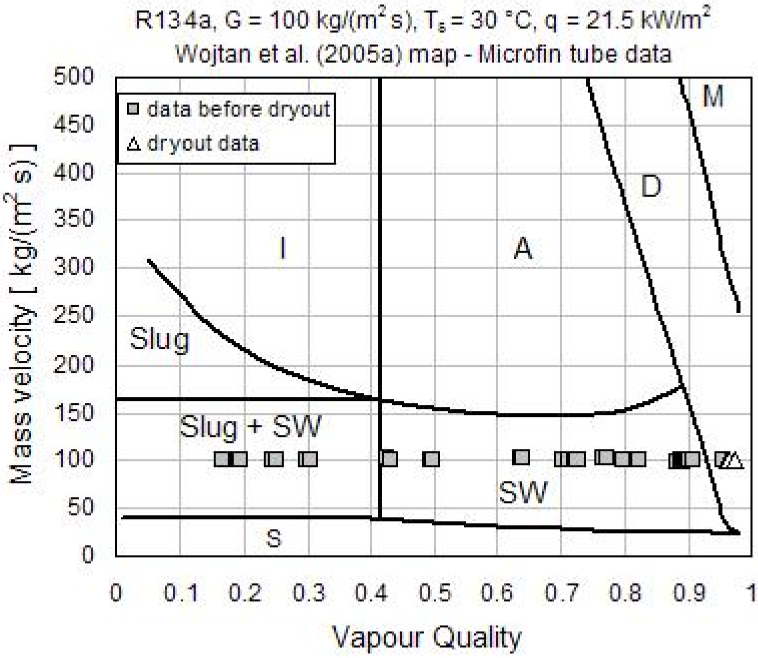

Figure 6.15. Experimental flow boiling data for R134 in microfin tube and flow pattern map by Wojtan *et al.* (2005a). The average saturation temperature is 30 °C, mass velocity is 100 kg/(m^2 s) and the average heat flux is 21.5 kW/m^2.

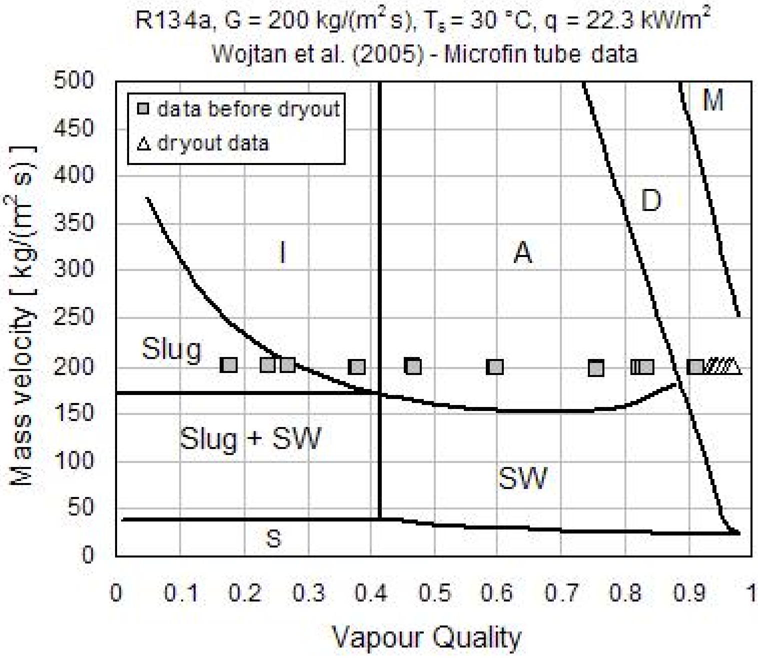

Figure 6.16. Experimental flow boiling data for R134 in microfin tube and flow pattern map by Wojtan *et al.* (2005a). The average saturation temperature is 30 °C, mass velocity is 200 kg/(m^2 s) and the average heat flux is 22.3 kW/m^2.

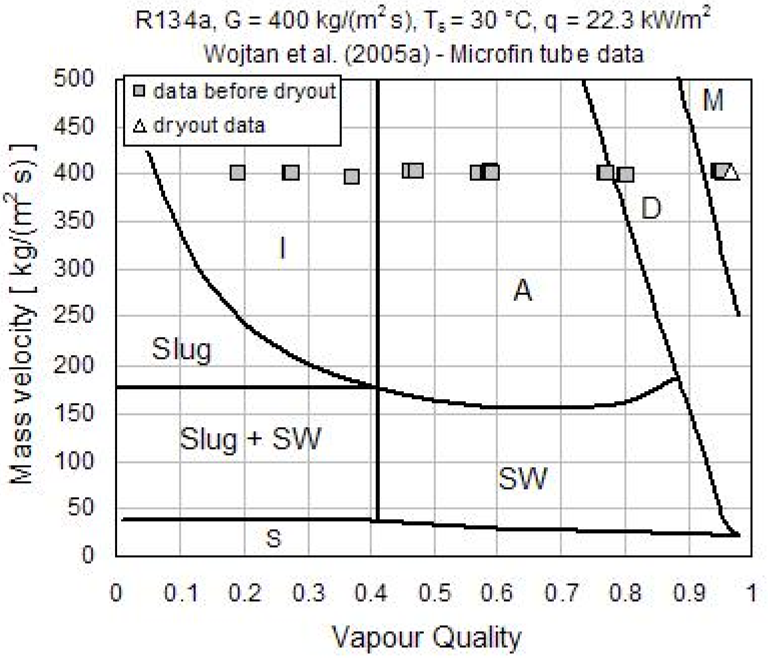

Figure 6.17. Experimental flow boiling data for R134 in microfin tube and flow pattern map by Wojtan *et al.* (2005a). The average saturation temperature is 30 °C, mass velocity is 400 kg/(m^2 s) and the average heat flux is 22.3 kW/m^2.

6.3 Prediction of dry-out inception vapour quality in microfin tube

The knowledge of the onset of dry-out is fundamental in the design of an evaporator. When dry-out occurs, the liquid film on the tube wall disappears or disrupts and heat transfer becomes worse. Few correlations are available in the open literature to predict the vapour quality at which dry-out takes place, in particular for the microfin tube. It has been experimentally observed as dry-out regime occurs in the microfin tube at higher vapour quality as compared to a smooth tube, due to the action of the fins. Thus, a specific correlation is required to predict the inception of dry-out in a microfin tube.

Mori *et al.* (2000) proposed a correlation to estimate the dry-out inception quality in a microfin tube, based on experimental measurements performed for R134a at 5° C saturation temperature, mass velocity from 100 to 600 kg/(m^2 s) and heat flux from 5 to 50 kW/m^2. They investigated the effect of mass velocity and heat flux on the quality inception of dry-out, and they found a strong dependence on q and G. According to the effects of mass velocity and heat flux, they classified the dry-out qualities in two characteristics regimes, named Regime-G1 and Regime-G2. Regime-G1 is approximately characterized by low mass velocity G and low ratio of mass velocity and heat flux (q/G), or high mass velocity G and low or medium ratio q/G. Regime-G2 approximately occurs at low mass velocity G and medium to high ratio q/G or high mass velocity G and high q/G. Using the data collected, they developed a correlation for each characteristic flow regime. When Regime-G1 takes place, the dry-out inception quality is equal to 0.92:

$$x_{d1} = 0.92 \tag{6.4}$$

When Regime-G2 occurs, the dry-out inception quality is calculated as:

$$x_{d2} = \min(x_{di2a}, x_{di2b}) \tag{6.5}$$

$$x_{d2a} = 0.44 Fr^{0.04} Bo^{-0.07} \tag{6.6}$$

$$x_{d2b} = 0.44 Fr^{0.02} Bo^{-0.33} \tag{6.7}$$

where Bo and Fr_v are the boiling number and the Froude number, defined as:

$$Bo = \frac{q}{h_{lv}} \tag{6.8}$$

$$Fr_v = \frac{G^2}{g\ d\ \rho_v(\rho_l - \rho_v)} \tag{6.9}$$

Thus, for a given data set, the dry-out inception quality x_d is determined as:

$$x_d = \min(x_{d1}, x_{d2}) \tag{6.10}$$

Experimental measurements of dry-out inception vapour quality have been taken at saturation temperature of 30 ° C and 40 ° C for R134a and R410A. Experimental dry-out inception vapour quality has been here determined as the last point before a “great” drop in the heat transfer coefficient, higher than the experimental uncertainty, occurs.

Figure 6.18 reports the dry-out inception vapour quality measured for R134a as a function of heat flux for three different mass velocities. For G = 200 kg/(m^2 s) and G = 400 kg/(m^2 s), dry-out takes place at lower vapour quality as heat flux increases. This result is in agreement with the measurements by Mori *et al.* (2000). Any particular dependence by mass velocity has been found.

The predicting correlation by Mori *et al.* (2000) is compared with the entire database collected for R134a and R410A. On the whole, 21 experimental measurements of dry-out inception quality taken for R134a at 30 °C saturation temperature and 10 measurements taken for R410A at 30 °C and 40 °C are used in the comparison.

In Figure 6.20 the difference between the calculated and the experimental dry-out inception quality is reported as a function of mass velocity. As mass velocity increases the prediction capability of the correlation improves. Figure 6.21 reports the difference between the calculated and the measured dry-out quality as a function of heat flux. However, the correlation underestimates all the experimental measurements

A better agreement with the experimental measurements is found if the calculated value is obtained with Eq. (6.6) for Regime-*G*2, as it can be observed in Figure 6.22 and Figure 6.23 In this case the prediction capability increases with mass velocity and heat flux.

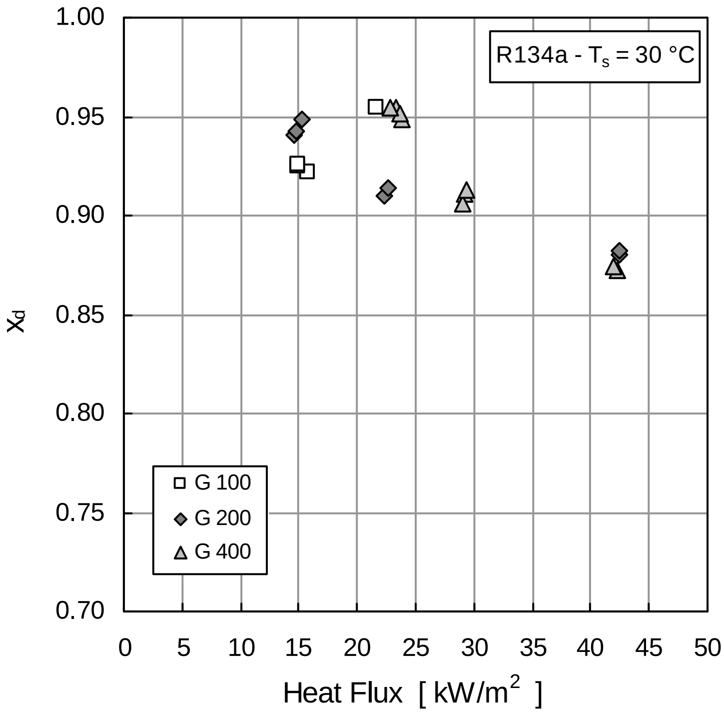

Figure 6.18. Experimental dry-out inception vapour quality vs. heat flux for R134a: saturation temperature is 30 °C, mass velocity is 100, 200 and 400 kg/(m^2 s).

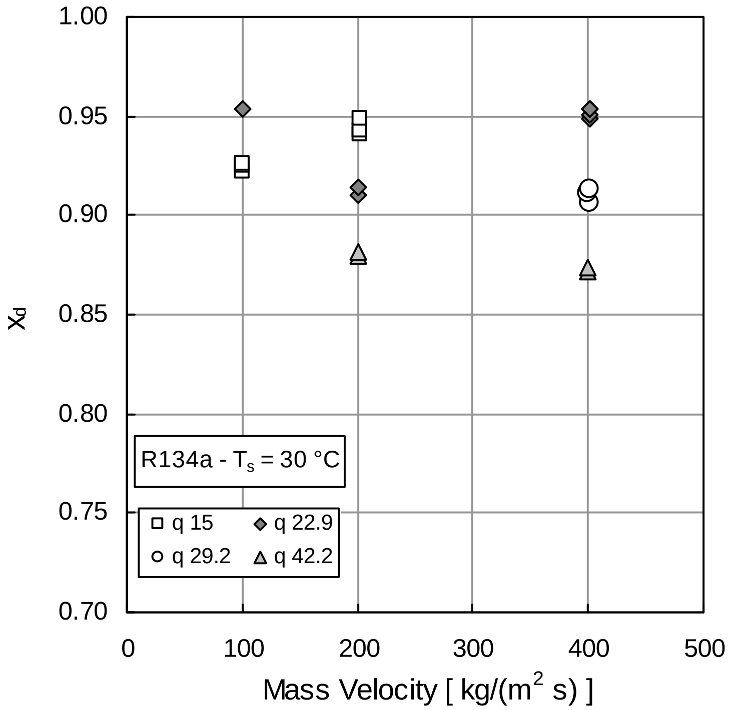

Figure 6.19. Experimental dry-out inception vapour quality vs. mass velocity: saturation temperature is 30 °C, heat flux is from 15 to around 42 kW/m^2.

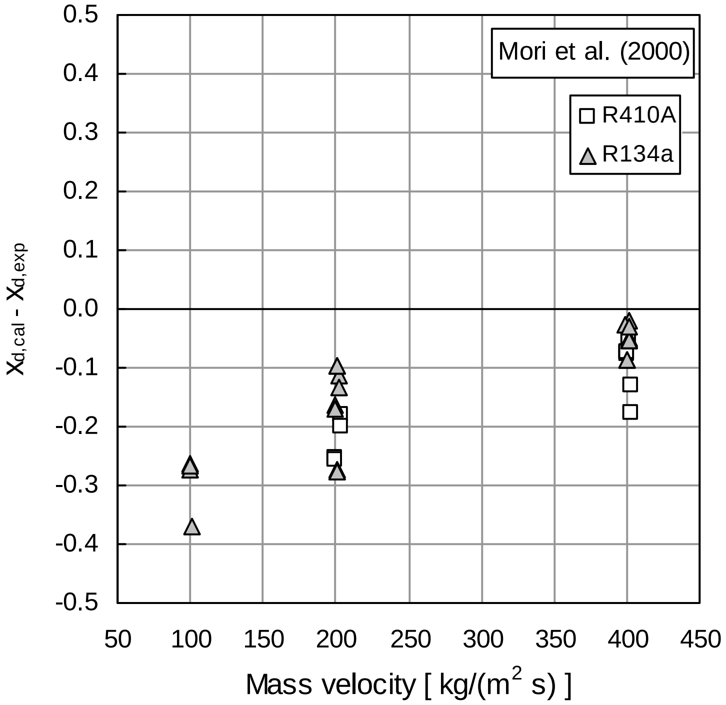

Figure 6.20. Difference between calculated and experimental dry-out inception quality vs. mass velocity. The calculated values are obtained with the model by Mori *et al.* (2000).

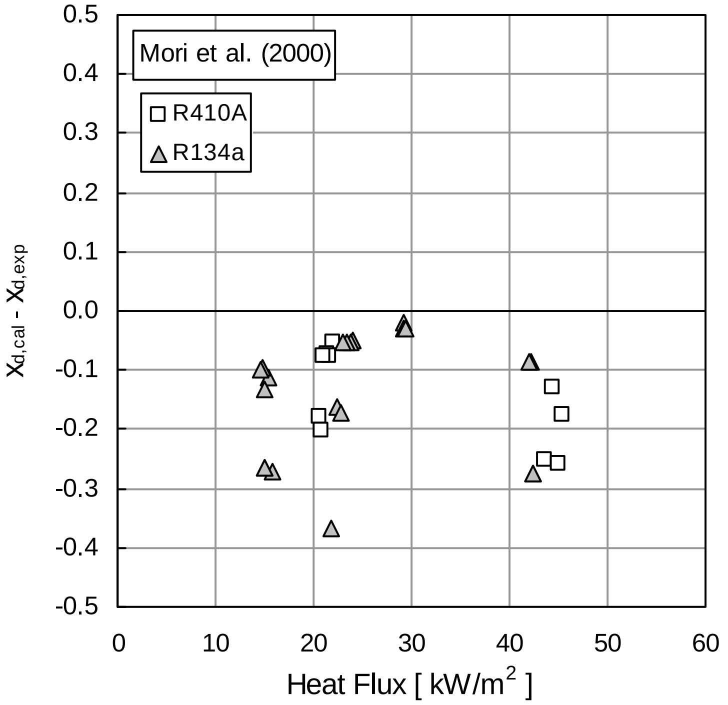

Figure 6.21. Difference between calculated and experimental dry-out inception quality vs. heat flux. The calculated values are obtained with the model by Mori *et al.* (2000).

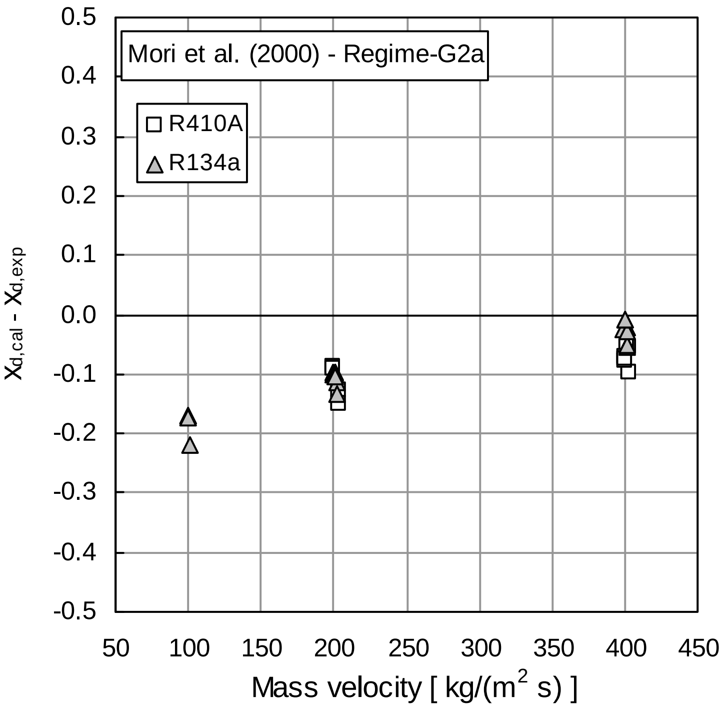

Figure 6.22. Difference between calculated and experimental dry-out inception quality vs. mass velocity. The calculated values are obtained with Eq. 6.6.

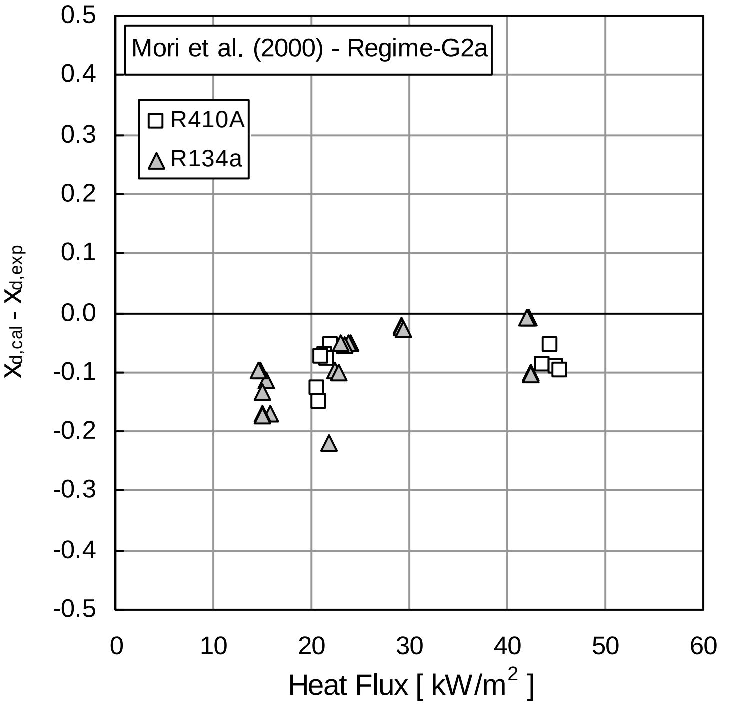

Figure 6.23. Difference between calculated and experimental dry-out inception quality vs. heat flux. The calculated values are obtained with Eq. 6.6.

CHAPTER 7

EXPERIMENTAL MEASUREMENTS OF PRESSURE DROP IN MICROFIN TUBE

7.1. Experimental measurements of pressure drop during adiabatic two-phase flow

Experimental measurements of pressure drop during adiabatic two-phase flow inside the microfin tube are presented in this section. Measurements have been performed at 30 °C and 40 °C saturation temperature for R134a and R410A. Pressure drop is measured on the whole microfin tube test section, which is 1.4 m long, by a differential pressure transducer connected to manometric taps upstream and downstream of the test tube. The accuracy of the differential pressure transducer (type B component of the uncertainty) is ±200 Pa

The frictional pressure gradient measured during adiabatic two-phase flow of R134a and R410A is plotted as a function of in the following graphs. The pressure gradient increases with vapour quality and mass velocity. In Figure 7.1 experimental measurements of pressure gradient is reported for R134a at 30 °C saturation temperature for mass velocity 200, 400 and 600 kg/(m^2 s).

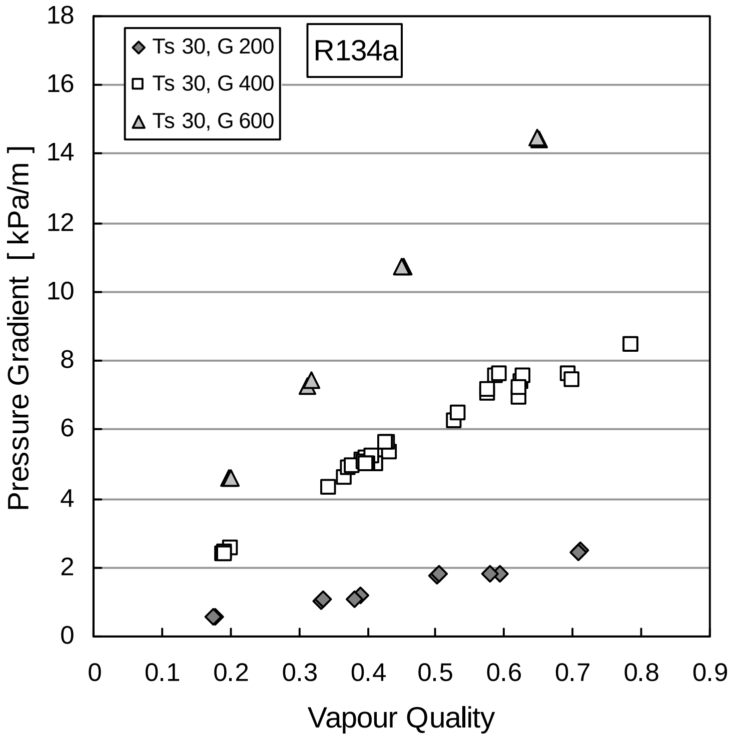

Figure 7.1. Experimental pressure gradient vs. vapour quality during adiabatic two-phase flow of R134a. Saturation temperature is 30 °C, mass velocity is 200, 400 and 600 kg/(m^2 s).

In Figure 7.2 measurements taken at 30 °C saturation temperature are compared with the pressure gradient measured at 40 °C saturation temperature for 200 and 400 kg/(m^2 s) mass velocity: as saturation temperature increases vapour density also increases and a lower pressure gradient is measured at 40 °C, for a fixed value of vapour quality and mass velocity.

Figure 7.3 reports the measured pressure gradient as a function of vapour quality for R410A at 30 °C saturation temperature and mass velocity 200, 400 and 600 kg/(m^2 s).

In Figure 7.4 pressure gradients measured at 30 °C for R134 and R410A are compared. At 30 °C saturation temperature, R134a has a vapour density of 37 kg/m^3, while a vapour density of 77 kg/m^3 is associated to R410A

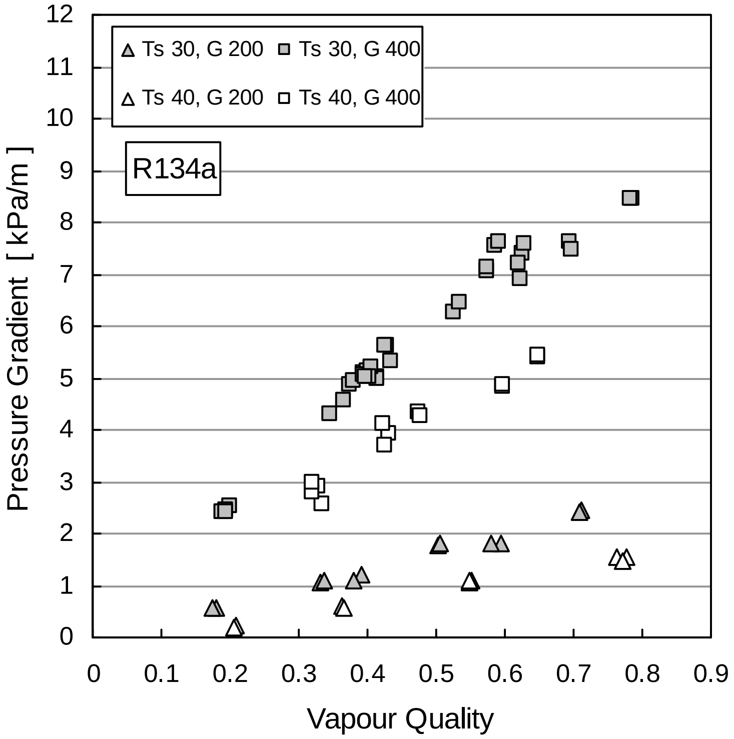

Figure 7.2. Experimental pressure gradient vs. vapour quality during adiabatic two-phase flow of R134a. Saturation temperature is 30 °C and 40 °C, mass velocity is 200 and 400 kg/(m^2 s).

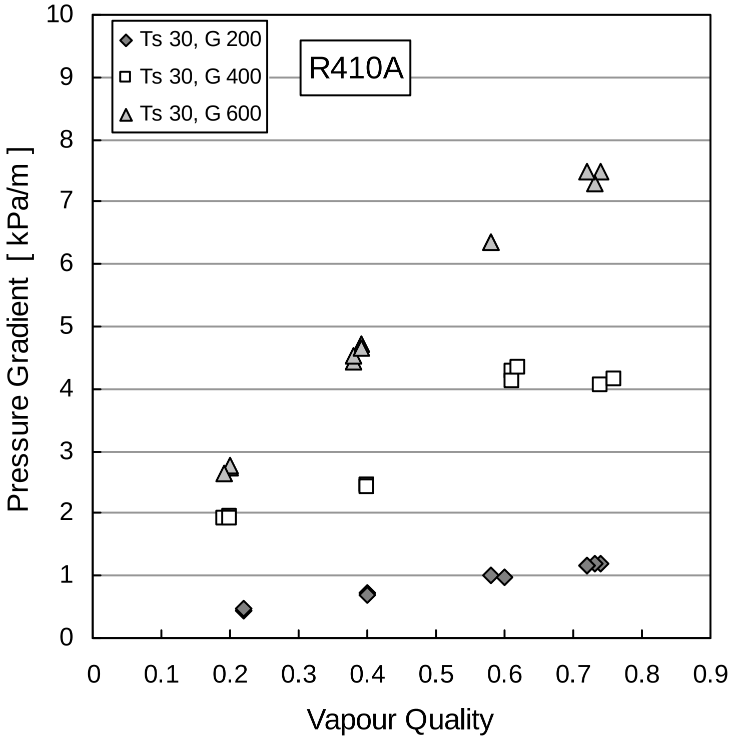

Figure 7.3. Experimental pressure gradient vs. vapour quality during adiabatic two-phase flow of R410A. Saturation temperature is 30 °C, mass velocity is 200, 400 and 600 kg/(m^2 s).

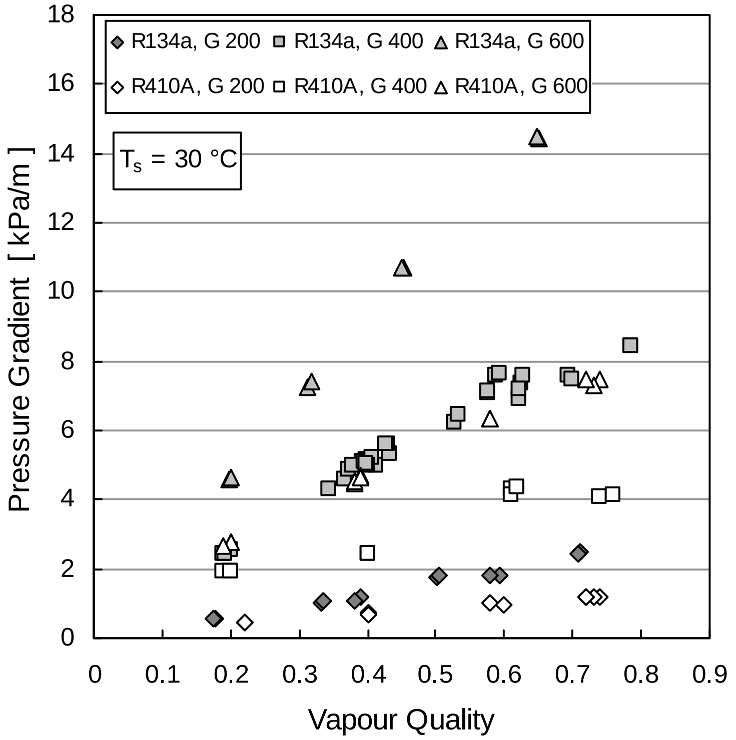

Figure 7.4. Experimental pressure gradient vs. vapour quality during adiabatic two-phase flow. Comparison between R134a and R410A. Saturation temperature is 30 °C and mass velocity is 200, 400 and 600 kg/(m^2 s).

7.2 Comparison with predictive method by Cavallini *et al.* (1999)

Experimental measurements of pressure gradient during adiabatic two-phase flow of R134a inside the microfin tube at 30 °C and 40 °C are compared with the model by Cavallini *et al.* (1999). The version of the model which uses the procedure by Friedel (1979) has been here applied.

Figure 7.5 reports the comparison between the experimental pressure gradient and the calculated values by Cavallini *et al.* (1999) at 30 ° C saturation temperature and mass velocity from 200 to 600 kg/(m^2 s).

In Figure 7.6 the experimental measurements taken at 40 °C saturation temperature and mass velocity 200 and 400 kg/(m^2 s) are compared with the method by Cavallini *et al.* (1999).

By comparing the two graphs, at 40° C and 200 kg/(m^2 s), the model tends to overestimate experimental data as compared to 30 °C. At 400 kg/(m^2 s) mass velocity a similar prediction capability is observed for 30 °C and 40 °C saturation temperature.

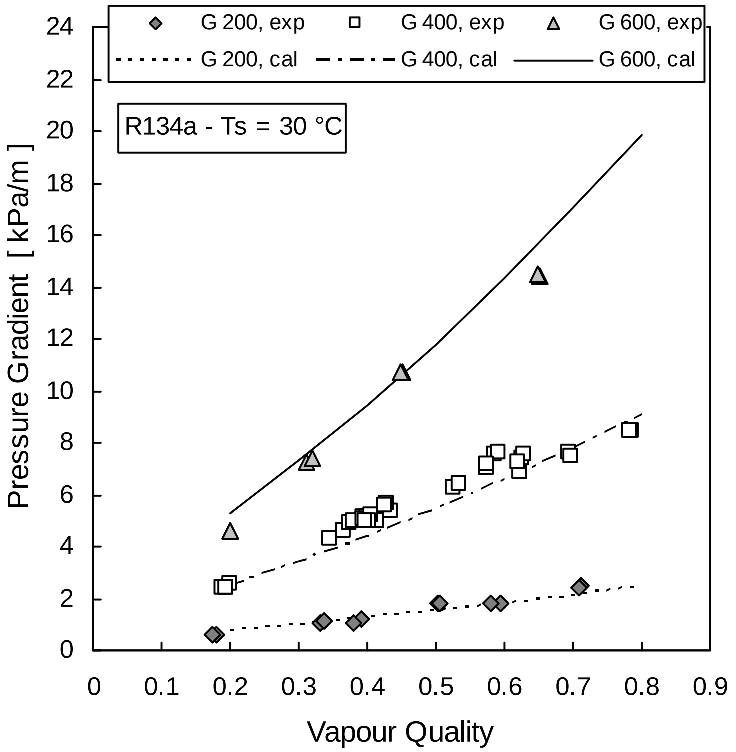

Figure 7.5. Pressure gradient vs. vapour quality during adiabatic two-phase flow of R134a: comparison between calculated and experimental values. Saturation temperature is 30 °C, mass velocity is 200, 400 and 600 kg/(m^2 s).

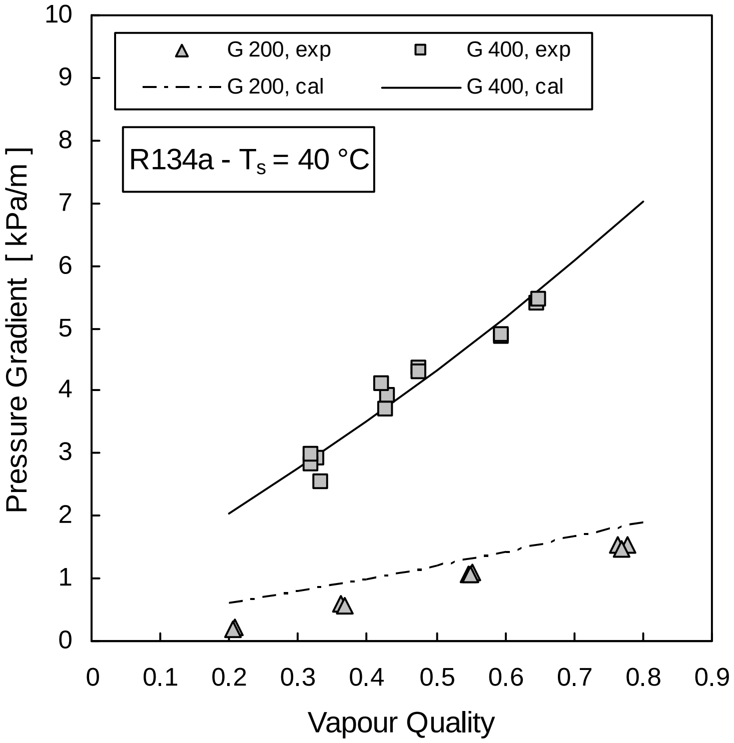

Figure 7.6. Pressure gradient vs. vapour quality during adiabatic two-phase flow of R134a: comparison between calculated and experimental values. Saturation temperature is 40 °C, mass velocity is 200 and 400 kg/(m^2 s).

CONCLUSIONS

In this thesis an experimental study during flow boiling of refrigerants inside horizontal tubes has been presented. New measurements of heat transfer coefficient in a microfin tube at saturation temperature of 30 °C and 40 °C have been reported for R134a and R410A. A wide range of operative conditions has been experimentally investigated: mass velocity from 80 to 600 kg/(m^2 s), heat flux from 14 to 83.5 kW/m^2 and vapour quality from 0.1 to 0.99. Measurements of pressure drop during adiabatic two-phase flow of R134a and R410A in microfin tube at 30 °C and 40 °C are also reported. A detailed description of the test section and the measuring technique has been provided. Heat transfer coefficients presented here are quasi local values, since vapour quality change across the measuring section is lower than 0.20. They are obtained using hot water as heating source and they have been reduced from the difference between the measured values of wall and saturation temperature. It should be noted that in most of flow boiling experimental works the test section is electrically heated. The average experimental uncertainty of heat transfer coefficient is around ±5 % and 8.5 %. Higher uncertainty values are sometimes observed, especially near the onset of dry-out, due to the more unstable flow conditions.

At high saturation temperature quite different thermo-physical and thermodynamic properties occur as compared to evaporating temperatures conventional for refrigeration and air-conditioning applications; this yields different two-phase flow conditions and heat transfer characteristics. Most of data available in the open literature refer to a narrow range of saturation temperatures, resulting in a limited range of reduced pressure in the refrigerant vaporization data sets. Present data are characterized by higher reduced pressure values, from 0.19 to 0.5, and this allows to extend the reduced pressure range in the databases. For instance, the adoption of new refrigerants, such as carbon dioxide, with different thermodynamics and thermo-physical properties, requires to extend the pressure range of application of existing heat transfer predictive methods. When evaporating at 2 °C, carbon dioxide has a saturation pressure of 3673 kPa and 0.5 reduced pressure, which is far higher as compared to common halogenated refrigerants. For R410A, 2 °C saturation temperature corresponds to 0.17 reduced pressure, while 0.39 reduced pressure is associated to 30 °C saturation temperature. The influence of reduced pressure on thermodynamic and thermo-physical properties has been analyzed.

The new measurements of heat transfer coefficient taken for R134a and R410A in the microfin tube have been discussed. In the case of R134a, at the lower heat flux investigated, around 14 kW/m^2, the heat transfer coefficient is increasing with vapour quality up to the inception of dry-out. As heat flux is increased, the heat transfer coefficient shows a trend almost independent of vapour quality, in the low quality region; however it abruptly increases at higher vapour qualities. This trend depends on the competition between nucleate boiling and convective mechanisms.

The effect of mass velocity on heat transfer coefficient has been found only at mass fluxes lower than 200 kg/(m^2 s), where heat transfer coefficient increases with mass velocity. By further increasing mass velocity to 400 kg/(m^2 s), the heat transfer coefficient does not raise. At 400 and 600 kg/(m^2 s), the heat transfer coefficient is lower as compared to 200 kg/(m^2 s). This behaviour has been also found in other experimental studies at high reduced pressure.

In the case of R410A, a strong effect of nucleate boiling mechanism is observed, by comparing test runs at the same mass velocity but different heat flux: for instance at 30 °C saturation temperature and 400 kg/(m^2 s) mass velocity, when heat flux is increased from 21 to 44 kW/m^2, the heat transfer coefficient is higher over the entire quality range. Moreover, by comparing test runs at the same mass velocity and heat flux but different saturation pressure, the effect of nucleate boiling appears at vapour quality lower than around 0.7. Near the inception of dry-out the heat transfer coefficient for R410A show an increase with vapour quality as in the case of R134a.

The comparison between heat transfer coefficients in smooth and microfin tube has shown that the presence of the fins can significantly modify the two-phase flow pattern and the behaviour during heat transfer. For instance, when R410A evaporates at 40 °C inside the smooth tube, the trend of heat transfer coefficient is continuously decreasing as vapour quality increases; this behaviour is very different from the one obtained in microfin tube. Moreover, in plain tube the inception of dry-out occurs much earlier as compared to microfin tube.

For this reason, flow boiling data in microfin and smooth tube have been plotted in the two-phase flow pattern map by Wojtan *et al.* (2005a) for vaporization inside a plain tube; a map for flow boiling in microfin tube does not exist at the moment. In the case of experimental smooth tube data for R134a the map predicts with accuracy the dry-out region. Moreover, the map predicts the local minimum, observed in R134a heat transfer coefficient, nearby the slug to intermittent transition boundary; this is in agreement with the experimental results for R134a by other authors. In the case of R410A evaporating in the smooth tube, the map does not seem to provide an accurate prediction of flow pattern; these data have a very high reduced pressure and show a behaviour similar to the one obtained in the case of carbon dioxide. In microfin tube dry-out occurs at higher vapour quality as compared to the value predicted by Wojtan *et al.* (2005a) map.

The comparison of heat transfer coefficient in microfin tube with predictive models has provided that the model by Chamra and Mago (2007) gives the better agreement with experimental data of R134a. When the comparison is performed only with data at 80 and 100 kg/(m^2 s) mass velocity, the model by Thome *et al.* (1997) becomes the more accurate. In the case of R410A data, reduced pressure is higher and the model by Cavallini *et al.* (2006) provides the better prediction capability.

For plain tube data, the model by Wojtan *et al.* (2005b) does not give any significant improvement of the prediction capability as compared to the other correlations considered here, whereas it is a flow pattern based method.

New experimental measurements of dry-out inception vapour quality have been presented for R134a and R410A. Any significant influence of mass velocity as been observed on the dry-out inception quality; on the contrary dry-out takes place earlier as heat flux increases. The correlation by Mori *et al.* (2000) has provided some underestimation of the experimental dry-out inception quality, but an improvement of the prediction capability is observed at higher values of mass velocity.

NOMENCLATURE

A	annular flow regime
D	diameter or dry-out regime in Wojtan *et al.* (2005a) map
d	diameter, m
e_p	percentage error = $[(\alpha_{\mathrm{cal}} - \alpha_{\mathrm{exp}})/\alpha_{\mathrm{exp}}]100$, %
G	mass velocity, kg/(m^2 s)
h	enthalpy, J/kg
I	intermittent flow regime
M	molecular mass
MAD	mean absolute deviation = $(1/N)\sum[\,[\,\vert\alpha_{\mathrm{cal}} - \alpha_{\mathrm{exp}}\vert/\alpha_{\mathrm{exp}}]100$, %
MD	mean deviation = $(1/N)\sum[(\alpha_{\mathrm{cal}} - \alpha_{\mathrm{exp}})/\alpha_{\mathrm{exp}}]100$, %
N	number of points
SD	standard deviation = $[\sum(e_p\text{-}MD)^2/(\mathrm{N}\text{-}1)]^{1/2}$
p_r	reduced pressure
Q	heat flow rate, W
q	heat flux, W/m^2
S	stratified flow regime
SW	stratified-wavy flow regime
T	temperature, °C
u	standard uncertainty
U	experimental uncertainty 95 % confidence level
x	vapour quality

Greek symbols

α	heat transfer coefficient, W/(m^2 K)
λ	thermal conductivity, W/(m K)
μ	viscosity, [Pa s]
σ	surface tension, N m
ρ	density, kg/m^3

Subscripts

c	critical
cal	calculated
d	dry-out inception
exp	experimental
l	liquid
nb	nucleate boiling
cv	convective
r	reduced
s	saturation
v	vapour
w	water or wall

REFERENCES

Bandarra Filho, E., P., and Saiz Jabardo, J., M., Convective boiling performance of refrigerant R134a in herringbone and microfin copper tubes, International Journal of Refrigeration, 29 (2006) 81-91.

Cavallini, A., Del Col, D., Doretti, L., Longo, G., A., and Rossetto, L., A new model for refrigerant vaporisation inside enhanced tubes, Proceedings of Third International Conference on Multiphase Flow, Lyon, France, 1998.

Cavallini, A., Del Col, D., Doretti, L., Longo, G., A., and Rossetto, L., A new computational procedure for heat transfer and pressure drop during condensation inside enhanced tubee, Enhanced Heat Transfer, 6 (1999) 441-456.

Cavallini, A., Del Col, D., Doretti, L., Longo, G., A., and Rossetto, L., Refrigerant vaporisation inside enhanced tubes: a heat transfer model, Heat and Technology, 17 (2) (1999).

Cavallini, A., Del Col, D., and Rossetto, L., Flow boiling inside microfin tubes: prediction of the heat transfer coefficient, Proceedings of International Conference on Boiling Heat Transfer, Spoleto, Italy, 2006.

Chamra, L., M., and Mago, P.,J., Modelling of evaporation heat transfer of pure refrigerants and refrigerant mixtures in microfin tubes, Proceedings of IMechE, 2007.

Chamra, L., M., and Webb, R., L., Condensation and Evaporation in micro-fin tubes at equal saturation temperatures, Journal of Enhanced Heat Transfer, 2 (1995) 219-229.

Cheng, L., Ribatski, G., Wojtan, L., and Thome, R., New flow boiling heat transfer model and flow pattern map for carbon dioxide evaporation inside horizontal tubes, International Journal of Heat and Mass Transfer, 49 (2006) 4082-4094.

Cho, M., J., and Kim, M, S., Experimental studies on evaporative heat transfer and pressure drop of CO_2 in smooth and micro-fin tube of diameters 5 and 9.52 mm, International Journal of Refrigeration, 30 (2007) 986-994.

Cieslinski, J., T., and Targanski, W., Flow boiling of R22 and R134a in enhanced tubes, Proocedings of Eurotherm Seminar, 2003.

Cooper, M., G., Saturation nucleate pool boiling: a simple correlation, Int. Chem. Eng. Symposium, (1984) 786-793.

Del Col, D., Webb, R., L., and Narayanamurthy, R., Heat transfer mechanisms for condensation and vaporization inside a microfin tube, Journal of Enhanced Heat Transfer, 9 (2002) 25-37.

Eckels, S., J., and Pate, M., B., An experimental comparison of evaporation and condensation heat transfer coefficients for HFC-134a and CFC-12, International Journal of Refrigeration, 14 (1991) 70-77.

Doretti, L., Fantini, F., and Zilio, C., Flow patterns during condensation of three refrigerants: microfin vs. smooth tube, Proceedings of IIR International Conference: Thermophysical Properties and Transfer Processes of Refrigerants, Vicenza, Italy, 2005.

Filho, E., P., B., and Jabardo, J., M., S., Convective boiling performance refrigerant R-134a in herringbone and microfin copper tubes, International Journal of Refrigeration, 29 (2009) 81-91.

Filho, E., P., B., Jabardo, J., M., S., and Barbieri, P., E., L., Convective boiling pressure drop of refrigerant R-134a in horizontal smooth and microfin tubes, International Journal of Refrigeration, 27 (2004) 895-903.

Gao, L., Honda, T., and Koyama, S., Experiments on Flow Boiling Heat Transfer of Almost Pure CO_2 and CO_2-Oil Mixtures in Horizontal Smooth and Microfin Tubes, HVAC&R Research, 13 (2007) 415-425.

Gorenflo, D., Chandra, U., Kotthoff, S., and Luke, A., Influence of thermophysical properties on pool boiling heat transfer of refrigerants, International Journal of Refrigeration, 27 (2004) 492-502.

Greco, A., Convective boiling of pure and mixed refrigerants: an experimental study of the major parameters affecting heat transfer, International Journal of Heat and Mass Transfer, 51 (2008) 896-909.

Greco, A., and Vanoli, G., P., Flow boiling heat transfer with HFC mixtures in a smooth horizontal tube. Part I: experimental investigations, Experimental Thermal and Fluid Science, 29 (2005) 189-198.

Gungor, K., E., and Winterton, R., H., S., Simplified general correlation for saturated flow boiling and comparisons of correlations with data, Chemical Engineering Research & Design, 65 (2) (1987) 148-156.

Hamilton, L., J., Kedzierski, M., A., and Kaul, M., P., Horizontal convective boiling of pure and mixed refrigerants within a micro-fin tube, Journal of Enhanced Heat Transfer, 15 (3) (2008) 211-226.

Hu, H., Ding, G., and Wang, K., Heat transfer characteristics of R410A-oil mixture flow boiling inside a 7 mm straight microfin tube, International Journal of Refrigeration, 31 (2008) 1081-1093.

Kandlikar, S., G., A general correlation for saturated two-phase flow boiling heat transfer inside horizontal and vertical tubes, Journal of Heat Transfer, 112 (1990) 219-228.

Kattan, N., Thome, J., R., and Favrat, D., Flow boiling in horizontal tubes: Part 1 – Development of a diabatic two-phase flow pattern map, Journal of Heat Transfer, 20 (1998) 140-147.

Kim, Y., Seo, K., and Chung, J. T., Evaporation heat transfer characteristics of R-410A in 7 and 9.52 mm smooth/micro-fin tubes, International Journal of Refrigeration, 25 (2002) 716-730.

Kim, M.-H., and Shin, J.-S., Evaporating heat transfer of R22 and R410A in horizontal smooth and microfin tubes, International Journal of Refrigeration, 28 (2005) 940-948.

Koyama, S., Yu, J., Momoki, S., Fujii, T., and Honda, H., Forced convective flow boiling heat transfer of pure refrigerants inside a horizontal microfin tube, Proceedings of Convective Flow Boiling International Conference, Alberta, Canada, 1995.

Lucchini, A., Colombo, L., and Muzzio, A., Flow pattern visualization during evaporation and condensation of R134 in smooth and microfin tube, Proceedings of UIT Conference, 2009.

Liu, Z., and Winterton, R., H., S., General correlation for saturated and subcooled flow boiling in tubes and annuli, based on a nucleate pool boiling equation, International Journal of Heat and Mass Transfer, 34 (11) (1991) 2759-2766.

Mori, H., Yoshida, K., Ohishi, K., and Kakimoto, Y., Dryout quality and post-dryout heat transfer coefficient for a refrigerant flowing in horizontal evaporator tubes, Proceedings of 20th International Congress of Refrigeration, IIR/IIF, Sydney, Australia, 1999.

Mori, H., Yoshida, S., Ohishi, Y., and Kokimoto, Y., Dryout qualità and post dryout heat transfer coefficient in horizontal evaporator, Proceedings of 3rd European Thermal Sciences Conference, 2000.

Muller-Steinhagen, H., and Spindler, K., Heat transfer and pressure drop during flow boiling of R134a and R404A in a microfin tube at low mass fluxes, Proceedings of 13th International Heat Transfer Conference, Sidney, Australia, 2006.

Oh, H.-K., Hak, Ku, H.-K., Roh, G.-S., Son, C.-H., and Park, S.-J., 2008, Flow boiling heat transfer characteristics of carbon dioxide in a horizontal tube, Applied Thermal Engineering, 28 (2008) 1022-1030.

Park, C., Y., and Hrnjak, P., S., CO_2 and R410A flow boiling heat transfer, pressure drop, and flow pattern at low temperatures in a horizontal smooth tube, International Journal of Refrigeration, 30 (2006) 166-178.

Rabah, A., and Kabelac, S., Flow boiling of R134a and R134a/propane mixtures at low saturation temperatures inside a plain horizontal tube, Journal of Heat Transfer, 130 (2008).

Rouhani, Z., and Axelsson, E., Calculation of volume void fraction in the subcooled and quality region, International Journal of Heat and Mass Transfer, 13 (1970) 383-393.

Saitoh, S., Daiguji, H., and Hihara, E., Correlation for boiling heat transfer of R-134a in horizontal tubes including the effect of tube diameter, International Journal of Heat and Mass Transfer, 50 (2007) 5215-5225.

Schael, A-E., and Kind, M., Flow pattern and heat transfer characteristics during flow boiling of CO_2 in a horizontal micro fin tube and comparison with smooth tube data, International Journal of Refrigeration, 28 (2005) 1186-1195.

Silva Lima, R., J., Quiben, J., M., and Thome, J., R., Flow boiling in horizontal smooth tubes: new heat transfer results for R134a at three saturation temperatures, Applied Thermal Engineering, 29 (2009) 1289-1298.

Singh, A., Ohadi, M., M., and Dessiatoun, S., Flow boiling heat transfer coefficients of R134a in a microfin tube, Journal of Heat Transfer, 118 (1996) 497-499.

Spindler, K., and Muller-Steinhagen, H., Flow boiling heat transfer of R134a and R404A in a microfin tube at low mass fluxes and low heat fluxes, Heat Mass Transfer, 45 (2009) 967-977.

Sun, Z., and Groll, E., A., flow boiling heat transfer in horizontal tubes. Part I: flo regime and prediction of dryout., Proceedings of the 5th IIR Gustav Lorentzen Conference on Natural Working Fluids, 2002.

Thome, J., R., Boiling of new refrigerants: a state-of-the-art review, International Journal of Refrigeration, 19 (1996), 435-457.

Thome, J., R., and El Hajal, J., Two-phase flow pattern map for evaporation in horizontal tubes: latest version, International Conference on Heat Transfer, Fluid Mechanics and Thermodynamics, Kruger Park, South Africa, 2002, pp. 182-188.

Thome, J., R., Kattan, N., and Favrat, D., Evaporation in microfin tubes: a generalized prediction model, Proceedings of Convective Flow and Pool Boiling Conference, Kloster Irsee, 1997.

Yoshida, S., Mantsunaga, T., Hong, H. P., and Nishikawa, K., Heat transfer enhancement in horizontal, spirally grooved evaporator tubes, JSME Int. J., 31 (3) (1988) 505-512.

Yu, M., Lin, T., and Tseng, C., Heat transfer and flow pattern during two-phase flow boiling of R134a in horizontal smooth and microfin tubes, International Journal of Refrigeration, 25 (2002), 789-798.

Yun, R., Kim, Y., Kim, M., S., and Choi, Y., Boiling heat transfer and dryout phenomenon of CO_2 in a horizontal smooth tube, International Journal of Heat and Mass Transfer, 46 (2003) 2353-2361.

Wang, C., C., Yu, J., G., Lin, S., P., and Lu, D., C., An experimental study of convective boiling of refrigerants R-22 and R-410A, ASHRAE Trans., 104 (1998) 1144-1150.

Wattelet, J., P., Chato, B., R., Christoffersen, J., A., Gaibel, J., A., Ponchner, M., Kenny, P., J., Shimon, R., L., Villanueva, T., C., Rhines, N., L., Sweeney, K., A., Allen, D., G., and Heshberger, T., T., Heat transfer flow regimes of refrigerants in a horizontal tube evaporator, ACRC TR-55, University of Illinois at Urbana-Champaign, 1994.

Wojtan, L. W., Ursenbacher, T., and Thome, J., R., Investigation of flow boiling in horizontal tubes: Part I - Development A new diabatic two-phase flow pattern map, International Journal of Heat and Mass Transfer, 48 (2005a) 2955-2969.

Wojtan, L. W., Ursenbacher, T., and Thome, J., R., Investigation of flow boiling in horizontal tubes: Part II - Development of a new heat transfer model for stratified - wavy dryout and mist flow regimes, International Journal of Heat and Mass Transfer, 48 (2005b) 2970-2985.

Zhao, X., and Bansal, P., K., Flow boiling heat transfer characteristics of CO_2 at low saturation temperatures, International Journal of Refrigeration, 30 (2007) 937-945.

APPENDIX

NEW EXPERIMENTAL APPARATUS FOR TESTING THE PERFORMANCE OF SOLAR COLLECTORS

Davide Del Col, Andrea Padovan

Dipartimento di Fisica Tecnica, University of Padova, Via Venezia 1
35131 Padova, Italy – Tel: +39 049 827 6891 – Fax: +39 049 827 6896

davide.delcol@unipd.it, a.padovan@unipd.it

SUMMARY

In this paper a new experimental apparatus for the measurement of the performance of solar collectors is presented. The test rig and the instrumentation are described. Two types of heating liquid collectors are installed: a flat-plate and an evacuated tube collector. Measurements of efficiency and pressure drop can be performed for both the collectors. The method of calculation indicated by the standard EN 12975-2 is adopted to perform tests and to determine the efficiency curve. Much attention is paid to the experimental uncertainty of the measurements, being a decisive aspect in the comparison of the performance of different collectors. The present experimental setup allows to perform measurements of the global and diffuse solar radiation on the horizontal plane and on the collector.

INTRODUCTION

The environmental scenario pushes towards new solutions to limit the use of conventional energy sources. The combustion of fossil fuels is responsible for introducing in the atmosphere several pollutant gases. SO_2 and NO_x pollutants contribute to the acid rains. CO_2 plays a decisive role in the anthropogenic greenhouse effect, responsible of the global climate change. GWP (Global Warming Potential) is a parameter which indicates the direct effect of a substance on the global warming of the earth: CO_2 has a very low value of GWP with respect to other substances, such as refrigerant fluids; therefore the crucial aspect is the great quantity of CO_2 which is introduced into the atmosphere by the combustion processes. The limitation of the energy consumption from conventional sources is a way to give a fundamental contribution in terms of environmental benefits.

Renewable energies are an answer in this direction, but they have properties of discontinuity in space and in time; moreover each renewable technology has proper characteristics which make it suitable to different applications. So the rational use of these technologies is a key point to ensure their diffusion and a concrete aid to limit the use of fossil fuels.

Solar thermal systems can give an effective contribution. Useful applications are heating domestic water, space of buildings, swimming pools and cooling in combination with several types of systems. Kalogirou [1] investigates the environmental benefits for a solar water heating system and a solar space and water heating system in Nicosia, Cyprus; electricity and Diesel are considered as auxiliary sources. In the case of the hot water units, he reports that the savings of pollutants respect to a conventional system is about 80%, both with electric and Diesel backup. For the case of the space heating the percentage is smaller, but the absolute quantity of emissions saved is bigger.

Another important aspect is the energy analysis of the solar plants in comparison to a conventional apparatus, considering both the embodied and the operational energy of the systems. A low energy payback period is clearly a crucial characteristic. Some studies, reporting the energy analysis of solar thermal systems, are available in the open literature. Kalogirou [1] found that the total energy used in the manufacture and installation of the solar plants was recouped in about 1.2 years both for the water heating and the space heating systems. Crawford and Treloar [2] present a net energy analysis of solar and conventional domestic hot water units in Melbourne, Australia: the energy payback period is found to vary from 0.5 to 2 years depending on the reference system considered in the comparison.

In any case the diffusion of solar plants is mostly related to the economic viability, which can be verified by comparing the avoided costs due to energy savings to the initial investment cost. In this context the financial aids promoted by the national and local governments play a decisive role.

Two main types of heating liquid solar collectors exist: flat-plate collectors and evacuated collectors. They are characterized by different costs and performances. So it is very important to choose the right collector for each application to optimize the behaviour of the whole system, the energy saved and the finance payback.

In this work the authors present a new experimental apparatus for the measurement of the performances of heating liquid solar collectors. The apparatus is located in the terrace roof of the Dipartimento di Fisica Tecnica of the University of Padova. Padova is located in the northern Italy at a latitude of 45°. The present apparatus has been designed following the main guidelines of the standard EN 12975-2 (Thermal solar systems and components. Solar collectors. Test methods) [3], with reference to the characteristics of the installation site. The efficiency and the pressure drop along the collector can be measured. It is worth pointing out that when a solar collector is installed, its operating conditions are submitted to the atmospheric agents that can deposit dust and pollutants on the surface of the panel and can reduce the energy performance of the collector. Therefore an accurate measurement of the efficiency with different conditions of the surface of the collector can provide the effective energy penalization.

FINANCIAL AIDS FOR SOLAR THERMAL SYSTEMS

The economic viability of a solar thermal plant is a key aspect for its diffusion. This means that these systems must be competitive with conventional plants. The initial cost of a solar thermal apparatus is higher, due mainly to the additional components in the plant. The costs avoided, due to the energy savings, must ensure a short economy payback time. Considering the actual cost of these systems in Italy, a financial action by the local government is desirable.

Cardinale et al [4] studied the economic optimization of domestic hot waters plants. Their system considers that the circulations of fluids are ensured by pumps powered by photovoltaic panels. The incentives considered was a reduction of VAT rate to 10% for buying solar plants components and a tax rebate of the 36% of the cost of the total solar plant in the first 5 years. They concluded that the raise of the italian finance aids was decisive for the economic viability of the system under study. In particular this was considered very important to increase the diffusion of solar plants and to decrease the production costs of the plants.

New finance aids are today available thanks to the new Financial Italian Law 2007 for the installation of solar thermal systems for water heating in domestic and industrial applications, and for swimming pools, sport buildings, hospitals, schools and universities. The incentive consists of a tax rebate of the 55% of the cost of the plant in three equal yearly parts.

STANDARD FOR MEASUREMENTS WITH SOLAR COLLECTORS

In 2006 the new standard EN 12975-2 (Thermal solar systems and components. Solar collectors. Test methods) [5] was approved. It contains the methods and the procedures to determine the thermal performances of glazed and unglazed solar collectors. For the present work the interesting part regards to the outdoor tests of glazed solar collectors. This standard reports the guidelines for the installation of the apparatus and the instruments along with the procedure to experimentally obtain the efficiency and the pressure drop curves. The standard gives the characteristics of the site of installation, the building characteristics of the test rig, the level of accuracy of the instruments and their location on the apparatus, the test conditions and the methods of calculation. Table 1 reports the accuracy required by the instruments of measurement according to the standard EN 12975-2 [5].

The method of calculation, that will be adopted to determine the efficiency, is described in the following. The solar power intercepted by the collector is given as the product of the solar irradiance G and the area of the collector A. This area can be referred to the absorber or to the aperture. The useful heat flow rate extracted by the fluid is calculated as:

$$q = mc\Delta T \qquad (1)$$

where m is the mass flow rate of the fluid, c is the specific heat capacity of the fluid at the mean temperature and ΔT is the difference of the fluid temperature between the outlet and the inlet of the collector. The instantaneous efficiency of the collector is obtained as:

$$\eta = q/(AG) \qquad (2)$$

The efficiency of each single experimental test is reported in a diagram as a function of the reduced temperature T_m^* defined as:

$$T_m^* = (T_m - T_a)/G \qquad (3)$$

where T_m is the mean temperature of the fluid between inlet and outlet of the collector and T_a is the ambient air temperature. For a complete characterization, the instantaneous efficiency curve must be calculated by a statistical method, fitting the experimental data. The standard suggests to use a second order model in the form of:

$$\eta = \eta_0 - a_1 T_m^* - a_2 G_0 (T_m^*)^2 \qquad (4)$$

where η_0 is the efficiency of the collector when the mean fluid temperature T_m is equal to the air ambient temperature T_a. A value of G_0 equal to 800 W/m^2 shall be assumed. At least four test runs at operating conditions must be performed, varying the inlet temperature: data points shall be spaced over the operating range of the collector tested. In order to obtain an accurate determination of the parameter η_0, one test run must comply with a constraint in the mean fluid temperature to air temperature difference, which should be not higher than 3 K. To ensure the steady state conditions during each measurement the parameters must keep constant within the range expressed by the standard.

The assessment of the experimental uncertainty is another key point, because it indicates the accuracy of the experimental results. The assessment of the experimental uncertainty can be lead using the law of error propagation. To determine the experimental uncertainty of the efficiency curve, the standard indicates a procedure based on the statistical analysis. A more detailed study is reported in Mathioulakis et al [6], Sabatelli at al [7], Muller-Scholl and Frei [8].

Table 1. Required accuracy of measurements according to the standard EN 12975-2.

Inlet fluid temperature	± 0.1 K
Temperature difference	± 0.05 K
Ambient air temperature	± 0.5 K
Flow rate	± 1%
Solar radiation	first class pyranometer
Collector area	± 0.3%
Air speed	± 0.5 m/s
Pressure drop	± 5% or ± 10 Pa

EXPERIMENTAL APPARATUS

The experimental apparatus is located on the terrace roof of the Dipartimento di Fisica Tecnica of the University of Padova. The apparatus has been set up to allow the measurement of efficiency and pressure drop of solar collectors in agreement with the main guidelines of the standard EN 12975-2 [3]. On the whole three collectors have been installed: two standard glazed flat-plate collectors, connected in parallel, and an evacuated tube collector.

A schematic view of the closed test loop is reported in figure 1: the flat-plate collectors are represented as a single one. The flat-plate collectors present a copper absorber surface, covered by a selective coating, with parallel tubes; the performances are measured for the two collectors in parallel. The evacuated collector is a direct flow through type with external CPC (compound parabolic concentrator) reflectors to optimize the absorption of the solar radiation. Figure 2 shows a picture of the collectors. In table 2 some characteristics of the collectors installed are reported: in the case of the flat-plate types the sum of the two collectors area is reported. For all the collectors it is possible to vary the tilt angle to the horizontal plane. A mixture of water and propylene glycol is used as fluid to ensure no freeze during the winter season. The hydraulic loop is divided in two lines: the first one for the flat-plate collectors and the second one for the evacuated tube collector. Two pumps are used to move the liquid. Before entering the collectors, the fluid temperature is controlled in a storage, where four electrical heaters are located. Each heater has an electrical power of 5 kW. A control system, connected to a temperature sensor inserted in the storage 2, acts on these heaters to ensure an accurate control of the liquid temperature at the inlet of the collectors. The liquid temperature at the inlet and at the outlet of the collectors is measured, both for the plate and the evacuated types. The fluid, coming from the collectors, enters the storage 1 and then goes to a plate heat exchanger which works as a heat sink. In the plate heat exchanger the heat flow rate provided by the solar radiation is taken away by a secondary fluid, which is again a mixture of water and propylene glycol. Finally the heat flow rate is dissipated in a second plate heat exchanger to the ground water of the Dipartimento.

Figure 3 shows a part of the hydraulic loop and the acquisition system. Three all black thermopile based pyranometers are used to measure the solar irradiance. A Kipp & Zonen pyranometer, classified as secondary standard by the WMO (World Meteorological Organization), measures the solar irradiance on the same plane of the collectors. Other two measurements are taken on the horizontal plane. A first class pyranometer measures the global solar irradiance on the horizontal plane. Finally a third pyranometer (first class classified), shaded against the direct solar radiation, measures only the diffuse component. The theoretical relationship allows to obtain the direct component of the solar radiation on the horizontal plane:

$$G = B\cos(i) + D \tag{5}$$

where *G*, *B*, *D* are the global, direct and diffuse solar irradiance, respectively, and *i* is the angle between the solar radiation and the normal to the horizontal plane.

A Coriolis effect and a magnetic type flow meter are used to measure the fluid flow rate. The second instrument measures a volumetric flow rate, thus the density of the mixture must be known. For the calibration of the test rig, the two flow meters can be connected in series: this allows to check the measurements obtained by the magnetic flow meter using the more accurate Coriolis effect instrument. Measurements are possible on both the flat-plate and evacuated collectors at the same time. Copper-constantan thermocouples are used to measure the fluid temperature at the inlet of the collectors. Small fluid temperature difference between inlet and outlet of the collector can be measured with reasonable accuracy: this is obtained with a four-junction copper-constantan thermopile. In any case a difference of temperature less than 1 K shall not be considered because of the great experimental uncertainty. Pressure drop along the collectors are measured by a differential digital strain gauge transducer. Finally an anemometer measures the air speed, being a parameter that influences the heat loss from the collector. In table 3 the accuracy of the instruments installed in the apparatus is reported.

SOLAR COLLECTORS

The technology has developed several types of heating liquid collectors. Glazed flat-plate, evacuated tube and unglazed collectors are the most widespread. The simplest and less expensive is the unglazed type. It does not have the glass cover thus it works with a good efficiency only at very low operating temperatures: this makes it suitable to seasonal applications such as heating of open air swimming pools. Glazed flat-plate collectors present generally a metal absorber in a flat rectangular housing. The glass cover on the upper surface and the insulation on the other side limit the thermal losses. The solar energy absorbed by the plate is transferred to the liquid flowing into copper tubes in good thermal contact with the absorber surface. Air is present in the space between the plate absorber and the transparent cover. The evacuated tube collector allows to reduce the convection and the conduction thermal losses. It consists of glass vacuum-sealed tubes; the absorber surface is located into the inner glass tube and it can have several building forms.

Table 2. Characteristics of the collectors installed in the test rig.

	Plate collector	Evacuated collector
Gross area	5.16 m^2	3.9 m^2
Aperture area	4.76 m^2	3.5 m^2

Table 3. Accuracy of sensors and parameters at typical test conditions.

Inlet fluid temperature	± 0.05 K
Temperature difference	± 0.03 K
Ambient air temperature	± 0.3 K
Flow rate	± 0.2%
Solar radiation	Secondary standard sensor
Air speed	± 0.2 m/s
Pressure drop	± 0.1% f.s.

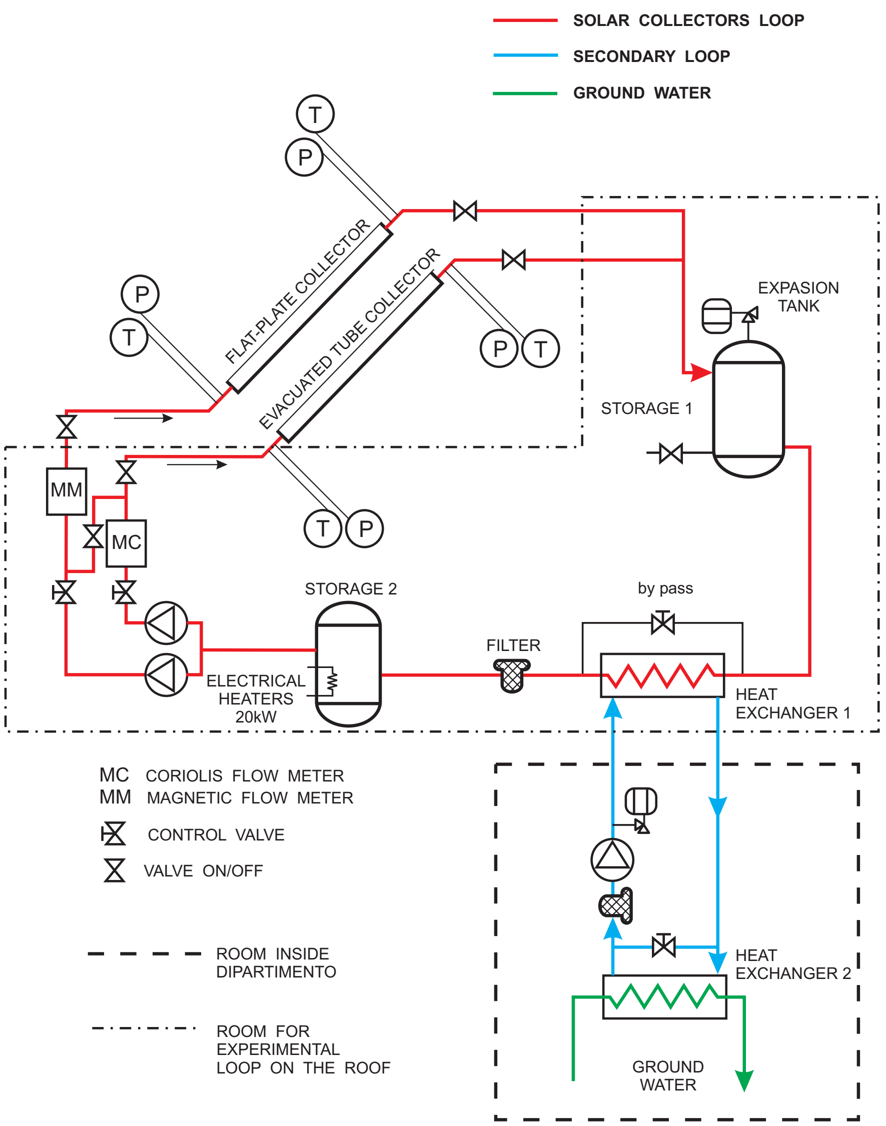

Figure 1 . Schematic view of the experimental test rig.

Two types of evacuated tube collectors exist. In the direct flow through collector the heat transfer liquid flows in the evacuated tubes. A second type consists of heat pipes inside vacuum sealed glass tubes. A reflector can be present to optimize the absorption of the solar radiation. If the reflector is external, a critical question could be the possible penalization of the efficiency when pollutants and dust deposit on the reflectors.

The performances of solar collectors decrease as the temperature difference between the fluid in the collector and the ambient temperature increases: this is usually visualized plotting the efficiency versus the reduced temperature T_m^*.

Figure 5 reports the efficiency curves of both the collectors installed, as declared by the manufacturer according to the standard EN 12975-2 [3]. The aperture area is assumed as reference. As T_m^* rises, the evacuated tube collector shows a higher efficiency compared to the flat-plate. Assuming a solar irradiance of 800 W/m^2 and a temperature difference between the heating fluid and the ambient of 8 K, the efficiency is 0.69 for the flat-plate collector and 0.67 for the evacuated tube collector. But considering a difference between the mean fluid temperature and the ambient air temperature of 40 K, the efficiency is 0.49 and 0.63 for the flat-plate and the evacuated tube collector, respectively. This means that the choice of the collector depends on the level of temperature required by the application and on the climatic conditions of the site of installation. Thus, in terms of efficiency, each collector presents functional characteristics which make it suitable to a certain application.

Heating of buildings associated to low temperature systems is a field of application for solar collectors, although the demand of heat does not correspond to the time distribution of solar energy input. Moreover during the summer an excessive production of energy can occur and proper measures should be taken to prevent the collectors from possible damages if there is an excess of solar input. In this context solar cooling can be an interesting system to use the summer production. The cooling process is also important in the choice of the collector.

MEASUREMENTS OF SOLAR RADIATION

Some experimental measurements of the solar radiation on the horizontal plane are reported. Measurements are taken both with the secondary standard and the first class pyranometers in order to check the instruments. Instantaneous readings are acquired with a time step of 10 s.

Figure 2. Collectors installed in the test apparatus.

Figure 3. Test rig and data acquisition system.

Figure 4. Pyranometers for global and diffuse solar radiation.

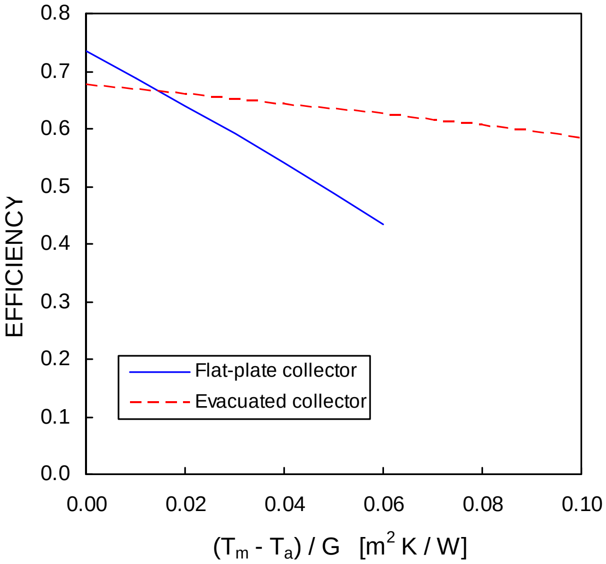

Figure 5. Efficiency curves of the collectors installed in the test rig, as declared by the manufacturer.

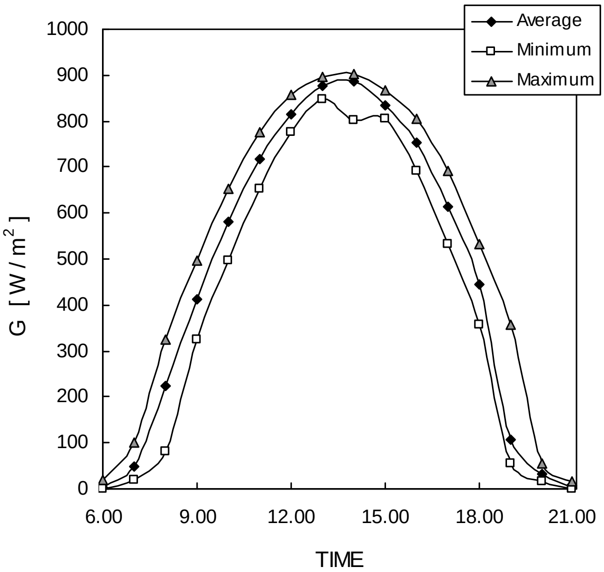

Figure 6. Global solar irradiance on the horizontal plane in Padova on May 24, 2007. The measurements are taken using a Kipp & Zonen pyranometer.

Figure 6 shows the daily curve of the global solar irradiance during a springtime day: the curves obtained by the average, maximum and minimum hourly values are depicted. The measurements obtained by different radiation sensors are compared to each other. With this purpose the deviation δ is defined as:

$$\delta = |\Delta G| / G \qquad (6)$$

where ΔG is the irradiance difference given by sensors. Figure 7 shows the percentage deviation between two secondary standard pyranometers. In figure 8 the comparison of a secondary standard and a first class sensor is reported. In both cases the higher values of percentage deviation occur in the first hours of the morning and in the evening, when the solar radiation is quite low.

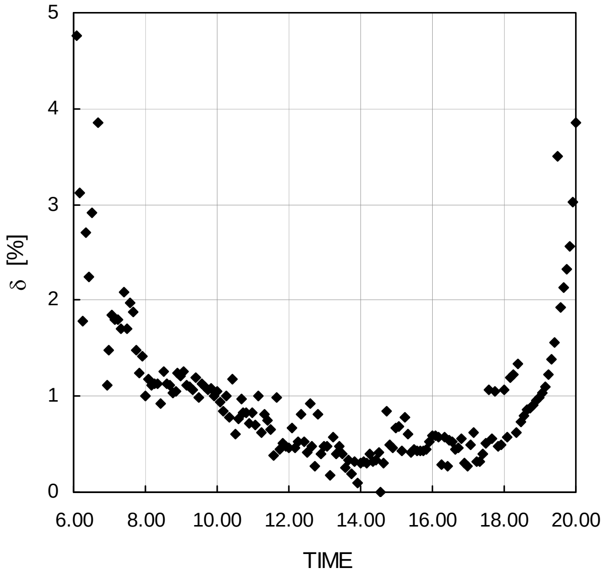

Figure 7. Percentage deviation between two secondary standard pyranometers.

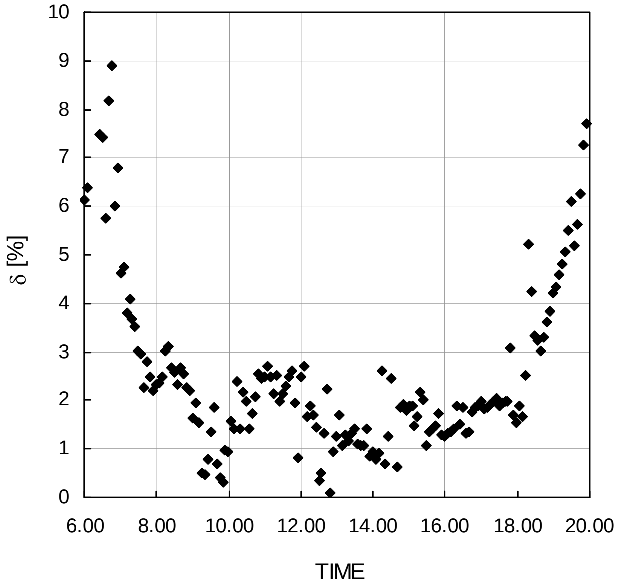

Figure 8. Percentage deviation between a secondary standard and a first class pyranometer.

However, for most of the time between 8 am and 6 pm, the percentage deviation is less than 1% when comparing two Kipp & Zonen pyranometers and less than 2.5% when comparing a secondary standard and a first class pyranometer. This is in agreement with the nominal accuracy provided by the instruments.

CONCLUSIONS

A new experimental apparatus for testing the performance of solar collectors has been presented. Two types of collectors have been installed: flat-plate and evacuated tube collectors. The method that is adopted to experimentally obtain the efficiency of the collectors, according to the standard EN 12975-2 [5], is also presented. The first solar radiation data used for the calibration of the system is shown and discussed in the paper.

The future work will be devoted to the full experimental characterization of the solar collectors with the aim of studying their possible integration in new advanced heating and cooling systems.

NOMENCLATURE

A	area [m^2]
a_1	coefficient [W/(m^2 K)]
a_2	coefficient [W/(m^2 K^2)]
B	direct solar irradiance [W/m^2]
c	heat fluid capacity [J/(kg K)]
D	diffuse solar irradiance [W/m^2]
G	global solar irradiance [W/m^2]
i	angle [rad]
m	mass flow rate [kg/s]
q	heat flow rate [W]
T	temperature [K]
T^*	reduced temperature [(m^{2}K)/W]
δ	deviation
ΔG	solar irradiance difference [W/m^2]
ΔT	temperature difference [K]
η	efficiency

Subscripts

a	ambient air
m	mean

ACKNOWLEDGEMENTS

The authors would like to acknowledge the financial support of the italian Fondazione per l’Università e l’Alta Cultura in Provincia di Belluno.

REFERENCES

1. S. A. Kalogirou, Environmental benefits of domestic solar energy systems, Energy Conversion and Management, vol. 45, pp. 3075-3092, 2004.
2. R. H. Crawford and G. J. Treloar, Net energy analysis of solar and conventional domestic hot water systems in Melbourne, Australia, Solar Energy, vol. 76, pp.159-163, 2004.
3. EN 12975-2: 2001. Thermal solar systems and components - Solar collectors - Part 2: Test methods.
4. N. Cardinale, F. Piccininni, P. Stefanizzi, Economic optimization of low-flow solar domestic hot water plants, Renewable Energy, vol. 28, pp. 1899-1914, 2003.
5. EN 12975-2: 2006. Thermal solar systems and components - Solar collectors - Part 2: Test methods.
6. E. Mathioulakis, K. Voropoulos, V. Belessiotis, Assessment of uncertainty in solar collector modelling and testing, Solar Energy, vol. 66, pp. 337-347, 1999.
7. V. Sabatelli, D. Marano, G. Braccio, V.K. Sharma, Efficiency test of solar collectors: uncertainty in the estimation of regression parameters and sensitivity analysis, Energy Conversion and Management, vol. 43, pp. 2287-2295, 2002.
8. C. Muller-Scholl and U. Frei, Uncertainty analyses in solar collector measurement, Proceedings of Eurosun 2000, Copenhagen.

Proceedings of the 2nd International Conference on Energy Sustainability
ES2008
August 10-14, 2008, Jacksonville, Florida, USA

ES2008 – 54257

MEASUREMENT OF SOLAR RADIATION FOR RENEWABLE ENERGY SYSTEMS

Andrea Padovan
University of Padova, Italy
a.padovan@unipd.it

Davide Del Col
University of Padova, Italy
davide.delcol@unipd.it

ABSTRACT

In this paper the authors present a new set of solar radiation data taken at the latitude of 45.4°, in Padova, Italy. These measurements are performed within a new laboratory for the study of solar energy conversion systems.

The global and the diffuse irradiance is measured on the horizontal plane and the global irradiance is also measured on sloped planes. The experimental uncertainty of the measurement of solar radiation is fully analyzed.

In the design of a solar system, it is crucial to know the solar radiation on the inclined surface, but generally only data on the horizontal is available and solar radiation on the tilted plane is predicted using the information collected on the horizontal. There is need for assessment of prediction methods for estimating the solar radiation on inclined surfaces.

In this paper, new data of global and diffuse radiation is compared to some most used correlations. Besides, the values calculated for the tilted plane are compared against those directly measured by a pyranometer installed on the sloped plane.

1. INTRODUCTION

The development of renewable energy systems is fundamental in terms of environmental benefits. Solar energy can give an effective contribution in reducing the use of conventional fossil sources. Making accurate measurements of solar radiation is very important in the design of photovoltaic and solar thermal systems, in the performance evaluation of solar collectors and in the energy and economic analysis of sun tracking systems. Besides, solar databases from different sources are sometimes in disagreement among each other.

The design of a solar system requires to know the solar radiation on the sloped surfaces. Usually only data of global solar radiation on the horizontal plane is available. The solar radiation on a tilted plane can be evaluated by knowing both the global solar radiation and the diffuse component. If the second one is unknown, it can be calculated using only the measurement of the global radiation. Several empirical correlations are available in the open literature to predict the diffuse solar radiation as a function of the clearness index: each one is developed from a database of some european or american stations. These models are well known and simple to use, but their accuracy must be carefully evaluated if they are used for locations different from the ones they were developed for.

The complete measurement of the solar radiation requires to measure the global solar radiation and the direct normal or the diffuse component. The use of a pyranometer to measure the global irradiance and a phyreliometer for the measurement of the normal beam leads to accurate results. But a very expensive equipment is needed for the measurement of the direct normal radiation. The diffuse component can also be accurately measured by a tracking shadow disk that blocks the direct radiation: this system is also pretty costly, though. The most economic road is the use of a shadow ring to occult the sensing element of the pyranometer. This procedure requires the introduction of a correction factor for the experimental readings. Several models are available in the open literature to calculate this correction factor.

In this paper the authors present a new laboratory for the experimental study of solar energy conversion systems. The laboratory includes a set of instrumentation for the measurement of solar radiation.

New experimental data of global and diffuse solar radiation is reported here. The accuracy of the measurement is fully analyzed. The evaluation of the experimental uncertainty is a key aspect to improve the quality of data points collected. Determination of instrument errors is important in the studies that involve instantaneous, hourly and daily profiles. Data of diffuse solar radiation is then compared with some available correlations that estimate the fraction of diffuse radiation: the objective is to evaluate if the compared existing correlations are accurate for this location.

Finally, the measurements taken on the horizontal are used to predict the solar radiation on the tilted plane and compared to the radiation measured on the inclined surface.

2. SOLAR ENERGY CONVERSION LABORATORY

A new laboratory has been set up at the Dipartimento di Fisica Tecnica of the University of Padova to study experimentally solar energy conversion systems. Padova is located in the north east of Italy at a latitude of 45.4°. The laboratory is composed by a photovoltaic plant, an experimental apparatus for the measurement of the efficiency of solar collectors and the sensors for solar radiation.

The photovoltaic system is a 1 kW peak power grid connected plant, installed in the south direction. Commercial modules, made of a thin monocrystalline silicon wafer surrounded by ultra-thin amorphous silicon layers, are installed at the moment. The tilt angle of the modules can be manually modified.

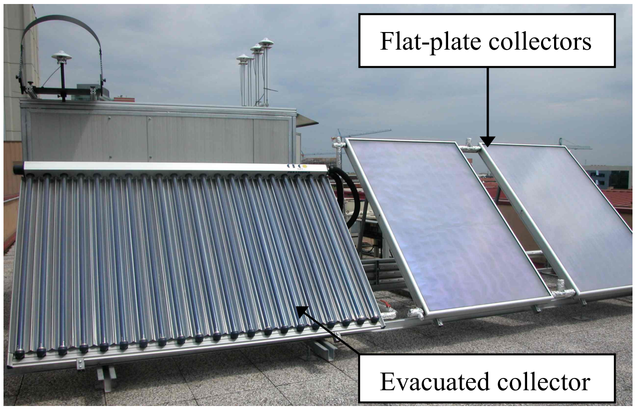

Figure 1. Experimental apparatus for the measurement of efficiency of solar collectors.

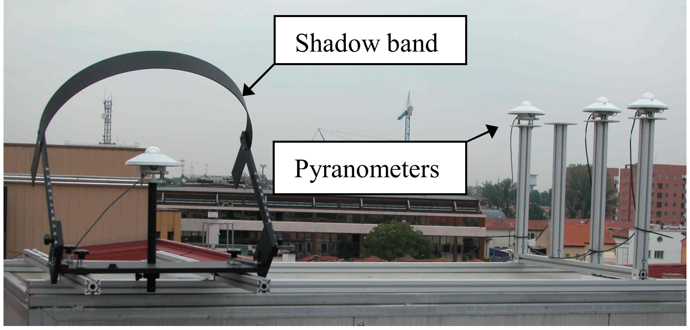

Figure 2. Pyranometers installed for the measurement of global and diffuse solar radiation.

A data logger is used to acquire data of solar irradiance on the plane of the modules, along with data of electrical power, voltage, current, total, daily and hourly produced energy, modules and air temperature. A thermopile based pyranometer measures the solar irradiance.

The second apparatus in the laboratory is a test rig for efficiency evaluation of solar collectors. Two standard glazed flat-plate collectors and an evacuated tube collector are installed at the moment (figure 1). The evacuated collector is a direct flow through type with external CPC (compound parabolic concentrator) reflectors to optimize the absorption of the solar radiation. This test rig allows to make measurements on the flat-plate or on the evacuated collector by simply acting on the valves to modify the circuit. The solar irradiance on the aperture area is measured by a pyranometer. The thermal power extracted is obtained by measuring the liquid temperature at the inlet and the outlet of the collectors and the mass flow rate by a Coriolis effect flow meter. The ambient air temperature is measured to calculate the reduced temperature, that it is used to present the experimental results according to the standard EN 12975-2 [1]. An anemometer measures the air speed, being a parameter that influences the heat losses from the collector. A more detailed description of the experimental apparatus is reported in Del Col and Padovan [2].

Two pyranometers are installed to measure the global and the diffuse solar irradiance on the horizontal plane. The diffuse component is measured by shading the sensing element of the pyranometer with a shadow band, as shown in figure 2. All the pyranometers can be installed on the horizontal at the same time in order to perform a periodic check of the sensors.

3. MEASUREMENT OF THE SOLAR RADIATION

3.1 Instrumentation and data

The solar instrumentation installed consists of four all black thermopile based pyranometers: two Kipp&Zonen CM11 instruments classified as secondary standard, and two Delta Ohm LP PYRA 02 classified as first class. The measurement of the global irradiance is performed with both a first class LP PYRA 02 and a secondary standard CM11 pyranometer. The second one is also used for the measurement of the irradiance on the collector's area during the efficiency tests. A first class pyranometer LP PYRA 02 measures the diffuse irradiance. The other CM11 pyranometer measures the solar irradiance on the photovoltaic module plane. The status of the glass dome of pyranometers is periodically checked to prevent dust, dew, water droplets and bird droppings.

The measurements of solar irradiance are acquired with a time step of 10 s: the maximum, minimum and medium values of irradiance and the standard deviation of the measurements are recorded every 5 minutes. A numerical integration is used to obtain the hourly energy values. By measuring the global and the diffuse irradiance, the following theoretical relationship is used to obtain the direct component of the solar radiation on the horizontal plane:

$$G = B_n \cos(\vartheta) + D \qquad (1)$$

where G, B_n, D are the global, direct normal and diffuse solar irradiance, respectively, and θ is the angle between the solar beam and the normal to the horizontal plane.

Figure 3 reports the typical daily curves of the solar radiation for a clear sky day. The standard deviation of irradiance is an index of the sky conditions: a clear sky or an overcast day is characterized by a uniform and low value of standard deviation. On the contrary, a scattering in the values of standard deviation indicates the fast alternate of sun and clouds. Figure 4 shows the standard deviation of the global irradiance measurements for a clear sky (September 8) and a cloudy day (September 9): in the second case the data shows high variability of irradiance.

The solar experimental data reported here was measured from September 5, 2007 to February 21, 2008 in Padova. On the whole, the present data refers to 34 days, in autumn and winter. Four data sets have been collected: global and diffuse solar radiation on the horizontal plane, global radiation on the 20° tilted plane and global radiation on the 30° tilted plane. Table 1 reports the total number of hourly values of solar radiation collected for each data set. The measurements characterized by a zenith angle greater than 70° have not been considered because of the high experimental uncertainty. Moreover data acquired has been checked using the same criteria as applied by Reindl *et al.* [3]. Data showing a physical violation, such as diffuse fraction (k) greater than one and beam radiation exceeding the extraterrestrial beam radiation, has been deleted from the database. The diffuse fraction (k) is the ratio between the diffuse irradiance and the global irradiance.

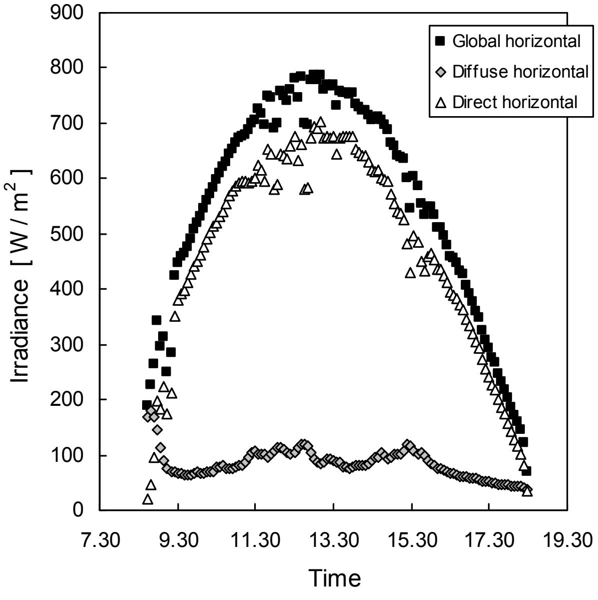

Figure 3. Solar radiation curves (September 8, 2007).

Table 1. Total hourly measurements taken in Padova (latitude 45.4°).

	Total number of points	Number of filtered points
Global radiation on horizontal plane	544	168
Diffuse radiation on horizontal plane	544	168
Global radiation on 20° tilted plane	80	40
Global radiation on 30° tilted plane	464	128

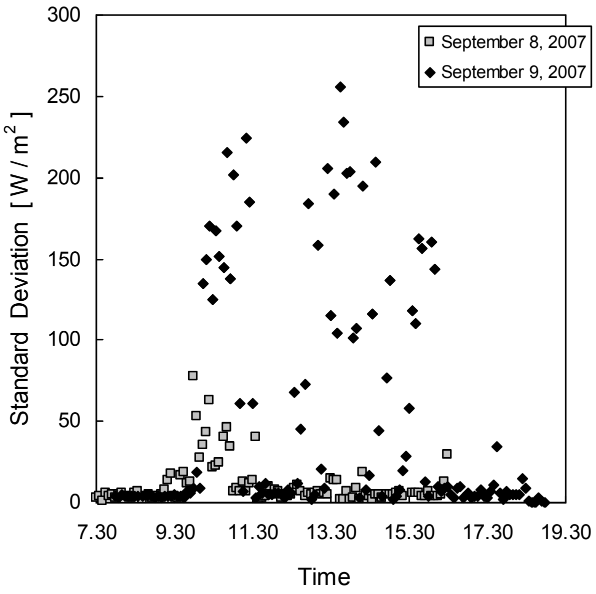

Figure 4. Standard deviation of the global irradiance measurements.

At the same time the data points displaying diffuse fraction lower than 0.90 and clearness index lower than 0.20 and diffuse fraction higher than 0.80 with clearness index greater 0.60 have not been considered. The clearness index (k_t) is defined as the ratio between the global and the horizontal extraterrestrial irradiance. As a result of the filters applied, the number of hourly data points used here is considerably reduced, as reported in table 1.

3.2 Experimental uncertainty in the measurement with pyranometers

In all black thermopile based pyranometers a black painted disk increases its temperature when absorbs the solar radiation.

A thermopile measures the temperature difference between the black surface near the centre of the disk and a reference surface that does not receive the solar radiation.

Table 2. Accuracy of pyranometers.

	CM11	LPPYRA02
Directional response	< ±10 W/m^2	< ±18 W/m^2
Temperature response	< ±1%	< ±4%
Non linearity	< ±0.5%	< ±1%
Spectral response	< ±2%	< ±5%
Tilt response	< ±0.2%	< ±2%
Zero offset A	< ±7 W/m^2	< ±15 W/m^2
Zero offset B	< ±2W/m^2	< ±4 W/m^2
Non stability	< ±0.5%	<±1.5%
Resolution	±1 W/m^2	±5 W/m^2

Figure 5. All black thermopile pyranometer.

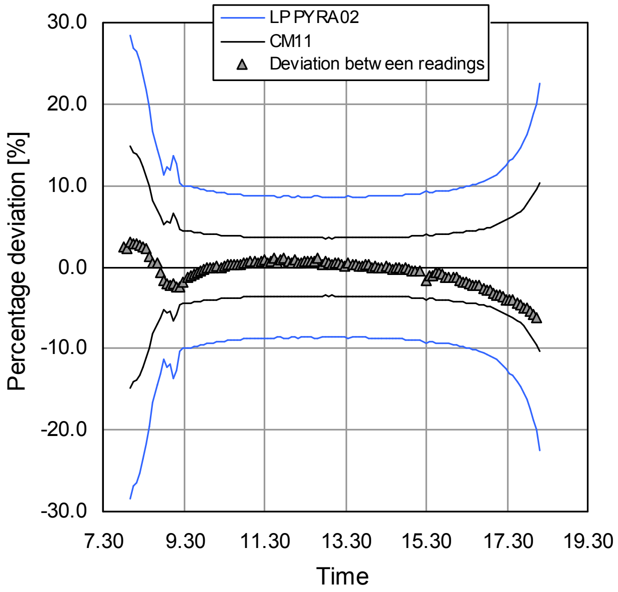

Figure 6. Error bands for a secondary standard (CM11) and a first class (LP PYRA 02) pyranometer and percentage deviation between the instruments. On September 8, 2007.

A thermopile is built connecting in series several thermocouples: in the CM11 type 100 hot and 100 cold junctions are used. Figure 5 shows a picture of the CM11 pyranometer. A black and white sensor instead has alternating black and white receiving elements located on the same disk: hot and cold junctions of the thermopile are in contact with the black and white surfaces respectively. A pyranometer produces an electrical signal proportional to the irradiance: the instrument's response, the ratio between the output voltage and solar irradiance, is expressed as μVm^2/W. The calibration report of the pyranometers provides the sensitivity of the instruments and the procedure used for the calibration. Both the types of pyranometers, installed in the present measuring system, are calibrated with an indoor procedure by comparison with a reference pyranometer, calibrated from year to year by the WRC (World Radiometric Center). The calibration report specifies the accuracy of the reference pyranometer.

The evaluation of the accuracy of the measurement needs to account for all the components of error that are involved in the measurement. These terms are indicated by the manufacturer and depend on the classification of the pyranometer: for each component of error the highest deviation is specified. Table 2 reports a list of the terms of error for both the instruments installed here, as declared by the manufacturer.

The directional error accounts for the cosine and azimuth response. The first one is related with the zenith angle. The azimuth term is due to the imperfections of the glass dome and to the angular reflection properties of the black paint. It is expressed as a fixed value and derives by assuming that the normal incidence responsivity is valid for all the directions. The value indicated refers to a normal beam of 1000 W/m^2. The pyranometer's response depends on the temperature. The maximum deviation for a change in the ambient temperature between -10°C and +40°C is specified in table 2. The non linearity error accounts for the variation of the sensitivity with the irradiance. The spectral response depends on the spectral absorptance of the black coating and on the spectral transmittance of the glass domes. The tilt error considers the deviation in the response due to a change in tilt from 0 to 90° at an irradiance of 1000 W/m^2. Zero offset is the consequence of the lack of thermal equilibrium in the instrument. It can be observed when the sensor does not absorb radiation with wavelengths in the spectral range of the instrument and there is still a signal. All black pyranometers are rarely in thermal equilibrium outdoor: the thermal energy exchanged results in a negative offset. On the contrary pyranometers with black and white receivers show less zero offset because all the junctions of the thermopile see the same ambient. From experimental observations, Myers [4] stated that during clear days an underestimation of the global irradiance has to be expected if the pyranometer has been calibrated using a reference instrument with an all black sensor. From the moment the instrument is exposed to the solar radiation, the sensitivity will deviate with time: this is considered in the non stability term. The resolution is also indicated.

The manufacturer, in agreement with the WMO (World Meteorological Organization), always specifies an achievable experimental uncertainty with 95% confidence level that shall be expected. In the case of hourly measurements it is equal to 3% and 8% for a secondary standard and a first class instrument respectively; for a daily measurement the expanded uncertainty is equal to 3% and 5% respectively. In the daily measurement the accuracy is higher, because in the integration process some response variations cancel out each other. To have a better knowledge of the accuracy, the specific experimental uncertainty should be calculated for each measurement. The analysis of the experimental uncertainty has been performed in agreement with the indications provided in [5], [6].

Accuracy is often specified by two boundaries symmetrically arranged around the "true" value. If the distribution of the measurements is considered as rectangular, the standard uncertainty u is given as:

$$u = \frac{a}{\sqrt{3}} \tag{2}$$

where a is the maximum deviation from the "true" value. The final uncertainty is calculated according to the law of uncertainties combination:

$$u = \sqrt{\sum_i u_i^2} \tag{3}$$

A coverage factor equal to 2 is assumed to expand the uncertainty. Before starting the measurements, the pyranometers have been compared to each other.

Figure 6 reports the percentage deviation between a CM11 secondary standard and a LP PYRA 02 first class pyranometer during a clear sky day. The lines represent the expanded uncertainty (95% confidence level), calculated accounting for the various sources of error listed in table 2. The tilt response is not considered because of the horizontal installation of the pyranometers. The higher values of percentage deviation occur in the first hours of the morning and in the evening, when the solar irradiance is quite low and the zenith angle is higher. For most of the day the expanded uncertainty is around 3.5% for the CM11 pyranometer and around 8.5% for the first class instrument. This is in agreement with the hourly expanded uncertainty declared by the manufacturers. In any case, in the first and last hours of the day it increases abruptly.

3.3 Measurement of the diffuse solar radiation

The diffuse solar irradiance is measured using a first class pyranometer LP PYRA 02 and a shadow band with a polar axis design to block the beam radiation. The occulting band is coated with a black paint to avoid any reflection. This system needs a periodical manual adjustment as the declination of the sun changes in the time. The band obscures a part of the sky, reducing the effective diffuse radiation that reaches the sensor. Thus, a corrective factor which increases the irradiance measured by the pyranometer must be introduced. The best known is the Drummond's correction [7], which can be applied worldwide: it is a geometrical calculation based on the assumption that the diffuse radiation has an isotropic distribution. The portion of the hemispherical radiation screened by the band is:

$$f = \frac{2b}{\pi r}(\cos^3 \delta)(t_0 \sin\phi \sin\delta + \cos\phi \cos\delta \sin t_0) \tag{4}$$

where r is the radius of the shadow band, b the width of the band, t_0 is the sunrise/sunset angle, ϕ the latitude and δ the declination. The isotropic correction C_D is calculated as:

$$C_D = \frac{1}{1-f} \tag{5}$$

Drummond noted that an additional correction was necessary, equal to 7% and 3% for clear and overcast sky conditions, respectively. This is due to the anisotropic distribution shown by the diffuse radiation.

LeBaron *et al.* [8] developed a correction accounting for both the band's geometry and the sky condition, that considers how the diffuse radiation is distributed. The effect of the reflection is considered minimal because of the black paint of the band. Four parameters are used to define the sky condition: the isotropic correction, the zenith angle, and other two parameters indicating the sky's clearness and brightness. The zenith angle is an index of the position of the sun in the vertical plane. All the parameters can be easily calculated by the measurement of the global and uncorrected diffuse irradiance. In this way a variety of states can be identified: totally 256 categories are created as a function of the geometric and sky characteristics. The model was developed using hourly data based on global and normal direct irradiance measurements and it is not dependent on the geographic location. Data of two years from Albany (New York) and Blufield (West Virginia) was used for the development and validation. LeBaron *et al.* [8] found that the model provided a significantly better correction under partially cloudy sky condition, which represents the most anisotropic distribution. A more accurate correction was somewhat found on clear days and low solar zenith angle. A little improvement was observed under overcast conditions because of the isotropic distribution.

Lopez *et al.* [9] compared several shadow band correction models using two independent databases of hourly values from Bracknell (51.4°N, 0.8°W), England, and Beer Sheva (31.4°N, 34.8°E), Israel. Both the databases consisted of measurements of global, beam normal and diffuse irradiance. The Le Baron *et al.* [8] model showed the best results.

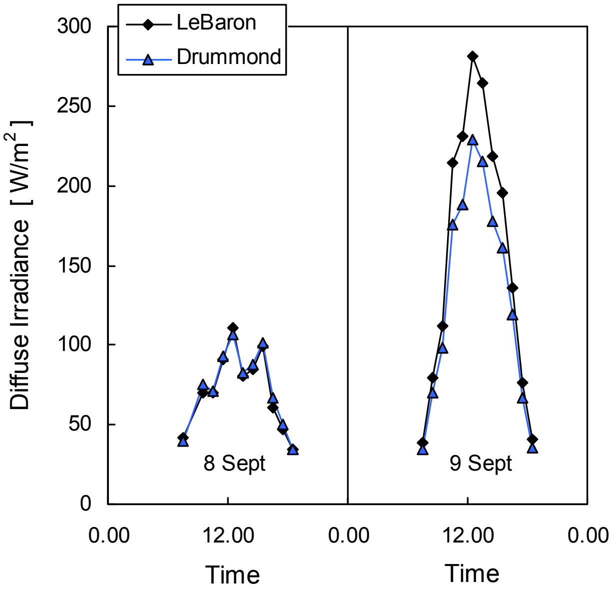

Figure 7. Comparison between the LeBaron *et al.* [8] and Drummond [7] model correction.

Figure 7 shows a comparison between the model by LeBaron *et al.* [8] and the Drummond's correction [7] for the same days considered in figure 4: average hourly values of irradiance are reported. As discussed above, the days considered represent clear and partially cloudy conditions. From figure 4 the anisotropy is evident on September 9: the LeBaron *et al.* [8] model provides a higher correction in this condition. The diffuse irradiance results about 8% higher as compared to the value corrected using the Drummond's model [7].

When the diffuse irradiance is not known it can be calculated using only the measurement of the global irradiance. Several correlations exist in the open literature to evaluate the diffuse fraction as a function of the clearness index. Orgill and Hollands [10] stated the need for a specific correlation to predict the hourly diffuse radiation. Erbs *et al.* [11] developed an empirical correlation to estimate the hourly diffuse fraction as a function of the clearness index, based on data recorded in locations between 31° and 42° of latitude. The solar radiation components were measured following three different methods: with a pyrheliometer, a pyranometer with a shadow band and a pyranometer with an occulting disk. Reindl *et al.* [3] studied the influence of several predicting variables in addition to the clearness index. This is because if for example the clearness index is equal to 0.5, the diffuse fraction can range between 0.2 and 0.8: other variables are necessarily involved. They considered data from five european and north american locations: in the first ones the diffuse radiation was measured by a shaded pyranometer, while in the case of the north american stations the beam component was measured by a pyrheliometer. On the whole they developed three correlations. The first one is based on the clearness index, the solar altitude, the ambient air temperature and the relative humidity. The second is based on the clearness index and the solar altitude; the last one is the classic correlation based only on the clearness index. In the present work the second correlation, named in this work as "Reindl 1", and the third correlation, named as "Reindl 2", are considered.

Figure 8 reports the difference between the calculated and the measured hourly diffuse irradiance against the measured irradiance. The bands of the expanded uncertainty are also drawn. The "Reindl 1" correlation has been used because it considers both the clearness index and the solar altitude. The LeBaron *et al.* [8] model has been used to correct the measurements acquired. When the diffuse irradiance is less than 100 W/m^2 the correlation provides an evident overprediction. But as the level of diffuse irradiance increases most of points are within the experimental uncertainty bands. It should be noted that no data points taken in spring and summer seasons are used here.

In figure 9 data points are plotted against the clearness index. The correlation of "Reindl 2" [3] and Erbs *et al.* [11] are also reported. The critical region is that characterized by the clearness index between 0.7 and 0.8, where both the models overpredict measured data. When the clearness index is lower than 0.7 the agreement improves for both the correlations. However the Erbs *et al.* [11] model seems to describe better the trend of data. It must be underlined that Erbs *et al.* [11] found that their correlation overpredicted the diffuse radiation in the autumn and winter season, while underpredicted in the spring and summer.

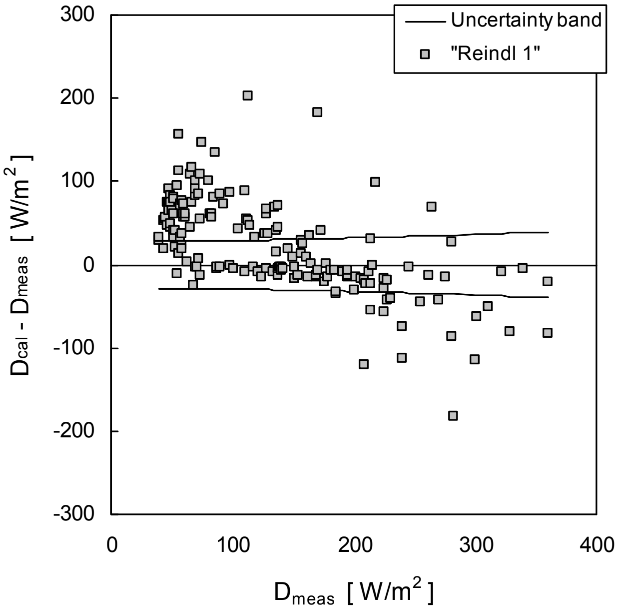

Figure 8. Difference between calculated and measured diffuse irradiance against measured irradiance. Calculated values are obtained from the "Reindl 1" model [3].

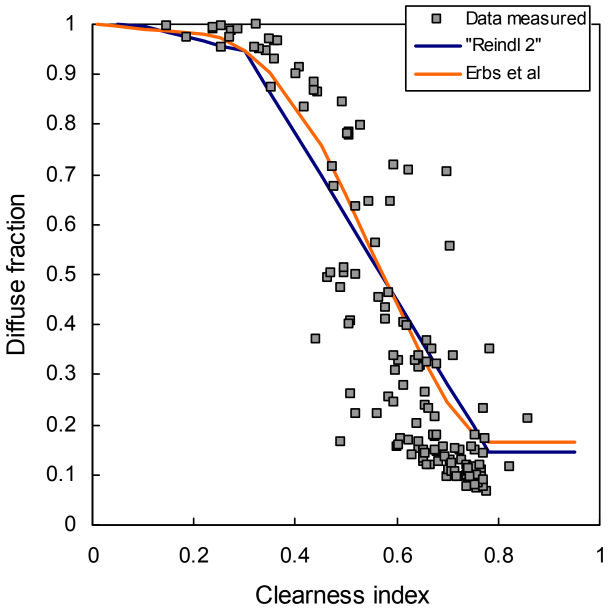

Figure 9. Hourly diffuse fraction vs. clearness index: experimental data, “Reindl 2” [3] and Erbs *et al.* [11] models.

From the analysis of the graphs, all the models considered here provide an overprediction of the experimental data when sky conditions are characterized by high clearness index and low diffuse fraction. When the diffuse fraction increases, which corresponds to higher measured diffuse irradiance, the models perform better. Finally, it is important to observe that Myers [4] measured the clear sky diffuse irradiance with an all black and a black and white pyranometer. The all black instrument provided an approximately constant underestimation of 20 W/m^2 because of the thermal offset.

3.4 Solar irradiance on the tilted plane

The accurate knowledge of the solar radiation on the sloped surface is crucial to optimize the design and the analysis of thermal and photovoltaic systems. Figure 10 shows the solar radiation curves measured on the horizontal surface and on the photovoltaic module’s plane, tilted of 20°. During most of the day, when the irradiance reaches the higher levels, the tilted surface manages to capture a higher solar radiation as compared to the horizontal plane. The optimal slope for solar installations has always to be searched.

The measurements of the global and diffuse radiation obtained from the pyranometers installed on the horizontal are used here to calculate the solar radiation on the tilted plane. The values calculated are compared with those directly measured on the module’s plane by the CM11 pyranometer. The model developed by Liu and Jordan [12] is adopted for this purpose. The model considers the radiation on the tilted surface made by three components: the beam radiation, the diffuse radiation and the radiation diffusely reflected by the ground. Supposing an isotropic distribution of the diffuse radiation, the ratio between the global radiation on the tilted plane and the global radiation on the horizontal can be expressed as:

$$R = \frac{B}{G} R_b + \frac{D}{G}\left(\frac{1+\cos\beta}{2}\right) + \rho\left(\frac{1-\cos\beta}{2}\right) \tag{6}$$

where R_b is the ratio between the beam radiation on the tilted surface and the beam radiation on the horizontal; β is the tilt angle of the surface and ρ is the reflectance. The factor R_b can be calculated as:

$$R_b = \frac{B_n \cos\theta_\beta}{B_n \cos\theta} \tag{7}$$

The term R_b can be obtained as a function of the latitude, hour angle and tilt angle [12]. A value of the reflectance equal to 0.2, suggested in absence of snow, is used in the present calculations.

Figure 11 reports the comparison between the hourly irradiance measured on the tilted plane and that obtained from the measurement of the global and the diffuse radiation on the horizontal. The expanded uncertainty bands of the CM11 pyranometer are also drawn.

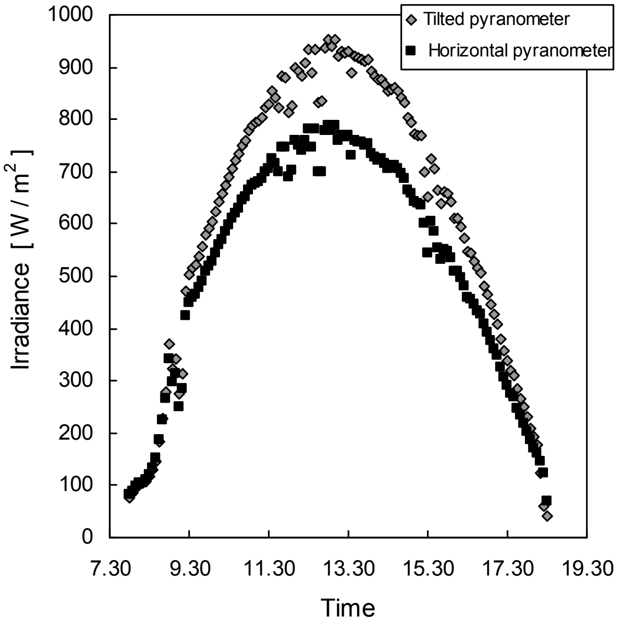

Figure 10. Solar irradiance measured on the tilted and horizontal plane (tilt angle: 20°); measurements are taken with secondary standard CM11 pyranometers (September 8, 2007).

Table 3. Prediction of the irradiance on the tilted plane.

	MBE [W/m^2]	RMSE [W/m^2]	MD [%]	MAD [%]
Measured values	-17	51	-3.2	8.5
Orgill and Hollands [10]	-35	73	-4.3	11.4
Erbs *et al.* [11]	-30	69	-4	10.7
"Reindl 1" [3]	-29	68	-3.5	10.5
"Reindl 2" [3]	-32	70	-3.8	10.8

Data refers to tilt angle of 20° and 30°. Most of the points are within the experimental uncertainty of the measurement: this also confirms the consistency of the experimental data. As the diffuse radiation on the horizontal is often unknown, it is also interesting to calculate the hourly solar irradiance on the tilted plane using the experimental value of the global radiation on the horizontal and estimating the diffuse irradiance by means of correlations. The diagram in figure 12 plots the comparison between the hourly irradiance measured on the tilted surface and that calculated using the "Reindl 1" correlation [3] for the evaluation of the diffuse component. A slight underprediction of data is shown, above all at higher values of irradiance.

Table 3 reports the mean bias error MBE, the root mean square error RMSE, the mean deviation MD and the mean absolute deviation MAD obtained in the prediction of the irradiance on the tilted plane. The case named as "measured values" refers to the irradiance calculated using both the measurements of the global and diffuse irradiance on the horizontal. In the other cases, the global radiation is known from experimental values while the diffuse radiation is calculated by means of the specified correlation.

CONCLUSIONS

The new laboratory for the study of the solar energy conversion installed at the Dipartimento di Fisica Tecnica of the University of Padova has been presented. The measurement of the solar radiation has been discussed in the present paper, paying attention to the experimental accuracy. In the case of the hourly measurements, during the central part of the day, the expanded uncertainty has been shown to be consistent with that declared by the manufacturers. Much care has to be paid to the readings in the first and last hours of the day because the accuracy falls down abruptly. If the diffuse radiation is measured by a pyranometer shaded by a band, the choice of the model to correct the measurements is very important. During the days characterized by evident anisotropic conditions, the LeBaron *et al.* model [8] has provided a correction by 8% higher than that given by the Drummond isotropic model [7].

The experimental diffuse hourly irradiance has been compared against some empirical correlations available in the open literature. The comparison has shown some disagreement in the case of high values of clearness index and low values of diffuse irradiance.

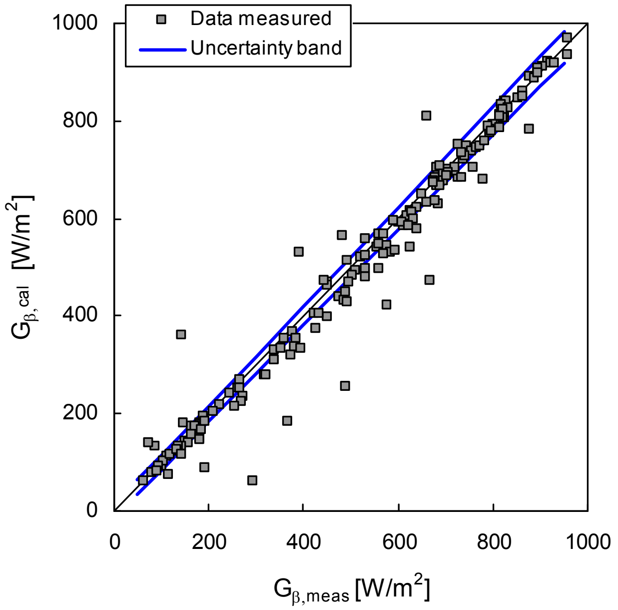

Figure 11. Comparison between the irradiance calculated with equations 6-7 (Liu and Jordan model [12]) and the irradiance measured on the tilted plane. The global and diffuse irradiance on the horizontal is measured.

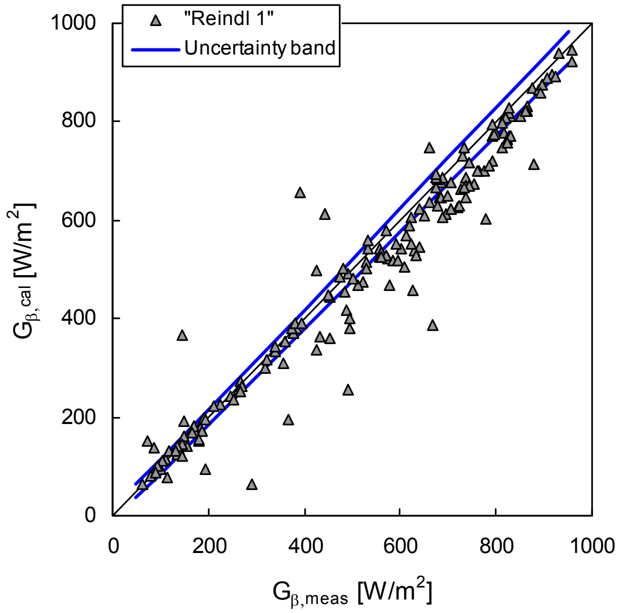

Figure 12. Comparison between the solar irradiance calculated with eq. 6-7 (Liu and Jordan model [12]) and the irradiance measured on the tilted plane. The global irradiance in eq. 6 is the measured value on the horizontal while the diffuse irradiance is estimated with the "Reindl 1" correlation [9].

In the other cases a reasonably agreement has been found between correlations and experimental data.

Finally, the measurements taken on the horizontal have been used to estimate the irradiance on the tilted plane of photovoltaic modules or thermal collectors. The values calculated have been compared against those directly measured using a pyranometer installed on the tilted plane and a satisfactory agreement has been found. The same comparison has been performed using only the measurements of the global radiation: the diffuse radiation has been calculated from some diffuse fraction empirical correlations. A reasonable agreement was obtained, with no significant influence of the different correlation adopted. However, as it can be observed in table 3, the Liu and Jordan model [12] provides an underestimation of solar radiation captured by the inclined surface. As a further step, this database will be also compared against models which consider diffuse solar radiation as anisotropic, as the Perez *et al.* model [13]. Future work will be also addressed to enlarge the database collected in order to obtain a comprehensive comparison with available long term solar data.

NOMENCLATURE

a	maximum deviation from the "true" value, [%] or [W/m^2]
B	direct solar irradiance, [W/m^2]
b	width of the shadow band, [m]
C_D	Drummond's correction
D	diffuse solar irradiance, [W/m^2]
f	fraction of the hemispherical irradiance blocked by the shadow band, Drummond's model
G	global solar irradiance, [W/m^2]
k	diffuse fraction = ratio between diffuse irradiance and global irradiance
k_t	clearness index = ratio between global irradiance on the horizontal plane and extraterrestrial irradiance on the horizontal plane
MAD	mean absolute deviation $= (1/Np)\sum[\,|G_{\beta,cal} - G_{\beta,meas}|/G_{\beta,meas}]100$, [%]
MBE	mean bias deviation $= \sum(G_{\beta,cal} - G_{\beta,meas})/N_p$, [W/m^2]
MD	mean deviation $= (1/Np)\sum[(G_{\beta,cal} - G_{\beta,meas}) / G_{\beta,meas}]100$, [%]
N_p	number of experimental points
r	radius of the shadow band, [m]
RMSE	root mean square error $[\sum(G_{\beta,cal} - G_{\beta,meas})^2/N_p]^{1/2}$, [W/m^2]
u	standard uncertainty, [%] or [W/m^2]
t_0	sunrise (sunset) angle, [rad]

Greek symbols

β	tilt angle [rad]
δ	declination [rad]
θ	angle of incidence of the solar radiation [rad]
ρ	reflectance
ϕ	latitude [rad]

Subscripts

cal	calculated
meas	measured
n	normal direction
β	tilted plane

ACKNOWLEDGMENTS

The authors would like to acknowledge the financial support of the Italian Fondazione per l'Università e l'Alta Cultura in Provincia di Belluno.

REFERENCES

[1] EN 12975-2, 2006. "Thermal solar systems and components - Solar collectors - Part 2: Test methods."

[2] Del Col, D., and Padovan, A., 2007, "New experimental apparatus for testing the performance of solar collectors", Proceeding of 62th Congresso Nazionale ATI, Salerno, 2, pp.635-640.

[3] Reindl, D. T., Beckman, W. A., and Duffie, J. A., 1990, "Diffuse fraction correlations", Solar Energy, 45(1), pp. 1-7.

[4] Myers, D. R., 2005, "Solar radiation modeling and measurements for renewable energy applications: data and model quality", Energy, 30, 1517-1531.

[5] ISO, 1995 "Guide to the Expression of Uncertainty in Measurement".

[6] Mathioulakis, E., Voropoulos, K., and Belessiotis, V., 1999, "Assessment of uncertainty in solar collector modeling and testing", Solar Energy, 66(5), pp. 337-347.

[7] Drummond, A. J., 1956, "On the measurements of sky radiation", Arch. Meteor. Geophys. Bioklim, 7, 413-436.

[8] LeBaron, B. A., Michalsky, J. J., and Perez, R., 1990, "A simple procedure for correcting shadowband data for all sky conditions", Solar Energy, 44(5), pp. 249-256.

[9] Lopez, G., Muneer, T., and Claywell, R., 2004, "Assessment of four shadow band correction models using beam normal irradiance data from the United Kingdom and Israel", Energy Conversion and Management, 45, pp. 1963-1979.

[10] Orgill, J. F., and Hollands, K. G. T., 1977, "Correlation equation for hourly diffuse radiation on a horizontal surface", Solar Energy, 19, pp. 357-359.

[11] Erbs, D. G., Klein, S. A., and Duffie, J. A., 1982, "Estimation of the diffuse radiation fraction for hourly, daily and monthly-average global radiation", Solar Energy, 28(4), pp. 293-302.

[12] Duffie, J. A., and Beckman, W. A., 1980, "Solar Engineering of Thermal Processes", John Wiles & Sons, Chap. 2.

[13] Perez, R., Seals, R., Ineichen, P., Stewart, R., and Menicucci, D., 1987, "A new simplified version of the Perez diffuse irradiance model for tilted surfaces", Solar Energy, 39(3), pp. 221-231.